STUDYING INTERSTELLAR PLASMA TURBULENCE THROUGH PRECISION FARADAY ROTATION MEASUREMENTS OF EXTRAGALACTIC RADIO SOURCES

by

Anthony Minter

An Abstract

Of a thesis submitted in partial fulfillment
of the requirements for the Doctor of
Philosophy degree in Physics
in the Graduate College of
The University of Iowa

August 1995

Thesis supervisor: Professor Steven R. Spangler

ABSTRACT

The Faraday rotation measures of 38 extragalactic sources have been measured in order to provide new information on the properties of plasma turbulence in the Interstellar Medium. Of particular interest is the possibility that such Faraday Rotation measurements can provide information on the magnetic field component of interstellar turbulence. The observations were made in an area of the sky that is unique in that it is the only region away from the galactic plane where the Hα intensity has been mapped completely, both spatially and in velocity. A portion of the thesis work consisted of the development of a new and more realistic model for the ionospheric contribution to the rotation measure.

The rotation measures were found to vary in a relatively smooth fashion across the entire region. The structure functions of rotation measure and emission measure were analyzed in order to extract information on the nature of the plasma turbulence in the interstellar medium. This analysis was carried out by comparing the observed rotation measure and emission measure structure functions with theoretical expressions developed here for the first time. The measured structure functions for angular lags $\delta\theta > 1.0°$ are consistent with two dimensional turbulence for both the magnetic field and plasma density. A model with Kolmogorov turbulence with an outer scale of 3 pc being contained inside of thin sheets is found to be consistent with the data. For all angular scales, the level of the rotation measure structure

function is larger than would be expected from only plasma density fluctuations in an otherwise uniform galactic magnetic field. The data require, in addition to the plasma density fluctuations, a turbulent magnetic field with an RMS amplitude of ~ 1 μG. To the author's knowledge, this represents the first measurement of magnetic field fluctuations in the interstellar plasma on spatial scales which appropriately may be described as turbulence. The data are consistent with a model in which a transition from isotropic to two dimensional turbulence occurs on spatial scales of about 3 parsecs. This transition scale is interpreted as the thickness of sheets containing the turbulence.

Abstract approved: _____
Thesis supervisor

_____
Title and department

_____
Date

STUDYING INTERSTELLAR PLASMA TURBULENCE THROUGH PRECISION FARADAY ROTATION MEASUREMENTS OF EXTRAGALACTIC RADIO SOURCES

by

Anthony Minter

A thesis submitted in partial fulfillment
of the requirements for the Doctor
of Philosophy degree in Physics
in the Graduate College of
The University of Iowa

August 1995

Thesis supervisor: Professor Steven R. Spangler

To Mali “Con Queso”

"Man may penetrate the outer reaches of the universe, he may solve the very secret of eternity itself, but for me, the ultimate human experience is to witness the flawless execution of a hit-and-run."

Branch Rickey, The Official Major League Baseball 1993 Calendar

ACKNOWLEDGMENTS

I would like to thank my advisor, Dr. Spangler, for his guidance and tutelage throughout my graduate school years. Thanks goes to Dr. Molnar for his helpful discussions on error analysis and the structure of the Milky Way. Dr. Fix deserves much credit for helping me keep my sanity during my studies through his many baseball trivia questions. Dr. Mutel also deserves thanks for his helpful discussions. I would also like to thank Dr. Goertz for his help with finding a suitable model for the ionosphere to use in my thesis research. I am also indebted to Dr. Nicholson, Dr. Spangler and Dr. Dennison of Virginia Tech for their extraordinary efforts that have allowed me to pursue my graduate studies at the University of Iowa.

I would like to thank Dr. R. J. Reynolds of the University of Wisconsin for allowing me have machine readable copies of his H_α data. Dr. Simonetti of Virginia Tech deserves thanks for providing helpful notes.

I also thank Dr. Carl Bignell of NRAO for discussions concerning the polarization calibration of data obtained with the VLA.

There are many friends who deserve acknowledgment. I thank Dave Dunn for his shared enthusiasm for sports. Mike LeDocq for living with and putting up with me for several years and for being an unknowing participant in the great duct tape incident. Mark Mulhern for teaching me how to speak Minnesotain, for providing an endless amount of entertainment and for being an adamant victim in the duct tape incident. Tracy Ellis for his stoic and noble demeanor while putting up with me as his officemate. Julia Andersen for many interesting discussions and also putting up with me as her officemate. Chris Halas deserves much credit for her great parties,

undaunting friendship and her moral support. Kim Leo deserves thanks for being the inspiration for many ice cream trips. Remember, no hot fudge on your soft serve! Ralph Lano for being my roommate and for not stabbing anyone while peeling his apples. Bill Theisen for his love of ultimate. Finally, Jim Thompson deserves thanks for being everyones scapegoat as well as a good friend.

Very special thanks goes to Mali. Without you none of this would have any meaning! Also my spelling and grammar would have also have been much worse. You have provided me with much support and understanding. I am eternally indebted to you.

I would also like to thank my parents for everything they have done for me over the years. I would especially like to thank my mother for all the transportation services she has provided over the years and my father for throwing ball with me until his shoulder was numb. Without you none of this would have been possible.

ABSTRACT

The Faraday rotation measures of 38 extragalactic sources have been measured in order to provide new information on the properties of plasma turbulence in the Interstellar Medium. Of particular interest is the possibility that such Faraday Rotation measurements can provide information on the magnetic field component of interstellar turbulence. The observations were made in an area of the sky from $1^h\ 50^m$ to $3^h\ 10^m$ Right Ascension, and from $32°$ to $44°$ Declination. This area is unique in that it is the only region away from the galactic plane where the Hα intensity has been mapped completely, both spatially and in velocity. A portion of the thesis work consisted of the development of a new and more realistic model for the ionospheric contribution to the rotation measure.

The rotation measures were found to vary in a relatively smooth fashion across the entire region. Simple galactic models for the rotation measure did not provide an entirely satisfactory representation of the observed rotation measures. We attribute this to plasma structures smaller than galactic scales, but larger than turbulent variations. The structure functions of rotation measure and emission measure were analyzed in order to extract information on the nature of the plasma turbulence in the interstellar medium. This analysis was carried out by comparing the observed rotation measure and emission measure structure functions with theoretical expressions developed here for the first time. The measured structure functions for angular lags $\delta\theta > 1.0°$ are consistent with two dimensional turbulence for both the magnetic field and plasma density. A model with Kolmogorov turbulence with an outer scale of 3 pc being contained inside of thin sheets is found to be consistent

with the data. For all angular scales, the level of the rotation measure structure function is larger than would be expected from only plasma density fluctuations in an otherwise uniform galactic magnetic field. The data require, in addition to the plasma density fluctuations, a turbulent magnetic field with an RMS amplitude of ~ 1 μG. To the author's knowledge, this represents the first measurement of magnetic field fluctuations in the interstellar plasma on spatial scales which appropriately may be described as turbulence. The data are consistent with a model in which a transition from isotropic to two dimensional turbulence occurs on spatial scales of about 3 parsecs. This transition scale is interpreted as the thickness of sheets containing the turbulence.

TABLE OF CONTENTS

LIST OF TABLES

LIST OF FIGURES

CHAPTER 1
INTRODUCTION

There are many processes in the interstellar medium (ISM) in which electron density and magnetic field fluctuations associated with interstellar turbulence play an important role. Electron density fluctuations in our galaxy affect the propagation of radio waves through the ISM and introduce noise signals in radio astronomical measurements. Cosmic ray acceleration and diffusion depend on the magnetic component of this turbulence (Chevalier and Fransson 1984). The dissipation of this turbulence might play an important role in the heating of the ISM; with the importance of turbulent heating being dependent on the mode structure of the turbulence and the value of its outer scale (McIvor 1977, Cesarsky 1980, Spangler 1991). The fluctuations in the galactic magnetic field may also be important in the galactic dynamo mechanism, as well as playing an important role in the star formation process.

Recently, Armstrong et al. (1995) have presented observational evidence that a single power law spectrum can describe the observed electron density fluctuations on scale lengths from $\sim 10^{10}$ cm (perhaps down to 10^6 cm) to an outer scale $\gtrsim 10^{20}$ cm. Scale lengths of 10^{10} cm to 10^{15} cm have been extensively investigated via observations of pulsars and compact extragalactic radio sources; it is on these scales that the evidence for a Kolmogorov spectra with an index of 3.7 is most secure. The evidence compiled by Armstrong et al. (1995) is suggestive of a spectral cascade in which turbulent energy is transferred between adjacent spatial

scales. However, there is no direct evidence that such a cascade is occurring in the interstellar medium, nor even that the fluctuations on widely disparate scales are related. The power law nature of the spectrum has not been determined as securely near the outer scale. The 10^{18} cm to 10^{20} cm scale regime can be explored using interstellar cloud densities, gradients in the average electron density, emission measure (EM) fluctuations and rotation measure (RM) fluctuations of extragalactic radio sources as discussed in Armstrong et al. (1995). Since we will be concerned with the determination of turbulence properties from measurements of the Faraday rotation measure and the emission measure, it is worth defining these quantities at the outset and reviewing how their measurement has allowed the deduction of turbulence characteristics. A number of observable astronomical quantities, such as the intensity of an emission line or the intensity of free-free emission, are dependent on the emission measure, EM, defined as

$$\mathrm{EM} = \int_0^{\mathrm{L}} \mathrm{n_e^2}\ \mathrm{ds}. \tag{1.1}$$

When a linearly polarized radio wave propagates through a plasma permeated by a magnetic field, the polarization position angle is rotated by an amount which depends on a quantity termed the rotation measure, RM,

$$\chi(\mathrm{L}) = \chi_\mathrm{o} + \mathrm{RM} \cdot \lambda^2 \tag{1.2}$$

where the rotation measure is given by,

$$\mathrm{RM} = \frac{\mathrm{e}^3}{2\pi \mathrm{m_e^2 c^4}} \int_0^{\mathrm{L}} \mathrm{n_e}\ \vec{\mathrm{B}} \cdot \vec{\mathrm{ds}}. \tag{1.3}$$

The physics of Faraday rotation are discussed in Davies (1965) and Thompson et al. (1991). These references discuss the conditions for the validity of equations (1.2)

and (1.3), particularly the validity of the quasi-longitudinal approximations. The quasi-longitudinal approximation is highly satisfied for the frequencies of observations and ISM phases considered in this thesis. In equations (1.1) through (1.3), e and m_e are the charge and mass of an electron, c is the speed of light, λ is the wavelength of the observation and L is the distance through the medium to the source. The polarization position angle is denoted by χ; χ_o indicates the value which would be measured prior to propagation through the magnetized interstellar medium. The emission measure is typically given in units of pc cm^{-3} and the rotation measure can be expressed as

$$RM = 0.81 \int_0^L n_e(cm^{-3}) \vec{B}(\mu G) \cdot \vec{ds}(pc) \tag{1.4}$$

with the units being rad m^{-2}. For the case of a turbulent plasma, the density and magnetic field will be of the form $n_e = n_o + \delta n$ and $\vec{B} = \vec{B_o} + \delta\vec{B}$, where a subscript "o" indicates the static or large scale quantity, and δn and $\delta\vec{B}$ are the fluctuating, zero mean quantities associated with turbulence. As may be seen from equations (1.1) and (1.2), the turbulent fluctuations δn and $\delta\vec{B}$ will induce fluctuations in the emission measure and the rotation measure. Simonetti et al. (1984), Lazio et al. (1990) and Clegg et al. (1992) have used rotation measure fluctuations to study the ISM turbulence, but have only put lower limits on the outer scale of $\sim 10^{18}$ cm. Virtually all previous studies of interstellar turbulence via radio propagation measurements have constrained only the plasma density fluctuations.

Another extremely important feature of the interstellar turbulence to determine is the magnitude of magnetic field fluctuations, and perhaps velocity fluctuations. In the case of the solar wind, where we have direct measurements, the turbulent energy density is dominated by magnetic field fluctuations and velocity fluctuations, with density fluctuations being a dynamically unimportant tracer (Marsch 1991).

An understanding of interstellar turbulence and an assessment of its role in the interstellar medium will require measurements of the magnetic field fluctuations $\delta\vec{\mathrm{B}}$, and that of the velocity $\delta\vec{\mathrm{v}}$.

As discussed previously by Simonetti and Cordes (1984), and elaborated at length below, rotation measure fluctuations are caused by both δn and $\delta\vec{\mathrm{B}}$. However, with only Faraday rotation measurements, it is impossible to determine the relative contributions of the two types of fluctuations. However, variations in the emission measure can be measured on the same spatial scales as the rotation measure, and this quantity is exclusively dependent on the spectral characteristics and spatial distribution of δn.

In this thesis we present new observational results which we hope will further the understanding of interstellar turbulence. We have made high precision rotation measure measurements of 38 extragalactic sources in order to determine the properties of the electron density and magnetic field fluctuations on spatial scales of 10^{17} cm to 10^{20} cm. All of the extragalactic sources lie in the region from $1^{\mathrm{h}}\ 50^{\mathrm{m}}$ to $3^{\mathrm{h}}\ 10^{\mathrm{m}}$ right ascension and 32° to 44° declination. The unique attribute of this part of the sky is that the H_{α} intensity (and thus the emission measure) has been mapped out, both spatially and in velocity (Reynolds 1980). The basic data in this thesis consists of precision Faraday rotation measurements of extragalactic radio sources. An important aspect of the calibration of such observations is an accurate removal of the rotation due to the Earth's ionosphere. We have thus developed a new model for the precision removal of ionospheric Faraday rotation. We have applied our model to two sets of VLA observations.

With a combination of rotation measure and emission measure measurements it is possible to estimate the electron density and magnetic field power spectra separately. We compute spatial structure functions rather than spatial power spectra,

since the former are more conveniently calculated in the case of sparse, unevenly sampled data. The rotation measure structure function (D_{RM}) is defined as follows:

$$D_{RM}(\delta\theta) = \left\langle [RM(\theta) - RM(\theta + \delta\theta)]^2 \right\rangle \tag{1.4}$$

where the brackets represent an ensemble average, θ is any line of sight and $\delta\theta$ is the separation between any two lines of sight. D_{RM} is assumed to be independent of position and orientation (i.e. it is homogeneous and isotropic). The emission measure structure function (D_{EM}) is defined in a similar manner as D_{RM}.

The outline of the thesis is as follows. In Chapter 2 we describe in full detail the AIPS model for ionospheric Faraday rotation calibration and the improved ionospheric Faraday rotation model that we have developed. A comparison of these two models is also presented in Chapter 2. In Chapter 3 the observations and calibrations of the 38 extragalactic radio sources is presented. The results of the observations and a brief description of each source is presented in Chapter 4. Using a simple model for the galactic structure of n_e and $\vec{B}$, we predict the smoothly varying component of the rotation measure and emission measure in Chapter 5. The measured structure functions for rotation measure and emission measure are presented in Chapter 6 along with theoretical expressions for the rotation measure and emission measure. The measure structure functions are also compared to the theoretical expressions in Chapter 6. The heating of the interstellar medium due to magnetohydrodynamical waves which comprise the turbulence is discussed in Chapter 7. Finally, our conclusions are presented in Chapter 8.

CHAPTER 2
CORRECTIONS OF RADIOASTRONOMICAL OBSERVATIONS FOR IONOSPHERIC FARADAY ROTATION

2.1 Introduction

Historically, the Astronomical Imaging Processing System (AIPS) of the National Radio Astronomy Observatory used measurements of the total electron content (TEC) of the ionosphere (i.e. column density towards the zenith) to estimate the ionospheric contribution to the rotation measure for an astronomical source. The ionospheric measurements used Faraday rotation of a geosynchronous spacecraft signal to determine the TEC of the ionosphere. This procedure had the virtue that the ionospheric measurements and the observables to be corrected both involved the same physical process, Faraday rotation. The TEC values, however, have not been available to the VLA since March 1990 due to the demise of the satellite which served as the trans-ionospheric beacon. In the absence of a direct measurement of the TEC, it is important to develop a reliable theoretical model. A desirable feature of such a model should be the ability to accommodate input information which can improve the a priori model of the ionosphere.

In this chapter we will discuss the removal of the ionospheric Faraday rotation from observations made with the Very Large Array. In section 2.2 we will briefly discuss the structure of the ionosphere. A review of the response to and calibration of polarization data with the Very Large Array will be presented in section 2.3. The AIPS model for ionospheric Faraday rotation will be reviewed in section 2.4.

Although the AIPS model for ionospheric Faraday rotation works well as a first order correction and is entirely adequate for most VLA applications, we will show that this model has several shortcomings, especially when no TEC values are available. In section 2.5 we will introduce a new model for Ionospheric Faraday rotation based on the International Reference Ionosphere model (Rawer and Bilitza 1989) and the International Geomagnetic Reference Field model (Peddie 1982). The development of this model is motivated by the need for higher precision removal of ionospheric Faraday rotation from radioastronomical observations and for the need of a model which could also be applied to VLBA and VLBI observations. Finally, in section 2.6 we will present a comparison of the AIPS ionospheric Faraday rotation model with that developed in this thesis and described in section 2.5.

2.2 The Structure of the Ionosphere

Since the objective of this work is to study the plasma turbulence characteristics of the interstellar medium of our galaxy, it is necessary to remove the Faraday rotation caused by the Earth's ionosphere from the data. The interplanetary and intergalactic medium make negligible contributions to to the observations discussed in Chapter 3 and thus can be ignored. Faraday rotation within the source itself is potentially a concern, but as will be discussed in Chapter 3, it appears to be negligible for the sources and observations considered in this thesis. The ionosphere results from the ionization of the Earth's upper atmosphere by ultraviolet and x-ray radiation from the sun and to a smaller extent from cosmic rays. The ionosphere is influenced by winds, turbulence, traveling disturbances and by variations in the geomagnetic field. The ionospheric electron density and TEC are thus subject to diurnal and seasonal variations as well as having dependences on geomagnetic latitude and the sunspot cycle of the sun.

A typical daytime and nighttime profile of electron density in the Earth's ionosphere during a period of high solar activity is shown in Figure 2-1 as determined using the International Reference Ionosphere model (Rawer and Bilitza 1989). The structure of the ionosphere is separated into four main regions called the D, E, F and topside regions. These regions may be further divided into several re-occurring features such as the F1 and F2 layers. These features are labeled in Figure 2-1. The D region lies between 75 and 95 km above the Earth's surface. The E region is between 95 and 150 km above the Earth. The F region lies above 150 km up to the peak electron density altitude. The F1 layer is a stratification feature that regularly occurs at temperate latitudes. The F2 layer consists of the peak of the electron density in the ionosphere. Finally the topside region lies above the peak in the F2 layer and extends upward as high as 1100 km. Since the ionosphere is also permeated by the geomagnetic field, Faraday rotation will occur for linearly polarized radio waves propagating through the ionosphere. The ionospheric Faraday rotation typically amounts to a rotation of $5^\circ - 15^\circ$ in the polarization position angle for observations at 1.4 GHz. During periods of high solar activity (i.e. near solar maximum) the amount of rotation can be even greater, reaching values as high as 50°.

2.3 Polarimetry With the Very Large Array

We will now briefly discuss the response of an interferometer such as the Very Large Array (VLA)[1] to a polarized signal. This discussion is obtained in part from the discussion presented in Sakurai and Spangler (1994). It will be assumed that the reader has a basic understanding of both interferometry and polarimetry. The

[1] The Very Large Array is operated by the National Radio Astronomy Observatory, under contract from the National Science Foundation.

VLA antennas are each equipped with a right and left circularly polarized receiver. The outputs from these receivers are given by

$$V_R = G_R \left[E_R e^{i(-\psi+\theta_R)} + D_L E_L e^{i(\psi+\theta_L)} \right] \tag{2.1a}$$

and

$$V_L = G_L \left[E_L e^{i(\psi+\theta_L)} + D_R E_R e^{i(-\psi+\theta_R)} \right] \tag{2.1b}$$

where G_R and G_L are the right and left complex gains, E_R and E_L are the right and left circular components of the electric field due to the source, ψ is the parallactic angle, θ_R and θ_L are the phase shifts due to propagation through the Earth's ionosphere and D_R and D_L are the complex polarization leakage terms (Bignell 1982). The D terms account for the fact that the feeds are not exactly orthogonal and for other imperfections in the antenna so that a small amount of right circular polarization shows up in the left circular polarization channel and vice versa. The complex gains, G_R and G_L, contain all amplitude and phase shifts that affect the signal due to the instrumentation.

The actual measured quantities in an interferometer are the cross-correlations of receiver outputs between pairs of antennas. The correlator outputs for two antennas i and j for a simple two element interferometer and a point source are given as

$$\begin{aligned} V_{Ri} V_{Rj}^* = G_{Ri} G_{Rj}^* \big(& E_{Ri} E_{Rj}^* + E_{Ri} E_{Lj}^* D_{Rj}^* e^{-i\phi} \\ & + E_{Li} E_{Rj}^* D_{Ri} e^{i\phi} + E_{Li} E_{Lj}^* D_{Ri} D_{Rj}^* \big) \end{aligned} \tag{2.2a}$$

$$\begin{aligned} V_{Li} V_{Lj}^* = G_{Li} G_{Lj}^* \big(& E_{Li} E_{Lj}^* + E_{Li} E_{Rj}^* D_{Lj}^* e^{i\phi} \\ & + E_{Ri} E_{Lj}^* D_{Li} e^{-i\phi} + E_{Ri} E_{Rj}^* D_{Li} D_{Lj}^* \big) \end{aligned} \tag{2.2b}$$

$$\begin{aligned} V_{Ri} V_{Lj}^* = G_{Ri} G_{Lj}^* \big(& E_{Ri} E_{Lj}^* e^{-i\phi} + E_{Ri} E_{Rj}^* D_{Lj}^* \\ & + E_{Li} E_{Lj}^* D_{Ri} + E_{Li} E_{Rj}^* D_{Ri} D_{Lj}^* e^{i\phi} \big) \end{aligned} \tag{2.2c}$$

$$V_{Li}V_{Rj}^{*} = G_{Li}G_{Rj}^{*}\left(E_{Li}E_{Rj}^{*}e^{i\phi} + E_{Li}E_{Lj}^{*}D_{Rj}^{*} + E_{Ri}E_{Rj}^{*}D_{Li} + E_{Ri}E_{Lj}^{*}D_{Li}D_{Rj}^{*}e^{-i\phi}\right) \tag{2.2d}$$

where an asterisk denotes complex conjugation and $\phi = 2\left(\psi - \theta_{FR}\right)$ with the Faraday rotation due to the Earth's ionosphere being given by $\theta_{FR} = \left(\theta_R - \theta_L\right)/2$. The correlator outputs can be rewritten in terms of the more familiar Stokes parameters (Kraus 1986)

$$I = E_{Ri}E_{Rj}^{*} + E_{Li}E_{Lj}^{*} \tag{2.3a}$$

$$V = E_{Ri}E_{Rj}^{*} - E_{Li}E_{Lj}^{*} \tag{2.3b}$$

$$Q = E_{Ri}E_{Lj}^{*} + E_{Li}E_{Rj}^{*} \tag{2.3c}$$

$$U = i\left(E_{Li}E_{Rj}^{*} - E_{Ri}E_{Lj}^{*}\right) \tag{2.3d}$$

so that equations (2.2) become

$$V_{Ri}V_{Rj}^{*} = \frac{1}{2}\left[I + V\right] \tag{2.4a}$$

$$V_{Li}V_{Lj}^{*} = \frac{1}{2}\left[I - V\right] \tag{2.4b}$$

$$V_{Ri}V_{Lj}^{*} = \frac{1}{2}\left[I\left(D_{Ri} + D_{Lj}^{*}\right) + \left(Q + iU\right)e^{-i\phi}\right] \tag{2.4c}$$

$$V_{Li}V_{Rj}^{*} = \frac{1}{2}\left[I\left(D_{Li} + D_{Rj}^{*}\right) + \left(Q - iU\right)e^{i\phi}\right] \tag{2.4d}$$

where we have ignored second order terms in Q, U, V, D_R, D_L and their products since these terms are small.

The standard technique for calibration of VLA data having polarization measurements is to observe a weakly polarized point source at several parallactic angles, a source with a known flux density and a strongly polarized source with known Q and U parameters (Perley et al. 1989). In the standard calibration it is assumed that the D_R and D_L terms are constant in time while the complex gains, G_R and

G_L, are time variable. External information is then used to provide estimates of θ_{FR} during the observations. These estimates come either from direct observations of the ionosphere or from models of the Earth's ionosphere and the geomagnetic field. Using the polarization calibrator (weakly polarized point source), the terms D_R, D_L, G_R and G_L are then determined for each antenna by fitting equations (2.4) to the data. The phases of each polarization channel for each antenna are determined with respect to the phase in the same polarization channel of a reference antenna. In general there will be a remaining phase difference between the right and left hand polarization channels at each frequency which is the same for each antenna. This phase difference can then be calibrated using the polarized source with known Q and U properties. The flux calibrator allows the relative values of the output voltage from the correlator outputs to be expressed in terms of an absolute flux scale.

From the calibration scheme described above, it is easily seen that accurate determination of the ionospheric Faraday rotation is essential if high precision Faraday rotation measurements of extragalactic sources are to be made. Any large uncertainty in the ionospheric Faraday rotation will result in errors in the determination of the D factors. This in turn will cause a larger uncertainty in the determination of the source polarization properties as well as resulting in a lower dynamic range and signal to noise for the polarization observations. The dynamic range is defined as the ratio of the highest to the lowest brightness levels (Thompson et al. 1991). Accurate removal of the ionospheric Faraday rotation is also necessary if polarization data sets from different observing sessions are to be combined.

It should be pointed out that one need only predict the correct time evolution of the ionospheric rotation measure when correcting for the ionospheric Faraday rotation of a single source or for a group of sources in a small region of the sky. The

model corrected position angles can differ by a constant amount over the time of the observations from the true trans-ionospheric position angles without having an effect on the results of the calibration. Consider an observation of a source whose polarization position angle is χ_o upon entering the top of the ionosphere. Upon reaching the antennas on the Earth's surface, the polarization position angle will be

$$\chi = \theta_{FR} + \chi_o. \tag{2.5}$$

We can separate the ionospheric Faraday rotation into two components

$$\theta_{FR} = \theta_o + \theta(t) \tag{2.6}$$

where θ_o represents the ionospheric Faraday rotation due to the constant ionospheric rotation measure term which is not described by the model and $\theta(t)$ is the ionospheric Faraday rotation described by the models. After determining the values of the gains and D terms the polarization position angles for the ith antenna will be

$$\chi_i = \chi_o + \theta_o + \delta\chi \tag{2.7}$$

where $\delta\chi$ is the remaining phase difference between the right and left hand polarization channels which is due to instrumental factors. This error factor ($\delta\chi$) will also affect the observation of the position angle calibrator (the source with known Q and U values), and so calibration of the origin of the position angle will remove this error. The models for ionospheric Faraday rotation must then only predict the time evolution of the ionospheric rotation measure to be useful in the calibration.

When considering several sources which are separated by several tens of degrees in the sky (i.e. they are not contained in a small region of the sky) the above argument will no longer be valid. This is due to the fact that the ionospheric

Faraday rotation varies with azimuth and zenith angle at any given time. Thus if the observed sources are in a small region of the sky and all have similar azimuth and zenith angles, there will be little variation in the ionospheric Faraday rotation over the whole region. However, if the sources are well separated on the sky then the ionospheric Faraday rotation will show significant variations between the sources at any given time, and the above remarks are not pertinent.

2.4 Estimation of Ionospheric Faraday Rotation in AIPS

2.4.1 The Standard Method

The standard routine for the calibration of ionospheric Faraday rotation in Astronomical Image Processing System (AIPS) is the task FARAD. We will now discuss how FARAD calculated the ionospheric Faraday rotation when TEC data were available (prior to 1990). The TEC values were obtained from the World Data Center in Boulder, Co. The TEC values were calculated from Faraday rotation observations of linearly polarized signals from geostationary satellites measured at Boulder, $\sim 6^\circ$ of latitude north of the VLA. The measurements were made on an hourly basis (Davies et al. 1975). The sub-ionospheric point, defined as the point on the Earth's surface directly below the peak electron density in the ionosphere for a given line of sight was about $\sim 2^\circ$ of latitude north of the VLA (Bignell 1982). The AIPS documentation claims that this allows the TEC values measured hourly at Boulder to be valid at the VLA without having to extrapolate the data due to the global structure of the ionosphere.

FARAD approximates the ionosphere as a thin slab of constant electron density and constant height above the Earth's surface. This approximation is based on the fact that the F2 layer dominates the electron density profile of the ionosphere and is usually strongly peaked. The height of the thin slab is chosen to be constant

since the height of the peak in the F2 layer is normally between 250 and 400 km depending on solar activity and shows only small diurnal variations. The FARAD program documentation claims that these variations cause corresponding variations in the ionospheric rotation measure that are typically $< 1\%$ in magnitude. It is also assumed that the curvature of the Earth and the ionosphere can be ignored so that the path length through the ionosphere follows a simple $\frac{1}{\cos z}$ law where z is the zenith angle. Although the height of the F2 layer does not vary greatly during the course of a day for a given latitude and longitude, it does vary with magnetic latitude and longitude. Thus for lines of sight at large zenith angles the approximation of constant height can break down. Ignoring the curvature of the Earth results in the $\frac{1}{\cos z}$ law overestimating the path length through the ionosphere and thus overestimating the ionospheric Faraday rotation. Finally, it is assumed that the electron density in the thin slab remains constant for all points (i.e. the density is constant for all longitudes and latitudes). This is an invalid assumption since there are significant diurnal variations in the electron density, especially at sunrise and sunset, resulting in electron density variations with longitude and latitude. Thus the approximation that the electron density is constant everywhere and equal to the zenith electron density breaks down for large zenith angles, especially around sunrise and sunset.

When the observer chooses to calibrate the ionospheric Faraday rotation with the TEC data from Boulder, the choice is given to specifying the height of the thin slab (h) or to allow FARAD to determine the appropriate height to use. The height of the thin slab is computed using the ionospheric model of Chiu (1975) if the user does not specify a value. For a given line of sight towards a source with an azimuth angle, A_z, and zenith angle, z, from an antenna at a given longitude and latitude (λ, ϕ) FARAD calculates the ionospheric Faraday rotation as follows. An important

quantity in the FARAD algorithm is the sub-ionospheric point (SIP). The SIP is defined, in this case, as the latitude and longitude for which the altitude of the line of sight equals the thin slab height, h. The zenith and azimuth angles in local coordinates at the SIP are given by (FARAD FORTRAN code)

$$\sin\left(z_{SIP}\right) = \sin z' = \frac{R_e \sin z}{R_e + h} \tag{2.8}$$

$$\cos\left(A_{SIP}\right) = \cos A'_z = \cos\left(\arcsin\left(\tan\lambda \, \tan A_z\right)\right) \cos A_z \tag{2.9}$$

where R_e is the mean radius of the Earth. The ionospheric rotation measure (RM_i) is then determined using an interpolation of the TEC data in time and is given by

$$RM_i = 3.62 \times 10^{-17} \frac{B_{\|} \cdot TEC}{\cos z'} \text{ rad m}^{-2} \tag{2.10}$$

where the TEC is given in units of 10^{15} m^{-2} and $B_{\|}$ is the line of sight component of the geomagnetic field in the thin slab given in Gauss. The use of the zenith angle in the local coordinates of the SIP point results in a first order correction to the path length problem created by using a $\frac{1}{\cos z}$ law. Models of the geomagnetic field generally use the following coordinate system: the 1 axis is pointing away from the surface of the Earth, the 2 axis is pointed towards the East and the 3 axis is pointed towards the North. The line of sight component of the geomagnetic field is then simply given by

$$B_{\|} = -\left[B_1 \cos z' + B_2 \sin z' \sin A'_z + B_3 \cos A'_z \sin z'\right]. \tag{2.11}$$

FARAD calculates the ionospheric Faraday rotation at the sub-ionospheric point but it uses the TEC values measured at Boulder, Co. without any attempt to extrapolate the TEC value in order to take into account the diurnal or geographic dependences of the TEC. This allows for the possibility that the true TEC value

that should be used in the calculation of ionospheric Faraday rotation could be significantly different than the model value.

The determination of the ionospheric Faraday rotation using simultaneous TEC data is the prefered method of use in the AIPS model since it relies on direct measurements of the ionosphere and thus day to day and hourly variations in the ionosphere are taken into account. Bignell (1982) states that the accuracy of this technique for determining the ionospheric Faraday rotation is about $10-20\%$ and is limited by anomalies in the ionospheric electron density and the geomagnetic field. Bignell (1982) also notes that the corrections are not always successful. Observations at large zenith angles will obviously experience problems with these corrections since remote features of the ionosphere will be affecting the observations. Furthermore, some of the assumptions in FARAD will start breaking down at large zenith angles.

2.4.2 The Ionospheric Model of Chiu Used in FARAD

We now turn our attention to the ionospheric model of Chiu (1975) used in FARAD to calculate the ionospheric Faraday rotation when no TEC data are available. This model has become more important since the demise in March 1990 of the geosynchronous satellites which provided TEC measurements. Any polarization observations made after the demise of these satellites must therefore rely on the Chiu model to estimate the TEC value of the ionosphere.

Chiu's ionospheric model is based on monthly averaged, hourly ionospheric sounding data from 50 worldwide stations from 1957 until 1970. The model allows for the variations of electron density with diurnal, annual and solar activity cycles. The model only considers the structure of the E, F1 and F2 layers of the ionosphere with only the F2 layer being used in the AIPS implementation of the Chiu model. The main ionospheric measurement going into this model is the F2

layer critical frequency f_oF2 which is the plasma frequency ν_p for the peak electron density in the F2 layer of the ionosphere. For an unpolarized signal in a plasma, the index of refraction is simply given by

$$n = \sqrt{1 - \frac{\nu_p^2}{\nu^2}} \tag{2.12}$$

where

$$\nu_p^2 = \frac{4\pi n_o e^2}{m_e}. \tag{2.13}$$

If the frequency of the signal is less than the plasma frequency then the index of refraction is imaginary and the wave cannot propagate in the plasma. When an unpolarized signal is sent into the ionosphere with a frequency $\nu \leq f_oF2$ then at some point the wave will no longer be able to propagate into the ionosphere and will be reflected. Thus f_oF2 can easily be measured from the ground by finding the highest frequency wave that is reflected by the ionosphere, with f_oF2 typically being in the range $5 - 15$ MHz. A profile of the the ionospheric electron density below the foF2 peak can be made by measuring the round trip propagation time of a wave with $\nu < f_oF2$. The wave is reflected by the point in the ionosphere where the local plasma frequency equals the wave frequency and the time delay gives the altitude which has this density.

The monthly averaged, hourly f_oF2 data for each station were fit using a second order spherical harmonic analysis (the relevant angles of the expansion being the geomagnetic latitude and the local time expressed as an angle) for each month in the Chiu model (Rawer and Bilitza 1989). The coefficients for the annual variations and the solar cycle dependence of the ionosphere were determined first by fitting the model to the noon-time f_oF2 data at each station (Ching and Chiu 1973). The coefficients from this analysis were then fit for diurnal variations at fixed points in

the annual and solar cycle. The Chiu model then gives a prediction of the ionosphere at a given local on the Earth with the only inputs being the location, the date and time and the monthly mean sunspot number.

When measured values of the TEC are not available, FARAD used the Chiu model to estimate the TEC in the following manner. First the Chiu model is used to predict the peak density of the F2 layer along with its altitude. Then a Chapman profile (Ratcliffe and Weekes 1960) is used to describe the shape of the F2 region. An equivalent thickness is then determined by performing an integration over the F2 layer profile. The TEC value is then found simply by multiplying the equivalent thickness by the peak density of the F2 layer. The relevant equations may be found in the FORTRAN code for FARAD.

The ionospheric model of Chiu describes the noon-time f_oF2 values to within 2 MHz and the TEC of the ionosphere to within 25% (Chiu 1975). However, the predicted ionospheric properties from this model represent the monthly mean ionosphere and do not reflect the daily variations in the ionosphere. This model was also derived for observations that cover slightly more than one solar cycle and thus spurious solar cycle variations during the 1957 to 1970 period could have a significant effect on the model. The model also implements a simple harmonic analysis of the global properties of the ionosphere which has since been shown to have too few coefficients to provide a good description of the global properties of the ionosphere (Rawer and Bilitza 1989). Chiu's intent was to develop a simple model of the ionosphere which did not involve many calculations. We thus see why the preferred method of determining the ionospheric Faraday rotation is to use the measured TEC values.

2.4.3 The Magnetic Field Model Used in FARAD

The task FARAD also utilizes a model for the geomagnetic field in calculating the ionospheric Faraday rotation. An offset dipole model is used for the geomagnetic field. The form of the model is adapted from the "Handbook of Geophysics and Space Environments" by Valley (1965) and from Chapman and Bartels (1940). In the FARAD model the geomagnetic field is expanded in terms of spherical harmonics, keeping only the terms which describe the dipole moment of the geomagnetic field. A detailed discussion of the expansion of the geomagnetic field into spherical harmonics will be presented in Section 2.5.1. The Gaussian coefficients used in the AIPS geomagnetic field model are presented in Table 2-1. The FARAD FORTRAN code states that these coefficients describe the geomagnetic field in the year 1922. The geomagnetic field is determined from the expansion of the Gaussian coefficients for the point where the line of sight to the source crosses the thin slab ionosphere (i.e. where the line of sight is at an altitude of h). This value for the magnetic field is then used to find the component along the line of sight in equation (2.11). This model for the magnetic field is claimed to return magnetic field values that are good to within 20% at the VLA site (documentation of FARAD). It seems likely that this claim is relevant only to the dipole moment of the geomagnetic field.

The task FARAD uses only the dipole term in calculating the magnitude of the geomagnetic field. The higher order terms are only used in defining where the center of the dipole is located. Another limitation of the FARAD model is that the Gaussian coefficients used in computing the geomagnetic field are from epoch 1922. This model for the geomagnetic field thus has two weaknesses. First, the geomagnetic field does change with time. Since there are ~ 70 years between the radioastronomical measurements and the epoch of the magnetic field coefficients,

the secular change in the magnetic field should be taken into account. There is $\sim 6\%$ difference in the dipole field strength as measured in 1920 and 1980 (Rikitake and Honkura 1985). Secondly, the dipole moment of the geomagnetic field only constitutes about 70% of the total amplitude of the geomagnetic field (Rikitake and Honkura 1985). We would thus expect a significant improvement in the model if higher order moments of the geomagnetic field were included in the model.

2.5 An Improved Ionospheric Faraday Rotation Model

Since TEC data are not presently available for use in the calibration of ionospheric Faraday rotation for data obtained with the VLA, and since the models for the ionosphere and geomagnetic field used in AIPS are outdated, we have developed a new model for use in the calibration of ionospheric Faraday rotation in VLA data. This model employs improvements in both the ionospheric and geomagnetic field model. As mentioned above, the geomagnetic field used in FARAD consists of a model based on measurements of the geomagnetic field in 1922. The geomagnetic field evolves with time so that the geomagnetic field model used in FARAD is no longer accurate. The amplitude of the geomagnetic field (solid line) and the strength of the dipole moment of the geomagnetic field (dashed line) are plotted versus time in Figure 2-2. These data were obtained from the the World Data Center and show that the geomagnetic field changes by $\sim 8\%$ per century. This plot represents the geomagnetic field at an altitude of 300 km above the VLA at approximately the height of the thin slab used to represent the ionosphere in FARAD. In addition to ignoring time dependence of the geomagnetic field, the model in FARAD used only the first two orders of the spherical harmonic expansion terms of the geomagnetic field. We have thus chosen to use the International Geomagnetic Reference Field (IGRF) model (Peddie 1982) in our improved ionospheric Faraday rotation model.

The IGRF Gaussian coefficients are updated every five years and thus accounts for the time evolution of the geomagnetic field.

Improvements have also been made in the model for the ionospheric electron density. FARAD treats the ionosphere as an unphysical, uniform thin slab. Newer and better models of the ionosphere are also now available, such as the International Reference Ionosphere (IRI) (Rawer and Bilitza 1989). Combining the IGRF and IRI models we have developed a model which treats the ionosphere in a more realistic manner than does the FARAD model. In this section we will first discuss the IGRF and IRI models separately before discussing how these two models are combined to produce the model for ionospheric Faraday rotation correction which comprises this portion of the thesis.

2.5.1 The International Geomagnetic Reference Field Model

The IGRF model was developed by the International Association of Geomagnetism and Aeronomy (Peddie 1982). The IGRF model consists of a series of spherical harmonics and their derivatives of up to tenth degree and order describing the geomagnetic scalar potential (V)

$$V = R_e \sum_{n=1}^{N} \sum_{m=0}^{n} \left(\frac{R_e}{r}\right)^{n+1} \left(g_n^m \cos m\lambda + h_n^m \sin m\lambda\right) P_n^m(\cos\theta) \tag{2.14}$$

where R_e is the mean radius of the Earth, λ is the longitude and θ is the co-latitude, $P_n^m(\cos\theta)$ are the Schmidt renormalized associated Legendre functions of degree n and order m, N is the maximum degree and order and g_n^m and h_n^m have been named the Gaussian coefficients and are in the units of Gauss. In the expansion of the scalar field, terms with $m < 0$ have been excluded. These terms arise from the part of the geomagnetic field which has an origin outside of the Earth, while terms with $m \geq 0$ arise from the part of the geomagnetic field whose origin is internal

to the Earth (Rikitake and Honkura 1985). Gauss (1839) showed that $g_n^m \gg g_n^{-m}$ and $h_n^m \gg h_n^{-m}$ for the geomagnetic field. Hence terms with $m < 0$ can be ignored. For a given longitude λ, co-latitude θ and height above the Earth's surface h, the magnetic field is given by

$$B_1' = -\frac{\partial V}{\partial r} \tag{2.15a}$$

$$B_2' = -\frac{1}{r \sin\theta}\frac{\partial V}{\partial \lambda} \tag{2.15b}$$

$$B_3' = \frac{1}{r}\frac{\partial V}{\partial \theta} \tag{2.15c}$$

where $r = R_e + h$, the 1 axis is radially upward, the 2 axis is towards the East and the 3 axis is towards the North.

The Gaussian coefficients in the IGRF model are specified at five year intervals, from 1945 to 1990 (IGRF documentation). The Gaussian coefficients for these epochs are complete to a degree and order of 10 (Peddie 1982). Linear interpolation of the Gaussian coefficients is used for observations which occur between these epochs. There also exists another set of Gaussian coefficients complete to a degree and order of 8 which predicts the secular evolution of the geomagnetic field for the period 1990 to 1995. Thus the IGRF model allows us to determine the geomagnetic field for the epoch of the VLA observations in Chapter 4. Also, it provides a more complete determination of the amplitude of the geomagnetic field since Gaussian coefficients of higher degree and order are used (8 or 10 for the IGRF model rather than 2 for the FARAD model).

In the documentation of the FARAD program, it is claimed that the AIPS geomagnetic field model is 6% low in dipole intensity and 11° W in magnetic declination $\cos D = \frac{B_2}{\sqrt{B_2^2+B_3^2}}$. These comparisons of the AIPS geomagnetic field with the true geomagnetic field were made for measurements of the true geomagnetic field in epoch 1965 (FARAD FORTRAN code). Comparing the geomagnetic field

models of AIPS and the IGRF at the VLA ($\lambda = 252.38°, \phi = 34.08°$) at an altitude of 300 km for the year 1965 we find B(AIPS) = $(.1099, .0022, -.2593)$ Gauss and B(IGRF) = $(.17394, .04002, -.45264)$ Gauss with a dipole moment of .3095 Gauss. The year 1965 was chosen for the IGRF model since the AIPS model was compared to measurements of the geomagnetic field in epoch 1965. The AIPS geomagnetic field yields a magnetic declination D = 1.1° E while the IGRF model yields D = 13.0° E. The dipole moment of the IGRF model is $\sim$ 10% greater than the dipole moment of the AIPS model and the magnetic declination of the AIPS model is 11.9° W of the magnetic declination of the IGRF model. Thus the IGRF model provides a better description of the geomagnetic field near the VLA than does the AIPS model geomagnetic field. The remaining $\sim$ .18 G difference in the AIPS model geomagnetic field and the IGRF geomagnetic field results from the fact that the AIPS geomagnetic field neglects the higher order moments of the field. In this case, the dipole field strength is approximately 67% of the total field strength with the remainder of the field strength being due to the higher order moments.

2.5.2 The International Reference Ionosphere Model

The International Reference Ionosphere (IRI) is a joint international project of the Committee on Space Research and the International Union of Radio Science to provide an empirical standard model of the ionosphere. The IRI is periodically updated and describes the electron density and temperature and the ion temperature and composition in the altitude range 60 to 2000 km. The model is based on data from a worldwide network of over 150 ionosondes, the ISIS and Alouette topside sounders, incoherent backscatter radars and in situ measurements with several satellites and rockets (Rawer and Bilitza 1989). The IRI is designed for producing a monthly averaged model of the ionosphere in non-auroral regions, for magnetically

quiet conditions and for twelve month running mean sunspot numbers below 130 (Bilitza 1986). The IRI model produces profiles of electron density, neutral temperature, electron and ion temperature and percentage of O II , H II , He II , NO^+ and O_2^+ ions for a given location (geographic or geomagnetic), time (local, universal or solar), season (month or day of year) and solar activity (mean sunspot number or 10.7 cm solar radio flux).

The IRI model, like the model of Chiu, is based largely on foF2 data. Unlike the Chiu model however, the IRI model is based on foF2 data from over 150 worldwide stations and over approximately four solar cycles (Rawer and Bilitza 1989). Monthly averaged, hourly foF2 data are used from each station as is done in the Chiu model. The monthly averaged foF2 data are then sorted at each station according to solar activity. The diurnal variations in foF2 for each station for a given month and solar activity level are then analyzed using a Fourier series. The Fourier coefficients from this analysis for all stations worldwide are then fit by worldwide Legendre functions. This then allows the value of foF2 to be predicted for any location on the Earth at any time and for any solar activity. The global foF2 data for each month and solar activity level require as many as 988 coefficients (Rawer and Bilitza 1989). Such an analysis (hereafter referred to as the Fourier-Legendre analysis) with a large number of coefficients would have been beyond the reasonable limits of computer processing available to the average researcher at the time the Chiu model was developed. This limitation played an important role in the choice of the analysis that Chiu used (Chiu 1975, 1973). Thus the Fourier-Legendre analysis scheme allows a much better global model of the foF2 data than does the Chiu model.

This analysis of the foF2 data, however, requires the addition of several "ghost stations" in areas where very few, if any, stations are located, such as over the Pacific Ocean. The ghost stations data arise from coastal stations data being copied to the

ghost station which is located at the same modified dip latitude (μ) as the coastal station. The modified dip latitude is defined as

$$\tan \mu = \frac{\psi}{\sqrt{\cos \phi}} \tag{2.16}$$

where $\sin \psi = \frac{-B_1}{\|B\|}$ is the magnetic dip angle and ϕ is the geographic latitude. These ghost stations then keep the model from predicting unphysical foF2 values, such as negative foF2, in the regions not monitored by the real stations. The ghost stations will not play a role in the determination of the ionospheric Faraday rotation for data obtained with the VLA since sources are not observed through parts of the ionosphere over the oceans. However, these ghost stations could play a critical role in ionospheric Faraday rotation corrections that may be applied to VLBA and VLBI data since there are antennas in such places as Mauna Kea, Hawaii and St. Croix, Virgin Islands. Also included in the IRI model are other effects such as the motion of the ionospheric plasma due to "average meteorological effects" and electromagnetic forces. The height of the electron density peak in the F2 layer (hmF2) is determined in a similar fashion as foF2 in the IRI model.

Once the location, time and solar activity have been specified, the IRI model then computes the foF2 and hmF2 values from the Fourier-Legendre expansion coefficients, as well as an electron density profile of the ionosphere. The profile is separated into three regions - the topside, middle (E and F layers) and lower (D layer) - which are combined to produce the complete profile using the Epstein step function

$$E_o(z) = \frac{1}{1 + e^{-x}} \tag{2.17}$$

where $x = \frac{z - H_x}{S_c}$ with H_x and S_c being experimentally determined values for each boundary between different regions. The model profiles used in the IRI model are

more complicated than the Chapman layers used in the Chiu model and thus allow a better representation of the true profile of the ionosphere.

The topside model profile is an empirical model that depends on foF2, the geomagnetic latitude and the level of solar activity. The topside model profile is based on the model of Benton et al. (1972) and has been modified by Bilitza (1985). The lower ionosphere profile describes primarily the D layer and to some extent the lower section of the E layer. The lower ionospheric profile model is based on the model of Ramanamurty and Rawer (1990) and is referenced to the E layer electron density peak which is determined in the middle ionosphere profile model.

The middle ionosphere profile model is more complicated than the topside and lower ionosphere profile models since the E, F1, and F2 layers as well as the valley (V region) between the E and F layers must be taken into account. The E, F1, F2 and V regions are each described by a LAY-function (Rawer and Bilitza 1989) given by

$$\begin{aligned} \mathrm{LAY} = & \ln\left[1+\exp\left(\frac{\mathrm{z}-\mathrm{H_x}}{\mathrm{S_c}}\right)\right] - \ln\left[1+\exp\left(\frac{\mathrm{hm}-\mathrm{H_x}}{\mathrm{S_c}}\right)\right] \\ & - \frac{(\mathrm{z}-\mathrm{hm})}{\mathrm{S_C}\left[1+\exp\left(\frac{\mathrm{hm}-\mathrm{H_x}}{\mathrm{S_c}}\right)\right]} \end{aligned} \tag{2.18}$$

where hm is the height of the peak electron density in a given region. The Lay-functions represent the height variations of the logarithm of the electron density in a given region normalized to the peak density in that region. The values of hmE and foE for the E layer are so well known that they are easily determined from the solar zenith angle using only empirical formulae. This also holds true for determining hmF1 and foF1 for the F1 region (Rawer and Bilitza 1989). The height of the valley region is determined from the peak densities and heights of the E, F1

and F2 regions. The middle ionosphere profile is then calculated by combining the LAY-functions for each region.

The IRI model is thus capable of producing a realistic profile of the ionosphere for any location, time and level of solar activity. The TEC predicted by the IRI model is then determined by performing a numerical integration of the electron density over the ionospheric profile. Since the IRI model is based on observations from more stations over more solar cycles than the Chiu model and produces a realistic profile of the ionosphere. The IRI model will provide an improved estimate of the ionospheric Faraday rotation with respect to FARAD, especially at low zenith angles. It should be noted that both the Chiu model ionosphere and the IRI model ionosphere model the "monthly averaged ionosphere" and do not attempt to take into account the day to day variations of the ionosphere.

It is important to know how true ionospheric characteristics, which are subject to day-to-day variations such as those caused by magnetic storms etc. differ from those produced by the IRI and Chiu models. To quantify this and demonstrate the improvement of using the IRI model ionosphere rather than the FARAD model ionosphere we have plotted the predicted TEC from each model versus the measured TEC values in Figure 2-3. The TEC values were measured at Boulder, Co. in March of 1990. In Figure 2-3a the IRI TEC values are plotted versus the measured values where only the location, time and sunspot numbers have been input into the IRI model. In Figure 2-3b we plot the AIPS model TEC predictions versus the measured TEC using only the same inputs as above. In Figure 2-3c we plot the IRI model TEC versus the measured TEC where values of foF2 measured at Boulder have also been input into the IRI model. Currently the AIPS task FARAD does not permit foF2 values to be input and used in its calculations of the TEC. In Figure 2-4 we

plot a histogram of the fractional error (ϵ) for each model presented in Figure 2-3 where

$$\epsilon = \frac{|\text{TEC(model)} - \text{TEC(measured)}|}{\text{TEC(measured)}}. \tag{2.19}$$

A statistical analysis of the data in Figures 2-3 and 2-4 is presented in Table 2-2. The first column lists the ionospheric model. The second column gives the average deviation

$$\alpha = \frac{1}{\text{N}} \sum_{1}^{\text{N}} [\text{TEC(measured)} - \text{TEC(model)}] \tag{2.20}$$

of the model from the data where N is the number of data points. A nonzero value of ϵ or α indicates a systematic error in the model estimate of the TEC. The third column gives the standard deviation of the mean

$$\sigma = \sqrt{\frac{\sum_{1}^{\text{N}} [\text{TEC(measured)} - \text{TEC(model)}]^2}{\text{N} - 1}} \tag{2.21}$$

between the model and the data. The fourth, fifth and sixth columns list the fractional error below which 50% (ϵ_{50}), 75% (ϵ_{75}), and 90% (ϵ_{90}) of the data occur. The seventh column lists the Kolmogorov-Smirnov statistic which is a measure of the greatest distance between the distributions of TEC in the measured data and the modeled data (Press et al. 1989). The eighth column gives the linear correlation coefficient (γ) between the model TEC values and the measured TEC values.

As can be seen from Tables 2-2 through 2-4, the IRI model provides a better prediction of the ionospheric TEC than does the AIPS model. The TEC values predicted by the IRI model have a higher correlation with the measured TEC values than do the AIPS TEC values in all years except one. In 1984 the AIPS model and the IRI model had the same correlation coefficient. In all cases the IRI model had a smaller standard deviation than did the AIPS model. During periods of enhanced solar activity the IRI model performs significantly better than the AIPS

ionospheric model. At solar minimum the two models become comparable although the IRI model still generally has a smaller standard deviation and larger correlation coefficients than the AIPS model.

When the foF2 data are used in the IRI model, the predicted TEC values show a drastic convergence with the measured TEC values (see Table 2-2). This is not surprising since we are providing information to the model about the conditions in the ionosphere at the time of the measurement. Recall that the TEC in the IRI model is calculated by integrating over a model profile of the electron density in the ionosphere and that the shape of the profile depends on the value of foF2. This comparison also serves to point out how important it is to have some information on the state of the ionosphere, such as the TEC or foF2 values, which can be input to the ionospheric models when computing the ionospheric Faraday rotation. With such information, the models are able to make much better predictions about the ionosphere.

From above we see that having information on the state of the ionosphere, such as TEC or foF2 values, help constrain the IRI model into making more realistic predictions. However, this result is true in a statistical sense for a large number of observations. For any given observation it is likely that specifying the TEC or foF2 into the model will improve the predictions but there is no guarantee that this will be the case. During periods when ionospheric and magnetospheric storms are occuring, the models may not be improved by the inclusion of information on the state of the ionosphere. This is due to the fact that the models make predictions for the "average ionosphere" and are not well suited for making predictions for the ionosphere during stormy periods. Typically the TEC is the best indicator of the state of the ionosphere at any given time. The value of foF2 alone is generally not as robust an indicator of the state of the ionosphere at any particular time.

2.5.3 The Improved Ionospheric Faraday Rotation Model

As we have seen, the IRI and IGRF models provide more realistic and up-to-date representations of the Earth's ionosphere and geomagnetic field than do the models currently used in the AIPS task FARAD. By combining the IRI ionospheric model and the IGRF geomagnetic field model, we have developed an improved model for ionospheric Faraday rotation. The improved ionospheric Faraday rotation model is thus capable of finding the electron density and the geomagnetic field at any point in the Earth's ionosphere, allowing the ionospheric Faraday rotation to be calculated by simply integrating along a given line of sight. Since the IRI model and the IGRF model both take into account changes in the ionosphere and the geomagnetic field along a line of sight that are not considered in the AIPS model, the improved ionospheric Faraday rotation model will provide a better description of ionospheric Faraday rotation at large zenith angles. It will also be possible, using the IRI model ionosphere, to utilize foF2 and TEC values from sites other than at Boulder, Co. to help predict the TEC above the VLA. This can be done by using the IRI model (without external inputs) to calculate scaling factors relating foF2 and TEC values from other locations to the VLA. This could not be done reliably with the AIPS model because of its unrealistic treatment of the structure of the ionosphere.

We will now give a description of the improved ionospheric Faraday rotation model. The inputs include the frequency of the observation (ν), the sunspot number (R), the right ascension and declination of the astronomical source (α and δ), the time, day, month and year of the observations, the geographical coordinates (λ, ϕ), time zone and height above sea level (H) of the antenna and the number of steps (N) to take through the ionosphere while integrating to determine the ionospheric

Faraday rotation. Hourly values of foF2 and hmF2 for the ionosphere above the antenna can also be input into the model to help provide a better description of the ionosphere. The model program was written so that a single astronomical source could be "tracked" as it moves across the sky, giving the ionospheric Faraday rotation towards the source at regular time intervals which are specified by the user.

After reading in the input parameters, the coordinates of the antenna are determined

$$\begin{pmatrix} \mathrm{x} \\ \mathrm{y} \\ \mathrm{z} \end{pmatrix} = \begin{pmatrix} (\mathrm{Ac} + \mathrm{H}) \cos\phi \cos\lambda \\ (\mathrm{Ac} + \mathrm{H}) \cos\phi \sin\lambda \\ \left(\frac{\mathrm{B}^2\mathrm{c}}{\mathrm{A}} + \mathrm{H}\right) \sin\lambda \end{pmatrix} \tag{2.22}$$

where

$$\mathrm{c} = \frac{\mathrm{A}}{\sqrt{\mathrm{A}^2 \cos^2\phi + \mathrm{B}^2 \sin^2\phi}}, \tag{2.23}$$

A is the equatorial radius of the Earth and B is the polar radius of the Earth. We have used an Earth centered reference frame with the x axis pointing towards $\lambda = 0°$, the y axis pointing towards $\lambda = 90°$ and the z axis pointing towards $\phi = 90°$. Next the unit vector $\hat{\mathrm{s}}$ along the line of sight from the antenna to the astronomical source is determined by

$$\hat{\mathrm{s}} = \begin{pmatrix} -\sin\lambda & -\sin\phi\cos\lambda & \cos\phi\cos\lambda \\ \cos\lambda & -\sin\phi\sin\lambda & \cos\phi\sin\lambda \\ 0 & \cos\phi & \sin\phi \end{pmatrix} \begin{pmatrix} \sin Z \sin A_z \\ \sin Z \cos A_z \\ \cos Z \end{pmatrix} \tag{2.24}$$

where Z is the zenith angle of the source, $\mathrm{A_z}$ is the azimuth angle of the source and we have used the same coordinate system as in equation (2.22). The Earth centered coordinates where the line of sight is 65 km ($\vec{\mathrm{s}}_{65}$) and 1000 km ($\vec{\mathrm{s}}_{1000}$) above the Earth's surface are then determined along with the step length used in the integration along the line of sight. The altitude range on the ionosphere is chosen to be from 65 km to 1000 km since nearly all the ionospheric Faraday rotation occurs within this altitude range.

The model now integrates the electron density (n_e) and the product $n_e B_{\|}$ along the line of sight from $\vec{s}_{65}$ to $\vec{s}_{1000}$ by simply summing n_e and δRM over the N intervals of length $\vec{ds} = \frac{\vec{s}_{1000} - \vec{s}_{65}}{N}$ through the ionosphere. For the center of each interval, the Earth centered coordinates are determined using equations (2.22) and (2.24). Then the IRI model ionosphere is used to find n_e and the IGRF geomagnetic field model is used to find $\vec{B}$ at the center of the interval. The rotation measure contribution of the interval k is given by

$$\delta \mathrm{RM_k} = 0.81 n_e \vec{B} \cdot \vec{ds_k} \tag{2.25}$$

with the rotation measure for the entire line of sight being given by

$$\mathrm{RM_i} = \sum_{k=1}^{N} \delta \mathrm{RM_k}. \tag{2.26}$$

The rotation measure is also calculated by keeping track of the right and left circular polarized phase shifts using an expression for the index of refraction of electromagnetic waves in a magnetized plasma (Davies 1965). This second calculation of the rotation measure is performed in case that the line of sight is perpendicular to the magnetic field for a large part of its path length through the ionosphere. This can happen for some lines of sight for observation made with the VLA when the source is near the horizon at azimuth angles ninety degrees away from the local direction of the geomagnetic field. However, there is rarely more than a few tenths of a percent difference between the two calculations of the ionospheric rotation measure when this is the case.

2.6 Comparison of the AIPS and the Improved Models

The results of a simulation using the improved ionospheric Faraday rotation model (IIFRM) are shown in Table 2-6, Figures 2-5 and 2-6. The calculations are for a source at $\alpha = 12^{\rm h}$ and $\delta = 70°$ observed on March 21, 1993 from $0^{\rm h}$ to $23^{\rm h}$ local time at the VLA ($\lambda = 252.38°, \phi = 34.08°, {\rm h} = 2.1$ km). The observing frequency used in this simulation was 1.4 GHz, the sunspot number was taken to be R = 89.46 and 500 steps were taken through the ionosphere in the integration of the ionospheric Faraday rotation. The first column of Table 2-6 gives the time of the calculations. The second and third columns give the azimuth and altitude angles of the source as seen from the VLA. The fourth column gives the rotation measure as calculated from equation (2.26). The fifth column gives the phase difference between the right and left hand circularly polarized waves and the sixth column gives the rotation measure as determined from the phase differences which includes the effects of any quasi-transverse propagation that occurs along the line of sight. The seventh column gives the TEC as calculated by the model. In Figure 2-5 we have plotted the phase difference versus time in panel (a), the left hand phase in panel (b), the right hand phase in panel (c) and the altitude and azimuth angles of the source versus time in panel (d). In Figure 2-6 the rotation measures calculated by the improved ionospheric Faraday rotation model (circles) and the AIPS model (diamonds) for the simulation are plotted versus time. For comparison, the results of the AIPS model for the same simulation as above, without any information on the TEC being input into the AIPS model, is given in Table 2-7. The first column gives the time, the second column gives the TEC and the third column gives the rotation measure as calculated by the AIPS model.

These models predict drastically different values for the ionospheric rotation measure. Although there are differences in the TEC values predicted by each model (see Tables 2-6 and 2-7) they cannot account for the differences in the predicted rotation measures, especially during the period from 10^h to 14^h local time when the models predict ionospheric rotation measures with different signs. Since the TEC cannot be negative the difference in the predicted ionospheric rotation measures must be a result of the geomagnetic field models and the geometry used in the two models. As mentioned previously the geomagnetic field model in the AIPS algorithm uses only the dipole moment of the field while the IGRF geomagnetic field model used in the improved ionospheric Faraday rotation model incorporates higher order multipoles of the field. These higher order multipole account for most of the difference in the predicted rotation measures from 0^h to 5^h and 21^h to 23^h local time in Figure 2-6 (see discussion of Figure 2-7 below).

The difference in the predicted ionospheric rotation measures from 6^h to 20^h local time not only depends on the moments used in the expansion of the geomagnetic field but also on how the ionosphere is modeled. The thin slab model used for the ionosphere in the AIPS model only allows for the geomagnetic field at one point along the line of sight to enter into the calculation of the ionospheric rotation measure. Thus, the AIPS model will be unable to account for the reversal of the line of sight component of the geomagnetic field along the line of sight. The value of the line of sight component of the geomagnetic field ($B_\parallel$) used in the AIPS model can even have the opposite sign from the average along the line of sight of the line of sight component of the geomagnetic field, i.e.

$$\mathrm{sgn}\left(B_\parallel(h)\right) \neq \mathrm{sgn}\left(\frac{1}{L}\int_0^L B_\parallel(s)ds\right) \tag{2.27}$$

where h is the point along the line of sight which defines the position of the thin slab. This is illustrated in Figure 2-7. This is particularly likely to occur when the source is at very low elevation angles towards the North as is the case for the source in Figure 2-6. The improved ionospheric Faraday rotation model does not encounter this problem since it uses realistic profiles of the ionosphere and integrates along the line of sight. Generally, sources are not observed at such low elevation angles with the VLA and this case should be taken as an extreme example of the problems with the ionospheric model used in AIPS.

This problem with the thin slab model of the ionosphere used in the AIPS model is made more apparent in Figure 2-8. Here we have repeated the simulations used to create Figure 2-6, but have replaced the AIPS dipole geomagnetic field model with the IGRF geomagnetic field model. Now the differences in the predicted ionospheric rotation measures from 0^h to 5^h and 21^h to 23^h local time are due primarily to the differences in the TEC values predicted by each model (i.e. due to differences in the predicted electron densities). However, it is clear that the rotation measures predicted by the AIPS model between 10^h and 14^h local time are still negative. The AIPS model for ionospheric Faraday rotation thus encounters severe problems when the line of sight component of the geomagnetic field undergoes drastic changes along the line of sight, especially when it changes sign. This is most likely to occur for sources at high zenith angles towards the North where the line of sight passes near the North geomagnetic pole for observations made in North America. To a smaller extent, we would expect a difference in the magnetic field in the thin slab in the AIPS model and the average along the line of sight for the line of sight component of the geomagnetic field of $\sim 10\%$ when the line of sight passes over a "higher order pole" (i.e. where the non-dipole geomagnetic field has a convergence point on the Earth's surface). One such pole exists over the United States and is

roughly centered over Iowa (see Figure 1.17 of Rikitake and Honkura 1985). This higher order pole could thus have an affect on the AIPS model calculations of the ionospheric Faraday rotation even if the IGRF geomagnetic field is used in the AIPS model for observation with the VLA or VLBA.

The above simulation and comparison has illuminated several of the shortcomings and problems the AIPS model for ionospheric Faraday rotation has, such as the thin slab ionosphere and the "incomplete" geomagnetic field model. We now seek a comparison of the AIPS model with the improved ionospheric Faraday rotation model under more commonly encountered conditions for observation with the VLA. We will thus look at the calibration of the ionospheric Faraday rotation for the observations of Sakurai and Spangler (1994) on March 21, 1990, the last month for which TEC data is available for use in the AIPS ionospheric Faraday rotation calibration scheme. The goal of the observations of Sakurai and Spangler was to measure rotation measure fluctuations due to magnetohydrodynamic waves in the solar wind and corona. It was known a priori that the amplitude of these fluctuations would be small and that they would occur on time scales of an hour or more. Thus high precision removal of the ionospheric Faraday rotation was desired and eventually prompted the development of the improved ionospheric Faraday rotation model.

The TEC values from Boulder, Co. are not the only measurements of ionospheric quantities that are available for use in the comparison of the AIPS model to the improved ionospheric Faraday rotation model for the observations of Sakurai and Spangler (1994). Data are also available for foF2 and hmF2 at Boulder during the same time period. These data were obtained from the World Data Center. In addition, the sunspot number for this period is known. Values of foF2 are available on an hourly basis for every hour of March 21, 1990 except for 5^{h} and 6^{h} UT during

which time no observations by Sakurai and Spangler were made. The values of hmF2 are only available for 18^h and 20^h to 23^h UT. Since a change of hmF2 = 300 km to hmF2 = 350 km results in only $\sim 0.4\%$ change in the ionospheric Faraday rotation predicted by the improved ionospheric Faraday rotation model, we have interpolated the hmF2 to all hourly values on March 21, 1990.

With the available TEC, foF2, hmF2 and sunspot data we are able to make a more detailed comparison of the two ionospheric Faraday rotation models. In Table 2-8 we list the TEC values of these models using various inputs and compare them to the values measured at Boulder, Co. The TEC values computed from the models are for the VLA, not Boulder. In the first column of Table 2-8 we give the UT time. Only hours for which the source 2230+114 is observable by the VLA are listed. We have chosen to look at the calibration of the source 2230+114 since it was the most frequently observed source in the observations of Sakurai and Spangler which was not near the sun. A plot of the azimuth and altitude angle of 2230+114 on March 21, 1990 as observed from the VLA are shown in Figure 2-9. In the second column of Table 2-8 the TEC values measured at Boulder are listed. In the third column the TEC values predicted by the improved ionospheric Faraday rotation model with only the sunspot number as an input are given. In the fourth column the TEC values from the improved ionospheric Faraday rotation model with the foF2 and hmF2 data being input into the model are listed. The fifth column gives the TEC as calculated by the AIPS model with only the sunspot number as an input to the model and the sixth column gives the TEC found by the AIPS model when the foF2 and hmF2 data are used as inputs. It is easily seen that the improved ionospheric Faraday rotation model with only the sunspot number as an input provides the best description of the measured TEC data.

The reason that including the measured foF2 values in the improved ionospheric Faraday rotation model did not result in an improvement of the TEC predictions is that the ionosphere was "stormy" during this period. The measured foF2 values were thus not easily measured and typically are only lower limits on the true values. The measurements of foF2 were influenced by the presence of stratification and spread echoes in the ionosphere, attenuation near the critical frequency and due to the fact that the height of the F2 layer was outside of the normal height range recorded by the ionosonde (World Data Center data documentation). This results in the foF2 values not being a reliable indicator of the state of the ionosphere for this particular time range and leads to a degradation of the predicted TEC values when used as inputs into the model.

In Tables 2-9 and 2-10 along with Figure 2-10 we present the ionospheric rotation measure values predicted by the AIPS model and the improved ionospheric Faraday rotation model with various inputs. The first column of Table 2-9 gives the time. The second column of Table 2-9 lists the ionospheric rotation measure predicted by the improved ionospheric Faraday rotation model with only the sunspot number being input to the model. The predicted ionospheric rotation measure values of the improved ionospheric Faraday rotation model with the foF2 and hmF2 values being input are listed in the third column. Various estimates of the ionospheric Faraday rotation by the AIPS model are listed in columns four through seven with the inputs being just the sunspot number in columns four and five and with the foF2 and hmF2 data being input for the predictions in columns six and seven. The default dipole geomagnetic field model of AIPS was used in the calculations in columns four and seven while the IGRF geomagnetic field model was used in the calculations presented in columns five and six. In Table 2-10 we present the ionospheric rotation measure values from the AIPS model and the values from the

improved ionospheric Faraday rotation model which were actually used by Sakurai and Spangler in their calibration of ionospheric Faraday rotation for the observations on March 21, 1990. The first column of Table 2-10 lists the time when the source 2230+114 was observed. The second column gives the ionospheric rotation measure of the improved ionospheric Faraday rotation model with only the sunspot number being input to the model. These values were found by interpolating from the values in Table 2-9. In the third column of Table 2-10 the ionospheric rotation measure values predicted by the AIPS model using the TEC measurements from Boulder are presented.

In Figure 2-10 we plot the various predictions of ionospheric rotation measure versus time from Tables 2-9 and 2-10. In Figure 2-10 the solid line represents the predictions of the improved ionospheric Faraday rotation model with the sunspot number as the only input. The values used by Sakurai and Spangler are given by the cross symbols (T. Sakurai, private communication). The AIPS model predictions using the TEC values is shown as the dashed line. The dotted line depict the predictions of the AIPS model with the measured values of foF2 and hmF2 being input into the model. Finally, the dash-dot line represents the ionospheric rotation measure predictions of the improved ionospheric Faraday rotation model with the foF2 and hmF2 values being input into the model.

We now present a general analysis of the predictions of the improved ionospheric Faraday rotation model and the AIPS model. Using the predicted ionospheric rotation measure for each model at 14^{h} UT as a reference point, we see that both the AIPS model predictions shown in Figure 2-10 show increasing ionospheric rotation measure values from 14^{h} to 18^{h} UT. From 18^{h} to 21^{h} UT both AIPS model predictions are nearly constant showing a smooth turnover in the ionospheric rotation measure versus time. From 21^{h} to 24^{h} UT both AIPS model predictions undergo

a steady decline in the ionospheric rotation measure. For both the improved ionospheric Faraday rotation model ionospheric rotation measure predictions there is an increase in the ionospheric rotation measure from 14^h UT through 21^h UT, after which only a modest decrease in the ionospheric rotation measure occurs.

We thus see that the major differences between the ionospheric rotation measure predictions of the AIPS model and the improved ionospheric Faraday rotation model are that the AIPS model reaches a peak at $\sim 19^h$ UT while the improved ionospheric Faraday rotation model reaches a peak at $\sim 21^h$ UT, and that after 21^h UT the AIPS model predicts a large decrease in the ionospheric rotation measure while the improved ionospheric Faraday rotation model predicts only a slight decrease. These differences are probably due to the differences in the geometries of the ionosphere used in each model. As can be seen from Figure 2-9 the first observation of 2230+114 occurred in the early morning when it was at an elevation angle of $\sim 30°$. There is a seven hour difference between UT and the local time at the VLA for these observations. The electron density in the ionosphere generally reaches its minimum value just before sunrise and increases steadily through the afternoon. After sunset the electron density drops rapidly for a few hours around sunset and then undergoes a steady decline until just before sunrise. This behavior of the ionospheric electron density thus explains the steady increase in the predicted ionospheric rotation measure values from 14^h to $\sim 20^h$ UT.

We now introduce the following picture of the ionosphere in order to help us understand the behavior of the models after 20^h UT. Since the sun is the dominant source of ionization in the ionosphere, the ionosphere can be thought of as being static (for short time periods - generally a few days) in a reference frame where the x axis extends from the Earth to the Sun, the z axis points towards the North celestial pole and the y axis lies in the plane of the ecliptic. In this reference frame

the electron density in the ionosphere is constant with time at any given point. Since the Earth rotates in this reference frame, a person on the Earth will observe changes in the ionosphere as the Earth rotates and different parts of the ionosphere are observed.

After 20^h UT the source 2230+114 was observed at decreasing elevation angles and towards the west (see Figure 2-9). This results in the source being viewed through parts of the ionosphere with local times less than the local time at the VLA. The observed TEC values at Boulder (almost due North of the VLA) were for local times near to sunset during this period. However, the source was observed through parts of the ionosphere whose electron densities had not started dropping (i.e. through parts of the ionosphere whose local times are nearer to noon). Since the AIPS model uses only local values of ionospheric quantities, such as the TEC and foF2 measurements, and makes no attempt to interpolate these quantities to changing longitudes along the line of sight, it will not predict the correct ionospheric rotation measure values near sunset for sources observed in the west (like 2230+114). The end result is that the AIPS model predicts that the ionospheric rotation measure decreases by a large amount near sunset for sources such as 2230+114, whereas in reality the ionospheric rotation measure values should decrease only slightly since the source is observed through parts of the ionosphere whose local times are not yet near sunset. The improved ionospheric Faraday rotation model avoids this problem because the model allows for the variation of the ionospheric quantities with the longitude as the model integrates along the line of sight. The improved ionospheric Faraday rotation model uses the local ionospheric quantities as a reference point for determining the ionospheric quantities along the line of sight through interpolation.

Based on this analysis of the ionospheric rotation measure as a function of time for the AIPS model and the improved ionospheric Faraday rotation models, we

would expect that the improved ionospheric Faraday rotation model would produce a better calibration of the ionospheric Faraday rotation and thus less scatter in the polarization position angles of 2230+114 versus time. If the true polarization position angles of 2230+114 are χ_o at all ν before entering the ionosphere then at the ground the observed polarization position angles are

$$\chi = \chi_o + \lambda^2 \mathrm{RM_i} \tag{2.28}$$

where $\mathrm{RM_i}$ is the ionospheric rotation measure. We would thus expect the polarization position angles of 2230+114 to decrease after $\sim 20^h$ UT when the ionospheric Faraday rotation is calibrated using the AIPS model since we predict that the AIPS model rotation measures are too small during this period. The polarization position angles obtained from a calibration employing the improved ionospheric Faraday rotation model should remain constant within the scatter of the data if the above remarks are correct.

The resulting calibrated polarization position angles for the source 2230+114 are plotted in Figures 2-11 and 2-12 using three different models of ionospheric Faraday rotation calibration. The first model is the improved ionospheric Faraday rotation model with the only input being the sunspot number. We also plot the IIFRM with the measured foF2 and hmF2 provided to the model and the AIPS model using the TEC values as input which is the recommended procedure for the calibration of VLA data. Errors on position angles were scaled from the plotted error bar symbols of Figure 4 of Sakurai and Spangler (1994) and are roughly 0.2° at both frequencies. In Figure 2-11 we have plotted the polarization position angles versus time for the 20 cm data while the 18 cm data appears in Figure 2-12. In both figures the solid line represents the calibration using the improved ionospheric Faraday rotation model with only the sunspot number as an input, the dashed line

represents the calibration using the improved ionospheric Faraday rotation model with the measured values of foF2 and hmF2 being used as inputs and the dash-dot line is the calibration using the AIPS model where the TEC values have been used as inputs.

It is clear that using the improved ionospheric Faraday rotation model for the ionospheric Faraday rotation calibrations leads to about a factor of two decrease in the RMS about the mean of the polarization position angles of 2230+114 at both 18 cm and 20 cm. From Figures 2-11 and 2-12 it is easily seen that the polarization position angles as calibrated using AIPS make a dramatic plunge towards more negative values for 22^h to 23^h UT. This is consistent with the behavior discussed above for the AIPS model in the late afternoon. The rise in the polarization position angles towards more positive values during the period 17^h to 21^h UT at both wavelengths is most likely due to the ionospheric Faraday rotation being over estimated by the all the models during this period or due to the underestimation of the ionospheric Faraday rotation outside of this time range. Our conclusion of an ionospheric Faraday rotation miscalibration is supported by a systematic time dependence at both frequencies rather than a scattering of the data about the mean. These systematic variations may be removed by a second order calibration scheme as discussed by Sakurai and Spangler (1994).

2.7 Conclusion

The RMS scatter in the polarization position angles about the mean of $5° - 7°$ encountered when the AIPS model is used in ionospheric Faraday rotation calibration has generally been treated as marginally acceptable values during periods of high solar activity. However, using the improved ionospheric Faraday rotation model of ionospheric Faraday rotation calibration we have shown that the RMS

scatter in polarization position angle can be reduced by better than a factor of two. The signal to noise and the dynamic range of the polarization observations will also be improved when the improved ionospheric Faraday rotation model is used, as is seen for the observation presented in Chapter 3. This is achieved because the improved ionospheric Faraday rotation model provides a more realistic and up to date model of the ionosphere than does the AIPS model. It was found that the AIPS model uses an out of date model for the geomagnetic field and that the slab model of the ionosphere can create problems for sources near the horizon, especially near sunset or sunrise and when the geomagnetic field undergoes large changes along the line of sight.

Table 2-1. The Gaussian coefficients used for the geomagnetic field in AIPS.

Coefficient	(Gauss)
g_1^0	−0.3095
g_1^1	−0.0226
g_2^0	−0.0067
g_2^1	0.0292
g_2^2	0.0143
h_1^1	0.0592
h_2^1	−0.0122
h_2^2	0.0133

Source: FARAD FORTRAN code.

Table 2-2. Comparison of predicted TEC from ionospheric models with measured TEC values for March 1990.

Model	$\alpha(10^{13}\mathrm{cm}^{-2})$	$\sigma(10^{13}\mathrm{cm}^{-2})$	ϵ_{50}	ϵ_{75}	ϵ_{90}	K − S	γ
AIPS	1.15	1.40	0.37	0.69	0.97	0.316	0.914
IRI	0.35	1.06	0.19	0.32	0.45	0.254	0.935
IRI[1]	0.28	0.85	0.12	0.22	0.39	0.098	0.952

[1] The IRI model ionosphere with measured foF2 input into the model.

Table 2-3. Comparison of predicted TEC from the IRI ionospheric model with the measured TEC values at Boulder, Co.

Year	α $(10^{13}\mathrm{cm}^{-2})$	σ $(10^{13}\mathrm{cm}^{-2})$	ϵ_{50}	ϵ_{75}	ϵ_{90}	K − S	γ	Γ
1980	0.10	0.80	0.18	0.32	0.47	0.07	0.90	0.93
1981	0.10	0.88	0.24	0.42	0.60	0.13	0.90	0.92
1982	0.17	0.72	0.22	0.40	0.58	0.07	0.91	0.91
1983	0.17	0.49	0.30	0.51	0.75	0.13	0.85	0.86
1984	−0.01	0.41	0.27	0.44	0.65	0.08	0.85	0.86
1985	0.10	0.26	0.31	0.58	1.13	0.20	0.78	0.78
1986	0.19	0.25	0.39	0.77	1.25	0.26	0.83	0.83
1987	−0.03	0.23	0.23	0.43	0.62	0.09	0.85	0.85
1988	−0.20	0.59	0.27	0.44	0.61	0.18	0.89	0.89
1989	−0.03	0.85	0.24	0.42	0.60	0.18	0.91	0.91

Table 2-4. Comparison of predicted TEC from the AIPS ionospheric model with the measured TEC values at Boulder, Co.

Year	α $(10^{13}\mathrm{cm}^{-2})$	σ $(10^{13}\mathrm{cm}^{-2})$	ϵ_{50}	ϵ_{75}	ϵ_{90}	K − S	γ	Γ
1980	0.36	1.03	0.31	0.54	0.84	0.11	0.82	0.84
1981	0.52	1.08	0.34	0.58	0.91	0.14	0.86	0.88
1982	0.48	0.91	0.32	0.58	0.93	0.12	0.87	0.88
1983	0.17	0.57	0.36	0.59	0.87	0.12	0.77	0.79
1984	−0.01	0.41	0.29	0.48	0.73	0.13	0.85	0.83
1985	0.06	0.30	0.36	0.64	1.04	0.11	0.71	0.72
1986	0.14	0.28	0.38	0.69	1.10	0.22	0.74	0.74
1987	−0.04	0.25	0.28	0.51	0.72	0.14	0.83	0.81
1988	−0.05	0.68	0.28	0.47	0.65	0.17	0.84	0.88
1989	0.22	1.15	0.36	0.62	0.89	0.14	0.81	0.81

Table 2-5. Monthly mean sunspot number for the period 1980 through 1989.

Year	Jan	Feb	Mar	Apr	May	Jun
1989	161.3	165.1	131.4	130.6	138.5	196.2
1988	59.0	40.0	76.2	88.0	60.1	101.8
1987	10.4	2.4	14.7	39.6	33.0	17.4
1986	2.5	23.2	15.1	18.5	13.7	1.1
1985	16.5	15.9	17.2	16.2	27.5	24.2
1984	57.0	85.4	83.5	69.7	76.4	46.1
1983	84.3	51.0	66.5	80.7	99.2	91.1
1982	111.2	163.6	153.8	122.0	82.2	110.4
1981	114.0	141.3	135.5	156.4	127.5	90.9
1980	159.6	155.0	126.2	164.1	179.9	157.3

Year	Jul	Aug	Sep	Oct	Nov	Dec
1989	126.9	168.9	176.7	159.4	173.0	165.5
1988	113.8	111.6	120.1	125.1	125.1	179.2
1987	33.0	38.7	33.9	60.6	39.9	27.1
1986	18.1	7.4	3.8	35.4	15.2	6.8
1985	30.7	11.1	3.9	18.6	16.2	17.3
1984	37.4	25.5	15.7	12.0	22.8	18.7
1983	82.2	71.8	50.3	55.8	33.3	33.4
1982	106.1	107.6	118.8	94.7	98.1	127.0
1981	143.8	158.7	167.3	162.4	137.5	150.1
1980	136.3	135.4	155.0	164.7	147.9	174.4

Source: Solar Geophysical Data

Table 2-6. Results of a simulation of ionospheric Faraday rotation using the improved ionospheric Faraday rotation model.

Time hr.	A_z deg	Z deg	RM rad m^{-2}	$\Delta\chi$ deg	RM(χ) rad m^{-2}	TEC 10^{13} cm^{-2}
0	2.2	54.0	0.527	2.77	0.527	8.39
1	353.6	53.6	0.536	2.82	0.536	8.32
2	346.0	51.3	0.540	2.84	0.540	8.52
3	340.4	47.7	0.503	2.64	0.503	8.34
4	337.0	43.1	0.431	2.26	0.431	7.45
5	335.7	38.1	0.415	2.18	0.415	7.16
6	336.0	33.0	0.539	2.83	0.539	9.64
7	337.7	28.0	0.729	3.83	0.729	15.67
8	340.5	23.6	0.800	4.20	0.800	22.88
9	344.2	19.8	0.706	3.71	0.706	27.77
10	348.7	16.9	0.589	3.10	0.589	30.01
11	353.6	14.9	0.522	2.74	0.522	31.97
12	358.8	14.1	0.485	2.55	0.485	34.24
13	4.1	14.4	0.467	2.46	0.467	35.45
14	9.2	15.9	0.493	2.59	0.493	34.96
15	13.9	18.4	0.587	3.08	0.587	33.65
16	18.0	21.8	0.741	3.89	0.741	31.98
17	21.2	26.0	0.896	4.71	0.896	28.71
18	23.3	30.4	0.935	4.91	0.935	24.25
19	24.4	35.5	0.856	4.50	0.857	19.04
20	23.9	40.6	0.712	3.74	0.712	14.21
21	21.6	45.4	0.596	3.13	0.596	10.89
22	17.1	49.6	0.542	2.85	0.542	9.31
23	10.5	52.6	0.531	2.79	0.531	8.72

Table 2-7. Results of a simulation of ionospheric Faraday rotation using the AIPS model ionosphere.

Time hr.	TEC 10^{13} cm^{-2}	RM rad m^{-2}
0	9.10	0.3055
1	8.12	0.2707
2	7.45	0.2406
3	7.13	0.2172
4	7.18	0.1997
5	7.68	0.1865
6	8.77	0.1738
7	10.65	0.1544
8	13.57	0.1173
9	17.73	0.0508
10	22.98	−0.0457
11	28.53	−0.1482
12	32.85	−0.2095
13	34.61	−0.2024
14	33.66	−0.1125
15	30.84	0.0301
16	27.20	0.1764
17	23.47	0.2900
18	20.01	0.3512
19	17.08	0.3824
20	14.66	0.3860
21	12.72	0.3734
22	11.18	0.3524
23	9.97	0.3282

Table 2-8. Comparison of predicted TEC values with measured values on March 21, 1990 during observations of 2230+114. Various inputs into the improved ionospheric Faraday rotation model (IIFRM) and the AIPS model have been used.

UT	TEC (10^{13} cm^{-2}) Observed	IIFRM	IIFRM[1]	AIPS	AIPS[2]
0.0	49.5	51.9	31.7	34.8	31.2
12.0	7.9	12.9	12.8	12.5	11.2
13.0	8.5	17.0	12.1	11.6	10.4
14.0	21.3	27.1	19.8	19.8	17.7
15.0	32.0	39.9	25.0	25.5	22.8
16.0	37.0	49.7	25.3	26.1	23.4
17.0	48.5	54.4	28.7	30.3	27.2
18.0	56.7	57.2	32.7	34.8	32.7
19.0	57.1	59.6	34.2	37.1	33.3
20.0	58.1	60.9	32.9	35.5	31.5
21.0	58.0	60.8	36.8	40.4	35.8
22.0	49.0	59.7	34.1	37.1	32.7
23.0	41.9	57.3	32.9	34.8	32.4
24.0	37.9	51.9	32.9	36.3	32.6

[1] IIFRM model with foF2 input.

[2] AIPS model with foF2 input.

Table 2-9. Comparison of predicted ionospheric rotation measures towards the source 2230+114 on March 21, 1990. Various inputs into the improved ionospheric Faraday rotation model (IIFRM) and the AIPS model have been used.

	Rotation Measure (rad m^{-2})					
UT	IIFRM	IIFRM[1]	AIPS[2]	AIPS[3]	AIPS[4]	AIPS[5]
0.000	6.39	3.96	0.99	0.86	0.60	0.85
12.000	1.19	1.24	0.50	0.89	0.75	0.45
13.000	1.58	1.16	0.56	1.01	0.91	0.51
14.000	2.67	2.00	1.06	1.97	1.81	0.97
15.000	4.23	2.65	1.42	2.72	2.51	1.31
16.000	5.59	2.76	1.51	2.93	2.71	1.38
17.000	6.28	3.21	1.78	3.50	3.24	1.63
18.000	6.67	3.68	2.05	4.07	3.90	1.96
19.000	7.02	3.95	2.16	4.21	3.89	1.99
20.000	7.30	3.85	2.02	3.84	3.52	1.84
21.000	7.42	4.35	2.20	4.03	3.70	2.01
22.000	7.39	4.09	1.86	3.19	2.91	1.68
23.000	7.19	3.97	1.44	2.12	1.99	1.36
24.000	6.38	4.12	1.00	0.82	0.54	0.85

[1] IIFRM model with foF2 input.

[2] AIPS model without TEC or foF2 input.

[3] AIPS model without TEC of foF2 input and using IGRF.

[4] AIPS model without TEC input but with foF2 input and using IGRF.

[5] AIPS model without TEC input but with foF2 input.

Table 2-10. Ionospheric rotation measure values towards the source 2230+114 on March 21, 1990 used by Sakurai (1994).

UT	IIFRM rad m^{-2}	AIPS rad m^{-2}
13.994	3.17	3.08
14.078	3.28	3.19
15.266	4.89	4.46
15.340	4.99	4.51
16.346	5.94	5.67
16.423	5.98	5.78
17.438	6.50	7.07
17.518	6.53	7.15
18.646	6.92	7.58
18.713	6.94	7.58
19.733	7.22	7.57
19.812	7.24	7.56
20.827	7.37	7.34
20.909	7.37	7.31
22.042	7.25	5.91
22.126	7.22	5.78
23.122	6.65	4.31
23.206	6.56	4.18

Source: Sakurai, T. private communication.

Figure 2-1. A typical daytime and nighttime profile of the electron density in the Earth's ionosphere as determined using the International Reference Ionosphere model. The four main region of the ionosphere, the D, E, and F regions are identified.

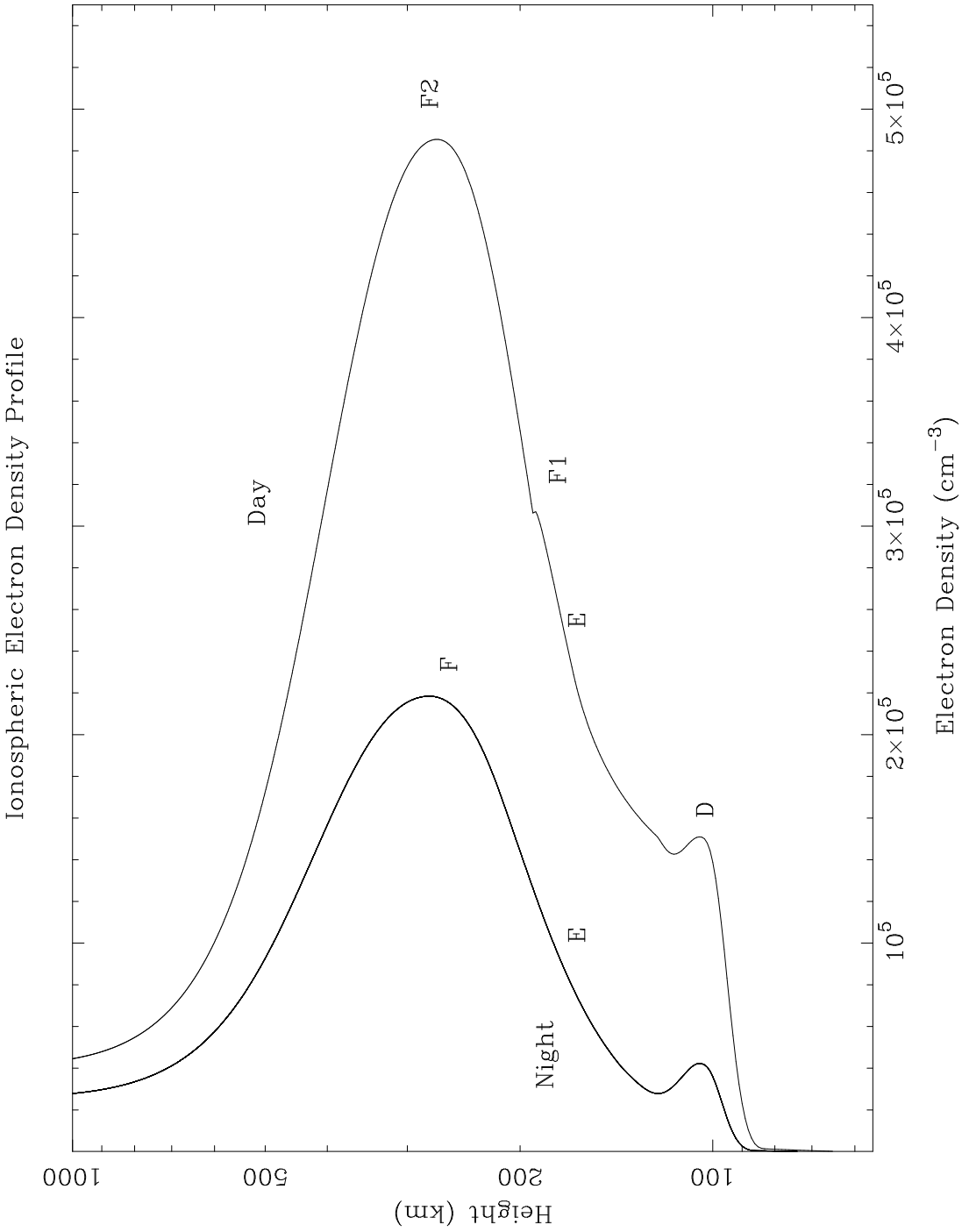
Ionospheric Electron Density Profile
Height (km)
Electron Density (cm^{-3})
1000
500
200
100
5×10^5
4×10^5
3×10^5
2×10^5
10^5
Day
Night
F2
F1
F
E
E
D

Figure 2-2. The secular change in the geomagnetic field at the VLA from 1940 through 1995 with predictions continuing through the year 2000. The solid line represents the total strength of the geomagnetic field at the VLA while the dashed line represents the strength of the dipole moment term of the geomagnetic field at the VLA. These data were obtained from the the World Data Center and show that the geomagnetic field changes by $\sim 8\%$ per century.

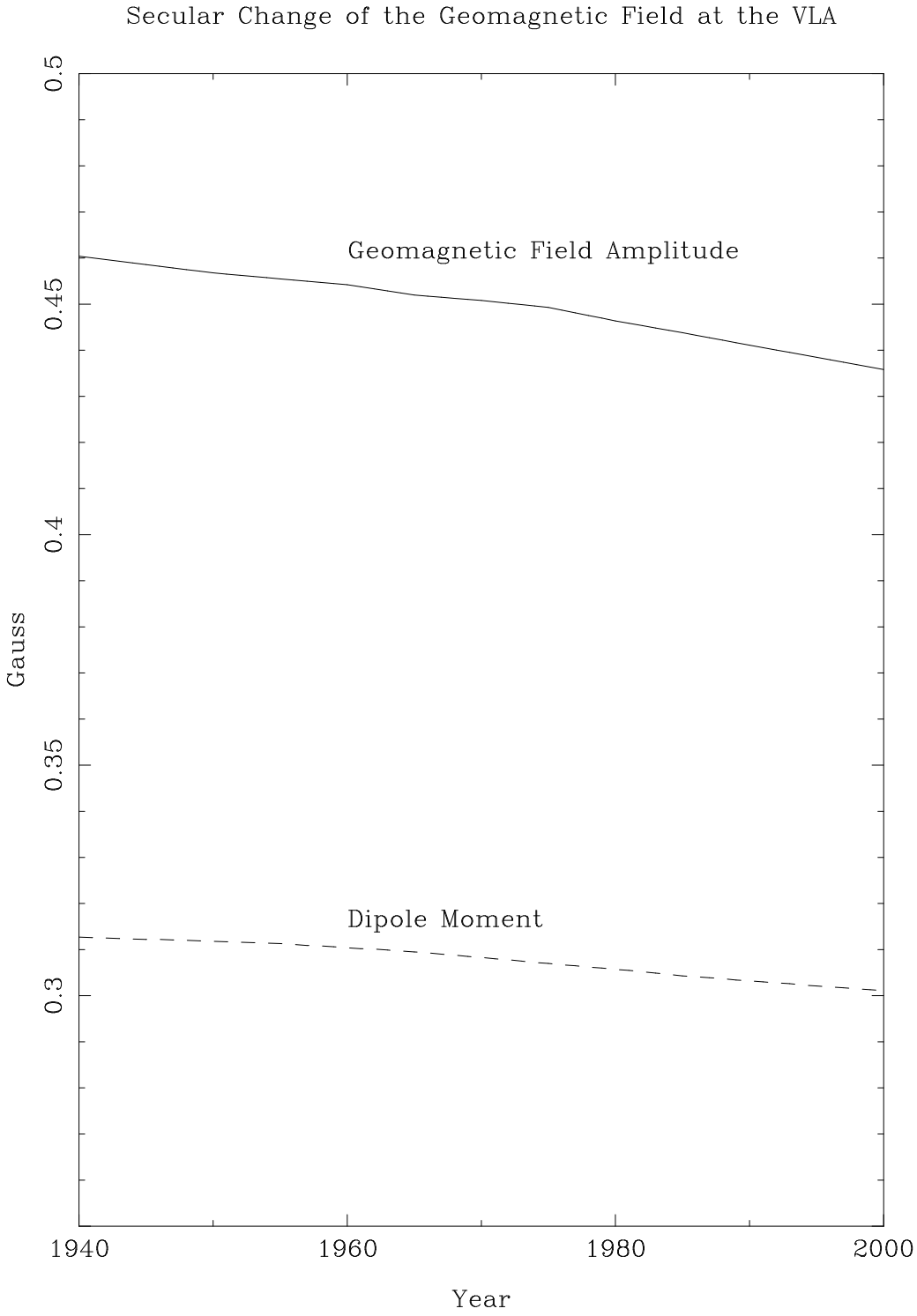
Secular Change of the Geomagnetic Field at the VLA
Geomagnetic Field Amplitude
Dipole Moment
Gauss
0.5
0.45
0.4
0.35
0.3
1940
1960
1980
2000
Year

Figure 2-3. Predicted TEC versus the measured TEC at Boulder, Co. during March 1990 for: (a) the IRI model, (b) the AIPS model, (c) the IRI model with foF2 values measured at Boulder, Co. input into the model.

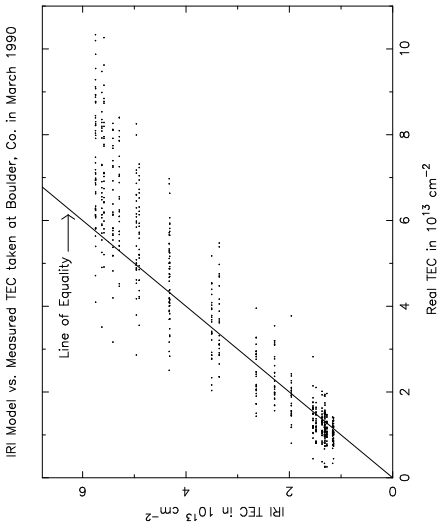
IRI Model vs. Measured TEC taken at Boulder, Co. in March 1990
Line of Equality
IRI TEC in 10^{13} cm^{-2}
Real TEC in 10^{13} cm^{-2}
0
2
4
6
8
10

(a)

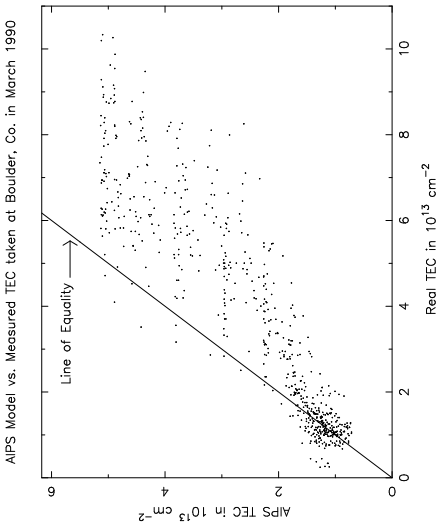
AIPS Model vs. Measured TEC taken at Boulder, Co. in March 1990
Line of Equality
AIPS TEC in 10^{13} cm^{-2}
Real TEC in 10^{13} cm^{-2}
0
2
4
6
8
10

(b)

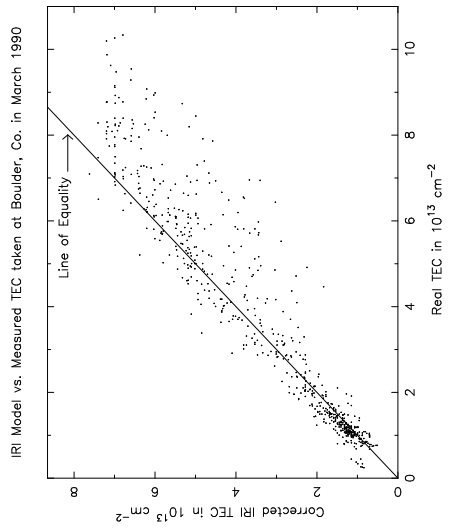
IRI Model vs. Measured TEC taken at Boulder, Co. in March 1990
Line of Equality
Corrected IRI TEC in 10^{13} cm^{-2}
Real TEC in 10^{13} cm^{-2}
0
2
4
6
8
10

(c)

Figure 2-4. Fractional error between the predicted TEC and the measured TEC at Boulder, Co. during March 1990 for: (a) the IRI model, (b) the AIPS model, (c) the IRI model with foF2 values measured at Boulder, Co. input into the model.

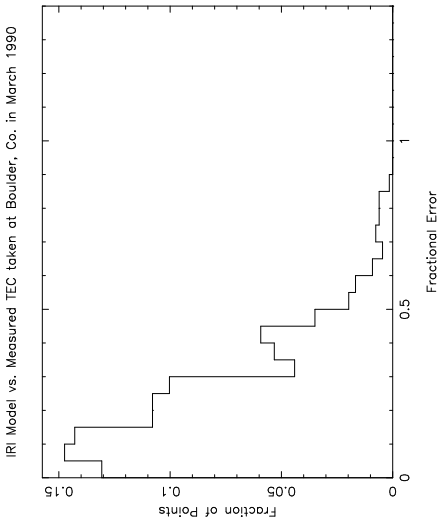
IRI Model vs. Measured TEC taken at Boulder, Co. in March 1990
Fraction of Points
0
0.05
0.1
0.15
0
0.5
1
Fractional Error

(a)

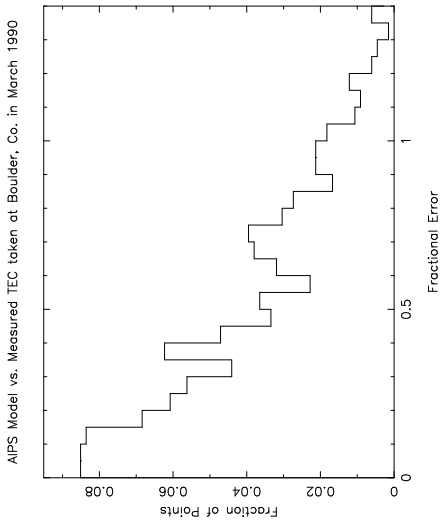
AIPS Model vs. Measured TEC taken at Boulder, Co. in March 1990
Fraction of Points
0
0.02
0.04
0.06
0.08
0
0.5
1
Fractional Error

(b)

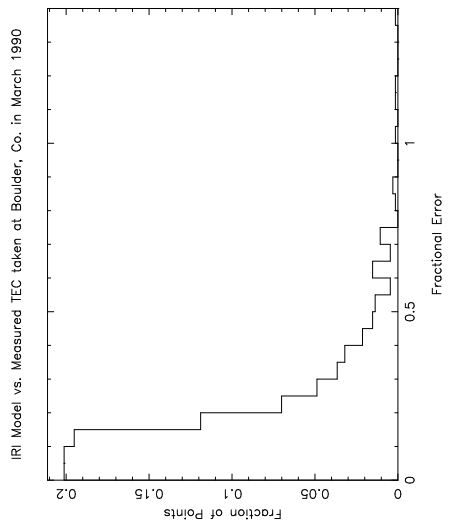
IRI Model vs. Measured TEC taken at Boulder, Co. in March 1990
Fraction of Points
0
0.05
0.1
0.15
0.2
0
0.5
1
Fractional Error

(c)

Figure 2-5. Sample output from the improved ionospheric Faraday rotation model. The simulation is for observations from the VLA on March 21, 1993 of the source 1200+700 at 1.4 GHz with a sunspot number of 89. Shown are: (a) the phase difference between the right and left circularly polarized waves due to their propagating through the ionosphere versus time, (b) the left circularly polarized phase versus time, (c) the right circularly polarized phase versus time and (d) the Azimuth (diamonds) and Altitude (circles) of 1200+700 versus time.

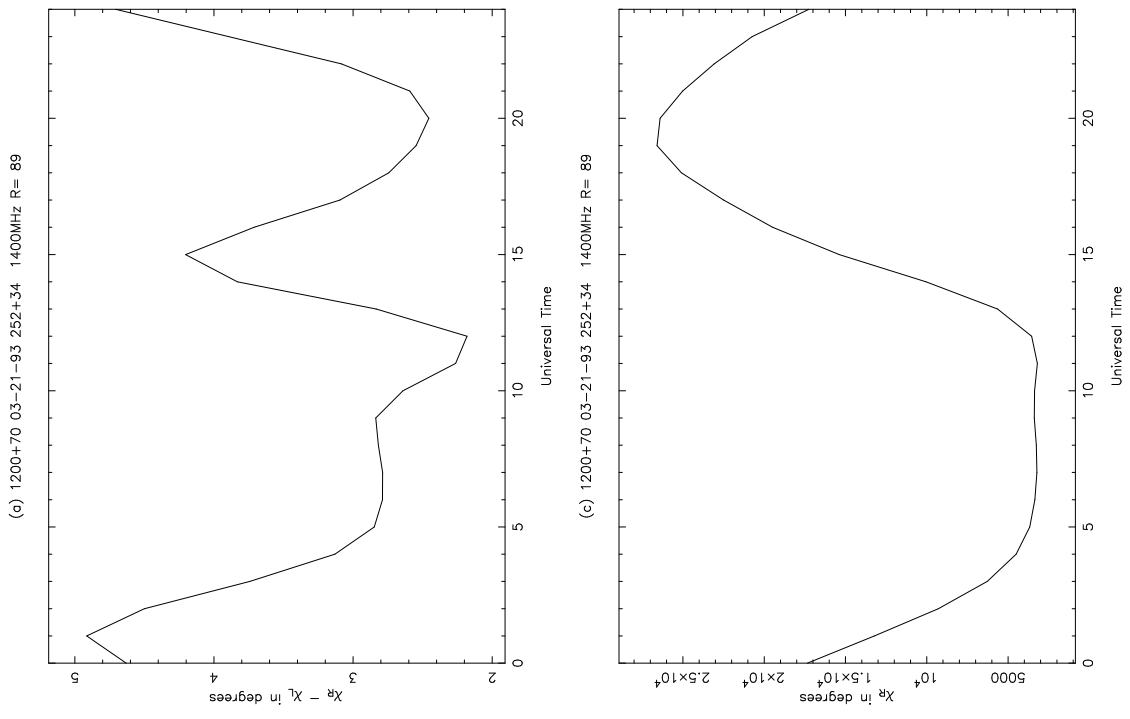
(a) 1200+70 03-21-93 252+34 1400MHz R= 89
$\chi_R - \chi_L$ in degrees
Universal Time
(b) 1200+70 03-21-93 252+34 1400MHz R= 89
χ_L in degrees
Universal Time
(c) 1200+70 03-21-93 252+34 1400MHz R= 89
χ_R in degrees
Universal Time
(d) 1200+70 03-21-93 252+34 1400MHz R= 89
Azimuth and Altitude in degrees
Universal Time

Figure 2-6. Sample output from the improved ionospheric Faraday rotation model. The simulation is for observations from the VLA on March 21, 1993 of the source 1200+700 at 1.4 GHz with a sunspot number of 89. The ionospheric rotation measure as predicted by the improved ionospheric Faraday rotation model versus time is shown as circles. The predicted ionospheric rotation measure values of the AIPS model for the same simulation are also shown as diamonds.

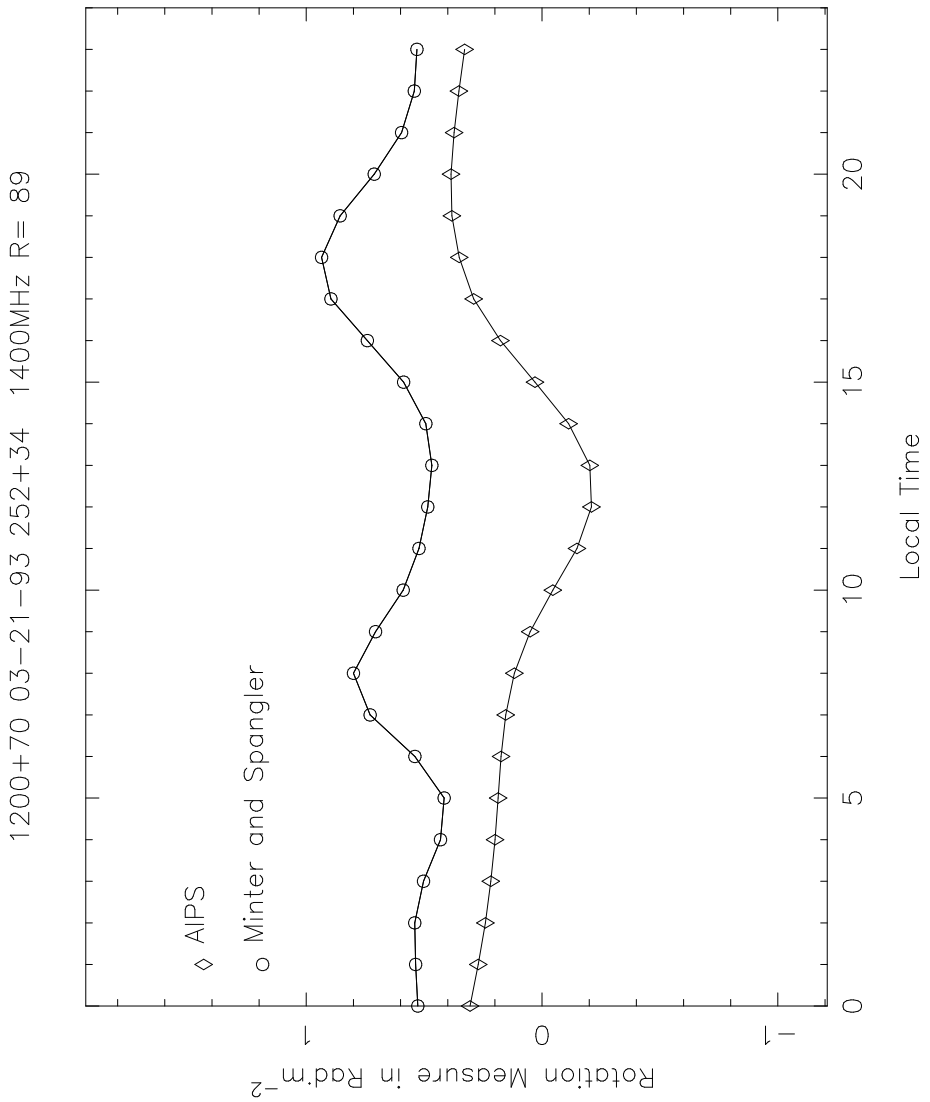
1200+70 03-21-93 252+34 1400MHz R= 89
◇ AIPS
o Minter and Spangler
Rotation Measure in Rad.m^{-2}
1
0
-1
0
5
10
15
20
Local Time

Figure 2-7. Illustration of how the AIPS model for ionospheric Faraday rotation can predict the wrong sign for the ionospheric rotation measure. The line of sight is passing over a magnetic pole and the AIPS model only evaluates the geomagnetic field at a height h. As can be seen the AIPS model uses a geomagnetic field which is pointed towards the observer in this illustration while the line of sight averaged geomagnetic field is pointed away from the observer.

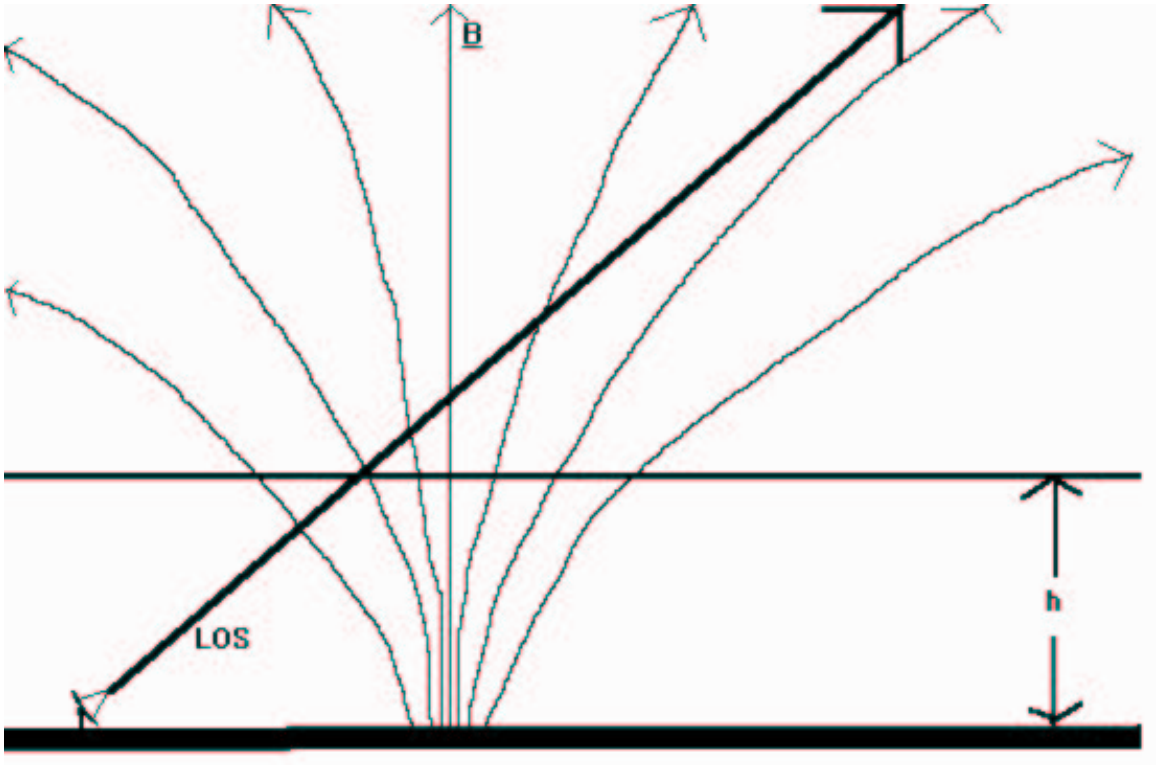
B
LOS
h

Figure 2-8. Sample output from the improved ionospheric Faraday rotation model. The simulation is for observations from the VLA on March 21, 1993 of the source 1200+700 at 1.4 GHz with a sunspot number of 89. The ionospheric rotation measure as predicted by the improved ionospheric Faraday rotation model versus time is shown as circles. The predicted ionospheric rotation measure values of the AIPS model using the IGRF geomagnetic field model for the same simulation are also shown as diamonds.

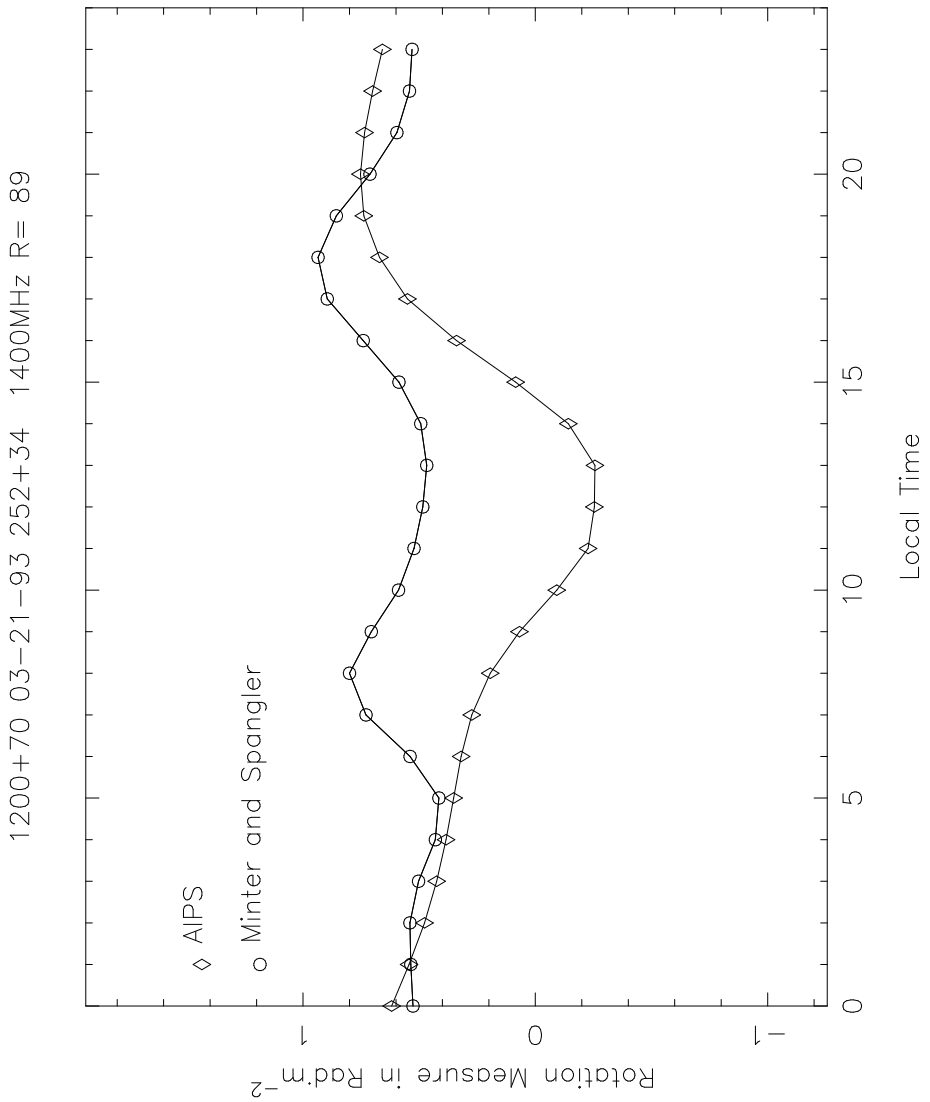
1200+70 03-21-93 252+34 1400MHz R= 89
◇ AIPS
o Minter and Spangler
Rotation Measure in Rad.m^{-2}
1
0
-1
0
5
10
15
20
Local Time

Figure 2-9. The azimuth (diamonds) and altitude (circles) angles for the source 2230+114 versus time on March 21, 1990.

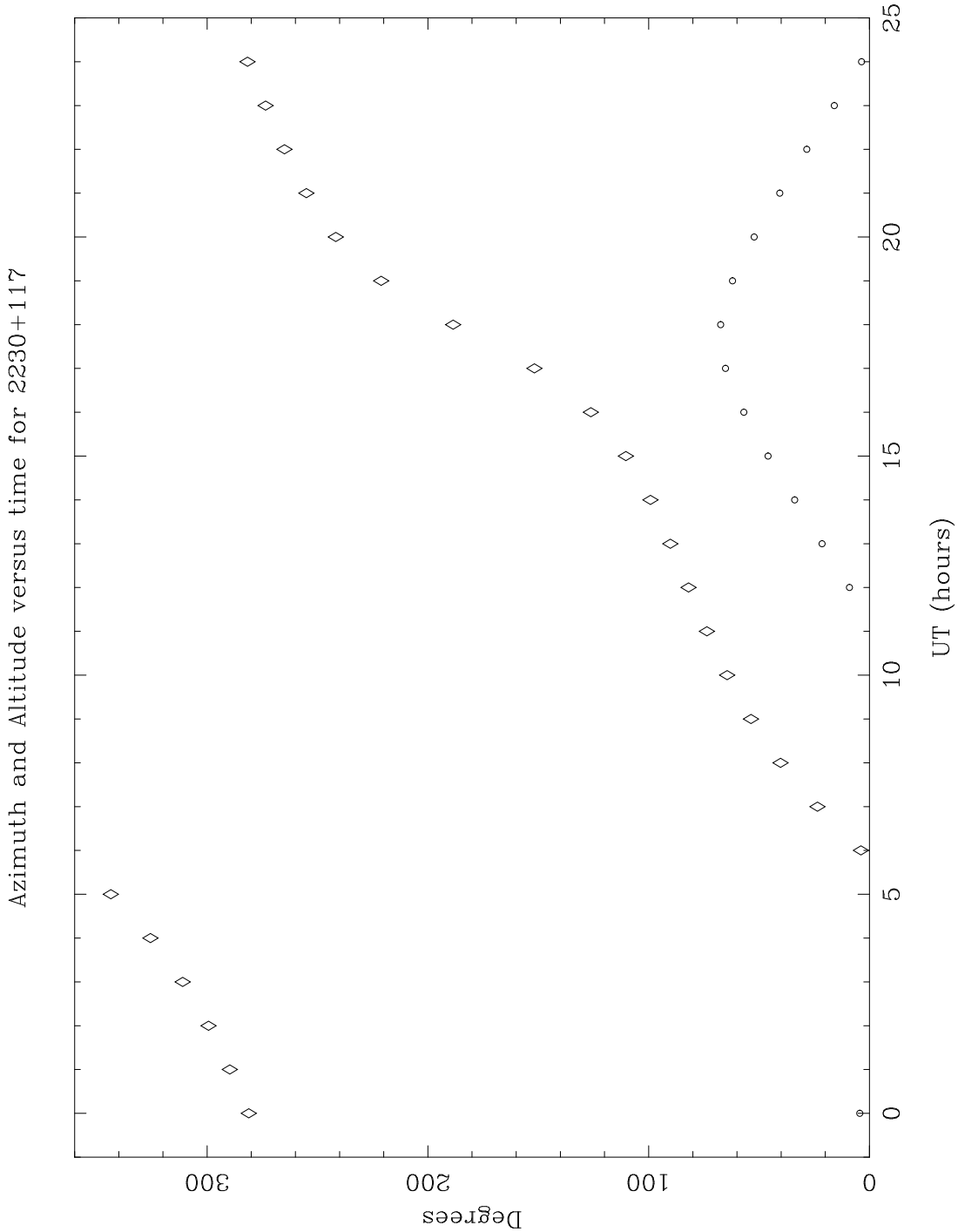
Azimuth and Altitude versus time for 2230+117
Degrees
0
100
200
300
0
5
10
15
20
25
UT (hours)

Figure 2-10. The ionospheric rotation measure predictions of the improved ionospheric Faraday rotation model (IIFRM) and the AIPS model for the source 2230+117 on March 21, 1990. The solid line is the prediction of the MS model. The dot-dash line is the prediction of the IIFRM with foF2 values being input into the model. The dotted line is the AIPS model without any inputs and the dashed line is the AIPS model with TEC values being input into the model.

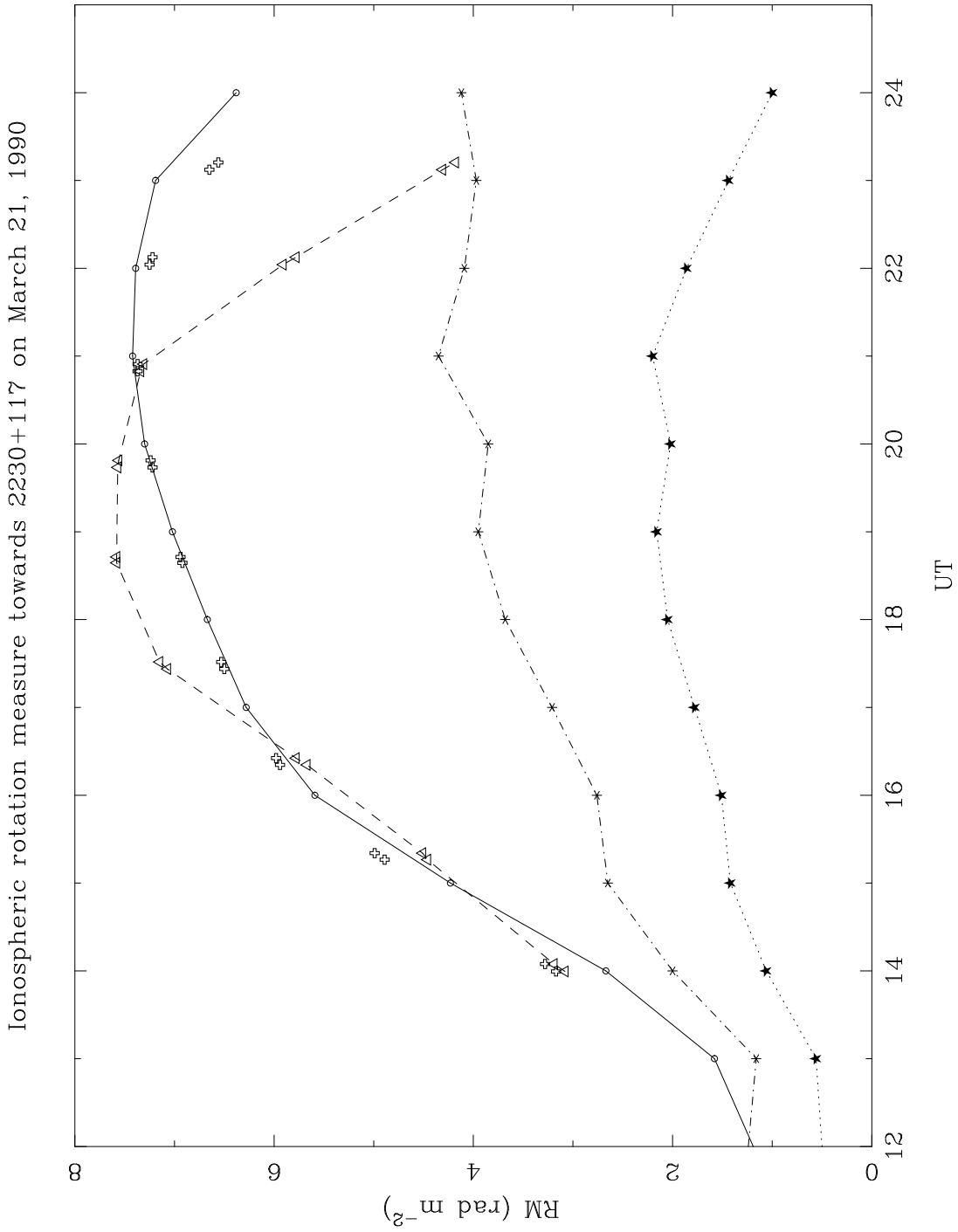
Ionospheric rotation measure towards 2230+117 on March 21, 1990
RM (rad m^{-2})
0
2
4
6
8
12
14
16
18
20
22
24
UT

Figure 2-11. The polarization position angles of the source 2230+114 on March 21, 1990 at 20 cm. Several ionospheric Faraday rotation calibration schemes have been implemented. The solid and dashed lines show the results when the improved ionospheric Faraday rotation model is used while the dot-dash line shows the results of the AIPS model.

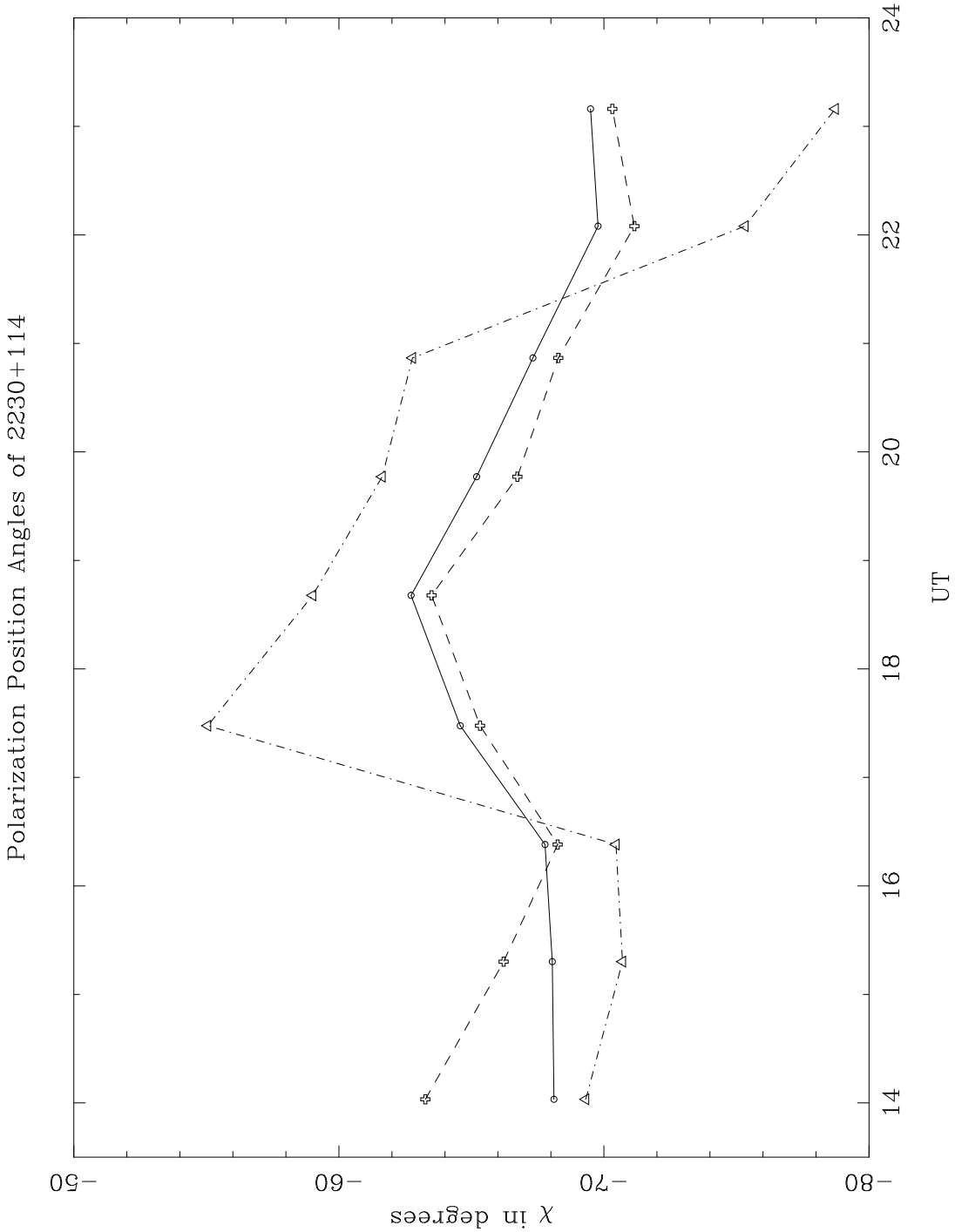
Polarization Position Angles of 2230+114
χ in degrees
UT
−80
−70
−60
−50
14
16
18
20
22
24

Figure 2-12. The polarization position angles of the source 2230+114 on March 21, 1990 at 18 cm. Several ionospheric Faraday rotation calibration schemes have been implemented. The solid and dashed lines show the results when the improved ionospheric Faraday rotation model is used while the dot-dash line shows the results of the AIPS model.

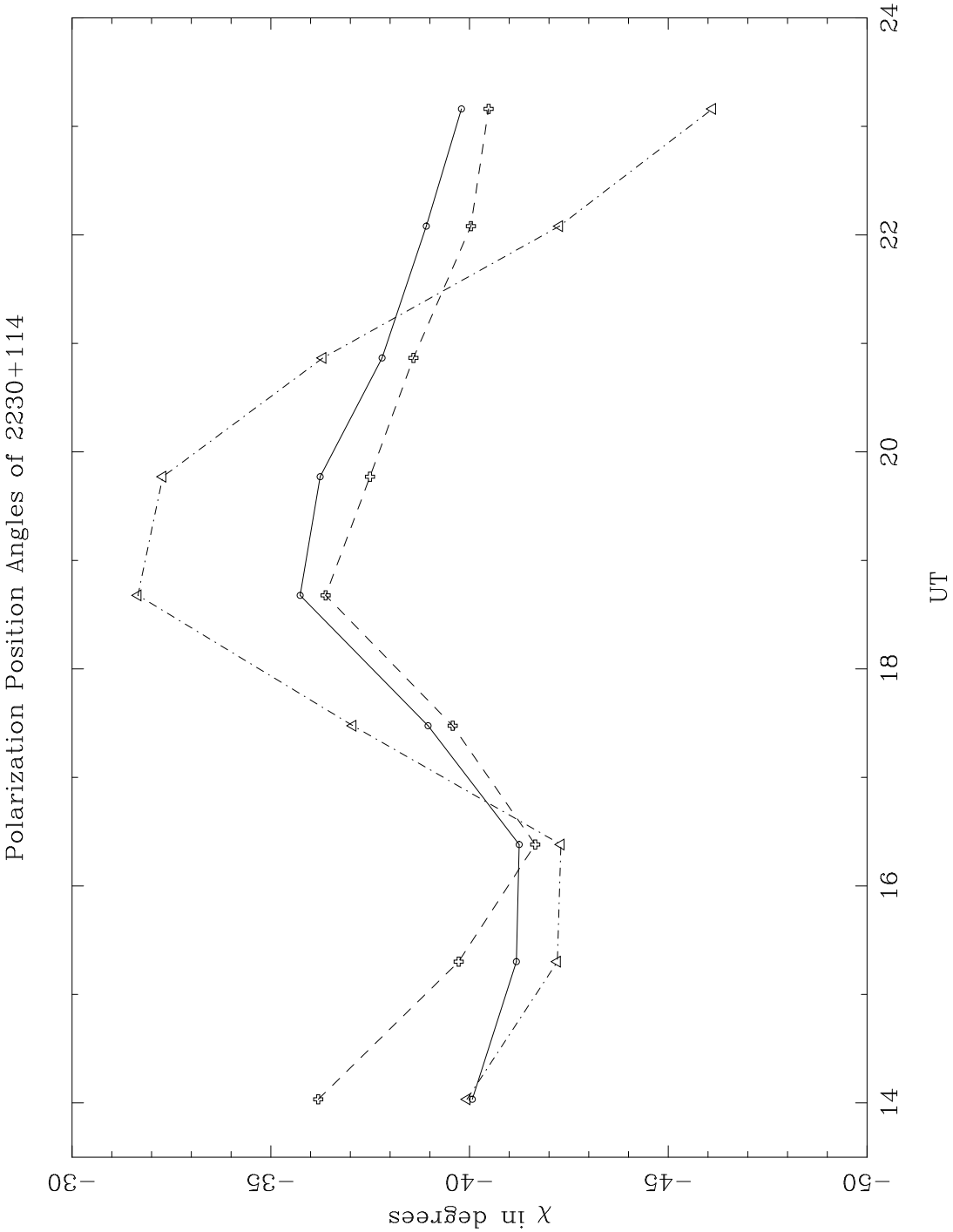
Polarization Position Angles of 2230+114
χ in degrees
UT
−30
−35
−40
−45
−50
14
16
18
20
22
24

CHAPTER 3

OBSERVATIONS AND DATA REDUCTION

3.1 Introduction

A preliminary list of radio sources (the majority presumably being extragalactic) in the area covered by Reynolds's H_α measurements was obtained from the Green Bank All Sky Survey (Condon and Broderick 1986). The literature was then searched for existing polarization data on these sources. Sources which were found to be unsuitable for rotation measure measurements as determined by polarization data from the literature search were rejected from the preliminary list of sources. An initial survey of the $\sim$ 80 preliminary sources was carried out during an eight hour observing session on March 13, 1993 using the VLA in the B configuration. A "snapshot" ($\leq$ 5 minute integration time) of each source was obtained at 1427.5 MHz and 1507.5 MHz to determine both the total and polarized intensities along with source structure. A total of 38 sources were found to be suitable for further observations. The elected sources were reobserved with the VLA in a hybrid C-B configuration during three eight hour observing sessions on June 1,5 and 6, 1993. Each source was observed with a longer total integration time (typically 10 to 25 minutes), determined so that $\sigma_{\rm RM} \leq 3$ rad m^{-2} for the major polarized components of each source at each of the two frequencies 1360.0 MHz and 1638.0 MHz.

For both the initial finding survey as well as the subsequent observations to precisely measure the rotation measures, a continuum bandwidth of 25 MHz was chosen to avoid serious problems with L band interference. The frequencies of the observations

were chosen to avoid known interference problems, while giving as large a range of λ^2 in the polarization measurements so as to maximize the precision of the rotation measure measurement. The sources 0316+413 (3C 84), 0248+430 and 0518+165 (3C 138) were observed every half hour as amplitude, phase and polarization calibrators. The source 3C 286 was observed once as an absolute amplitude and polarization position angle calibrator.

3.2 Calibration and Mapping

Standard calibration techniques were followed except that particular care was taken when estimating and removing the ionospheric Faraday rotation. A comparison of the AIPS model and the improved ionospheric Faraday rotation model, described in Chapter 2, for the source 0248+430 on June 1, 1993 is shown in Figures 3-1 and 3-2. In Figure 3-1 we plot the polarization position angle of 0248+430 versus time at 1360 MHz on June 1, 1993. The solid line and circles give the polarization position angles for 0248+430 when the improved ionospheric Faraday rotation model is used for the ionospheric Faraday rotation calibrations. The dashed line and triangles gives the polarization position angles of 0248+430 when the AIPS model is used for ionospheric Faraday rotation calibration. Figure 3-2 is the same as Figure 3-1 except that it is for the polarization position angles of 0248+430 at 1638 MHz. A factor of two reduction in the RMS of the residual polarization position angles about the mean is obtained when the improved ionospheric Faraday rotation model (IIFRM) is applied to the calibration, compared to when the AIPS model is used in the calibration. The RMS noise in Q and U are also found to be reduced by a factor of two when the IIFRM is used in the calibration of the data. The dynamic range of the polarization intensity was found to increase by a factor of 1.5 when the IIFRM model was used.

Subsequent to correction of the data for ionospheric Faraday rotation, we solved and corrected for the instrumental polarization of the VLA antennas, using observations of our calibrator sources, 3C 84 and 0248+430. This was carried out using the AIPS task POLCAL. Finally, the absolute values of all measured polarization position angles were established from observations of the sources 3C 286 and 3C 138. Description of these calibration procedures are given in Bignell (1982) or Sakurai and Spangler (1994). No attempt was made to correct for time variability of the instrumental polarization, as described in Sakurai and Spangler (1994). Such variations should be a small effect relative to the quantities we are measuring.

Once calibrated, the data were processed into Stokes I, Q and U images using AIPS. Again we had to be careful in the processing of the data since the two experiments were performed with the VLA in different configurations and thus with different beams and array responses to the source structure and polarization. Uniform weighting of the (u,v) data was used along with a two dimensional Gaussian taper with the e^{-1} level at 20 kλ in u and 30 kλ in v. This had the effect of making the effective beam nearly identical for all four frequencies and thus making the beam responses nearly identical at all four frequencies. The data were then Fourier transformed and CLEANED (Clark 1980) to deconvolve the beam response from the image. The images at all four frequencies were then convolved with the largest of the four beams, typically $11''$ by $6''$, to provide the same resolution at all four frequencies. Using a beam of this size has distinct advantages for our RM survey. It is small enough to separately resolve the core, jets and lobes of extragalactic radio sources without giving more than a few resolution elements in most of the radio lobes thus maximizing our sensitivity to weak, polarized features. It should be noted that the (u,v) plane coverage for the two frequencies in the "precision" experiment were nearly identical so that the above procedures were performed as a form of fine-tuning of the data. However, for comparing

the "finder survey" with the precision measurements, the (u,v) plane coverage is drastically different, so that the steps employed here are absolutely crucial to first order. It should also be emphasized that the second experiment, with more data and better (u,v) plane coverage, was used for precision measurement of rotation measures. Data from the initial survey was processed in the manner described above and compared with the second experiment to insure that derived rotation measures were not affected by $n\pi$ position angle ambiguities.

From the Stokes I, Q and U maps, maps of the polarized flux density

$$P = \sqrt{Q^2 + U^2} \tag{3.1}$$

and polarization position angle

$$\chi = \frac{1}{2} \arctan\left(\frac{U}{Q}\right) \tag{3.2}$$

were produced. The maps for P and χ were then clipped for $P \leq 5\sigma_P$ where

$$\sigma_P = \sqrt{\frac{Q^2\sigma_Q^2 + U^2\sigma_U^2}{4P^2}} \tag{3.3}$$

and

$$\sigma_\chi = \frac{\sigma_P}{2\ P} \tag{3.4}$$

to insure that only data with a high signal to noise ratio were used in our analysis. The values of σ_Q and σ_U were measured in off-source portions of the Q and U maps and were typically of the order of $0.05 - 0.10$ mJy/beam in maps from the second experiment.

3.3 Determination of the Rotation Measures

For each source, the data from the four frequencies of observation were processed as follows. We were fortunate in that for most of the sources there was more

than one significantly polarized component, or the polarized emission was resolved. The rotation measure and its error was determined for each pixel that had valid position angles at all four frequencies using a linear least squares fit to $\chi(\lambda^2)$. We checked each source for the possibility that multiple wraps of the polarization position angles (i.e. $n\pi$ ambiguities in determining the rotation measure) had occurred between adjacent frequencies. Such a wrapping would require RM $\geq$ 700 rad m^{-2} and was not found for any of our sources. The rotation measure was then determined for each component of each source by using a weighted average

$$< \mathrm{RM} >= \frac{\sum_{k=0}^{n} \mathrm{RM_k}/\sigma_k^2}{\sum_{k=0}^{n} 1/\sigma_k^2} \tag{3.5}$$

$$\sigma_{\mathrm{RM}}^2 = \frac{1}{N}\frac{1}{\sum_{k=0}^{n} 1/\sigma_k^2} \tag{3.6}$$

where N is the number of pixels in a beam, n is the number of pixels in a given source component and σ_k is the weight assigned to each pixel. The reason for the $^1/_N$ term is the fact that the N pixels in the beam are correlated, thus giving only $^n/_N$ independent measurements in each component. As noted above, the amount of data from the second experiment greatly exceeded that from the finder survey. This fact was reflected in the weights assigned to the data in the fitting procedure described above. In addition, rotation measure values were obtained utilizing only data from the precision experiment. The rotation measures obtained were in all cases equivalent within the errors to the values obtained as described above. The choice as to the number of components and location of the component pixels was made for each component on the basis of inspection of maps of I, P, and $\Delta\chi = \chi(1638) - \chi(1360)$. The criteria used in defining a component were a region of high signal to noise ratio and homogeneity in I, P, and $\Delta\chi$. The rotation measures determined in this manner were found to agree with

the rotation measures found at the peak polarization intensity for several randomly selected sources.

Figure 3-3 illustrates the type of data we worked with to extract the rotation measure data. Figure 3-3 shows the polarization position angles at all four frequencies measured at the location of peak polarized intensity in the two lobes of 0217+417. The position angles are plotted versus the square of the observing wavelength, so Faraday rotation will produce a linear relationship in such a plot. The top panel (component A) corresponds to the south-preceding component and the bottom panel represents the north-following component. The main points of Figure 3-3 are (a) the good adherence of the data to the λ^2 dependence of Faraday rotation, and (b) the similarity of the rotation measures of these two components, -81.7 ± 0.6 rad m^{-2} for A, and -86.1 ± 1.2 rad m^{-2} for D.

The rotation measure of each component was determined using equations (3-5) and (3-6) since gradients in the polarization position angle across a component were observed for many sources. However, in these cases the rotation measure either showed much smaller variations, or frequently no significant variations at all. The fact that intrasource variations in the rotation measure are in all cases very small is a strong argument that the rotation measures observed here are dominated by, if not solely comprised of Faraday rotation in our galaxy. As a further check for internal Faraday rotation, the depolarization

$$D = \frac{M_{1638\ \mathrm{MHz}}}{M_{1360\ \mathrm{MHz}}} \tag{3.7}$$

was calculated for every component where $M = P/I$ is the percent polarization. Cioffi and Jones (1980) have shown that internal Faraday rotation in a synchrotron-emitting source produces a correlated depolarization and position angle variation, in which the magnitude of the depolarization and the position angle changes are dependent on the

rotation measure within the source. A value of D significantly in excess of unity is thus an indicator of internal Faraday rotation, although a fine grained, Faraday rotating screen outside the synchrotron-emitting region is also a possibility. In either case it is an undesirable indicator demonstrating the importance of Faraday rotation at the source rather than in our galaxy. Components that showed significant depolarization effects, $D \gg 1$, were then removed from further analysis. Depolarization effects were also looked for by comparing the change in rotation measure and the change in D between components in a source. This allowed for the further detection of components that might be subject to internal Faraday rotation effects. The basic conclusion drawn from such analyses for the entire sample of sources is that the Faraday rotation we observe for these sources is dominated by magnetized plasma in our galaxy, with very few persuasive cases of Faraday rotation in the radio source or its host galaxy. We reach this conclusion, cognizant of the well known observations of patches of extremely high rotation measure observed for some extragalactic radio sources (e.g. Ge and Owen 1993). It appears to be the case that in all such observations the angular resolution was higher than in our observations, the observing frequency higher or the IF bandwidth narrower. Such equipment configurations are necessary in the observations of Ge and Owen (1993) to prevent depolarization by instrumental factors. Given our instrumental parameters, regions such as those discussed by Ge and Owen (1993) would have appeared unpolarized and would not have entered into our analysis.

Finally, perhaps the best argument that galactic Faraday rotation dominates our observations is that offered in previous discussions of this matter by Lazio et al. (1990); the rotation measure structure function, or mean square difference between rotation measures, is found to depend on the angular separation $\delta\theta$ between the components, and extrapolates to very small values for $\delta\theta \rightarrow 0$. This would not be the

case if source-related plasma were dominating or making a major contribution to our measurements.

This argument serves to indicate that most of the rotation measure we observe arises in the interstellar medium of our galaxy, but is least adequate for the relatively small, intrasource variations which will be of considerable interest to us in Chapter 6. In fact, Laing and Garrington (Garrington et al. 1988, Laing 1988) discovered Faraday rotation differences between components of radio sources which are interpreted as, and must be, intrinsic. We now briefly consider whether the Laing-Garrington effect might be important in our observations.

We have searched for the Laing-Garrington effect in our data and have found no evidence for its presence. Laing and Garrington found that for high-luminosity, compact ($< 30''$ separation) FR II sources the lobe on the jet side has little depolarization (D ~ 1.2) while the lobe on the counter-jet side has a large depolarization (D ~ 5) (Garrington et al. 1988). The likely source of the depolarization of the counter-jet side lobe is a Faraday rotating screen outside of the emitting region (Laing 1988). This then is capable of producing extremely large rotation measure variations for the counter-jet side lobe. In our data sample we have eliminated all lobes with large depolarizations (D > 1.5) and our smallest angular separation for two lobes is $\sim 70''$. Thus effects of the sort discussed by Laing and Garrington have been eliminated from our sample.

Figure 3-1. The polarization position angles of the source 0248+430 on June 1, 1993 at 1360 MHz. The solid line shows the results when the improved ionospheric Faraday rotation model is used while the dashed line shows the results of the AIPS model.

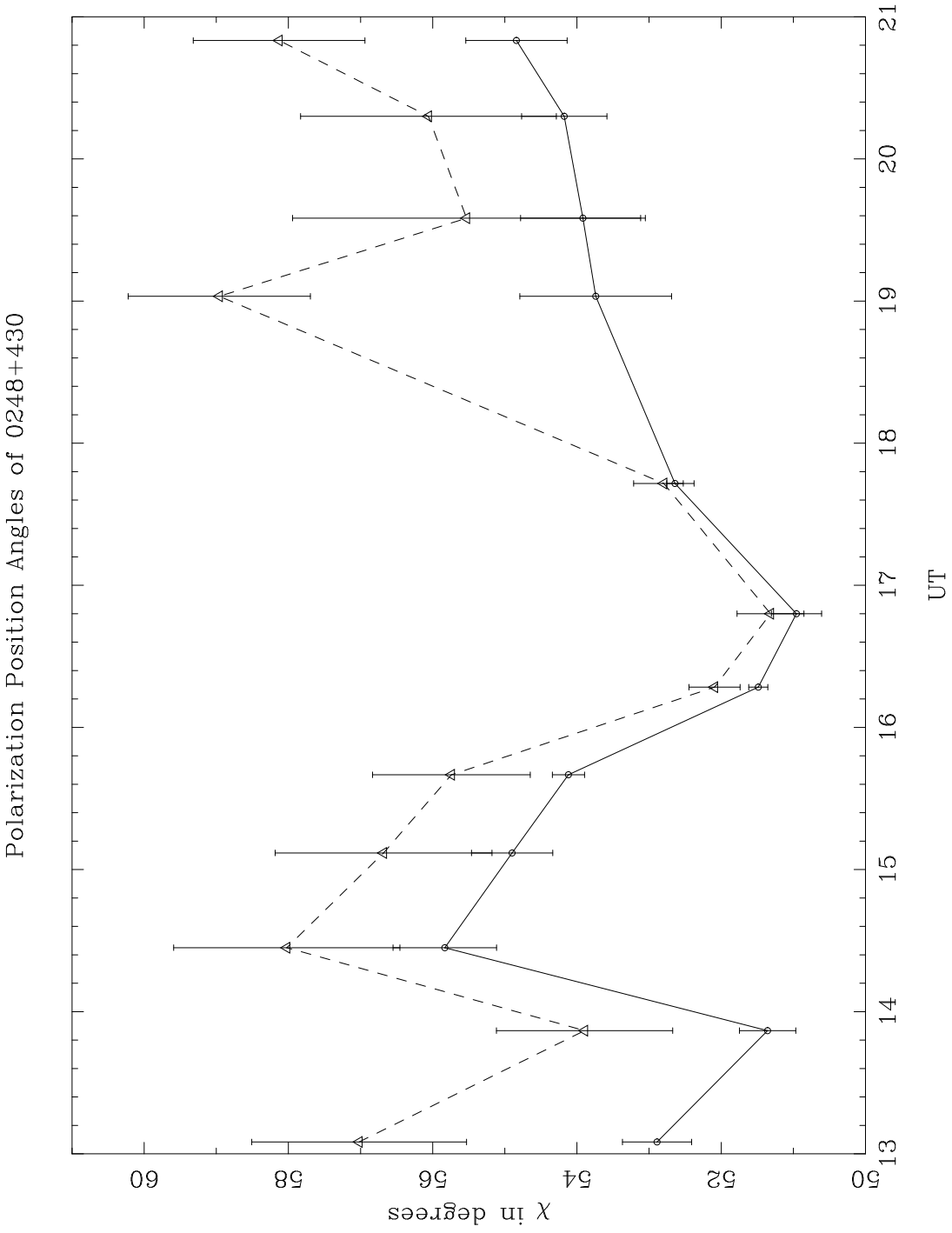
Polarization Position Angles of 0248+430
χ in degrees
UT
50
52
54
56
58
60
13
14
15
16
17
18
19
20
21

Figure 3-2. The polarization position angles of the source 0248+430 on June 1, 1993 at 1638 MHz. The solid line shows the results when the improved ionospheric Faraday rotation model is used while the dashed line shows the results of the AIPS model.

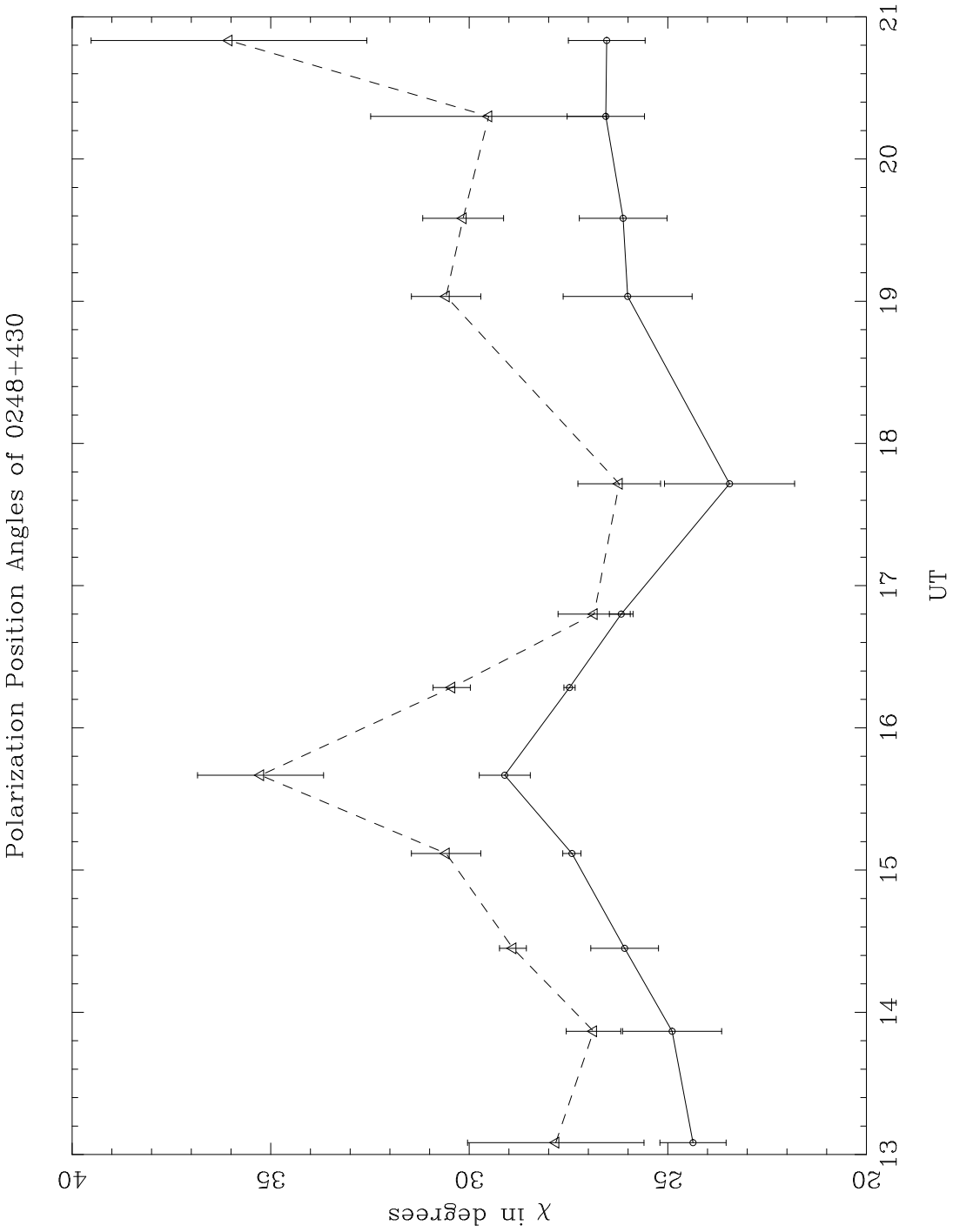
Polarization Position Angles of 0248+430
χ in degrees
UT
20
25
30
35
40
13
14
15
16
17
18
19
20
21

Figure 3-3. Fit of the rotation measure to the polarization position angles at the position of peak polarization intensity of the two lobes in 0217+417. Show are the least square fit of the rotation measure for: (a) component A; (b) component D. The values of the least square fit rotation measure are -81.7 ± 0.6 rad m^{-2} for component A, and -86.1 ± 1.2 rad m^{-2} for component D.

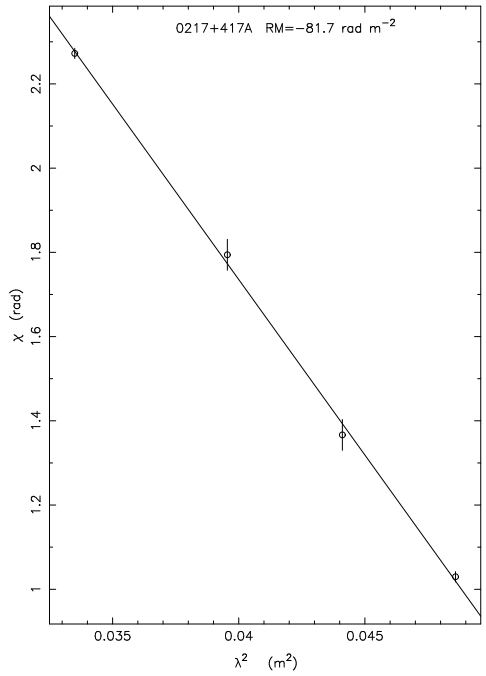
0217+417A RM=−81.7 rad m^{-2}
χ (rad)
λ^2 (m^2)
1
1.2
1.4
1.6
1.8
2
2.2
0.035
0.04
0.045

(a)

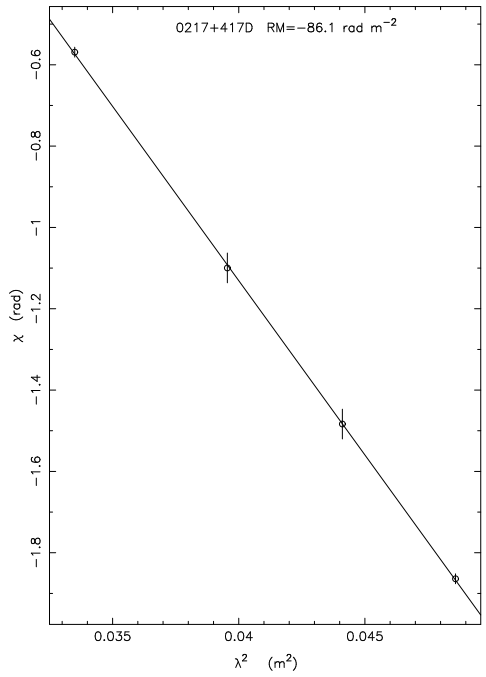
0217+417D RM=−86.1 rad m^{-2}
χ (rad)
λ^2 (m^2)
−0.6
−0.8
−1
−1.2
−1.4
−1.6
−1.8
0.035
0.04
0.045

(b)

CHAPTER 4

OBSERVATIONAL RESULTS AND SOURCE PROPERTIES

4.1 The Observed Rotation Measures

As a result of the data fitting and component selection described in Chapter 3, we finished with a sample of 69 components possessing high quality rotation measure values which could be used in our structure function analysis. A total of 29 components of the initial 98 sampled were discarded because they showed evidence of internal Faraday rotation. Components were discarded if they had a depolarization $D > 1.5$ or $D < 0.7$ (11 components). All 17 components of 0206+355 were discarded since it is a heavily resolved galactic disk. The source 0248+430 was also removed since it is observed through a cluster of galaxies which could introduce a non-galactic contribution to its observed rotation measure. Some sources contributed more than one component to our sample, while others possessed only a single component with a good measurement.

In Table 4-1 we present the rotation measures for all sources components. The first column gives the component name. A letter in the name indicates that there were two or more usable components in a single source. The second and third columns give the Right Ascension and Declination of each component in B1950 coordinates. The fourth column is the measured rotation measure and the fifth column is its error. The depolarization is listed in the sixth column. All components with a listed value for the depolarization are $> 5\sigma$ detections while components with no value for the depolarization listed are between 3σ and 5σ detections. It should be noted that

0206+355 is a heavily resolved, single component source having a large radio bridge of relatively constant intensity. The rotation measure "components" for this source arise from measuring the rotation measure across this resolved source at intervals separated approximately by a beam width.

A plot of all the observed rotation measures and the H_α measurements is shown in Figure 4-1. The field is centered near $l = 144°$, $b = -21°$. The H_α intensity (I_α) has been converted into emission measure assuming an effective temperature of 8000 K for the electrons (Reynolds 1991).

$$EM = 2.75\ T_4^{0.9}\ I_\alpha\ cm^{-6}\ pc \tag{4.1}$$

where T_4 is the electron temperature in units of 10^4 K and I_α is in Rayleighs

$$1\ R = 10^6/4\pi\ \text{photons}\ cm^{-2}\ s^{-1}\ sr^{-1}.$$

Reynolds et al. (1995) found that errors introduced by interstellar extinction are small. The emission measure is shown in grayscale while the positive rotation measures are shown as diamonds and the negative rotation measures are shown as circles. The sizes of the diamonds and circles are proportional to the magnitude of the rotation measure with a scale being shown on the left hand side of Figure 4-1. One source with a rotation measure of only -2.6 rad m^{-2} is also pointed out so that it is not missed by the reader. In the case of sources with two or more components, each component is represented with its own plotted symbol. The emission measure map originally had a resolution of 0.8° with a 1.0° separation between the center of pixels. The emission measure map has been convolved with a $^1/_2{}^\circ$ beam in order to produce an image without sharp edges in Figure 4-1. To the extent that a comparison can be made, our rotation measures are in agreement with the previous observations of Simard-Normandin et al. (1981) and Broten et al. (1988).

It should be noted that there are only a few sources that have components with large differences in rotation measure. These sources appear as annuli in Figure 4-1. This observation, of itself, is an indicator that most of the observed rotation measures are due to the interstellar medium of our galaxy. For each occurrence of an annulus, it was found that one component was heavily depolarized. In Figure 4-2 we plot the 69 "good" rotation measure components that are used in further analysis.

The rotation measures are predominantly negative and vary smoothly in this region. This region is on the edge of Simard-Normandin and Kronberg's (1980) Region A ($b \sim +10°$ to $-40°$ and $60° < l < 140°$). Region A is characterized by predominantly negative rotation measures that can be as large as -200 rad m^{-2} and approximately coincides with radio Loop II, whose edge lies near $2^h\ 50^m$ RA through this region. Radio Loop II has its center near $l = 100°, b = -32.5°$ ($23^h\ 23^m$ RA, $+26°\ 15^m$ DEC) and has a radius of $\sim 45°$. The region of our observations contains only one O star (HD 14633, O8.5 V, $2^h21^m.5\ +41.4°$, d $\sim$ 2 Kpc) that has no cataloged H II region associated with it. It has been suggested that the bright emission feature near the eastern edge of this region is associated with an extended H II region surrounding the 07 star ξ Per (Reynolds 1988). It is not known if this feature has any association with Loop II. Comparing Figure 14 of Wilkinson and Smith (1974) with Reynolds' (1980) H_α map, it can be seen that the bright H_α emission on the eastern edge of Reynolds map does coincide with a feature in the galactic continuum synchrotron emission which shows very little depolarization. We will hereafter assume that this H_α feature is part of the H II region of ξ Per and is not related to Loop II. ξ Per (B1950 $3^h\ 58^m\ 35.6^s$ RA, $+35°\ 46^m\ 30^s$ DEC) lies at a distance of $\sim$ 400 pc so the emission measure feature is $\sim$ 90 pc distance from ξ Per. Reynolds (1988) has shown that the H_α emission from this region is consistent with its origin being the outer edge of a Strömgren sphere about ξ Per with a radius of $\sim$ 90 pc and a RMS electron density

of 0.5 cm^{-3}. The rest of the emission measure portrayed in Figure 4-1 is assumed to originate from the diffuse galactic electron density distribution (the so-called Reynolds layer). The Reynolds' layer is characterized by clumps of density ~ 0.08 cm^{-3}, a filling factor of f ~ 0.25, an average galactic mid-plane density of 0.025 ± 0.005 cm^{-3} and an exponential scale height of 1 Kpc for the diffuse emission within $1 \sim 2$ Kpc of the sun (Reynolds 1991).

In Table 4-2 we present the peak intensities of the total intensity (I) and the linear polarization intensity (P) for each major source component. In the first column we identify the component. A letter in the name indicates that there were two or more components in a single source. The second column gives the peak total intensity and the third column gives the peak linear polarization intensity for each component at 1360 MHz. The fourth column gives the peak total intensity and the sixth column gives the peak linear polarization intensity at 1638 MHz. The fits to the source components were made using the AIPS program JMFIT which attempts to fit a two dimensional Gaussian to each source component. Source components which were highly extended and had no sharp peak in their intensity are thus not modeled well by JMFIT. These components have been omitted from Table 4-2.

4.2 The Observed Sources

In this section we briefly discuss the structure of each source. The NED[1] database was used for optical identifications, magnitudes and redshifts.

In Figures 4-3 through 4-43 we present plots of all 38 sources observed in the high precision survey. These plots show the polarization position angles at 1360

[1] The NASA/IPAC extragalactic database (NED) is operated by the Jet Propulsion Laboratory, California Institute of Technology, under contract with the National Aeronautics and Space Administration.

MHz and 1638 MHz plotted over contours of the total intensity in panels (a) and (b) of each plot. For each of the panels (a) and (b) the direction of the vectors is proportional to the polarization position angle while the length of the vectors is proportional to the linear polarization intensity. In panel (c) we plot $\chi_{1360} - \chi_{1638}$ (which is proportional to the rotation measure) over contours of the total intensity of the source. Finally in panel (d) we plot the linear polarization intensity in grayscale on contours of the total intensity.

4.2.1 Source Descriptions

0157+333 is also known as 4C+33.04 and has been optically identified as a 19th magnitude quasar. This source is just resolved as a double lobed radio source and is shown in Figure 4-2.

0201+414 is a point source with no known optical counterpart and is shown in Figure 4-3.

0206+355 is also known as 4C+35.03 and is identified optically as a 14.3 magnitude galaxy at a redshift of $z = 0.03737 \pm 0.00021$. The galaxy (UGC 01651) is cataloged as being a questionable elliptical galaxy with the dimensions $2.3'$ by $2.0'$. Our observations of 0206+355 are shown in Figure 4-4 with the measured intrinsic magnetic field for 0206+355 being shown in Figure 4-5. The observed radio emission at the 2 percent of the peak flux contour has dimensions $1.5'$ by $0.9'$. The intrinsic magnetic field shown in Figure 4-5 along the major axis of 0206+355 is typically perpendicular to the major axis. The magnetic field appears to form two complete loops, one northwest of the core of the galaxy and the other southeast of the core, with both loops being centered roughly on the major axis of the galaxy. To first order the magnetic field of 0206+355 appears as if it is a magnetic dipole resulting from a current loop lying in a plane passing through the major axis of the galaxy.

0211+326 is an FR II radio source with no known optical counterpart. The two radio lobes are separated by $\sim 7.5'$. A grey scale image of the total flux is shown in Figure 4-6. In Figure 4-7 the North following lobe is shown while the South preceding lobe is shown in Figure 4-8.

0211+348 is also known as 4C+34.06 and is shown in Figure 4-9. 0211+348 is a slightly resolved double lobed radio source. Each lobe is slightly extended towards the core of the object which could be interpreted as being emission from jets.

0212+344 is a point like radio source which shows hints of structure that is just starting to be resolved by our beam. 0212+344 is shown in Figure 4-10.

0213+432 is also a point like radio source which shows hints of structure that is just starting to be resolved by our beam. 0213+432 is shown in Figure 4-11.

0215+356 is a point like radio source with no known optical counterpart and is shown if Figure 4-12. At higher resolution with the VLA this source is resolved into several components (Rotterging et al. . 1994)

0215+423 is also known as 4C+42.06 and is shown in Figure 4-13. 0215+423 is a double lobed radio source.

0216+335 is shown in Figure 4-14. It has no known optical counterpart and is seen as a barely resolved double lobed radio source in our observations.

0217+417, shown in Figure 4-16, is optically identified as a quasar with a magnitude of 19.09 and a redshift of z = 1.43. This source is a double lobed radio source with emission from both jets being present and it is thus likely an FR II radio source. On the South preceding jet a knot of emission is seen on the south side of the jet while on the North following jet a know of emission is seen on the North side of the jet. This is suggestive of the jet encountering material and being partially deflected by ninety degrees such as occurs in X shaped radio sources.

0218+396 is also known as 4C+39.06 and NRAO 0100. 0218+396 is shown in Figure 4-16 and is likely an FR I radio source. Two radio lobes are observed with the jet on the south following lobe being clearly detected while a jet on the north preceding lobe is marginally detected.

0219+428 is also known as 3C 66A and is optically identified as a BL Lac object with a magnitude of 15.5 and a redshift of $z = 0.444$. 0219+428 is has also been observed as an X-ray source. 0219+428 is shown in Figure 4-17 and is a core dominated source with extended emission to the north and south of the core. The extended emission to the north of the core is brighter than that to the south. Both the core and the extended emission towards the north how linearly polarized emission.

0220+397 is also known as 3C 65 and is a radio galaxy. Optically it has been identified as a 23rd magnitude galaxy at a redshift of $z = 1.176$. 0220+397 is shown in Figure 4-18 and is seen as a double radio source that is partially resolved.

0224+393 has been identified with a 19th magnitude optical object, however the optical object has not been classified as to what type of object it is. 0224+393 is shown in Figure 4-19 and is seen as a point like source.

0227+403 has also been identified with an optical object of 17th magnitude which is yet to be classified. 0227+403 is shown in Figure 4-20 and appears as a point like source with possible extended emission to the east and west of the core.

0228+344 has no known optical counterpart and is shown in Figure 4-21. It appears as a double lobed radio source. The resolution of our observations is just sufficient to separate the emission from each lobe into individual components.

0228+393 is also known as 4C+39.08 is optically identified as a galaxy with a redshift of 0.801. 0228+393 is shown in Figure 4-22 and appears as a double lobed radio source.

0228+409is shown in Figure 4-23 and has no known optical counterpart. This source appears to be point like with possible extended emission to the north and source of the core.

0229+341 is also known as 3C 68.1 and NRAO 0105. It has been optically identified as a quasar with a magnitude of 19 and a redshift of $z = 1.238$. There are three absorption line systems seen against this quasar at redshifts of $z = 1.2248 \pm 0.0003$, $z = 0.7754 \pm 0.0003$ and $z = 0.2022$. 0229+341 is shown in Figure 4-24 and appears as a double lobed radio source. The north preceding lobe is seen as a point like source while the south following lobe was barely detected in our observations.

0229+352 is also known as 4C+35.05 and is shown in Figure 4-25. 0229+352 appears as a slightly resolved double lobed radio source.

0231+385 has no known optical counterparts and is shown in Figure 4-26. 0231+385 has three source components as is dominated by the core. The north following and south preceding components have no linearly polarized emission while the core is seen to have linearly polarized emission. This source is similar in structure to 0219+428 (3C 66A) and may possibly be a BL Lac type object.

0232+411 is also known as 4C+41.04 and is identified as a quasar with a magnitude of 17 and a redshift $z = 0.5$. 0232+411 is shown in Figure 4-27 and appears as an FR I radio source. The core of 0232+411 is seen to have a jet extending to the south preceding lobe while no jet is observed towards the north following lobe.

0241+393 is also known as 4C+39.09 and is shown in Figure 4-28. The physical structure of this source is somewhat ambiguous. As can be seen in Figure 4-28 three bright lobes of emission are present. However, the central lobe and the north following lobe has extended emission between themselves that is suggestive of these two lobes forming an FR II radio source with the south preceding lobe being another point like source. This interpretation of this source is supported by the fact that the

FR II source shows linearly polarized emission while none is observed for the point like source. Also a galaxy has been optically identified at the position of the core of the FR II source.

0244+377 is also known as 4C+37.07 and has no known optical counterpart. 0244+377 is shown in Figure 4-29 and appears as a single lobed radio source which is slightly extended.

0246+392 has no known optical counterpart and is shown in Figure 4-30. 0246+392 appears as a triple lobes radio source for which each component is just resolved. The south preceding lobe has the largest intensity while the core lobe is the next brightest lobe.

0247+393 is also known as 3C 73 and is optically identified as a magnitude 18.6 galaxy at a redshift of $z = 0.204$. 0247+393 is shown in Figure 4-31 and appears as an FR II radio source.

0247+404 is shown in Figure 4-32. 0247+404 appears as a core dominated source with extended emission suggestive of the fact that there are two radio lobes on either side of the core that are only slightly resolved.

0250+358 is shown in Figure 4-33 and appears as a point like radio source. 0250+358 has no known optical counterpart.

0250+393 is identified with a 15.4 magnitude optical source with an unknown physical structure. 0250+393 is shown in Figure 4-34 and appears as a double lobed radio source.

0254+409 is shown in Figure 4-35. 0254+409 appears as a single lobed source. However 0254+409 is not a point source and shows evidence that it is just starting to be resolved by our beam.

0255+355 has no known optical counterpart and is shown in Figure 4-36. This source appears to have three lobes with the core being the dominant lobe. There

is extended emission to the west of the south following lobe that has linear polarization emission associated with it. The south following lobe does not have any detected linearly polarized emission.

0256+423 is shown in Figure 4-37. It is an unresolved single component source.

0301+336 is also known as 4C+33.06 as is identified as an 18th magnitude galaxy. 0301+336 is shown in Figure 4-38 and appears to be a single lobed radio source which is showing evidence of having structure at higher resolutions.

0301+350 is shown in Figure 4-39. It appears to be an unresolved source and has no known optical counterpart.

0302+341 is also known as 4C+34.12 and is identified as a magnitude 17.5 quasar. 0302+341 is shown in Figure 4-40 and appears as a double lobed radio source.

0302+405 is shown in Figure 4-41 and has no known optical counterpart. 0302+405 is a double lobed radio source.

0248+430 appears to be an unresolved radio source and is shown in Figure 4-42. 0248+430 is optically identified as a quasar with a magnitude of 17.45 and a redshift $z = 1.31$. Four absorption line systems are seen along the line of sight to this quasar. This quasar is also seen through a cluster of galaxies.

Table 4-1. Observed Rotation Measures and Depolarization.

Name	RA h	RA m	RA s	DEC °	DEC ′	DEC ″	RM (rad m^{-2})	σ_{RM} (rad m^{-2})	D
0157+333A	1	57	51.134	+33	23	47.000	− 64.3	2.6	1.8
0157+333B	1	57	49.301	+33	23	42.660	− 75.1	0.9	1.0
0201+414	2	1	41.778	+41	27	31.940	− 79.6	1.0	1.2
0206+355A	2	6	42.415	+35	33	25.500	− 56.4	1.1	1.6
0206+355B	2	6	42.087	+35	33	15.000	− 39.4	1.0	1.7
0206+355C	2	6	40.981	+35	33	20.500	−125.6	0.8	1.3
0206+355D	2	6	40.367	+35	33	17.000	−126.6	1.2	1.7
0206+355E	2	6	38.851	+35	33	15.500	− 81.4	1.3	1.2
0206+355F	2	6	39.342	+35	33	23.000	− 77.1	1.4	1.1
0206+355G	2	6	38.482	+35	33	33.000	− 67.1	1.2	1.3
0206+355H	2	6	40.244	+35	33	30.500	− 64.7	0.8	1.2
0206+355I	2	6	39.793	+35	33	38.000	− 58.7	0.5	1.3
0206+355J	2	6	42.047	+35	33	40.000	− 97.0	1.0	1.6
0206+355K	2	6	40.818	+35	33	49.500	− 68.6	1.1	1.2
0206+355L	2	6	36.761	+35	33	42.000	− 63.0	1.3	1.4
0206+355M	2	6	37.949	+35	33	45.000	− 60.1	0.8	1.2
0206+355N	2	6	39.176	+35	33	49.000	− 80.0	0.6	1.5
0206+355O	2	6	37.703	+35	33	57.500	− 61.5	0.6	1.2
0206+355P	2	6	38.947	+35	34	5.500	− 67.8	1.2	1.3
0206+355Q	2	6	36.720	+35	34	7.500	− 43.3	0.9	1.7
0211+326A	2	11	9.802	+32	36	32.910	− 62.0	3.3	0.9
0211+326B	2	11	30.025	+32	38	9.610	− 68.1	0.4	1.0
0211+326C	2	11	26.817	+32	37	57.000	− 58.8	5.9	1.1
0211+326D	2	11	16.607	+32	36	58.970	− 62.1	2.5	0.9
0211+326E	2	11	8.029	+32	36	8.220	− 66.2	0.8	1.1
0211+348A	2	11	59.411	+34	53	2.700	− 52.3	1.4	1.1
0211+348B	2	11	58.462	+34	52	36.160	− 53.5	1.2	1.8
0212+344	2	12	50.199	+34	29	10.070	− 60.6	1.5	1.0
0213+432	2	13	32.933	+43	17	41.470	+ 51.7	1.2	1.9
0215+356	2	15	27.918	+35	36	10.260	− 71.8	1.5	1.3
0215+423A	2	16	3.338	+42	19	22.620	− 81.0	0.8	1.0
0215+423B	2	15	58.843	+42	19	4.430	− 79.6	0.5	1.1
0215+423C	2	16	1.091	+42	19	13.525	− 71.7	13.9	. . .

Table 4-1 –continued

Name	RA h	m	s	DEC °	′	″	RM (rad m^{-2})	$\sigma_{\rm RM}$ (rad m^{-2})	D
0216+335A	2	16	49.719	+33	34	38.920	− 65.4	1.6	1.6
0216+335B	2	16	49.732	+33	34	27.460	− 65.9	1.3	1.1
0216+335C	2	16	49.720	+33	34	33.190	− 63.0	4.8	1.2
0217+417A	2	17	4.486	+41	43	34.150	− 81.7	0.6	1.0
0217+417B	2	17	5.933	+41	43	42.011	− 81.0	1.5	1.1
0217+417C	2	17	7.434	+41	44	2.006	− 82.8	1.5	1.2
0217+417D	2	17	8.964	+41	44	10.530	− 86.1	1.2	1.3
0218+396A	2	18	44.975	+39	41	18.320	− 82.4	0.8	1.1
0218+396B	2	18	40.402	+39	42	28.110	− 80.3	2.6	1.1
0219+428A	2	19	29.575	+42	48	38.170	− 91.9	4.5	0.9
0219+428B	2	19	29.989	+42	48	29.340	− 88.3	4.5	1.0
0220+397A	2	20	36.536	+39	47	18.220	− 85.4	1.4	3.6
0220+397B	2	20	37.484	+39	47	16.550	− 90.7	0.5	3.0
0224+393	2	24	1.102	+39	18	14.900	− 68.6	1.6	1.4
0227+403	2	27	37.468	+40	19	35.980	− 76.3	0.6	1.0
0228+344A	2	28	58.598	+34	29	24.910	− 33.0	6.2	1.2
0228+344B	2	28	57.131	+34	29	8.420	− 38.5	1.1	1.2
0228+393A	2	28	42.352	+39	19	53.500	−103.9	7.6	1.5
0228+393B	2	28	41.246	+39	19	42.920	− 41.6	3.0	2.1
0228+409	2	28	29.654	+40	56	38.450	− 59.9	3.1	0.8
0229+341A	2	29	27.315	+34	10	11.760	− 70.3	1.6	. . .
0229+341B	2	29	27.028	+34	10	55.150	− 58.5	0.2	0.8
0229+352A	2	29	26.929	+35	17	42.220	− 44.2	6.4	3.0
0229+352B	2	29	25.982	+35	17	44.510	− 40.4	1.1	1.2
0231+385	2	31	21.657	+38	31	48.440	− 73.4	4.5	0.8
0232+411A	2	32	50.946	+41	10	32.140	− 80.4	0.3	1.0
0232+411B	2	32	44.494	+41	10	8.090	− 78.4	1.5	1.1
0232+411C	2	32	41.763	+41	9	55.140	− 83.2	0.7	1.0
0241+393A	2	41	27.744	+39	22	12.660	− 58.2	0.7	0.9
0241+393B	2	41	25.488	+39	21	58.770	− 58.4	0.7	1.1
0241+393C	2	41	22.166	+39	21	20.040	− 60.4	0.5	1.0
0241+393D	2	41	24.054	+39	21	37.860	− 58.1	0.9	1.2
0241+393E	2	41	20.195	+39	21	2.600	− 60.1	0.3	1.1
0244+377A	2	44	23.855	+37	42	20.570	− 63.2	3.1	1.2
0244+377B	2	44	23.897	+37	42	30.070	− 65.3	12.3	. . .

Table 4-1 –continued

Name	RA h	m	s	DEC °	′	″	RM (rad m^{-2})	$\sigma_{\rm RM}$ (rad m^{-2})	D
0246+392A	2	46	23.535	+39	17	6.420	− 37.2	3.1	1.0
0246+392B	2	46	23.194	+39	16	56.470	− 37.1	1.6	1.0
0246+392C	2	46	22.621	+39	16	42.960	− 40.1	3.1	1.1
0246+392D	2	46	22.439	+39	16	35.660	− 35.1	9.4	1.1
0247+393A	2	47	11.019	+39	22	4.680	− 40.6	0.3	1.0
0247+393B	2	47	4.342	+39	21	51.150	− 49.7	3.2	2.2
0247+393C	2	47	7.295	+39	22	3.400	− 42.6	1.6	1.2
0247+393D	2	46	59.082	+39	22	19.160	− 53.8	0.3	1.1
0247+404A	2	47	58.133	+40	29	52.620	− 71.9	1.2	1.4
0247+404B	2	47	58.213	+40	29	45.500	− 66.3	3.1	1.3
0247+404C	2	47	57.883	+40	30	3.750	− 72.6	4.6	1.2
0250+358	2	50	16.327	+35	48	53.260	− 72.8	0.8	1.4
0251+393	2	51	31.327	+39	19	25.220	− 60.1	3.0	0.7
0254+409	2	54	21.584	+40	55	46.680	− 47.1	1.5	1.2
0255+355A	2	55	25.390	+35	30	59.780	− 35.0	1.5	1.2
0255+355B	2	55	24.711	+35	30	49.620	− 39.7	1.5	1.1
0255+355C	2	55	25.168	+35	31	8.420	− 40.2	1.5	1.1
0255+355D	2	55	25.397	+35	31	22.110	− 41.6	4.5	1.3
0256+423	2	56	21.030	+42	23	55.200	− 82.0	1.5	0.3
0301+336	3	1	35.698	+33	37	5.090	− 27.6	0.5	1.1
0301+350	3	1	44.793	+35	0	30.930	− 2.6	0.9	1.2
0302+341A	3	2	33.200	+34	10	33.290	− 18.7	0.6	1.1
0302+341B	3	2	30.681	+34	10	7.570	− 18.2	1.6	1.0
0302+341C	3	2	32.235	+34	10	23.910	− 25.9	1.6	1.3
0302+341D	3	2	31.386	+34	10	14.460	− 20.8	0.6	1.1
0302+405A	3	2	19.413	+40	30	47.680	− 12.5	1.1	1.1
0302+405B	3	2	18.631	+40	30	38.650	− 9.9	1.6	1.1
0302+405C	3	2	18.142	+40	30	29.210	− 12.2	1.6	1.1
0302+405D	3	2	16.981	+40	30	13.600	− 12.8	1.1	1.0
0248+430	2	48	18.496	+43	2	56.940	+ 32.5	0.5	0.9

Table 4-2. Observed source component total and polarized peak intensities for components which could be fitted by a two dimensional Gaussian.

	1360 MHz		1638 MHz	
Name	Peak I (mJy)	Peak P (mJy)	Peak I (mJy)	Peak P (mJy)
0157+333A	185.41 ± 0.22	8.458 ± 0.387	159.81 ± 0.24	5.283 ± 0.031
0157+333B	198.45 ± 0.24	3.701 ± 0.574	177.79 ± 0.26	10.651 ± 0.039
0201+414	214.78 ± 0.27	12.422 ± 0.008	197.94 ± 0.29	13.904 ± 0.025
0211+326B	114.21 ± 0.33	19.480 ± 0.090	97.19 ± 0.26	16.993 ± 0.080
0211+326E	62.72 ± 0.31	6.430 ± 0.025	51.12 ± 0.26	5.780 ± 0.023
0211+348A	155.70 ± 2.00	6.131 ± 0.075	135.00 ± 1.70	5.656 ± 0.057
0211+348B	549.00 ± 2.00	8.007 ± 0.082	471.50 ± 1.70	11.477 ± 0.087
0212+344	158.53 ± 0.30	9.440 ± 0.009	153.90 ± 0.24	8.888 ± 0.010
0213+432	408.40 ± 0.50	9.562 ± 0.009	365.40 ± 0.30	15.669 ± 0.014
0215+356	303.70 ± 0.40	15.018 ± 0.019	260.70 ± 0.30	16.613 ± 0.020
0215+423A	151.97 ± 0.45	18.723 ± 0.053	128.17 ± 0.43	16.298 ± 0.056
0215+423B	383.70 ± 1.60	34.350 ± 0.160	331.50 ± 1.30	32.120 ± 0.160
0216+335A	237.71 ± 0.18	4.784 ± 0.013	219.34 ± 0.15	8.215 ± 0.550
0216+335B	154.42 ± 0.19	11.517 ± 0.006	135.59 ± 0.16	10.483 ± 0.007
0217+417A	84.43 ± 0.74	11.700 ± 0.213	74.00 ± 0.60	10.601 ± 0.200
0217+417D	50.91 ± 0.18	6.562 ± 0.024	43.99 ± 0.17	6.784 ± 0.018
0218+396A	328.50 ± 3.90	38.170 ± 0.200	279.30 ± 3.00	35.030 ± 0.220
0218+396B	207.02 ± 4.26	10.831 ± 0.192	180.65 ± 4.10	9.924 ± 0.181
0219+428B	1113.00 ± 9.00	17.769 ± 0.082	1112.70 ± 7.90	15.126 ± 0.060
0220+397A	2031.00 ± 3.70	25.830 ± 0.010	1699.00 ± 3.20	63.670 ± 0.020
0220+397B	1167.10 ± 2.10	8.588 ± 0.016	949.40 ± 1.80	24.043 ± 0.040
0224+393	245.40 ± 0.30	5.247 ± 0.006	343.70 ± 0.20	6.925 ± 0.006
0227+403	557.70 ± 0.50	26.360 ± 0.030	535.60 ± 0.50	24.841 ± 0.033
0228+344A	144.52 ± 0.29	7.797 ± 0.095	129.09 ± 0.22	7.971 ± 0.045
0228+344B	323.00 ± 0.80	24.138 ± 0.023	277.80 ± 0.70	23.419 ± 0.074
0228+393A	291.60 ± 2.30	4.103 ± 0.035	258.30 ± 2.00	5.190 ± 0.022
0228+393B	296.90 ± 1.70	6.686 ± 0.016	260.70 ± 1.40	12.382 ± 0.036
0228+409	296.70 ± 0.40	6.397 ± 0.017	264.60 ± 0.30	4.333 ± 0.017
0229+341A	92.00 ± 0.74	. . .	75.68 ± 0.61	. . .
0229+341B	2019.40 ± 2.90	138.190 ± 0.160	1784.90 ± 2.60	93.760 ± 0.180
0229+352A	320.70 ± 0.50	3.712 ± 0.043	285.70 ± 0.40	10.284 ± 0.041

Table 4-2 –continued

Name	1360 MHz Peak I (mJy)	1360 MHz Peak P (mJy)	1638 MHz Peak I (mJy)	1638 MHz Peak P (mJy)
0229+352B	268.10 ± 0.60	15.120 ± 0.046	241.30 ± 0.40	16.296 ± 0.039
0231+385	160.08 ± 0.12	5.545 ± 0.007	158.55 ± 0.15	4.269 ± 0.027
0231+385B[1]	18.69 ± 0.11	. . .	17.75 ± 0.12	. . .
0231+385C[2]	20.62 ± 0.10	. . .	14.17 ± 0.12	. . .
0232+411A	214.85 ± 1.17	38.490 ± 0.290	194.10 ± 1.02	34.640 ± 0.260
0232+411C	299.30 ± 1.20	17.708 ± 0.135	273.00 ± 1.00	16.131 ± 0.128
0241+393A	111.42 ± 1.17	18.112 ± 0.137	100.30 ± 0.97	16.107 ± 0.121
0241+393D	280.70 ± 1.90	42.330 ± 0.550	238.01 ± 1.75	38.460 ± 0.480
0241+393F[3]	194.85 ± 0.49	. . .	165.16 ± 0.48	. . .
0244+377A	583.00 ± 0.90	5.091 ± 0.007	525.80 ± 0.90	5.491 ± 0.012
0246+392A	29.49 ± 0.10	2.913 ± 0.033	26.17 ± 0.09	2.701 ± 0.036
0246+392B	32.74 ± 0.06	4.529 ± 0.029	29.59 ± 0.05	4.051 ± 0.032
0246+392C	77.85 ± 0.06	3.359 ± 0.035	68.08 ± 0.05	3.380 ± 0.039
0247+393A	109.99 ± 0.62	9.618 ± 0.087	96.04 ± 0.54	8.586 ± 0.077
0247+393B	25.69 ± 1.33	. . .	14.68 ± 0.18	. . .
0247+393D	127.72 ± 0.98	16.390 ± 0.300	112.22 ± 0.86	15.487 ± 0.296
0247+404	113.06 ± 0.46	6.791 ± 0.099	99.61 ± 0.41	9.201 ± 0.134
0250+358	443.60 ± 0.50	24.198 ± 0.020	405.90 ± 0.50	30.430 ± 0.010
0250+393	208.92 ± 0.19	3.879 ± 0.026	250.20 ± 0.20	3.078 ± 0.033
0250+393[4]	18.38 ± 0.16	. . .	17.10 ± 0.20	. . .
0254+409	218.15 ± 0.37	4.412 ± 0.045	195.82 ± 0.30	4.706 ± 0.050
0255+355C	77.26 ± 0.87	4.882 ± 0.071	72.85 ± 0.82	4.860 ± 0.067
0256+423	606.70 ± 0.30	14.027 ± 0.005	575.40 ± 0.40	3.853 ± 0.016
0301+336	723.70 ± 0.60	38.670 ± 0.070	702.50 ± 0.50	39.670 ± 0.070
0301+350	542.80 ± 0.30	18.800 ± 0.006	476.00 ± 0.20	19.154 ± 0.011

[1]Unpolarized component is at $2^{h}\ 31^{m}\ 22.317^{s}\ +38^{\circ}\ 31^{m}\ 59.74^{s}$

[2]Unpolarized component is at $2^{h}\ 31^{m}\ 21.587^{s}\ +38^{\circ}\ 31^{m}\ 36.96^{s}$

[3]Unpolarized component is at $2^{h}\ 41^{m}\ 17.184^{s}\ +39^{\circ}\ 20^{m}\ 46.76^{s}$

[4]Unpolarized component is at $2^{h}\ 51^{m}\ 33.276^{s}\ +39^{\circ}\ 19^{m}\ 19.52^{s}$

Table 4-2 –continued

Name	1360 MHz		1638 MHz	
	Peak I (mJy)	Peak P (mJy)	Peak I (mJy)	Peak P (mJy)
0302+341A	134.64 ± 0.52	19.081 ± 0.061	116.22 ± 0.45	18.666 ± 0.067
0302+341D	155.66 ± 0.76	20.888 ± 0.081	135.10 ± 0.70	18.822 ± 0.105
0302+405A	89.86 ± 0.26	8.399 ± 0.095	75.99 ± 0.20	7.466 ± 0.094
0302+405D	72.06 ± 0.51	9.747 ± 0.044	64.00 ± 0.47	8.694 ± 0.042
0248+430	997.60 ± 0.70	22.300 ± 0.011	1139.60 ± 0.70	24.368 ± 0.019

Figure 4-1. All the rotation measures and the emission measure in the field of the survey. The emission measure is shown in grayscale while the rotation measure is shown as a circle for negative rotation measures and as a diamond for positive rotation measures. There is a plotted symbol for each of the observed components. The size of the symbol is proportional to the magnitude of the rotation measure with a scale for the symbol size being shown on the left hand side of the figure. We also point out a source whose rotation measure is -2.6 rad m^{-2}. The pulsar 0320+39 is also included.

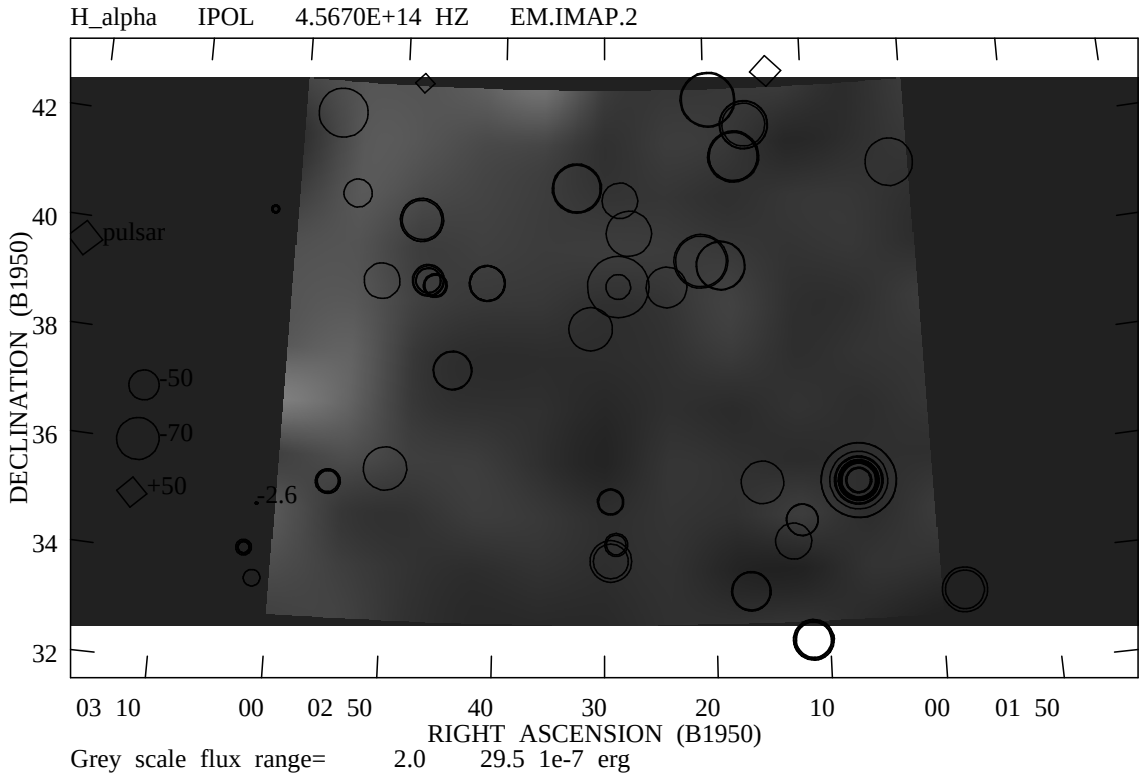
H_alpha IPOL 4.5670E+14 HZ EM.IMAP.2
42
40
38
36
34
32
DECLINATION (B1950)
pulsar
-50
-70
+50
-2.6
03 10
00
02 50
40
30
20
10
00
01 50
RIGHT ASCENSION (B1950)
Grey scale flux range= 2.0 29.5 1e-7 erg

Figure 4-2. The 69 usable rotation measures and the emission measure in the field of the survey. The emission measure is shown in grayscale while the rotation measure is shown as a circle for negative rotation measures and as a diamond for positive rotation measures. There is a plotted symbol for each of the 69 rotation measures used in the structure function analysis. The size of the symbol is proportional to the magnitude of the rotation measure with a scale for the symbol size being shown on the left hand side of the figure. We also point out a source whose rotation measure is -2.6 rad m^{-2}. The pulsar 0320+309 is also included.

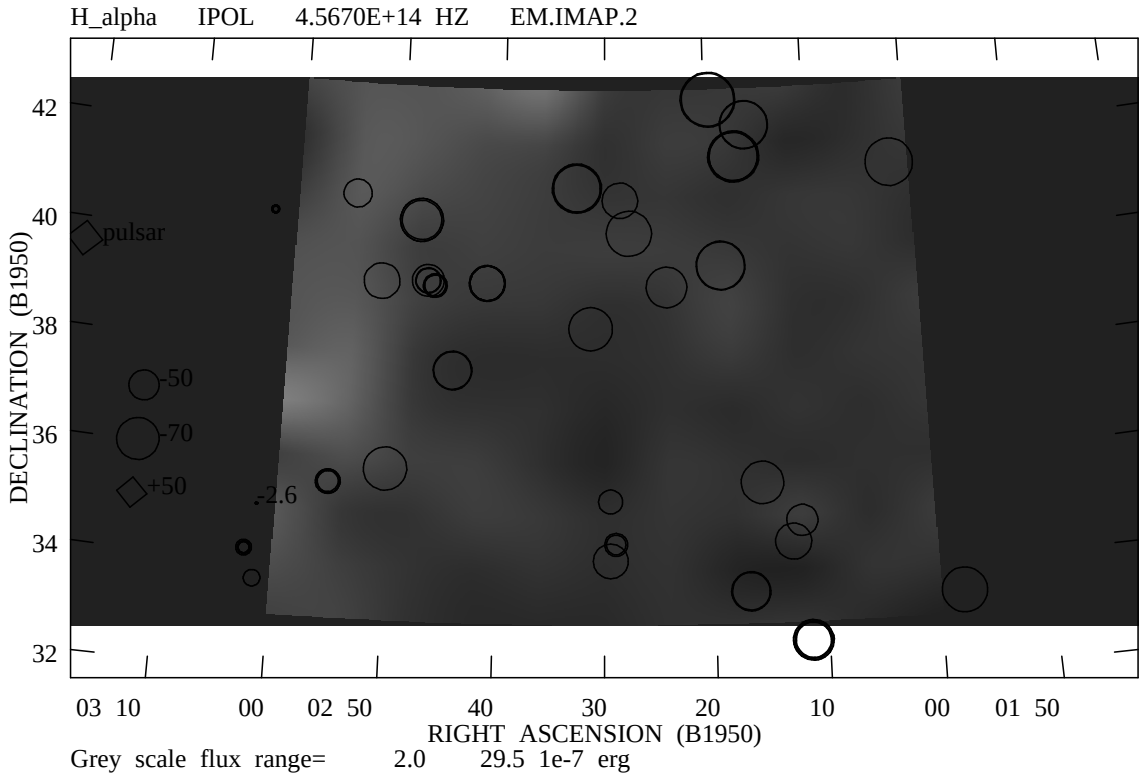
H_alpha IPOL 4.5670E+14 HZ EM.IMAP.2
42
40
38
36
34
32
DECLINATION (B1950)
pulsar
-50
-70
+50
-2.6
03 10
00
02 50
40
30
20
10
00
01 50
RIGHT ASCENSION (B1950)
Grey scale flux range= 2.0 29.5 1e-7 erg

Figure 4-3. Maps of the source 0157+333. Panels (a) through (c) show the total intensity contours of the source along with the polarization position angles. The positive total intensity contours for panels (a), (b) and (c) are 2, 4, 6, 8, 10, 20, 30, 50, 80, 90 and 99 percent of the peak intensity. The positive total intensity contours for panel (c) are 2 and 50 percent of the peak intensity. The position angle of the vectors are that of the polarization position angles, and the lengths of the vectors are proportional to the polarized intensity. The position angles plotted are: (a) 1360 MHz ; (b) 1638 MHz; (c) $\chi_{1360} - \chi_{1638}$. In panel (d) the linear polarization intensity is plotted in grayscale on the contours of the total intensity.

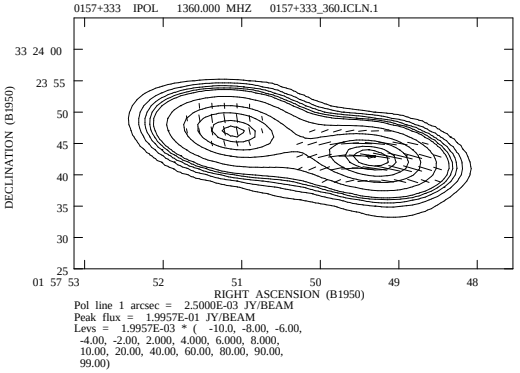
0157+333 IPOL 1360.000 MHZ 0157+333_360.ICLN.1
DECLINATION (B1950)
33 24 00
23 55
50
45
40
35
30
25
01 57 53
52
51
50
49
48
RIGHT ASCENSION (B1950)
Pol line 1 arcsec = 2.5000E-03 JY/BEAM
Peak flux = 1.9957E-01 JY/BEAM
Levs = 1.9957E-03 * (-10.0, -8.00, -6.00,
-4.00, -2.00, 2.000, 4.000, 6.000, 8.000,
10.00, 20.00, 40.00, 60.00, 80.00, 90.00,
99.00)

(a)

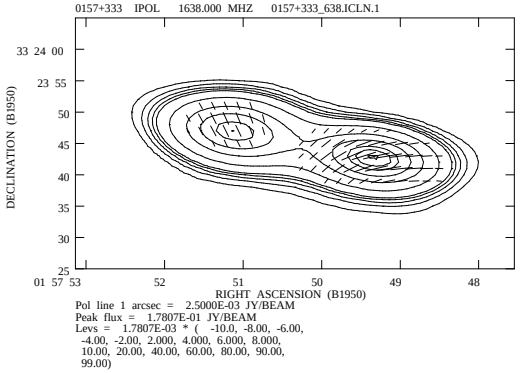
0157+333 IPOL 1638.000 MHZ 0157+333_638.ICLN.1
DECLINATION (B1950)
33 24 00
23 55
50
45
40
35
30
25
01 57 53
52
51
50
49
48
RIGHT ASCENSION (B1950)
Pol line 1 arcsec = 2.5000E-03 JY/BEAM
Peak flux = 1.7807E-01 JY/BEAM
Levs = 1.7807E-03 * (-10.0, -8.00, -6.00,
-4.00, -2.00, 2.000, 4.000, 6.000, 8.000,
10.00, 20.00, 40.00, 60.00, 80.00, 90.00,
99.00)

(b)

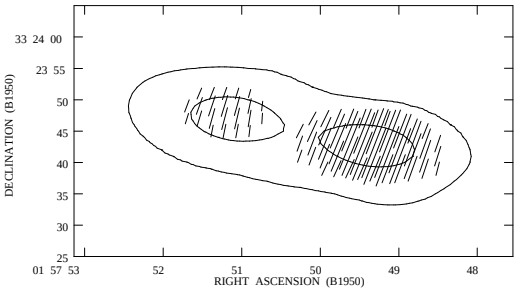
DECLINATION (B1950)
33 24 00
23 55
50
45
40
35
30
25
01 57 53
52
51
50
49
48
RIGHT ASCENSION (B1950)

(c)

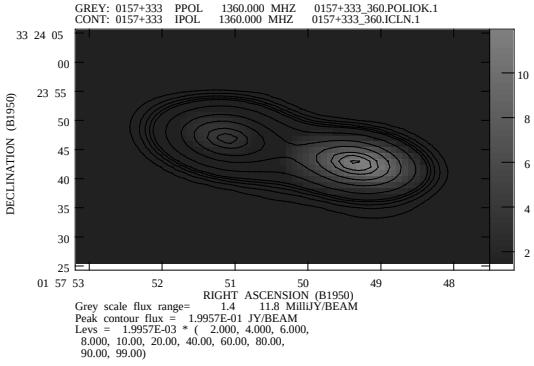
GREY: 0157+333 PPOL 1360.000 MHZ 0157+333_360.POLIOK.1
CONT: 0157+333 IPOL 1360.000 MHZ 0157+333_360.ICLN.1
DECLINATION (B1950)
33 24 05
00
23 55
50
45
40
35
30
25
01 57 53
52
51
50
49
48
RIGHT ASCENSION (B1950)
10
8
6
4
2
Grey scale flux range= 1.4 11.8 MilliJY/BEAM
Peak contour flux = 1.9957E-01 JY/BEAM
Levs = 1.9957E-03 * (2.000, 4.000, 6.000,
8.000, 10.00, 20.00, 40.00, 60.00, 80.00,
90.00, 99.00)

(d)

Figure 4-4. Maps of the source 0201+414. Panels (a) through (c) show the total intensity contours of the source along with the polarization position angles. The positive total intensity contours for panels (a), (b) and (c) are 2, 4, 6, 8, 10, 20, 30, 50, 80, 90 and 99 percent of the peak intensity. The positive total intensity contours for panel (c) are 2 and 50 percent of the peak intensity. The position angle of the vectors are that of the polarization position angles, and the lengths of the vectors are proportional to the polarized intensity. The position angles plotted are: (a) 1360 MHz ; (b) 1638 MHz; (c) $\chi_{1360} - \chi_{1638}$. In panel (d) the linear polarization intensity is plotted in grayscale on the contours of the total intensity.

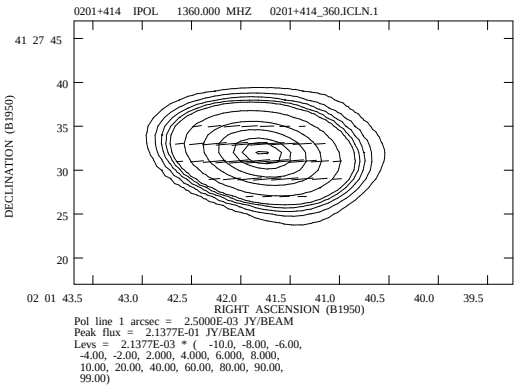
0201+414 IPOL 1360.000 MHZ 0201+414_360.ICLN.1
41 27 45
40
35
30
25
20
DECLINATION (B1950)
02 01 43.5 43.0 42.5 42.0 41.5 41.0 40.5 40.0 39.5
RIGHT ASCENSION (B1950)
Pol line 1 arcsec = 2.5000E-03 JY/BEAM
Peak flux = 2.1377E-01 JY/BEAM
Levs = 2.1377E-03 * (-10.0, -8.00, -6.00,
-4.00, -2.00, 2.000, 4.000, 6.000, 8.000,
10.00, 20.00, 40.00, 60.00, 80.00, 90.00,
99.00)

(a)

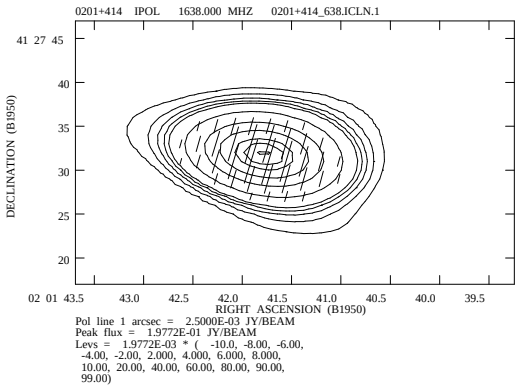
0201+414 IPOL 1638.000 MHZ 0201+414_638.ICLN.1
41 27 45
40
35
30
25
20
DECLINATION (B1950)
02 01 43.5 43.0 42.5 42.0 41.5 41.0 40.5 40.0 39.5
RIGHT ASCENSION (B1950)
Pol line 1 arcsec = 2.5000E-03 JY/BEAM
Peak flux = 1.9772E-01 JY/BEAM
Levs = 1.9772E-03 * (-10.0, -8.00, -6.00,
-4.00, -2.00, 2.000, 4.000, 6.000, 8.000,
10.00, 20.00, 40.00, 60.00, 80.00, 90.00,
99.00)

(b)

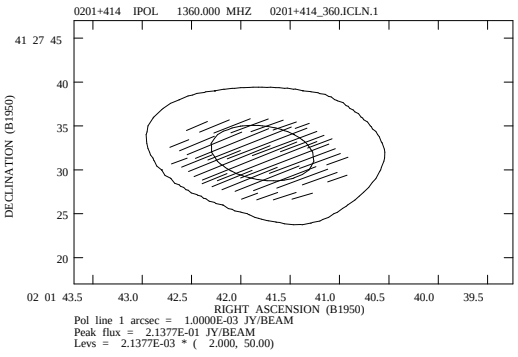
0201+414 IPOL 1360.000 MHZ 0201+414_360.ICLN.1
41 27 45
40
35
30
25
20
DECLINATION (B1950)
02 01 43.5 43.0 42.5 42.0 41.5 41.0 40.5 40.0 39.5
RIGHT ASCENSION (B1950)
Pol line 1 arcsec = 1.0000E-03 JY/BEAM
Peak flux = 2.1377E-01 JY/BEAM
Levs = 2.1377E-03 * (2.000, 50.00)

(c)

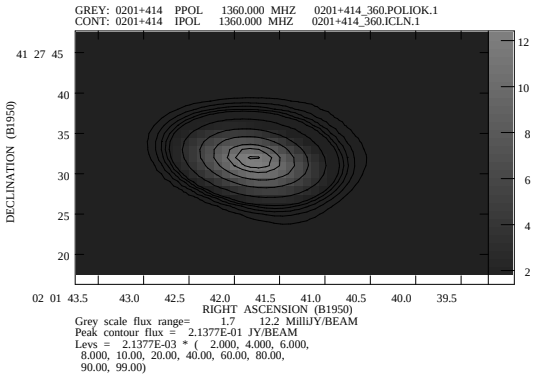
GREY: 0201+414 PPOL 1360.000 MHZ 0201+414_360.POLIOK.1
CONT: 0201+414 IPOL 1360.000 MHZ 0201+414_360.ICLN.1
41 27 45
40
35
30
25
20
DECLINATION (B1950)
12
10
8
6
4
2
02 01 43.5 43.0 42.5 42.0 41.5 41.0 40.5 40.0 39.5
RIGHT ASCENSION (B1950)
Grey scale flux range= 1.7 12.2 MilliJY/BEAM
Peak contour flux = 2.1377E-01 JY/BEAM
Levs = 2.1377E-03 * (2.000, 4.000, 6.000,
8.000, 10.00, 20.00, 40.00, 60.00, 80.00,
90.00, 99.00)

(d)

Figure 4-5. Maps of the source 0206+355. Panels (a) through (c) show the total intensity contours of the source along with the polarization position angles. The positive total intensity contours for panels (a), (b) and (c) are 2, 4, 6, 8, 10, 20, 30, 50, 80, 90 and 99 percent of the peak intensity. The positive total intensity contours for panel (c) are 2 and 50 percent of the peak intensity. The position angle of the vectors are that of the polarization position angles, and the lengths of the vectors are proportional to the polarized intensity. The position angles plotted are: (a) 1360 MHz ; (b) 1638 MHz; (c) $\chi_{1360} - \chi_{1638}$. In panel (d) the linear polarization intensity is plotted in grayscale on the contours of the total intensity.

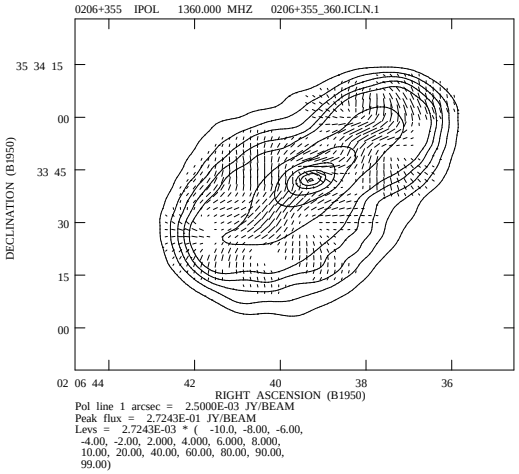
0206+355 IPOL 1360.000 MHZ 0206+355_360.ICLN.1
35 34 15
00
33 45
30
15
00
DECLINATION (B1950)
02 06 44
42
40
38
36
RIGHT ASCENSION (B1950)
Pol line 1 arcsec = 2.5000E-03 JY/BEAM
Peak flux = 2.7243E-01 JY/BEAM
Levs = 2.7243E-03 * (-10.0, -8.00, -6.00,
-4.00, -2.00, 2.000, 4.000, 6.000, 8.000,
10.00, 20.00, 40.00, 60.00, 80.00, 90.00,
99.00)

(a)

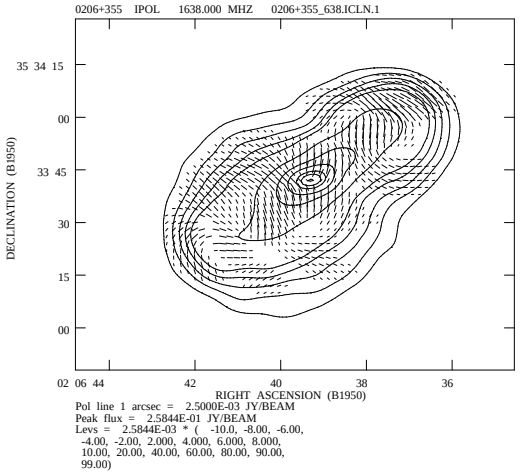
0206+355 IPOL 1638.000 MHZ 0206+355_638.ICLN.1
35 34 15
00
33 45
30
15
00
DECLINATION (B1950)
02 06 44
42
40
38
36
RIGHT ASCENSION (B1950)
Pol line 1 arcsec = 2.5000E-03 JY/BEAM
Peak flux = 2.5844E-01 JY/BEAM
Levs = 2.5844E-03 * (-10.0, -8.00, -6.00,
-4.00, -2.00, 2.000, 4.000, 6.000, 8.000,
10.00, 20.00, 40.00, 60.00, 80.00, 90.00,
99.00)

(b)

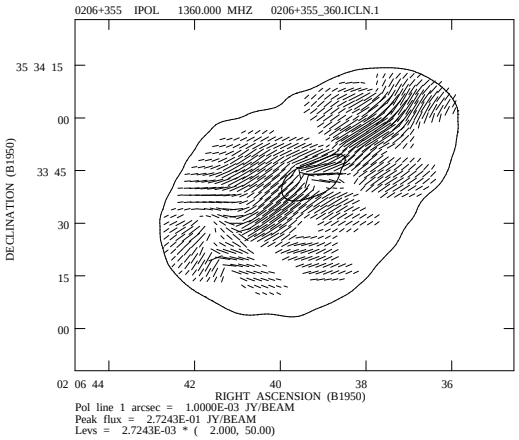
0206+355 IPOL 1360.000 MHZ 0206+355_360.ICLN.1
35 34 15
00
33 45
30
15
00
DECLINATION (B1950)
02 06 44
42
40
38
36
RIGHT ASCENSION (B1950)
Pol line 1 arcsec = 1.0000E-03 JY/BEAM
Peak flux = 2.7243E-01 JY/BEAM
Levs = 2.7243E-03 * (2.000, 50.00)

(c)

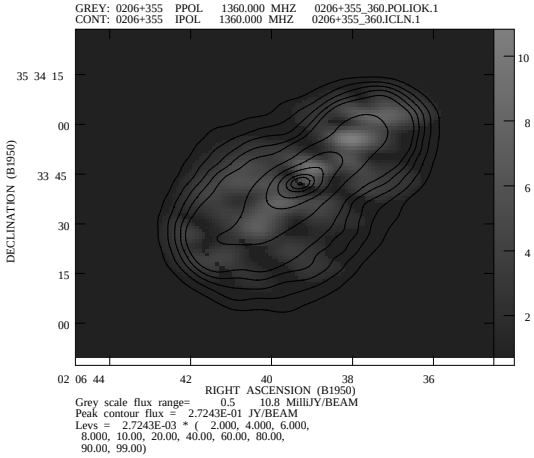
GREY: 0206+355 PPOL 1360.000 MHZ 0206+355_360.POLIOK.1
CONT: 0206+355 IPOL 1360.000 MHZ 0206+355_360.ICLN.1
35 34 15
00
33 45
30
15
00
DECLINATION (B1950)
02 06 44
42
40
38
36
RIGHT ASCENSION (B1950)
10
8
6
4
2
Grey scale flux range= 0.5 10.8 MilliJY/BEAM
Peak contour flux = 2.7243E-01 JY/BEAM
Levs = 2.7243E-03 * (2.000, 4.000, 6.000,
8.000, 10.00, 20.00, 40.00, 60.00, 80.00,
90.00, 99.00)

(d)

Figure 4-6. Map of the direction of the intrinsic magnetic field in 0206+355 found from $\chi_o + 90°$. Contours of the total intensity at 2, 4, 6, 8, 10, 20 ,40, 60, 80, 90 and 9 percent of the peak total intensity are also plotted.

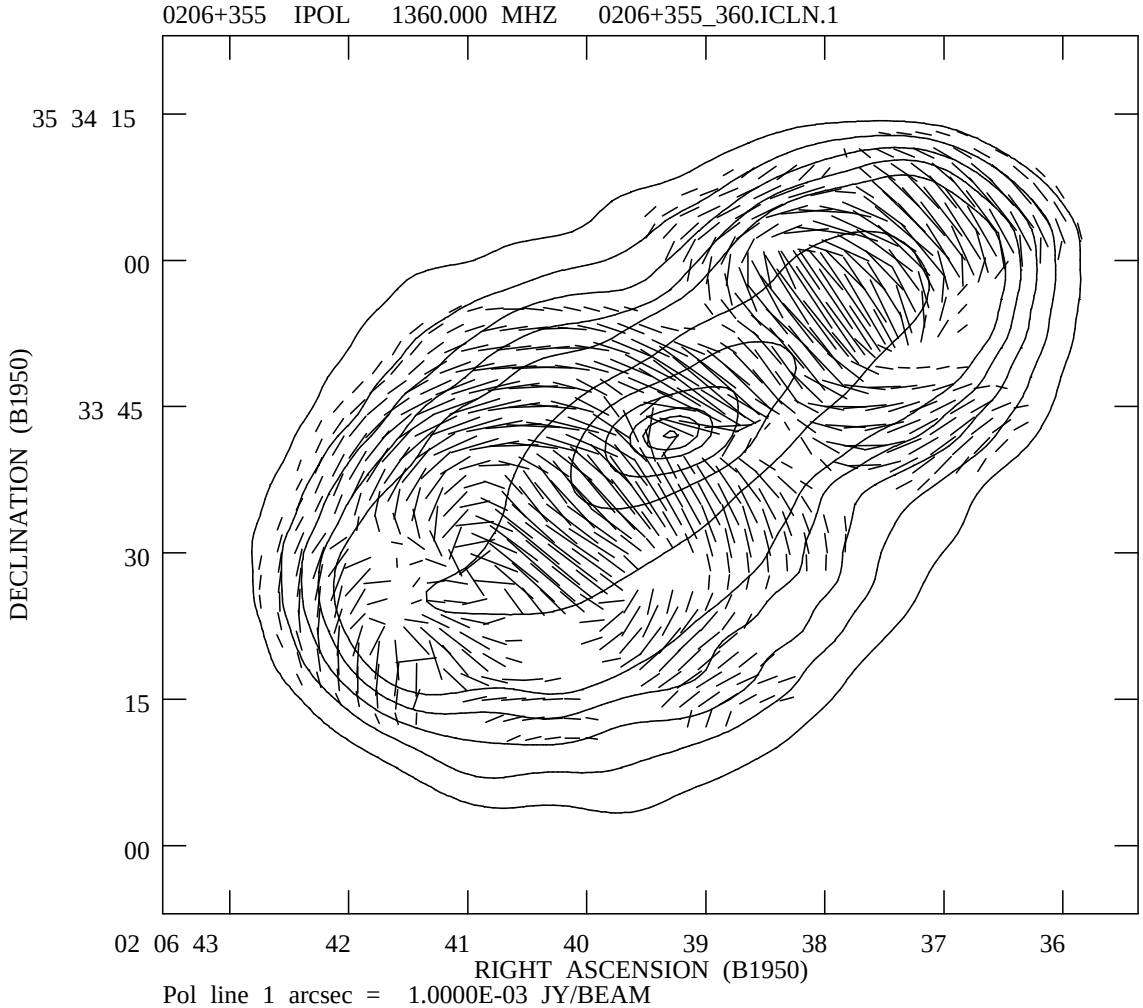

Pol line 1 arcsec = 1.0000E-03 JY/BEAM
Peak flux = 2.7243E-01 JY/BEAM
Levs = 2.7243E-03 * (2.000, 4.000, 6.000,
8.000, 10.00, 20.00, 40.00, 60.00, 80.00,
90.00, 99.00)

Figure 4-7. Map of the source 0211+326 showing the total intensity in grayscale.

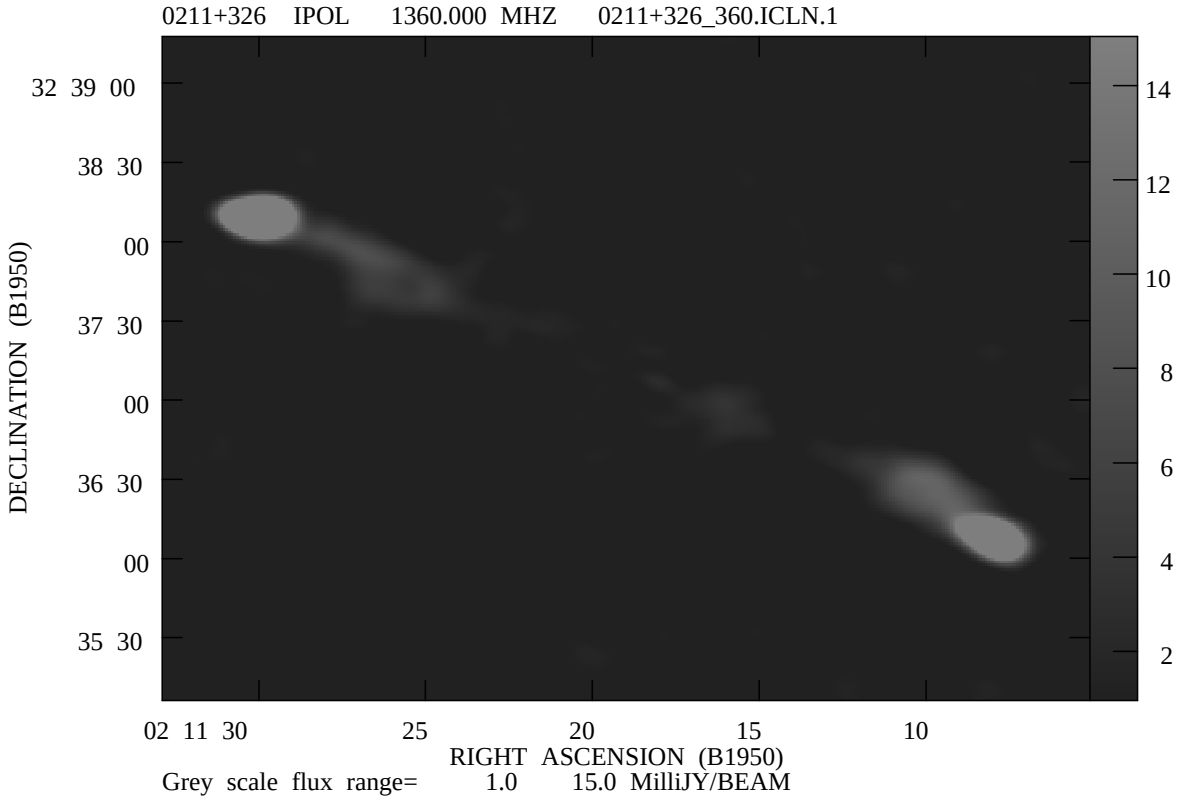
0211+326 IPOL 1360.000 MHZ 0211+326_360.ICLN.1
32 39 00
38 30
00
37 30
00
36 30
00
35 30
DECLINATION (B1950)
14
12
10
8
6
4
2
02 11 30
25
20
15
10
RIGHT ASCENSION (B1950)
Grey scale flux range= 1.0 15.0 MilliJY/BEAM

Figure 4-8. Maps of the North following lobe of 0211+326. Panels (a) through (c) show the total intensity contours of the source along with the polarization position angles. The positive total intensity contours for panels (a), (b) and (c) are 2, 4, 6, 8, 10, 20, 30, 50, 80, 90 and 99 percent of the peak intensity. The positive total intensity contours for panel (c) are 2 and 50 percent of the peak intensity. The position angle of the vectors are that of the polarization position angles, and the lengths of the vectors are proportional to the polarized intensity. The position angles plotted are: (a) 1360 MHz ; (b) 1638 MHz; (c) $\chi_{1360} - \chi_{1638}$. In panel (d) the linear polarization intensity is plotted in grayscale on the contours of the total intensity.

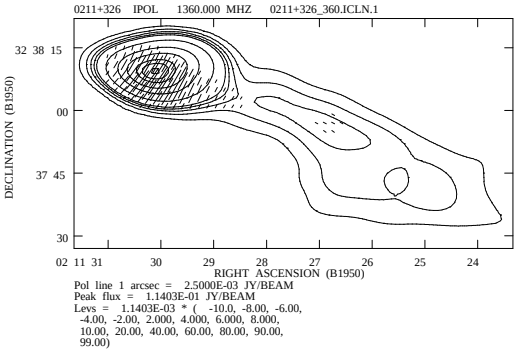
0211+326 IPOL 1360.000 MHZ 0211+326_360.ICLN.1
DECLINATION (B1950)
32 38 15
00
37 45
30
02 11 31
30
29
28
27
26
25
24
RIGHT ASCENSION (B1950)
Pol line 1 arcsec = 2.5000E-03 JY/BEAM
Peak flux = 1.1403E-01 JY/BEAM
Levs = 1.1403E-03 * (-10.0, -8.00, -6.00,
-4.00, -2.00, 2.000, 4.000, 6.000, 8.000,
10.00, 20.00, 40.00, 60.00, 80.00, 90.00,
99.00)

(a)

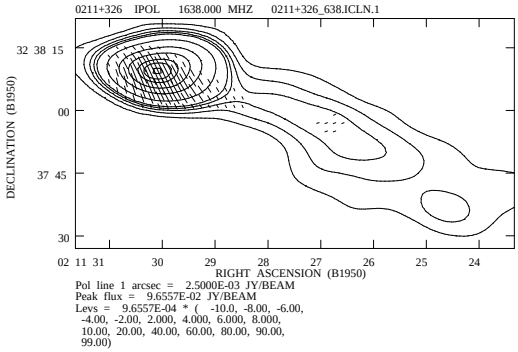
0211+326 IPOL 1638.000 MHZ 0211+326_638.ICLN.1
DECLINATION (B1950)
32 38 15
00
37 45
30
02 11 31
30
29
28
27
26
25
24
RIGHT ASCENSION (B1950)
Pol line 1 arcsec = 2.5000E-03 JY/BEAM
Peak flux = 9.6557E-02 JY/BEAM
Levs = 9.6557E-04 * (-10.0, -8.00, -6.00,
-4.00, -2.00, 2.000, 4.000, 6.000, 8.000,
10.00, 20.00, 40.00, 60.00, 80.00, 90.00,
99.00)

(b)

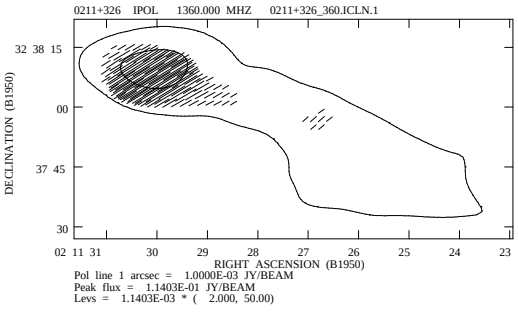
0211+326 IPOL 1360.000 MHZ 0211+326_360.ICLN.1
DECLINATION (B1950)
32 38 15
00
37 45
30
02 11 31
30
29
28
27
26
25
24
23
RIGHT ASCENSION (B1950)
Pol line 1 arcsec = 1.0000E-03 JY/BEAM
Peak flux = 1.1403E-01 JY/BEAM
Levs = 1.1403E-03 * (2.000, 50.00)

(c)

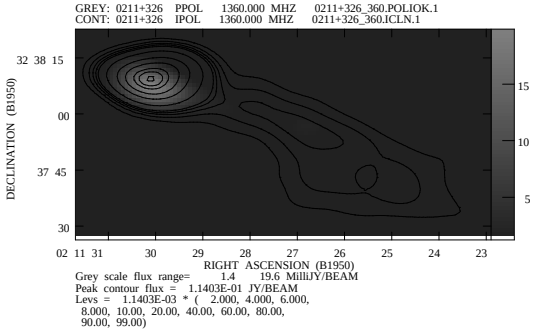
GREY: 0211+326 PPOL 1360.000 MHZ 0211+326_360.POLIOK.1
CONT: 0211+326 IPOL 1360.000 MHZ 0211+326_360.ICLN.1
DECLINATION (B1950)
32 38 15
00
37 45
30
02 11 31
30
29
28
27
26
25
24
23
RIGHT ASCENSION (B1950)
15
10
5
Grey scale flux range= 1.4 19.6 MilliJY/BEAM
Peak contour flux = 1.1403E-01 JY/BEAM
Levs = 1.1403E-03 * (2.000, 4.000, 6.000,
8.000, 10.00, 20.00, 40.00, 60.00, 80.00,
90.00, 99.00)

(d)

Figure 4-9. Maps of the South proceeding lobe of 0211+326. Panels (a) through (c) show the total intensity contours of the source along with the polarization position angles. The positive total intensity contours for panels (a), (b) and (c) are 2, 4, 6, 8, 10, 20, 30, 50, 80, 90 and 99 percent of the peak intensity. The positive total intensity contours for panel (c) are 2 and 50 percent of the peak intensity. The position angle of the vectors are that of the polarization position angles, and the lengths of the vectors are proportional to the polarized intensity. The position angles plotted are: (a) 1360 MHz ; (b) 1638 MHz; (c) $\chi_{1360} - \chi_{1638}$. In panel (d) the linear polarization intensity is plotted in grayscale on the contours of the total intensity.

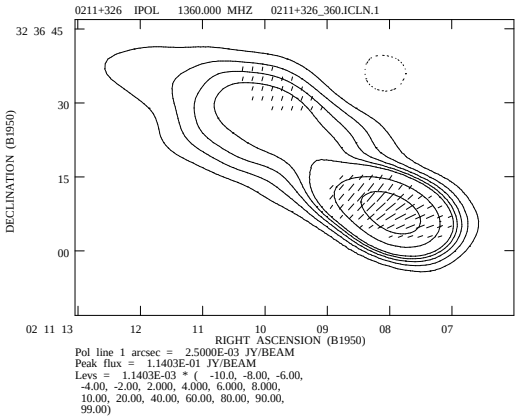
0211+326 IPOL 1360.000 MHZ 0211+326_360.ICLN.1
32 36 45
30
15
00
DECLINATION (B1950)
02 11 13
12
11
10
09
08
07
RIGHT ASCENSION (B1950)
Pol line 1 arcsec = 2.5000E-03 JY/BEAM
Peak flux = 1.1403E-01 JY/BEAM
Levs = 1.1403E-03 * (-10.0, -8.00, -6.00,
-4.00, -2.00, 2.000, 4.000, 6.000, 8.000,
10.00, 20.00, 40.00, 60.00, 80.00, 90.00,
99.00)

(a)

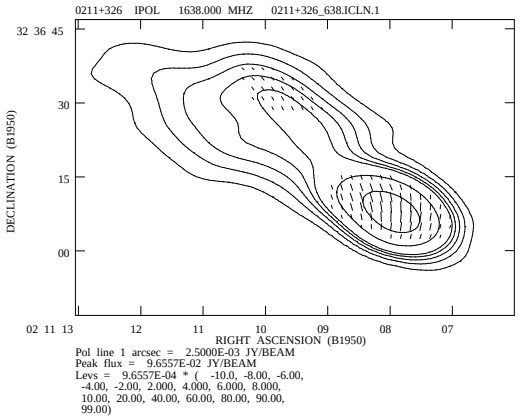
0211+326 IPOL 1638.000 MHZ 0211+326_638.ICLN.1
32 36 45
30
15
00
DECLINATION (B1950)
02 11 13
12
11
10
09
08
07
RIGHT ASCENSION (B1950)
Pol line 1 arcsec = 2.5000E-03 JY/BEAM
Peak flux = 9.6557E-02 JY/BEAM
Levs = 9.6557E-04 * (-10.0, -8.00, -6.00,
-4.00, -2.00, 2.000, 4.000, 6.000, 8.000,
10.00, 20.00, 40.00, 60.00, 80.00, 90.00,
99.00)

(b)

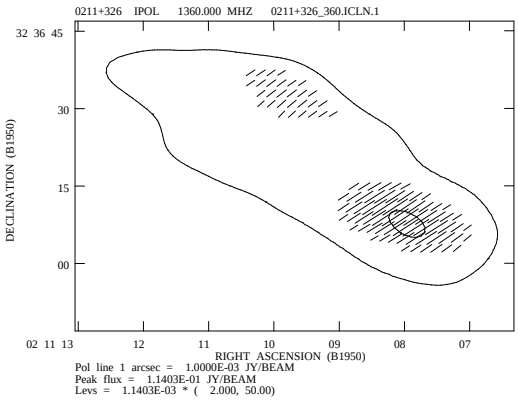
0211+326 IPOL 1360.000 MHZ 0211+326_360.ICLN.1
32 36 45
30
15
00
DECLINATION (B1950)
02 11 13
12
11
10
09
08
07
RIGHT ASCENSION (B1950)
Pol line 1 arcsec = 1.0000E-03 JY/BEAM
Peak flux = 1.1403E-01 JY/BEAM
Levs = 1.1403E-03 * (2.000, 50.00)

(c)

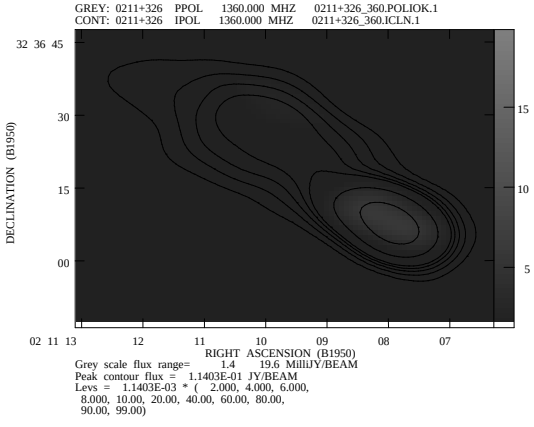
GREY: 0211+326 PPOL 1360.000 MHZ 0211+326_360.POLIOK.1
CONT: 0211+326 IPOL 1360.000 MHZ 0211+326_360.ICLN.1
32 36 45
30
15
00
DECLINATION (B1950)
15
10
5
02 11 13
12
11
10
09
08
07
RIGHT ASCENSION (B1950)
Grey scale flux range= 1.4 19.6 MilliJY/BEAM
Peak contour flux = 1.1403E-01 JY/BEAM
Levs = 1.1403E-03 * (2.000, 4.000, 6.000,
8.000, 10.00, 20.00, 40.00, 60.00, 80.00,
90.00, 99.00)

(d)

Figure 4-10. Maps of the source 0211+348. Panels (a) through (c) show the total intensity contours of the source along with the polarization position angles. The positive total intensity contours are 2, 4, 6, 8, 10, 20, 40, 60, 80, 90 and 99 percent of the peak intensity. The position angle of the vectors are that of the polarization position angles, and the lengths of the vectors are proportional to the polarized intensity. The position angles plotted are: (a) 1360 MHz ; (b) 1638 MHz; (c) $\chi_{1360} - \chi_{1638}$. In panel (d) the linear polarization intensity is plotted in grayscale on the contours of the total intensity.

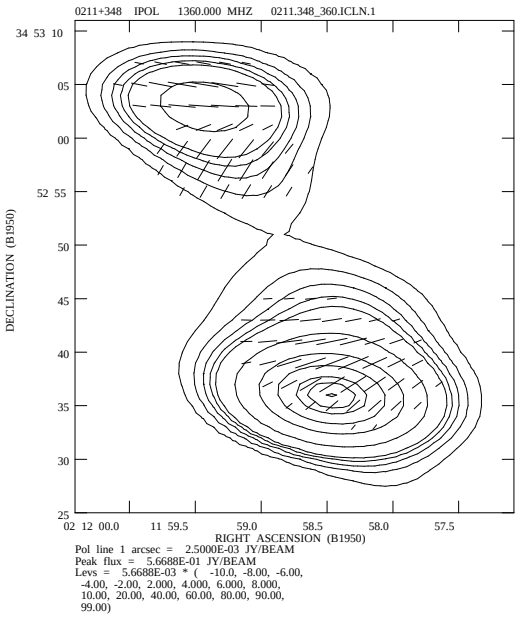
0211+348 IPOL 1360.000 MHZ 0211.348_360.ICLN.1
34 53 10
05
00
52 55
50
45
40
35
30
25
DECLINATION (B1950)
02 12 00.0
11 59.5
59.0
58.5
58.0
57.5
RIGHT ASCENSION (B1950)
Pol line 1 arcsec = 2.5000E-03 JY/BEAM
Peak flux = 5.6688E-01 JY/BEAM
Levs = 5.6688E-03 * (-10.0, -8.00, -6.00,
-4.00, -2.00, 2.000, 4.000, 6.000, 8.000,
10.00, 20.00, 40.00, 60.00, 80.00, 90.00,
99.00)

(a)

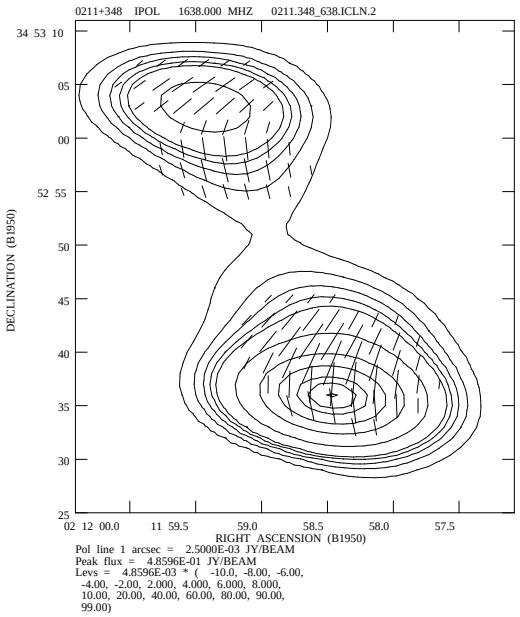
0211+348 IPOL 1638.000 MHZ 0211.348_638.ICLN.2
34 53 10
05
00
52 55
50
45
40
35
30
25
DECLINATION (B1950)
02 12 00.0
11 59.5
59.0
58.5
58.0
57.5
RIGHT ASCENSION (B1950)
Pol line 1 arcsec = 2.5000E-03 JY/BEAM
Peak flux = 4.8596E-01 JY/BEAM
Levs = 4.8596E-03 * (-10.0, -8.00, -6.00,
-4.00, -2.00, 2.000, 4.000, 6.000, 8.000,
10.00, 20.00, 40.00, 60.00, 80.00, 90.00,
99.00)

(b)

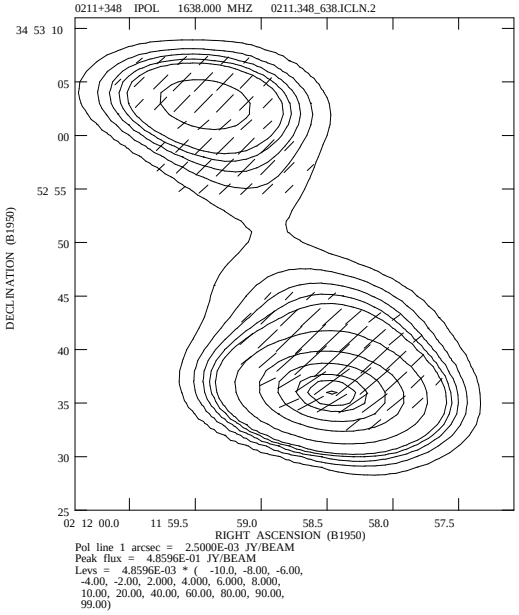
0211+348 IPOL 1638.000 MHZ 0211.348_638.ICLN.2
34 53 10
05
00
52 55
50
45
40
35
30
25
DECLINATION (B1950)
02 12 00.0
11 59.5
59.0
58.5
58.0
57.5
RIGHT ASCENSION (B1950)
Pol line 1 arcsec = 2.5000E-03 JY/BEAM
Peak flux = 4.8596E-01 JY/BEAM
Levs = 4.8596E-03 * (-10.0, -8.00, -6.00,
-4.00, -2.00, 2.000, 4.000, 6.000, 8.000,
10.00, 20.00, 40.00, 60.00, 80.00, 90.00,
99.00)

(c)

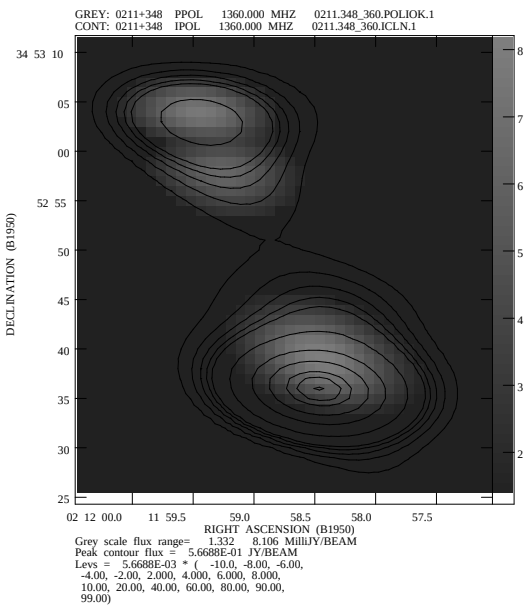
GREY: 0211+348 PPOL 1360.000 MHZ 0211.348_360.POLIOK.1
CONT: 0211+348 IPOL 1360.000 MHZ 0211.348_360.ICLN.1
34 53 10
05
00
52 55
50
45
40
35
30
25
DECLINATION (B1950)
8
7
6
5
4
3
2
02 12 00.0
11 59.5
59.0
58.5
58.0
57.5
RIGHT ASCENSION (B1950)
Grey scale flux range= 1.332 8.106 MilliJY/BEAM
Peak contour flux = 5.6688E-01 JY/BEAM
Levs = 5.6688E-03 * (-10.0, -8.00, -6.00,
-4.00, -2.00, 2.000, 4.000, 6.000, 8.000,
10.00, 20.00, 40.00, 60.00, 80.00, 90.00,
99.00)

(d)

Figure 4-11. Maps of the source 0212+344. Panels (a) through (c) show the total intensity contours of the source along with the polarization position angles. The positive total intensity contours are 2, 4, 6, 8, 10, 20, 40, 60, 80, 90 and 99 percent of the peak intensity. The position angle of the vectors are that of the polarization position angles, and the lengths of the vectors are proportional to the polarized intensity. The position angles plotted are: (a) 1360 MHz ; (b) 1638 MHz; (c) $\chi_{1360} - \chi_{1638}$. In panel (d) the linear polarization intensity is plotted in grayscale on the contours of the total intensity.

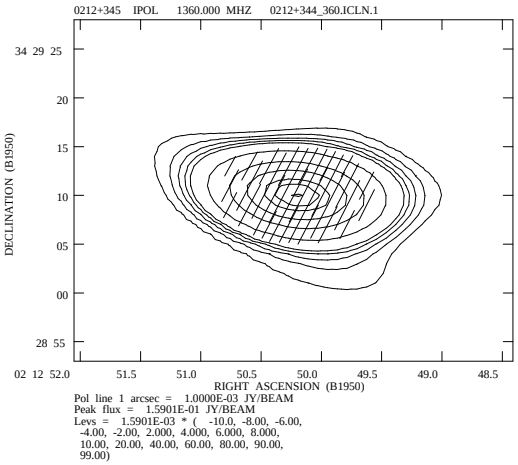
0212+345 IPOL 1360.000 MHZ 0212+344_360.ICLN.1
34 29 25
20
15
10
05
00
28 55
DECLINATION (B1950)
02 12 52.0
51.5
51.0
50.5
50.0
49.5
49.0
48.5
RIGHT ASCENSION (B1950)
Pol line 1 arcsec = 1.0000E-03 JY/BEAM
Peak flux = 1.5901E-01 JY/BEAM
Levs = 1.5901E-03 * (-10.0, -8.00, -6.00,
-4.00, -2.00, 2.000, 4.000, 6.000, 8.000,
10.00, 20.00, 40.00, 60.00, 80.00, 90.00,
99.00)

(a)

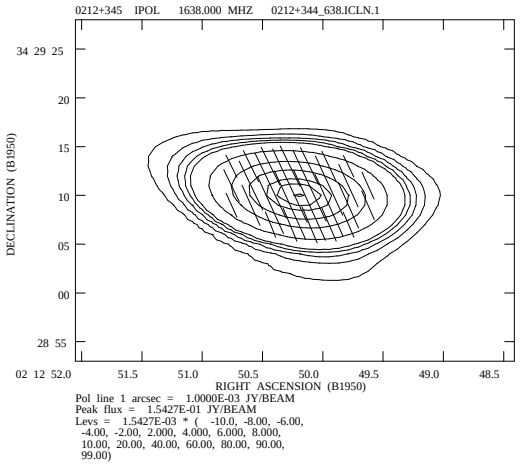
0212+345 IPOL 1638.000 MHZ 0212+344_638.ICLN.1
34 29 25
20
15
10
05
00
28 55
DECLINATION (B1950)
02 12 52.0
51.5
51.0
50.5
50.0
49.5
49.0
48.5
RIGHT ASCENSION (B1950)
Pol line 1 arcsec = 1.0000E-03 JY/BEAM
Peak flux = 1.5427E-01 JY/BEAM
Levs = 1.5427E-03 * (-10.0, -8.00, -6.00,
-4.00, -2.00, 2.000, 4.000, 6.000, 8.000,
10.00, 20.00, 40.00, 60.00, 80.00, 90.00,
99.00)

(b)

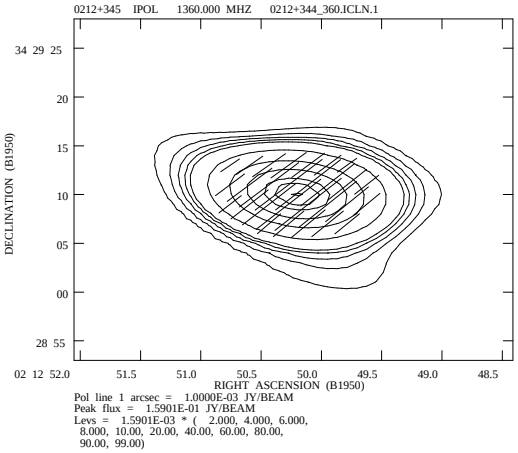
0212+345 IPOL 1360.000 MHZ 0212+344_360.ICLN.1
34 29 25
20
15
10
05
00
28 55
DECLINATION (B1950)
02 12 52.0
51.5
51.0
50.5
50.0
49.5
49.0
48.5
RIGHT ASCENSION (B1950)
Pol line 1 arcsec = 1.0000E-03 JY/BEAM
Peak flux = 1.5901E-01 JY/BEAM
Levs = 1.5901E-03 * (2.000, 4.000, 6.000,
8.000, 10.00, 20.00, 40.00, 60.00, 80.00,
90.00, 99.00)

(c)

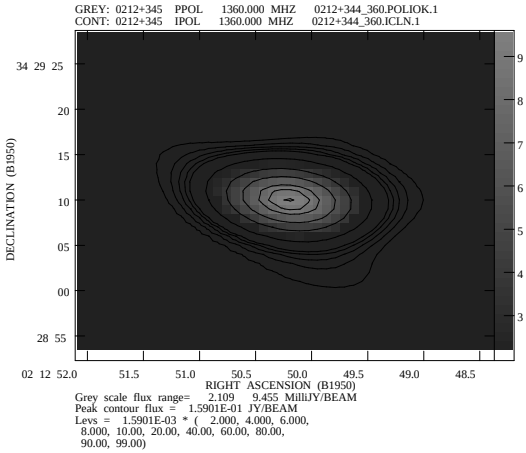
GREY: 0212+345 PPOL 1360.000 MHZ 0212+344_360.POLIOK.1
CONT: 0212+345 IPOL 1360.000 MHZ 0212+344_360.ICLN.1
34 29 25
20
15
10
05
00
28 55
DECLINATION (B1950)
02 12 52.0
51.5
51.0
50.5
50.0
49.5
49.0
48.5
RIGHT ASCENSION (B1950)
9
8
7
6
5
4
3
Grey scale flux range= 2.109 9.455 MilliJY/BEAM
Peak contour flux = 1.5901E-01 JY/BEAM
Levs = 1.5901E-03 * (2.000, 4.000, 6.000,
8.000, 10.00, 20.00, 40.00, 60.00, 80.00,
90.00, 99.00)

(d)

Figure 4-12. Maps of the source 0213+432. Panels (a) through (c) show the total intensity contours of the source along with the polarization position angles. The positive total intensity contours are 2, 4, 6, 8, 10, 20, 40, 60, 80, 90 and 99 percent of the peak intensity. The position angle of the vectors are that of the polarization position angles, and the lengths of the vectors are proportional to the polarized intensity. The position angles plotted are: (a) 1360 MHz ; (b) 1638 MHz; (c) $\chi_{1360} - \chi_{1638}$. In panel (d) the linear polarization intensity is plotted in grayscale on the contours of the total intensity.

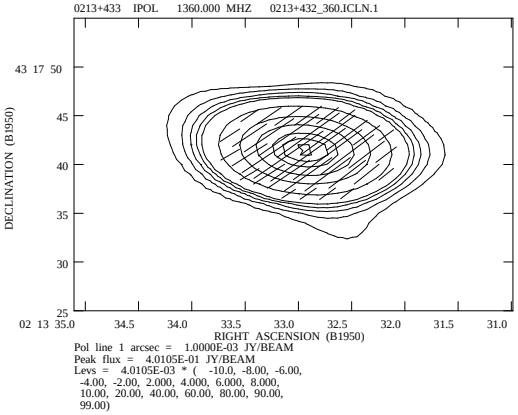
0213+433 IPOL 1360.000 MHZ 0213+432_360.ICLN.1
43 17 50
45
40
35
30
25
DECLINATION (B1950)
02 13 35.0 34.5 34.0 33.5 33.0 32.5 32.0 31.5 31.0
RIGHT ASCENSION (B1950)
Pol line 1 arcsec = 1.0000E-03 JY/BEAM
Peak flux = 4.0105E-01 JY/BEAM
Levs = 4.0105E-03 * (-10.0, -8.00, -6.00,
-4.00, -2.00, 2.000, 4.000, 6.000, 8.000,
10.00, 20.00, 40.00, 60.00, 80.00, 90.00,
99.00)

(a)

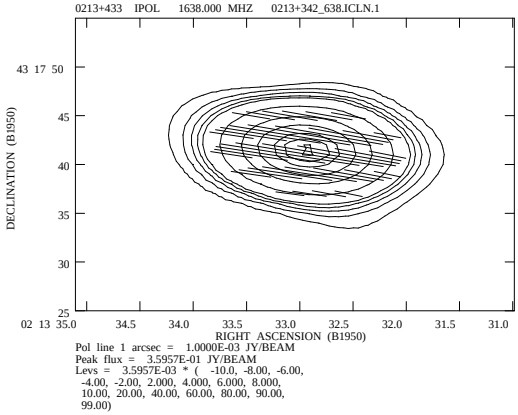
0213+433 IPOL 1638.000 MHZ 0213+342_638.ICLN.1
43 17 50
45
40
35
30
25
DECLINATION (B1950)
02 13 35.0 34.5 34.0 33.5 33.0 32.5 32.0 31.5 31.0
RIGHT ASCENSION (B1950)
Pol line 1 arcsec = 1.0000E-03 JY/BEAM
Peak flux = 3.5957E-01 JY/BEAM
Levs = 3.5957E-03 * (-10.0, -8.00, -6.00,
-4.00, -2.00, 2.000, 4.000, 6.000, 8.000,
10.00, 20.00, 40.00, 60.00, 80.00, 90.00,
99.00)

(b)

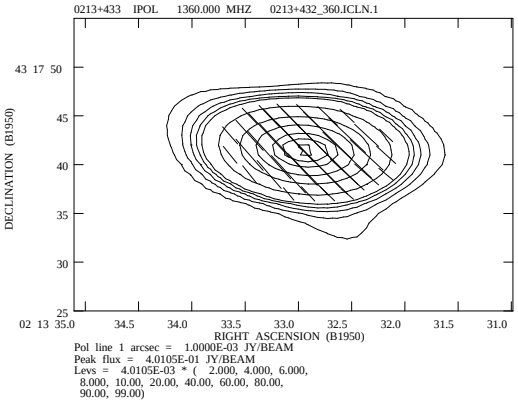
0213+433 IPOL 1360.000 MHZ 0213+432_360.ICLN.1
43 17 50
45
40
35
30
25
DECLINATION (B1950)
02 13 35.0 34.5 34.0 33.5 33.0 32.5 32.0 31.5 31.0
RIGHT ASCENSION (B1950)
Pol line 1 arcsec = 1.0000E-03 JY/BEAM
Peak flux = 4.0105E-01 JY/BEAM
Levs = 4.0105E-03 * (2.000, 4.000, 6.000,
8.000, 10.00, 20.00, 40.00, 60.00, 80.00,
90.00, 99.00)

(c)

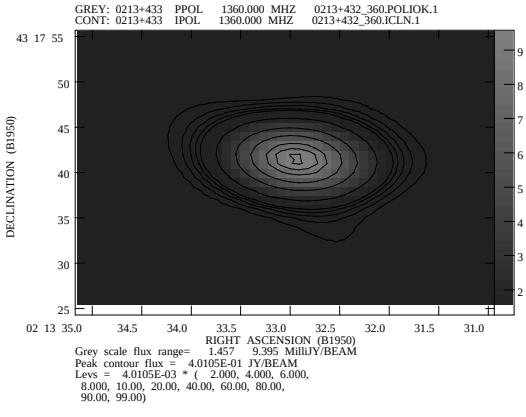
GREY: 0213+433 PPOL 1360.000 MHZ 0213+432_360.POLIOK.1
CONT: 0213+433 IPOL 1360.000 MHZ 0213+432_360.ICLN.1
43 17 55
50
45
40
35
30
25
DECLINATION (B1950)
02 13 35.0 34.5 34.0 33.5 33.0 32.5 32.0 31.5 31.0
RIGHT ASCENSION (B1950)
9
8
7
6
5
4
3
2
Grey scale flux range= 1.457 9.395 MilliJY/BEAM
Peak contour flux = 4.0105E-01 JY/BEAM
Levs = 4.0105E-03 * (2.000, 4.000, 6.000,
8.000, 10.00, 20.00, 40.00, 60.00, 80.00,
90.00, 99.00)

(d)

Figure 4-13. Maps of the source 0215+356. Panels (a) through (c) show the total intensity contours of the source along with the polarization position angles. The positive total intensity contours are 2, 4, 6, 8, 10, 20, 40, 60, 80, 90 and 99 percent of the peak intensity. The position angle of the vectors are that of the polarization position angles, and the lengths of the vectors are proportional to the polarized intensity. The position angles plotted are: (a) 1360 MHz ; (b) 1638 MHz; (c) $\chi_{1360} - \chi_{1638}$. In panel (d) the linear polarization intensity is plotted in grayscale on the contours of the total intensity.

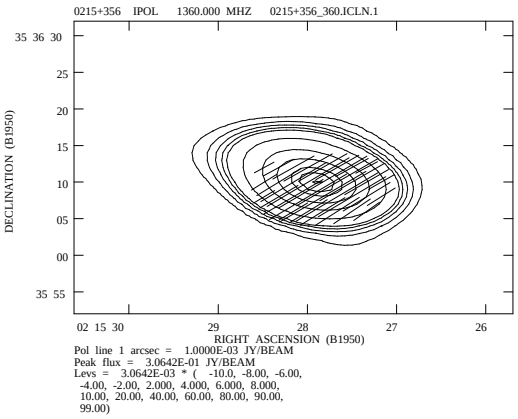
0215+356 IPOL 1360.000 MHZ 0215+356_360.ICLN.1
35 36 30
25
20
15
10
05
00
35 55
DECLINATION (B1950)
02 15 30
29
28
27
26
RIGHT ASCENSION (B1950)
Pol line 1 arcsec = 1.0000E-03 JY/BEAM
Peak flux = 3.0642E-01 JY/BEAM
Levs = 3.0642E-03 * (-10.0, -8.00, -6.00,
-4.00, -2.00, 2.000, 4.000, 6.000, 8.000,
10.00, 20.00, 40.00, 60.00, 80.00, 90.00,
99.00)

(a)

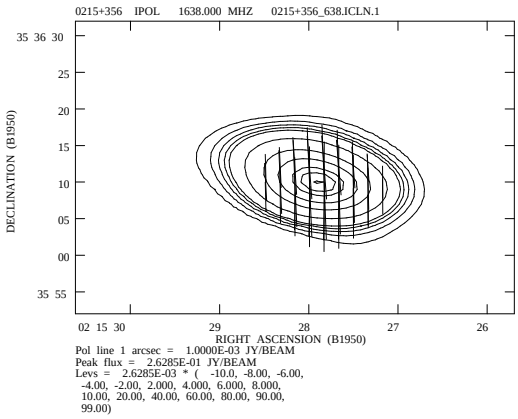
0215+356 IPOL 1638.000 MHZ 0215+356_638.ICLN.1
35 36 30
25
20
15
10
05
00
35 55
DECLINATION (B1950)
02 15 30
29
28
27
26
RIGHT ASCENSION (B1950)
Pol line 1 arcsec = 1.0000E-03 JY/BEAM
Peak flux = 2.6285E-01 JY/BEAM
Levs = 2.6285E-03 * (-10.0, -8.00, -6.00,
-4.00, -2.00, 2.000, 4.000, 6.000, 8.000,
10.00, 20.00, 40.00, 60.00, 80.00, 90.00,
99.00)

(b)

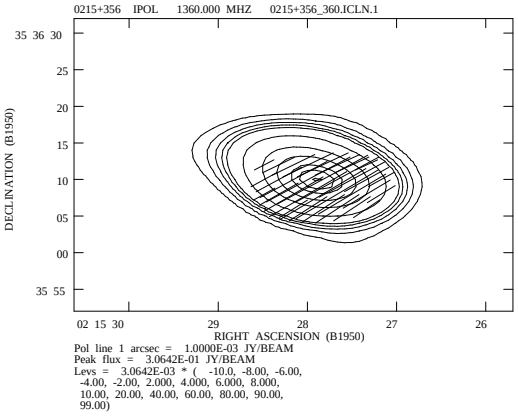
0215+356 IPOL 1360.000 MHZ 0215+356_360.ICLN.1
35 36 30
25
20
15
10
05
00
35 55
DECLINATION (B1950)
02 15 30
29
28
27
26
RIGHT ASCENSION (B1950)
Pol line 1 arcsec = 1.0000E-03 JY/BEAM
Peak flux = 3.0642E-01 JY/BEAM
Levs = 3.0642E-03 * (-10.0, -8.00, -6.00,
-4.00, -2.00, 2.000, 4.000, 6.000, 8.000,
10.00, 20.00, 40.00, 60.00, 80.00, 90.00,
99.00)

(c)

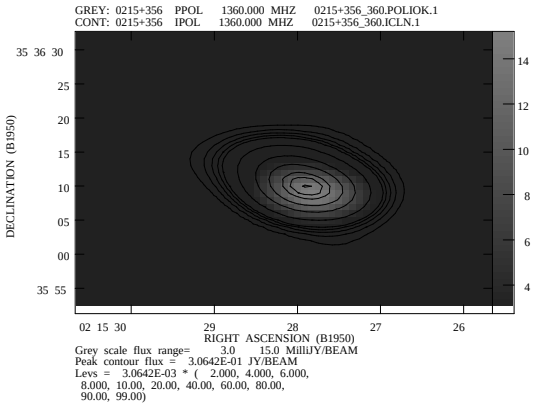
GREY: 0215+356 PPOL 1360.000 MHZ 0215+356_360.POLIOK.1
CONT: 0215+356 IPOL 1360.000 MHZ 0215+356_360.ICLN.1
35 36 30
25
20
15
10
05
00
35 55
DECLINATION (B1950)
14
12
10
8
6
4
02 15 30
29
28
27
26
RIGHT ASCENSION (B1950)
Grey scale flux range= 3.0 15.0 MilliJY/BEAM
Peak contour flux = 3.0642E-01 JY/BEAM
Levs = 3.0642E-03 * (2.000, 4.000, 6.000,
8.000, 10.00, 20.00, 40.00, 60.00, 80.00,
90.00, 99.00)

(d)

Figure 4-14. Maps of the source 0215+423. Panels (a) through (c) show the total intensity contours of the source along with the polarization position angles. The positive total intensity contours are 2, 4, 6, 8, 10, 20, 40, 60, 80, 90 and 99 percent of the peak intensity. The position angle of the vectors are that of the polarization position angles, and the lengths of the vectors are proportional to the polarized intensity. The position angles plotted are: (a) 1360 MHz ; (b) 1638 MHz; (c) $\chi_{1360} - \chi_{1638}$. In panel (d) the linear polarization intensity is plotted in grayscale on the contours of the total intensity.

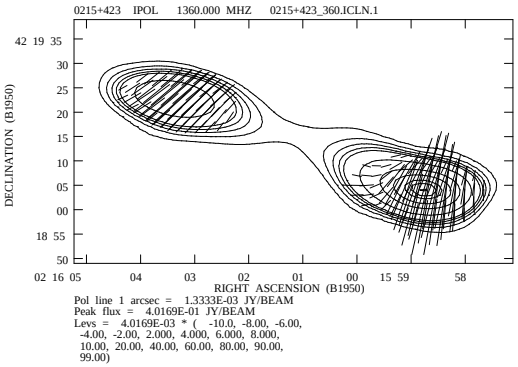
0215+423 IPOL 1360.000 MHZ 0215+423_360.ICLN.1
DECLINATION (B1950)
RIGHT ASCENSION (B1950)
Pol line 1 arcsec = 1.3333E-03 JY/BEAM
Peak flux = 4.0169E-01 JY/BEAM
Levs = 4.0169E-03 * (-10.0, -8.00, -6.00,
-4.00, -2.00, 2.000, 4.000, 6.000, 8.000,
10.00, 20.00, 40.00, 60.00, 80.00, 90.00,
99.00)

(a)

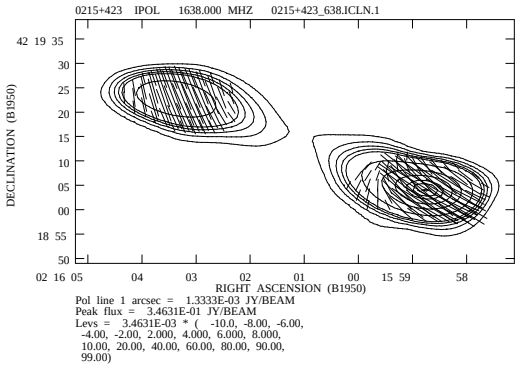
0215+423 IPOL 1638.000 MHZ 0215+423_638.ICLN.1
DECLINATION (B1950)
RIGHT ASCENSION (B1950)
Pol line 1 arcsec = 1.3333E-03 JY/BEAM
Peak flux = 3.4631E-01 JY/BEAM
Levs = 3.4631E-03 * (-10.0, -8.00, -6.00,
-4.00, -2.00, 2.000, 4.000, 6.000, 8.000,
10.00, 20.00, 40.00, 60.00, 80.00, 90.00,
99.00)

(b)

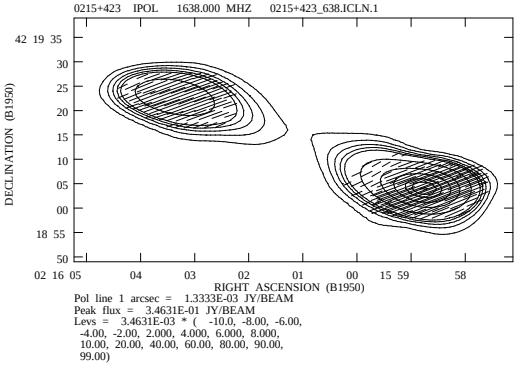
0215+423 IPOL 1638.000 MHZ 0215+423_638.ICLN.1
DECLINATION (B1950)
RIGHT ASCENSION (B1950)
Pol line 1 arcsec = 1.3333E-03 JY/BEAM
Peak flux = 3.4631E-01 JY/BEAM
Levs = 3.4631E-03 * (-10.0, -8.00, -6.00,
-4.00, -2.00, 2.000, 4.000, 6.000, 8.000,
10.00, 20.00, 40.00, 60.00, 80.00, 90.00,
99.00)

(c)

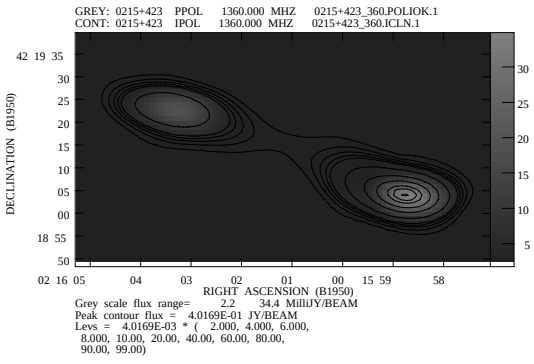
GREY: 0215+423 PPOL 1360.000 MHZ 0215+423_360.POLIOK.1
CONT: 0215+423 IPOL 1360.000 MHZ 0215+423_360.ICLN.1
DECLINATION (B1950)
RIGHT ASCENSION (B1950)
Grey scale flux range= 2.2 34.4 MilliJY/BEAM
Peak contour flux = 4.0169E-01 JY/BEAM
Levs = 4.0169E-03 * (2.000, 4.000, 6.000,
8.000, 10.00, 20.00, 40.00, 60.00, 80.00,
90.00, 99.00)

(d)

Figure 4-15. Maps of the source 0216+335. Panels (a) through (c) show the total intensity contours of the source along with the polarization position angles. The positive total intensity contours are 2, 4, 6, 8, 10, 20, 40, 60, 80, 90 and 99 percent of the peak intensity. The position angle of the vectors are that of the polarization position angles, and the lengths of the vectors are proportional to the polarized intensity. The position angles plotted are: (a) 1360 MHz ; (b) 1638 MHz; (c) $\chi_{1360} - \chi_{1638}$. In panel (d) the linear polarization intensity is plotted in grayscale on the contours of the total intensity.

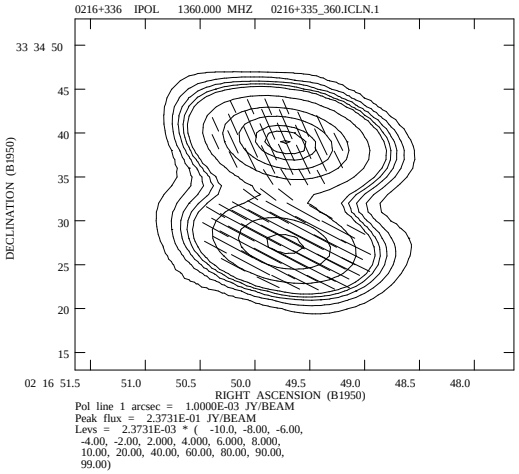
0216+336 IPOL 1360.000 MHZ 0216+335_360.ICLN.1
33 34 50
45
40
35
30
25
20
15
DECLINATION (B1950)
02 16 51.5
51.0
50.5
50.0
49.5
49.0
48.5
48.0
RIGHT ASCENSION (B1950)
Pol line 1 arcsec = 1.0000E-03 JY/BEAM
Peak flux = 2.3731E-01 JY/BEAM
Levs = 2.3731E-03 * (-10.0, -8.00, -6.00,
-4.00, -2.00, 2.000, 4.000, 6.000, 8.000,
10.00, 20.00, 40.00, 60.00, 80.00, 90.00,
99.00)

(a)

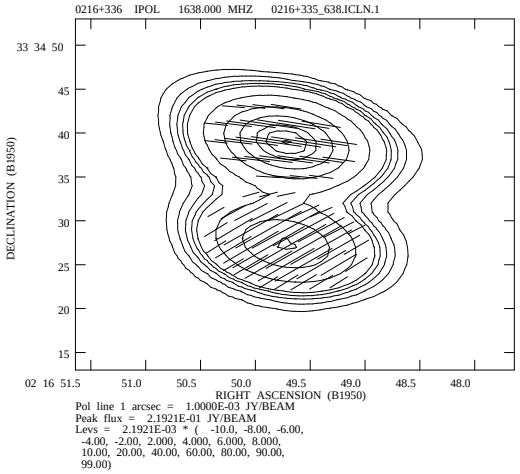
0216+336 IPOL 1638.000 MHZ 0216+335_638.ICLN.1
33 34 50
45
40
35
30
25
20
15
DECLINATION (B1950)
02 16 51.5
51.0
50.5
50.0
49.5
49.0
48.5
48.0
RIGHT ASCENSION (B1950)
Pol line 1 arcsec = 1.0000E-03 JY/BEAM
Peak flux = 2.1921E-01 JY/BEAM
Levs = 2.1921E-03 * (-10.0, -8.00, -6.00,
-4.00, -2.00, 2.000, 4.000, 6.000, 8.000,
10.00, 20.00, 40.00, 60.00, 80.00, 90.00,
99.00)

(b)

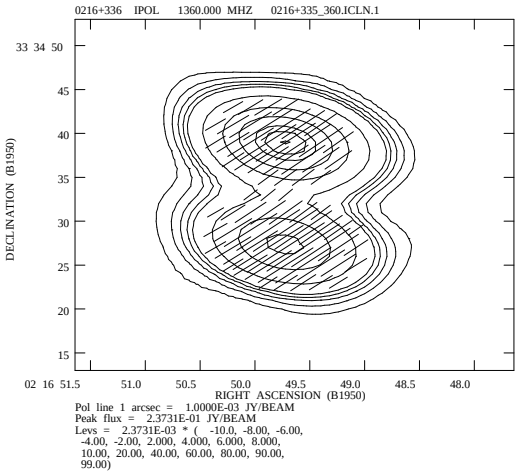
0216+336 IPOL 1360.000 MHZ 0216+335_360.ICLN.1
33 34 50
45
40
35
30
25
20
15
DECLINATION (B1950)
02 16 51.5
51.0
50.5
50.0
49.5
49.0
48.5
48.0
RIGHT ASCENSION (B1950)
Pol line 1 arcsec = 1.0000E-03 JY/BEAM
Peak flux = 2.3731E-01 JY/BEAM
Levs = 2.3731E-03 * (-10.0, -8.00, -6.00,
-4.00, -2.00, 2.000, 4.000, 6.000, 8.000,
10.00, 20.00, 40.00, 60.00, 80.00, 90.00,
99.00)

(c)

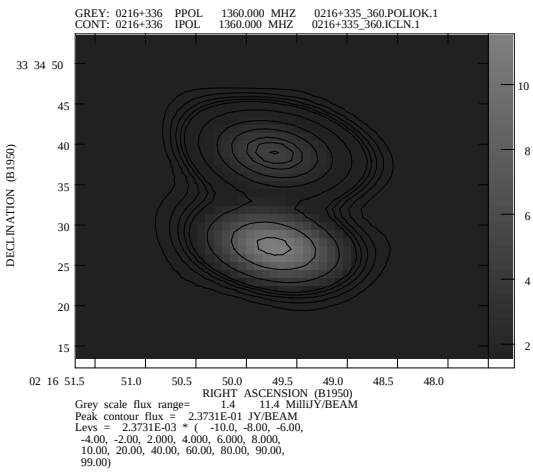
GREY: 0216+336 PPOL 1360.000 MHZ 0216+335_360.POLIOK.1
CONT: 0216+336 IPOL 1360.000 MHZ 0216+335_360.ICLN.1
33 34 50
45
40
35
30
25
20
15
DECLINATION (B1950)
10
8
6
4
2
02 16 51.5
51.0
50.5
50.0
49.5
49.0
48.5
48.0
RIGHT ASCENSION (B1950)
Grey scale flux range= 1.4 11.4 MilliJY/BEAM
Peak contour flux = 2.3731E-01 JY/BEAM
Levs = 2.3731E-03 * (-10.0, -8.00, -6.00,
-4.00, -2.00, 2.000, 4.000, 6.000, 8.000,
10.00, 20.00, 40.00, 60.00, 80.00, 90.00,
99.00)

(d)

Figure 4-16. Maps of the source 0217+417. Panels (a) through (c) show the total intensity contours of the source along with the polarization position angles. The positive total intensity contours are 2, 4, 6, 8, 10, 20, 40, 60, 80, 90 and 99 percent of the peak intensity. The position angle of the vectors are that of the polarization position angles, and the lengths of the vectors are proportional to the polarized intensity. The position angles plotted are: (a) 1360 MHz ; (b) 1638 MHz; (c) $\chi_{1360} - \chi_{1638}$. In panel (d) the linear polarization intensity is plotted in grayscale on the contours of the total intensity.

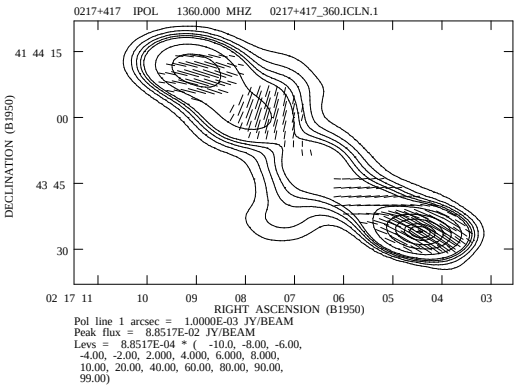
0217+417 IPOL 1360.000 MHZ 0217+417_360.ICLN.1
DECLINATION (B1950)
41 44 15
00
43 45
30
02 17 11
10
09
08
07
06
05
04
03
RIGHT ASCENSION (B1950)
Pol line 1 arcsec = 1.0000E-03 JY/BEAM
Peak flux = 8.8517E-02 JY/BEAM
Levs = 8.8517E-04 * (-10.0, -8.00, -6.00,
-4.00, -2.00, 2.000, 4.000, 6.000, 8.000,
10.00, 20.00, 40.00, 60.00, 80.00, 90.00,
99.00)

(a)

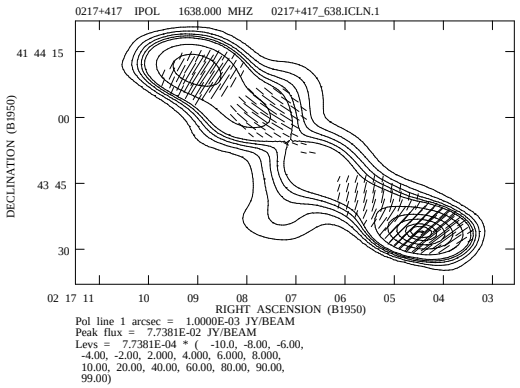
0217+417 IPOL 1638.000 MHZ 0217+417_638.ICLN.1
DECLINATION (B1950)
41 44 15
00
43 45
30
02 17 11
10
09
08
07
06
05
04
03
RIGHT ASCENSION (B1950)
Pol line 1 arcsec = 1.0000E-03 JY/BEAM
Peak flux = 7.7381E-02 JY/BEAM
Levs = 7.7381E-04 * (-10.0, -8.00, -6.00,
-4.00, -2.00, 2.000, 4.000, 6.000, 8.000,
10.00, 20.00, 40.00, 60.00, 80.00, 90.00,
99.00)

(b)

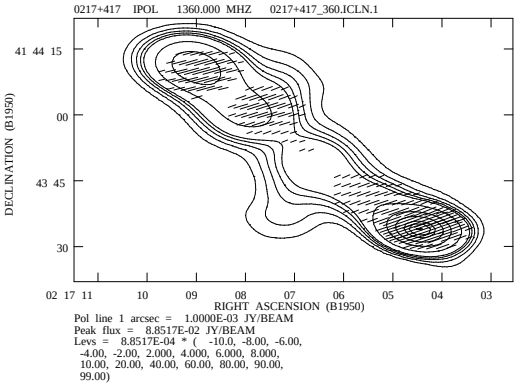
0217+417 IPOL 1360.000 MHZ 0217+417_360.ICLN.1
DECLINATION (B1950)
41 44 15
00
43 45
30
02 17 11
10
09
08
07
06
05
04
03
RIGHT ASCENSION (B1950)
Pol line 1 arcsec = 1.0000E-03 JY/BEAM
Peak flux = 8.8517E-02 JY/BEAM
Levs = 8.8517E-04 * (-10.0, -8.00, -6.00,
-4.00, -2.00, 2.000, 4.000, 6.000, 8.000,
10.00, 20.00, 40.00, 60.00, 80.00, 90.00,
99.00)

(c)

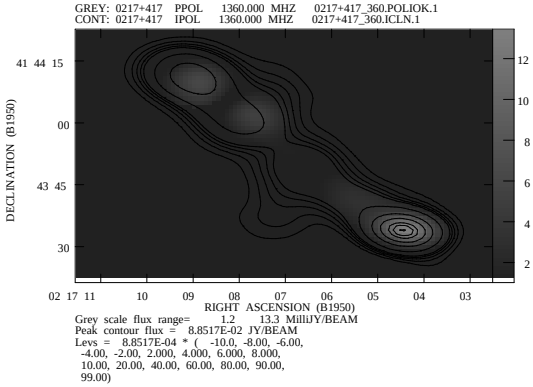
GREY: 0217+417 PPOL 1360.000 MHZ 0217+417_360.POLIOK.1
CONT: 0217+417 IPOL 1360.000 MHZ 0217+417_360.ICLN.1
DECLINATION (B1950)
41 44 15
00
43 45
30
12
10
8
6
4
2
02 17 11
10
09
08
07
06
05
04
03
RIGHT ASCENSION (B1950)
Grey scale flux range= 1.2 13.3 MilliJY/BEAM
Peak contour flux = 8.8517E-02 JY/BEAM
Levs = 8.8517E-04 * (-10.0, -8.00, -6.00,
-4.00, -2.00, 2.000, 4.000, 6.000, 8.000,
10.00, 20.00, 40.00, 60.00, 80.00, 90.00,
99.00)

(d)

Figure 4-17. Maps of the source 0218+396. Panels (a) through (c) show the total intensity contours of the source along with the polarization position angles. The positive total intensity contours are 2, 4, 6, 8, 10, 20, 40, 60, 80, 90 and 99 percent of the peak intensity. The position angle of the vectors are that of the polarization position angles, and the lengths of the vectors are proportional to the polarized intensity. The position angles plotted are: (a) 1360 MHz ; (b) 1638 MHz; (c) $\chi_{1360} - \chi_{1638}$. In panel (d) the linear polarization intensity is plotted in grayscale on the contours of the total intensity.

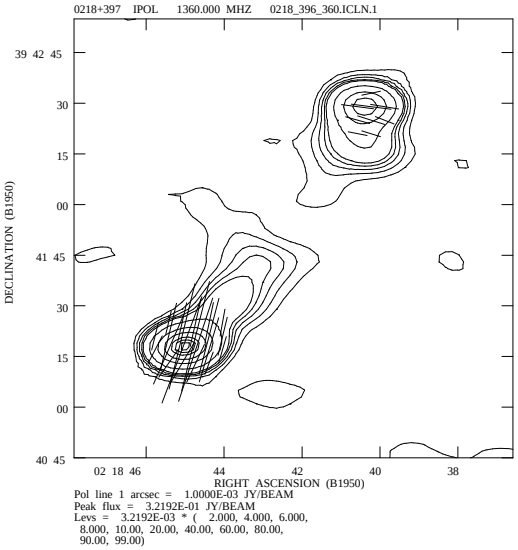
0218+397 IPOL 1360.000 MHZ 0218_396_360.ICLN.1
DECLINATION (B1950)
RIGHT ASCENSION (B1950)
Pol line 1 arcsec = 1.0000E-03 JY/BEAM
Peak flux = 3.2192E-01 JY/BEAM
Levs = 3.2192E-03 * (2.000, 4.000, 6.000,
8.000, 10.00, 20.00, 40.00, 60.00, 80.00,
90.00, 99.00)

(a)

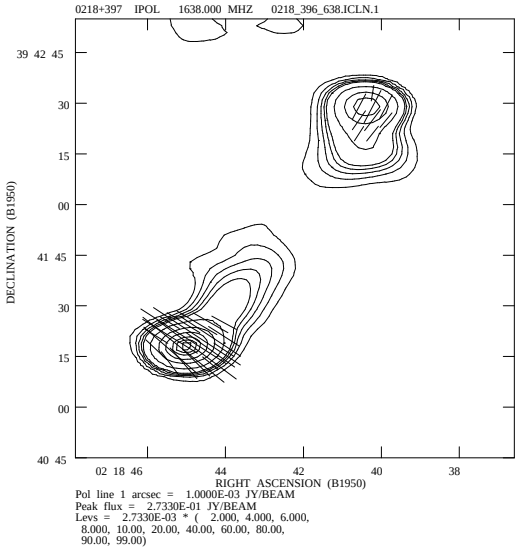
0218+397 IPOL 1638.000 MHZ 0218_396_638.ICLN.1
DECLINATION (B1950)
RIGHT ASCENSION (B1950)
Pol line 1 arcsec = 1.0000E-03 JY/BEAM
Peak flux = 2.7330E-01 JY/BEAM
Levs = 2.7330E-03 * (2.000, 4.000, 6.000,
8.000, 10.00, 20.00, 40.00, 60.00, 80.00,
90.00, 99.00)

(b)

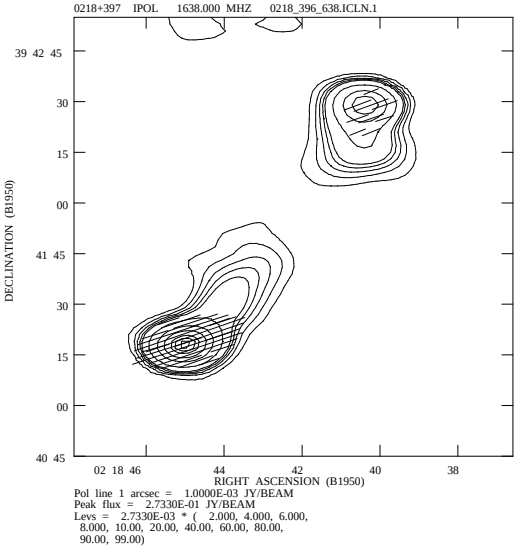
0218+397 IPOL 1638.000 MHZ 0218_396_638.ICLN.1
DECLINATION (B1950)
RIGHT ASCENSION (B1950)
Pol line 1 arcsec = 1.0000E-03 JY/BEAM
Peak flux = 2.7330E-01 JY/BEAM
Levs = 2.7330E-03 * (2.000, 4.000, 6.000,
8.000, 10.00, 20.00, 40.00, 60.00, 80.00,
90.00, 99.00)

(c)

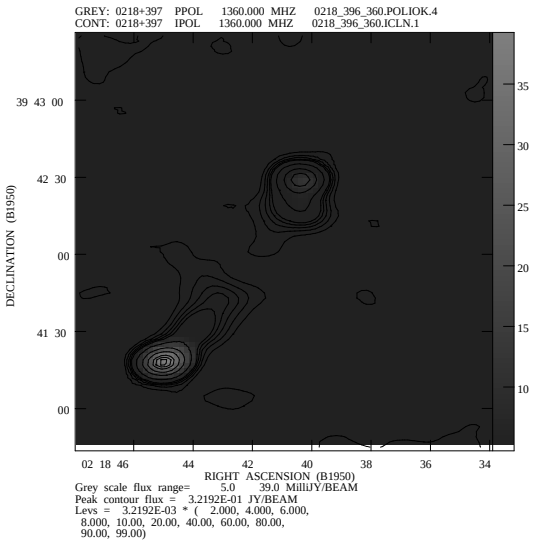
GREY: 0218+397 PPOL 1360.000 MHZ 0218_396_360.POLIOK.4
CONT: 0218+397 IPOL 1360.000 MHZ 0218_396_360.ICLN.1
DECLINATION (B1950)
RIGHT ASCENSION (B1950)
Grey scale flux range= 5.0 39.0 MilliJY/BEAM
Peak contour flux = 3.2192E-01 JY/BEAM
Levs = 3.2192E-03 * (2.000, 4.000, 6.000,
8.000, 10.00, 20.00, 40.00, 60.00, 80.00,
90.00, 99.00)

(d)

Figure 4-18. Maps of the source 0219+428. Panels (a) through (c) show the total intensity contours of the source along with the polarization position angles. The positive total intensity contours are 2, 4, 6, 8, 10, 20, 40, 60, 80, 90 and 99 percent of the peak intensity. The position angle of the vectors are that of the polarization position angles, and the lengths of the vectors are proportional to the polarized intensity. The position angles plotted are: (a) 1360 MHz ; (b) 1638 MHz; (c) $\chi_{1360} - \chi_{1638}$. In panel (d) the linear polarization intensity is plotted in grayscale on the contours of the total intensity.

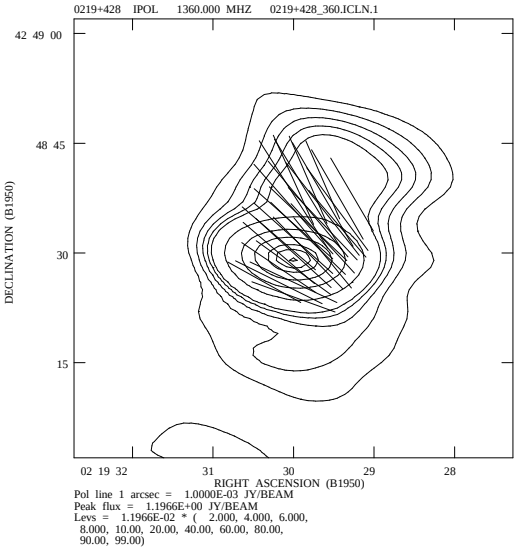
0219+428 IPOL 1360.000 MHZ 0219+428_360.ICLN.1
42 49 00
48 45
30
15
DECLINATION (B1950)
02 19 32
31
30
29
28
RIGHT ASCENSION (B1950)
Pol line 1 arcsec = 1.0000E-03 JY/BEAM
Peak flux = 1.1966E+00 JY/BEAM
Levs = 1.1966E-02 * (2.000, 4.000, 6.000,
8.000, 10.00, 20.00, 40.00, 60.00, 80.00,
90.00, 99.00)

(a)

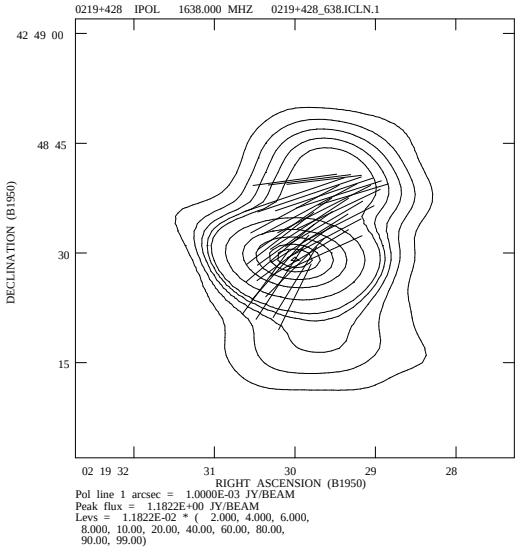
0219+428 IPOL 1638.000 MHZ 0219+428_638.ICLN.1
42 49 00
48 45
30
15
DECLINATION (B1950)
02 19 32
31
30
29
28
RIGHT ASCENSION (B1950)
Pol line 1 arcsec = 1.0000E-03 JY/BEAM
Peak flux = 1.1822E+00 JY/BEAM
Levs = 1.1822E-02 * (2.000, 4.000, 6.000,
8.000, 10.00, 20.00, 40.00, 60.00, 80.00,
90.00, 99.00)

(b)

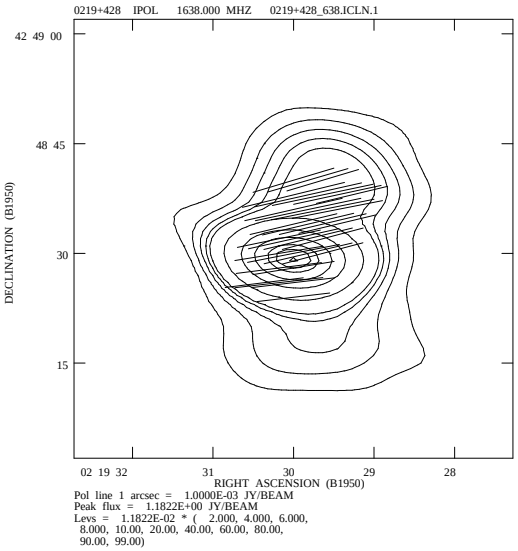
0219+428 IPOL 1638.000 MHZ 0219+428_638.ICLN.1
42 49 00
48 45
30
15
DECLINATION (B1950)
02 19 32
31
30
29
28
RIGHT ASCENSION (B1950)
Pol line 1 arcsec = 1.0000E-03 JY/BEAM
Peak flux = 1.1822E+00 JY/BEAM
Levs = 1.1822E-02 * (2.000, 4.000, 6.000,
8.000, 10.00, 20.00, 40.00, 60.00, 80.00,
90.00, 99.00)

(c)

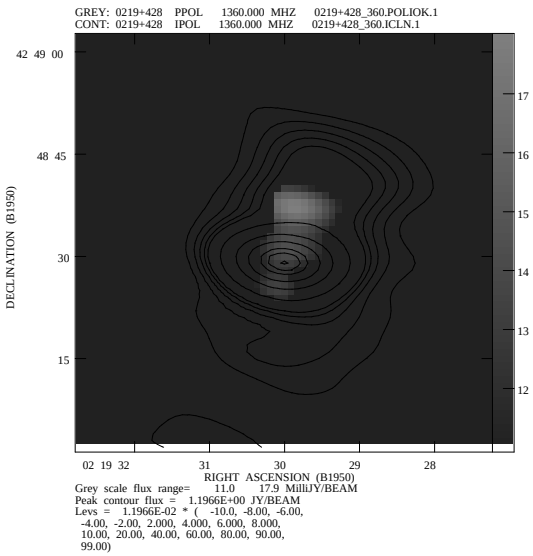
GREY: 0219+428 PPOL 1360.000 MHZ 0219+428_360.POLIOK.1
CONT: 0219+428 IPOL 1360.000 MHZ 0219+428_360.ICLN.1
42 49 00
48 45
30
15
DECLINATION (B1950)
17
16
15
14
13
12
02 19 32
31
30
29
28
RIGHT ASCENSION (B1950)
Grey scale flux range= 11.0 17.9 MilliJY/BEAM
Peak contour flux = 1.1966E+00 JY/BEAM
Levs = 1.1966E-02 * (-10.0, -8.00, -6.00,
-4.00, -2.00, 2.000, 4.000, 6.000, 8.000,
10.00, 20.00, 40.00, 60.00, 80.00, 90.00,
99.00)

(d)

Figure 4-19. Maps of the source 0220+397. Panels (a) through (c) show the total intensity contours of the source along with the polarization position angles. The positive total intensity contours are 2, 4, 6, 8, 10, 20, 40, 60, 80, 90 and 99 percent of the peak intensity. The position angle of the vectors are that of the polarization position angles, and the lengths of the vectors are proportional to the polarized intensity. The position angles plotted are: (a) 1360 MHz ; (b) 1638 MHz; (c) $\chi_{1360} - \chi_{1638}$. In panel (d) the linear polarization intensity is plotted in grayscale on the contours of the total intensity.

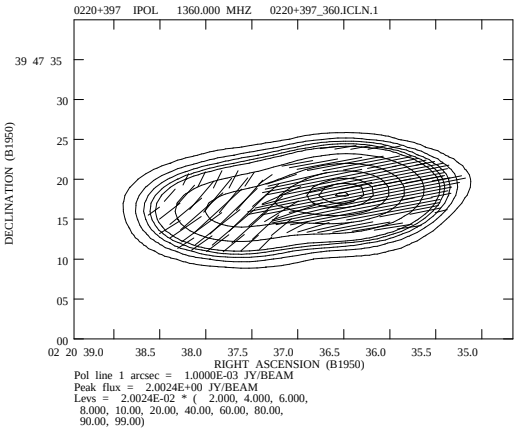
0220+397 IPOL 1360.000 MHZ 0220+397_360.ICLN.1
DECLINATION (B1950)
RIGHT ASCENSION (B1950)
Pol line 1 arcsec = 1.0000E-03 JY/BEAM
Peak flux = 2.0024E+00 JY/BEAM
Levs = 2.0024E-02 * (2.000, 4.000, 6.000,
8.000, 10.00, 20.00, 40.00, 60.00, 80.00,
90.00, 99.00)

(a)

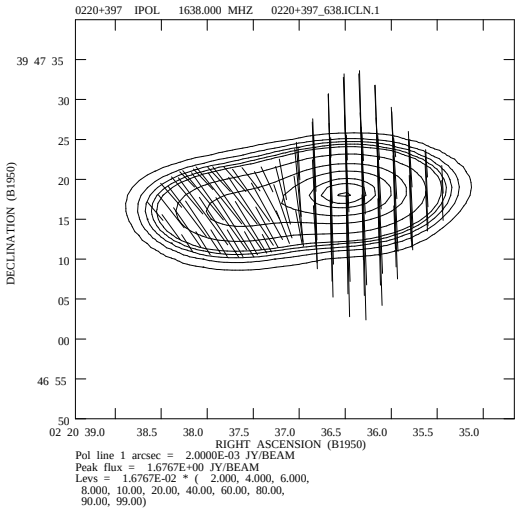
0220+397 IPOL 1638.000 MHZ 0220+397_638.ICLN.1
DECLINATION (B1950)
RIGHT ASCENSION (B1950)
Pol line 1 arcsec = 2.0000E-03 JY/BEAM
Peak flux = 1.6767E+00 JY/BEAM
Levs = 1.6767E-02 * (2.000, 4.000, 6.000,
8.000, 10.00, 20.00, 40.00, 60.00, 80.00,
90.00, 99.00)

(b)

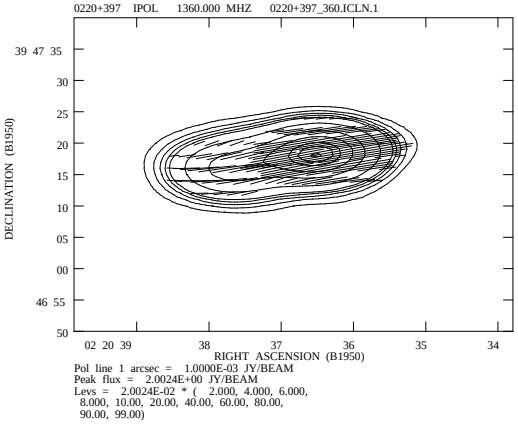
0220+397 IPOL 1360.000 MHZ 0220+397_360.ICLN.1
DECLINATION (B1950)
RIGHT ASCENSION (B1950)
Pol line 1 arcsec = 1.0000E-03 JY/BEAM
Peak flux = 2.0024E+00 JY/BEAM
Levs = 2.0024E-02 * (2.000, 4.000, 6.000,
8.000, 10.00, 20.00, 40.00, 60.00, 80.00,
90.00, 99.00)

(c)

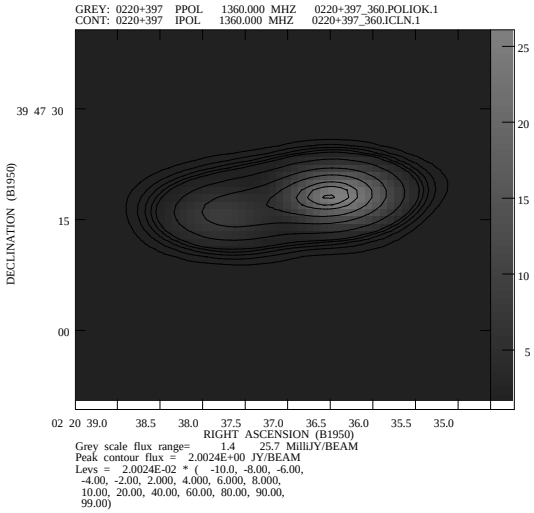
GREY: 0220+397 PPOL 1360.000 MHZ 0220+397_360.POLIOK.1
CONT: 0220+397 IPOL 1360.000 MHZ 0220+397_360.ICLN.1
DECLINATION (B1950)
RIGHT ASCENSION (B1950)
Grey scale flux range= 1.4 25.7 MilliJY/BEAM
Peak contour flux = 2.0024E+00 JY/BEAM
Levs = 2.0024E-02 * (-10.0, -8.00, -6.00,
-4.00, -2.00, 2.000, 4.000, 6.000, 8.000,
10.00, 20.00, 40.00, 60.00, 80.00, 90.00,
99.00)

(d)

Figure 4-20. Maps of the source 0224+393. Panels (a) through (c) show the total intensity contours of the source along with the polarization position angles. The positive total intensity contours are 2, 4, 6, 8, 10, 20, 40, 60, 80, 90 and 99 percent of the peak intensity. The position angle of the vectors are that of the polarization position angles, and the lengths of the vectors are proportional to the polarized intensity. The position angles plotted are: (a) 1360 MHz ; (b) 1638 MHz; (c) $\chi_{1360} - \chi_{1638}$. In panel (d) the linear polarization intensity is plotted in grayscale on the contours of the total intensity.

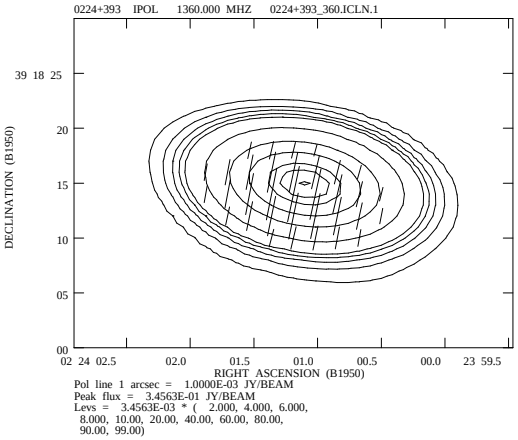
0224+393 IPOL 1360.000 MHZ 0224+393_360.ICLN.1
39 18 25
20
15
10
05
00
DECLINATION (B1950)
02 24 02.5 02.0 01.5 01.0 00.5 00.0 23 59.5
RIGHT ASCENSION (B1950)
Pol line 1 arcsec = 1.0000E-03 JY/BEAM
Peak flux = 3.4563E-01 JY/BEAM
Levs = 3.4563E-03 * (2.000, 4.000, 6.000,
8.000, 10.00, 20.00, 40.00, 60.00, 80.00,
90.00, 99.00)

(a)

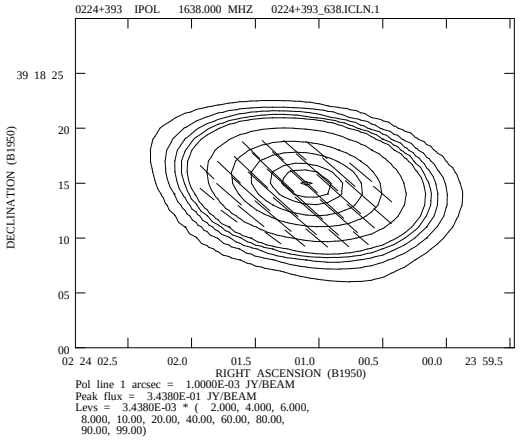
0224+393 IPOL 1638.000 MHZ 0224+393_638.ICLN.1
39 18 25
20
15
10
05
00
DECLINATION (B1950)
02 24 02.5 02.0 01.5 01.0 00.5 00.0 23 59.5
RIGHT ASCENSION (B1950)
Pol line 1 arcsec = 1.0000E-03 JY/BEAM
Peak flux = 3.4380E-01 JY/BEAM
Levs = 3.4380E-03 * (2.000, 4.000, 6.000,
8.000, 10.00, 20.00, 40.00, 60.00, 80.00,
90.00, 99.00)

(b)

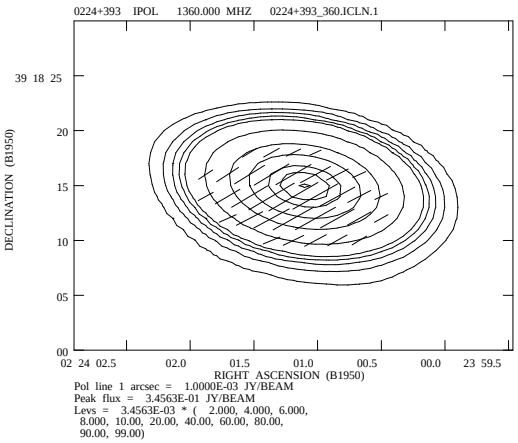
0224+393 IPOL 1360.000 MHZ 0224+393_360.ICLN.1
39 18 25
20
15
10
05
00
DECLINATION (B1950)
02 24 02.5 02.0 01.5 01.0 00.5 00.0 23 59.5
RIGHT ASCENSION (B1950)
Pol line 1 arcsec = 1.0000E-03 JY/BEAM
Peak flux = 3.4563E-01 JY/BEAM
Levs = 3.4563E-03 * (2.000, 4.000, 6.000,
8.000, 10.00, 20.00, 40.00, 60.00, 80.00,
90.00, 99.00)

(c)

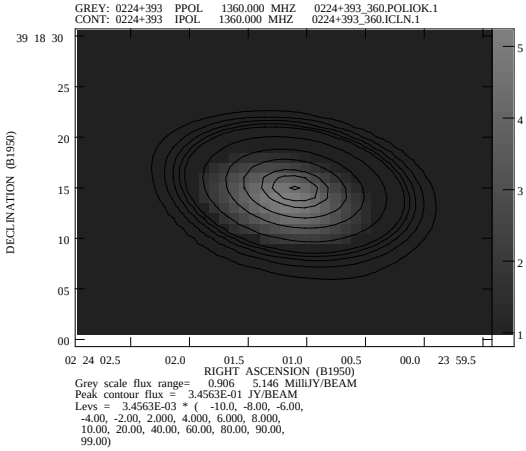
GREY: 0224+393 PPOL 1360.000 MHZ 0224+393_360.POLIOK.1
CONT: 0224+393 IPOL 1360.000 MHZ 0224+393_360.ICLN.1
39 18 30
25
20
15
10
05
00
DECLINATION (B1950)
5
4
3
2
1
02 24 02.5 02.0 01.5 01.0 00.5 00.0 23 59.5
RIGHT ASCENSION (B1950)
Grey scale flux range= 0.906 5.146 MilliJY/BEAM
Peak contour flux = 3.4563E-01 JY/BEAM
Levs = 3.4563E-03 * (-10.0, -8.00, -6.00,
-4.00, -2.00, 2.000, 4.000, 6.000, 8.000,
10.00, 20.00, 40.00, 60.00, 80.00, 90.00,
99.00)

(d)

Figure 4-21. Maps of the source 0227+403. Panels (a) through (c) show the total intensity contours of the source along with the polarization position angles. The positive total intensity contours are 2, 4, 6, 8, 10, 20, 40, 60, 80, 90 and 99 percent of the peak intensity. The position angle of the vectors are that of the polarization position angles, and the lengths of the vectors are proportional to the polarized intensity. The position angles plotted are: (a) 1360 MHz ; (b) 1638 MHz; (c) $\chi_{1360} - \chi_{1638}$. In panel (d) the linear polarization intensity is plotted in grayscale on the contours of the total intensity.

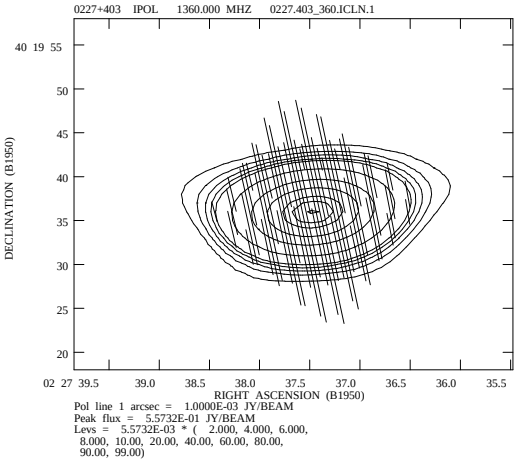
0227+403 IPOL 1360.000 MHZ 0227.403_360.ICLN.1
DECLINATION (B1950)
RIGHT ASCENSION (B1950)
Pol line 1 arcsec = 1.0000E-03 JY/BEAM
Peak flux = 5.5732E-01 JY/BEAM
Levs = 5.5732E-03 * (2.000, 4.000, 6.000,
8.000, 10.00, 20.00, 40.00, 60.00, 80.00,
90.00, 99.00)

(a)

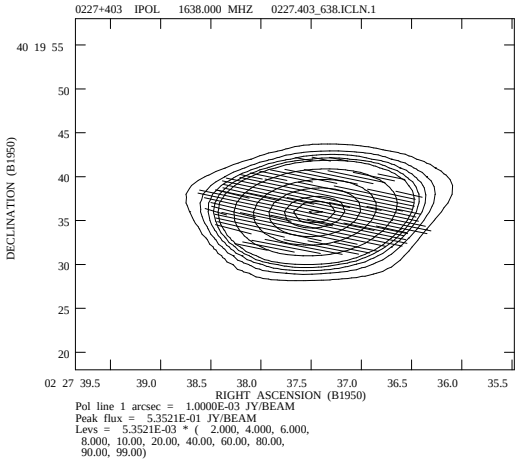
0227+403 IPOL 1638.000 MHZ 0227.403_638.ICLN.1
DECLINATION (B1950)
RIGHT ASCENSION (B1950)
Pol line 1 arcsec = 1.0000E-03 JY/BEAM
Peak flux = 5.3521E-01 JY/BEAM
Levs = 5.3521E-03 * (2.000, 4.000, 6.000,
8.000, 10.00, 20.00, 40.00, 60.00, 80.00,
90.00, 99.00)

(b)

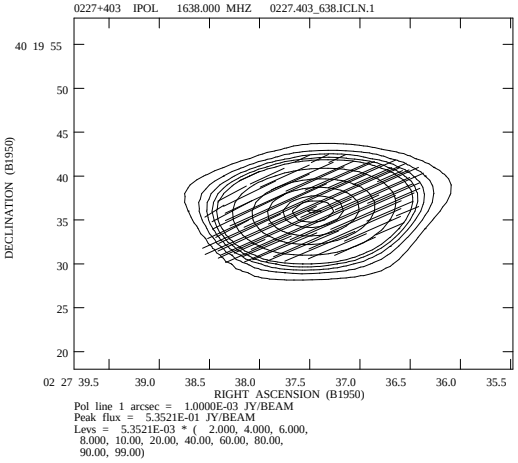
0227+403 IPOL 1638.000 MHZ 0227.403_638.ICLN.1
DECLINATION (B1950)
RIGHT ASCENSION (B1950)
Pol line 1 arcsec = 1.0000E-03 JY/BEAM
Peak flux = 5.3521E-01 JY/BEAM
Levs = 5.3521E-03 * (2.000, 4.000, 6.000,
8.000, 10.00, 20.00, 40.00, 60.00, 80.00,
90.00, 99.00)

(c)

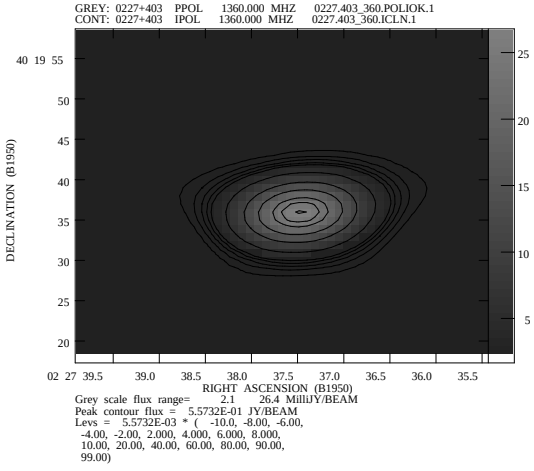
GREY: 0227+403 PPOL 1360.000 MHZ 0227.403_360.POLIOK.1
CONT: 0227+403 IPOL 1360.000 MHZ 0227.403_360.ICLN.1
DECLINATION (B1950)
RIGHT ASCENSION (B1950)
Grey scale flux range= 2.1 26.4 MilliJY/BEAM
Peak contour flux = 5.5732E-01 JY/BEAM
Levs = 5.5732E-03 * (-10.0, -8.00, -6.00,
-4.00, -2.00, 2.000, 4.000, 6.000, 8.000,
10.00, 20.00, 40.00, 60.00, 80.00, 90.00,
99.00)

(d)

Figure 4-22. Maps of the source 0228+344. Panels (a) through (c) show the total intensity contours of the source along with the polarization position angles. The positive total intensity contours are 2, 4, 6, 8, 10, 20, 40, 60, 80, 90 and 99 percent of the peak intensity. The position angle of the vectors are that of the polarization position angles, and the lengths of the vectors are proportional to the polarized intensity. The position angles plotted are: (a) 1360 MHz ; (b) 1638 MHz; (c) $\chi_{1360} - \chi_{1638}$. In panel (d) the linear polarization intensity is plotted in grayscale on the contours of the total intensity.

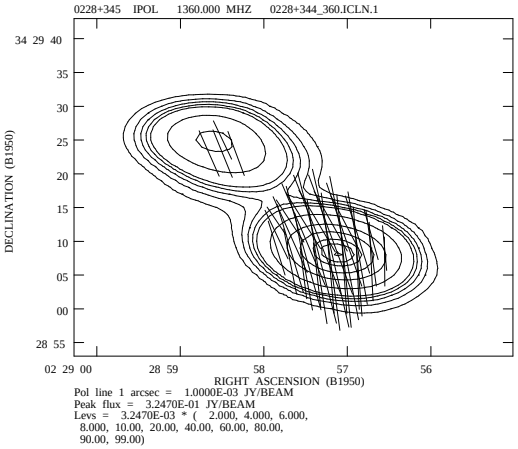
0228+345 IPOL 1360.000 MHZ 0228+344_360.ICLN.1
DECLINATION (B1950)
RIGHT ASCENSION (B1950)
Pol line 1 arcsec = 1.0000E-03 JY/BEAM
Peak flux = 3.2470E-01 JY/BEAM
Levs = 3.2470E-03 * (2.000, 4.000, 6.000,
8.000, 10.00, 20.00, 40.00, 60.00, 80.00,
90.00, 99.00)

(a)

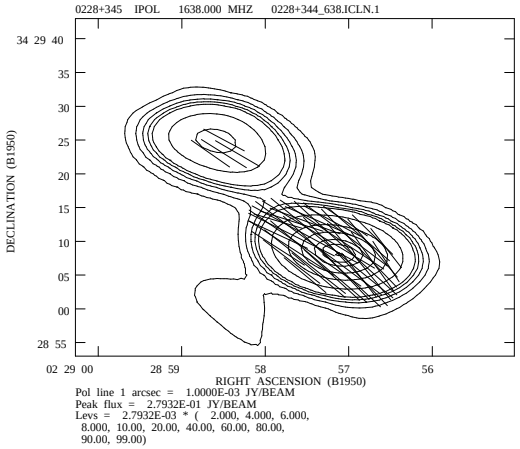
0228+345 IPOL 1638.000 MHZ 0228+344_638.ICLN.1
DECLINATION (B1950)
RIGHT ASCENSION (B1950)
Pol line 1 arcsec = 1.0000E-03 JY/BEAM
Peak flux = 2.7932E-01 JY/BEAM
Levs = 2.7932E-03 * (2.000, 4.000, 6.000,
8.000, 10.00, 20.00, 40.00, 60.00, 80.00,
90.00, 99.00)

(b)

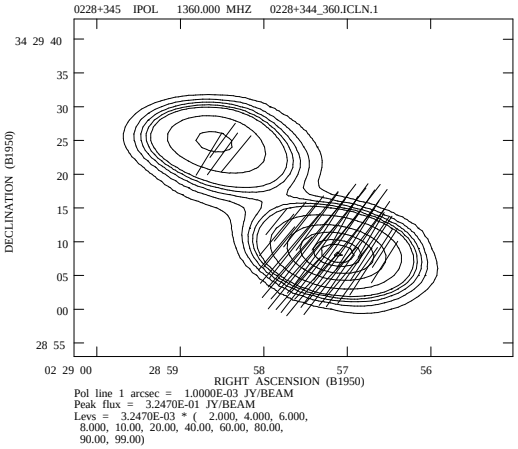
0228+345 IPOL 1360.000 MHZ 0228+344_360.ICLN.1
DECLINATION (B1950)
RIGHT ASCENSION (B1950)
Pol line 1 arcsec = 1.0000E-03 JY/BEAM
Peak flux = 3.2470E-01 JY/BEAM
Levs = 3.2470E-03 * (2.000, 4.000, 6.000,
8.000, 10.00, 20.00, 40.00, 60.00, 80.00,
90.00, 99.00)

(c)

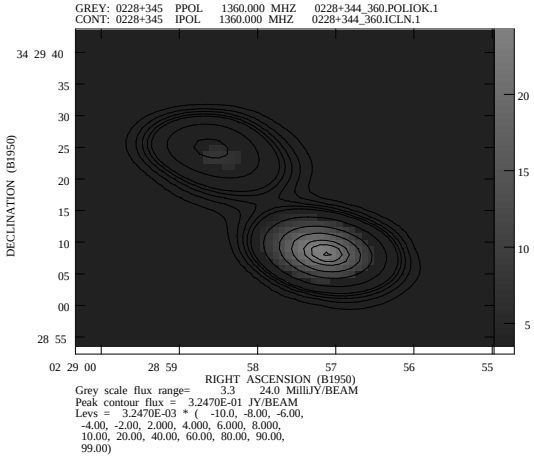
GREY: 0228+345 PPOL 1360.000 MHZ 0228+344_360.POLIOK.1
CONT: 0228+345 IPOL 1360.000 MHZ 0228+344_360.ICLN.1
DECLINATION (B1950)
RIGHT ASCENSION (B1950)
Grey scale flux range= 3.3 24.0 MilliJY/BEAM
Peak contour flux = 3.2470E-01 JY/BEAM
Levs = 3.2470E-03 * (-10.0, -8.00, -6.00,
-4.00, -2.00, 2.000, 4.000, 6.000, 8.000,
10.00, 20.00, 40.00, 60.00, 80.00, 90.00,
99.00)

(d)

Figure 4-23. Maps of the source 0228+393. Panels (a) through (c) show the total intensity contours of the source along with the polarization position angles. The positive total intensity contours are 2, 4, 6, 8, 10, 20, 40, 60, 80, 90 and 99 percent of the peak intensity. The position angle of the vectors are that of the polarization position angles, and the lengths of the vectors are proportional to the polarized intensity. The position angles plotted are: (a) 1360 MHz ; (b) 1638 MHz; (c) $\chi_{1360} - \chi_{1638}$. In panel (d) the linear polarization intensity is plotted in grayscale on the contours of the total intensity.

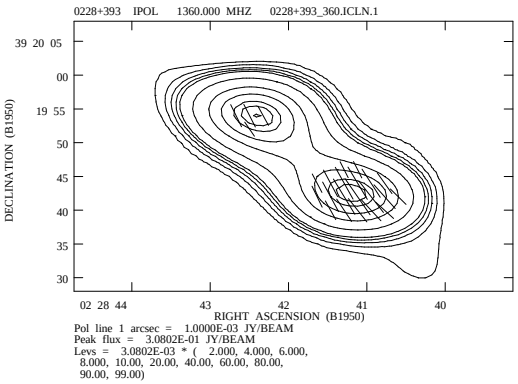
0228+393 IPOL 1360.000 MHZ 0228+393_360.ICLN.1
39 20 05
00
19 55
50
45
40
35
30
DECLINATION (B1950)
02 28 44
43
42
41
40
RIGHT ASCENSION (B1950)
Pol line 1 arcsec = 1.0000E-03 JY/BEAM
Peak flux = 3.0802E-01 JY/BEAM
Levs = 3.0802E-03 * (2.000, 4.000, 6.000,
8.000, 10.00, 20.00, 40.00, 60.00, 80.00,
90.00, 99.00)

(a)

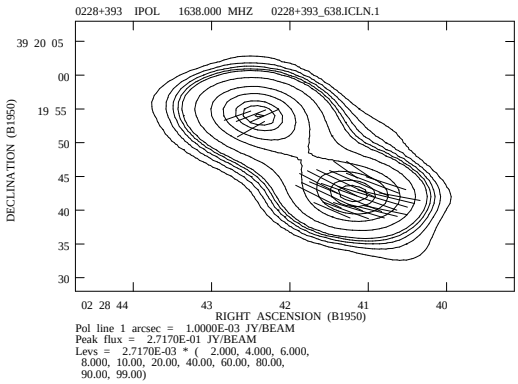
0228+393 IPOL 1638.000 MHZ 0228+393_638.ICLN.1
39 20 05
00
19 55
50
45
40
35
30
DECLINATION (B1950)
02 28 44
43
42
41
40
RIGHT ASCENSION (B1950)
Pol line 1 arcsec = 1.0000E-03 JY/BEAM
Peak flux = 2.7170E-01 JY/BEAM
Levs = 2.7170E-03 * (2.000, 4.000, 6.000,
8.000, 10.00, 20.00, 40.00, 60.00, 80.00,
90.00, 99.00)

(b)

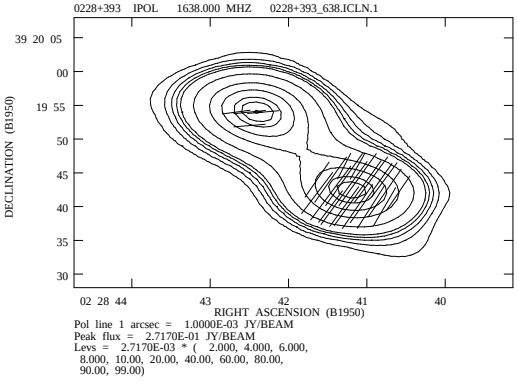
0228+393 IPOL 1638.000 MHZ 0228+393_638.ICLN.1
39 20 05
00
19 55
50
45
40
35
30
DECLINATION (B1950)
02 28 44
43
42
41
40
RIGHT ASCENSION (B1950)
Pol line 1 arcsec = 1.0000E-03 JY/BEAM
Peak flux = 2.7170E-01 JY/BEAM
Levs = 2.7170E-03 * (2.000, 4.000, 6.000,
8.000, 10.00, 20.00, 40.00, 60.00, 80.00,
90.00, 99.00)

(c)

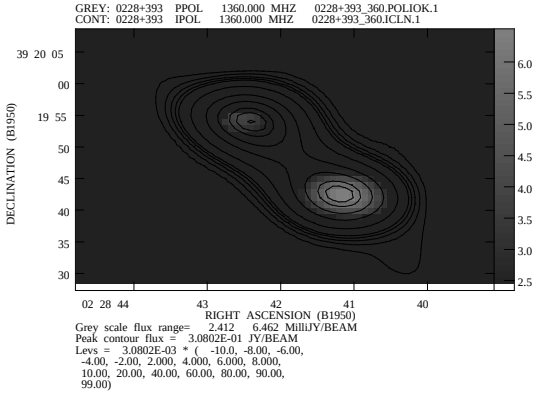
GREY: 0228+393 PPOL 1360.000 MHZ 0228+393_360.POLIOK.1
CONT: 0228+393 IPOL 1360.000 MHZ 0228+393_360.ICLN.1
39 20 05
00
19 55
50
45
40
35
30
DECLINATION (B1950)
6.0
5.5
5.0
4.5
4.0
3.5
3.0
2.5
02 28 44
43
42
41
40
RIGHT ASCENSION (B1950)
Grey scale flux range= 2.412 6.462 MilliJY/BEAM
Peak contour flux = 3.0802E-01 JY/BEAM
Levs = 3.0802E-03 * (-10.0, -8.00, -6.00,
-4.00, -2.00, 2.000, 4.000, 6.000, 8.000,
10.00, 20.00, 40.00, 60.00, 80.00, 90.00,
99.00)

(d)

Figure 4-24. Maps of the source 0228+409. Panels (a) through (c) show the total intensity contours of the source along with the polarization position angles. The positive total intensity contours are 2, 4, 6, 8, 10, 20, 40, 60, 80, 90 and 99 percent of the peak intensity. The position angle of the vectors are that of the polarization position angles, and the lengths of the vectors are proportional to the polarized intensity. The position angles plotted are: (a) 1360 MHz ; (b) 1638 MHz; (c) $\chi_{1360} - \chi_{1638}$. In panel (d) the linear polarization intensity is plotted in grayscale on the contours of the total intensity.

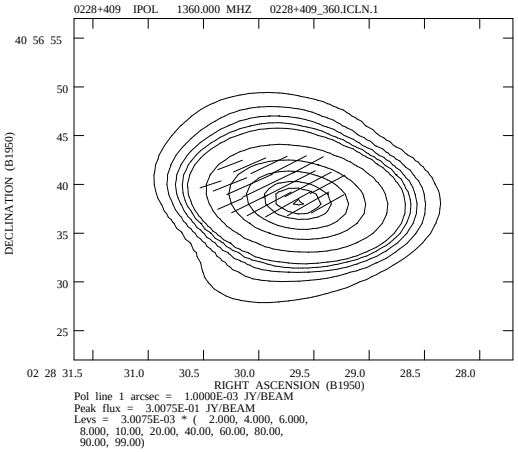
0228+409 IPOL 1360.000 MHZ 0228+409_360.ICLN.1
DECLINATION (B1950)
RIGHT ASCENSION (B1950)
Pol line 1 arcsec = 1.0000E-03 JY/BEAM
Peak flux = 3.0075E-01 JY/BEAM
Levs = 3.0075E-03 * (2.000, 4.000, 6.000,
8.000, 10.00, 20.00, 40.00, 60.00, 80.00,
90.00, 99.00)

(a)

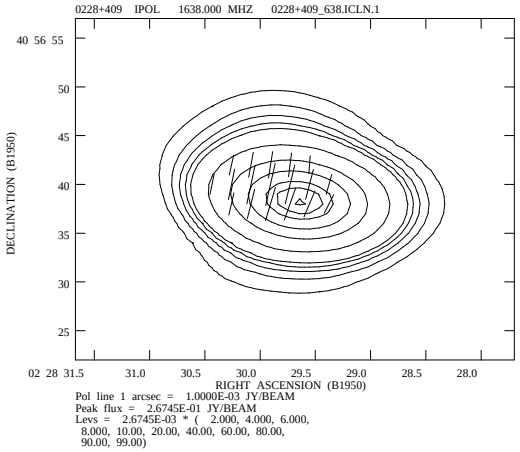
0228+409 IPOL 1638.000 MHZ 0228+409_638.ICLN.1
DECLINATION (B1950)
RIGHT ASCENSION (B1950)
Pol line 1 arcsec = 1.0000E-03 JY/BEAM
Peak flux = 2.6745E-01 JY/BEAM
Levs = 2.6745E-03 * (2.000, 4.000, 6.000,
8.000, 10.00, 20.00, 40.00, 60.00, 80.00,
90.00, 99.00)

(b)

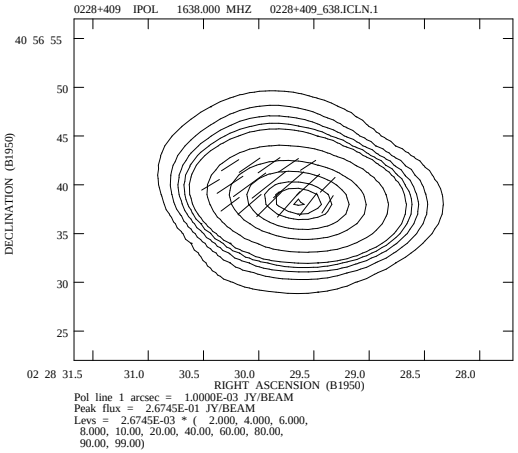
0228+409 IPOL 1638.000 MHZ 0228+409_638.ICLN.1
DECLINATION (B1950)
RIGHT ASCENSION (B1950)
Pol line 1 arcsec = 1.0000E-03 JY/BEAM
Peak flux = 2.6745E-01 JY/BEAM
Levs = 2.6745E-03 * (2.000, 4.000, 6.000,
8.000, 10.00, 20.00, 40.00, 60.00, 80.00,
90.00, 99.00)

(c)

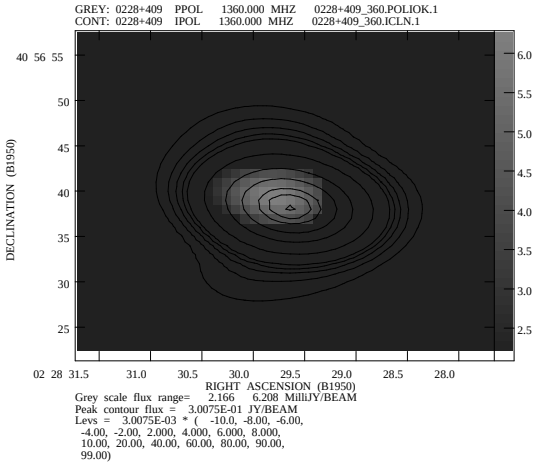
GREY: 0228+409 PPOL 1360.000 MHZ 0228+409_360.POLIOK.1
CONT: 0228+409 IPOL 1360.000 MHZ 0228+409_360.ICLN.1
DECLINATION (B1950)
RIGHT ASCENSION (B1950)
Grey scale flux range= 2.166 6.208 MilliJY/BEAM
Peak contour flux = 3.0075E-01 JY/BEAM
Levs = 3.0075E-03 * (-10.0, -8.00, -6.00,
-4.00, -2.00, 2.000, 4.000, 6.000, 8.000,
10.00, 20.00, 40.00, 60.00, 80.00, 90.00,
99.00)

(d)

Figure 4-25. Maps of the source 0229+341. Panels (a) through (c) show the total intensity contours of the source along with the polarization position angles. The positive total intensity contours are 2, 4, 6, 8, 10, 20, 40, 60, 80, 90 and 99 percent of the peak intensity. The position angle of the vectors are that of the polarization position angles, and the lengths of the vectors are proportional to the polarized intensity. The position angles plotted are: (a) 1360 MHz ; (b) 1638 MHz; (c) $\chi_{1360} - \chi_{1638}$. In panel (d) the linear polarization intensity is plotted in grayscale on the contours of the total intensity.

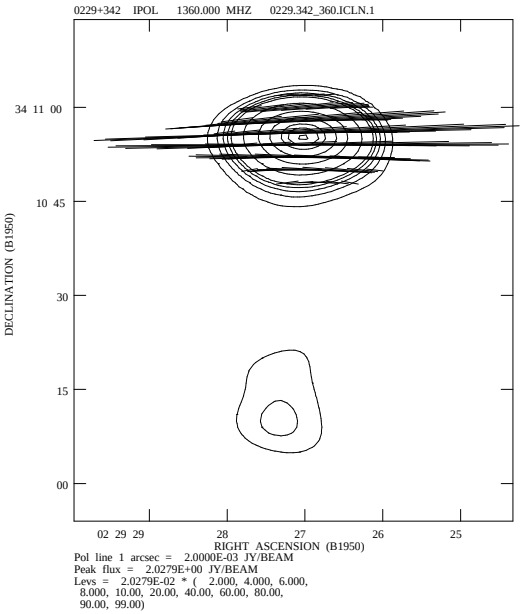
0229+342 IPOL 1360.000 MHZ 0229.342_360.ICLN.1
34 11 00
10 45
30
15
00
DECLINATION (B1950)
02 29 29
28
27
26
25
RIGHT ASCENSION (B1950)
Pol line 1 arcsec = 2.0000E-03 JY/BEAM
Peak flux = 2.0279E+00 JY/BEAM
Levs = 2.0279E-02 * (2.000, 4.000, 6.000,
8.000, 10.00, 20.00, 40.00, 60.00, 80.00,
90.00, 99.00)

(a)

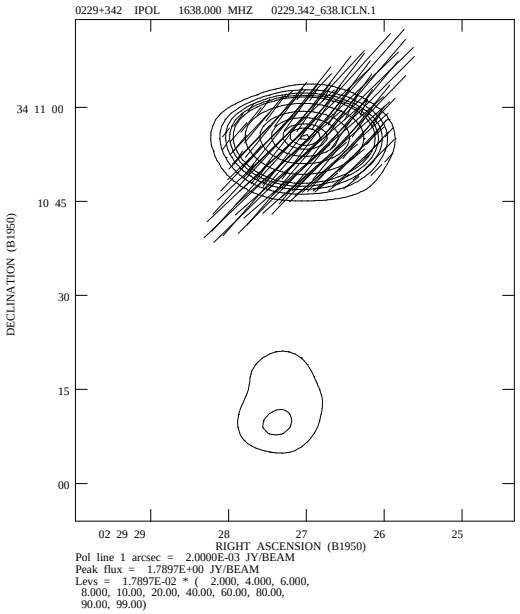
0229+342 IPOL 1638.000 MHZ 0229.342_638.ICLN.1
34 11 00
10 45
30
15
00
DECLINATION (B1950)
02 29 29
28
27
26
25
RIGHT ASCENSION (B1950)
Pol line 1 arcsec = 2.0000E-03 JY/BEAM
Peak flux = 1.7897E+00 JY/BEAM
Levs = 1.7897E-02 * (2.000, 4.000, 6.000,
8.000, 10.00, 20.00, 40.00, 60.00, 80.00,
90.00, 99.00)

(b)

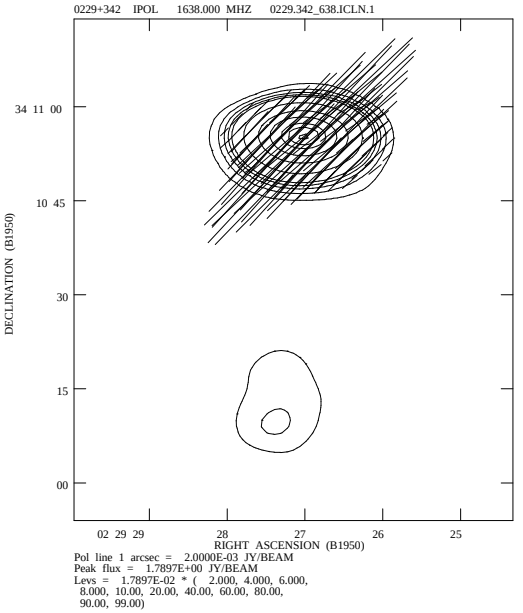
0229+342 IPOL 1638.000 MHZ 0229.342_638.ICLN.1
34 11 00
10 45
30
15
00
DECLINATION (B1950)
02 29 29
28
27
26
25
RIGHT ASCENSION (B1950)
Pol line 1 arcsec = 2.0000E-03 JY/BEAM
Peak flux = 1.7897E+00 JY/BEAM
Levs = 1.7897E-02 * (2.000, 4.000, 6.000,
8.000, 10.00, 20.00, 40.00, 60.00, 80.00,
90.00, 99.00)

(c)

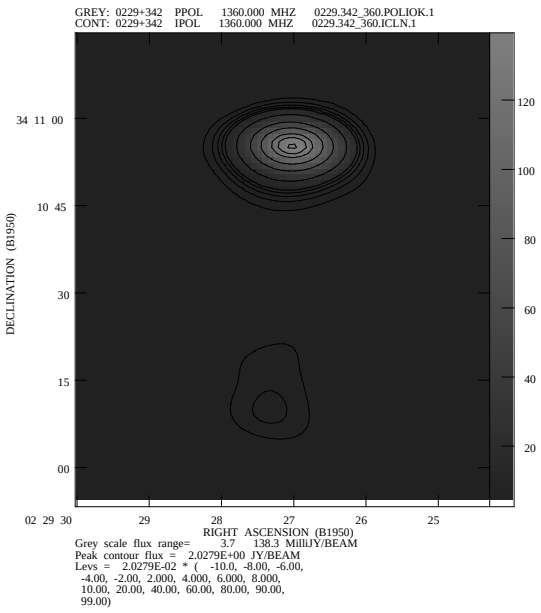
GREY: 0229+342 PPOL 1360.000 MHZ 0229.342_360.POLIOK.1
CONT: 0229+342 IPOL 1360.000 MHZ 0229.342_360.ICLN.1
34 11 00
10 45
30
15
00
DECLINATION (B1950)
02 29 30
29
28
27
26
25
RIGHT ASCENSION (B1950)
120
100
80
60
40
20
Grey scale flux range= 3.7 138.3 MilliJY/BEAM
Peak contour flux = 2.0279E+00 JY/BEAM
Levs = 2.0279E-02 * (-10.0, -8.00, -6.00,
-4.00, -2.00, 2.000, 4.000, 6.000, 8.000,
10.00, 20.00, 40.00, 60.00, 80.00, 90.00,
99.00)

(d)

Figure 4-26. Maps of the source 0229+352. Panels (a) through (c) show the total intensity contours of the source along with the polarization position angles. The positive total intensity contours are 2, 4, 6, 8, 10, 20, 40, 60, 80, 90 and 99 percent of the peak intensity. The position angle of the vectors are that of the polarization position angles, and the lengths of the vectors are proportional to the polarized intensity. The position angles plotted are: (a) 1360 MHz ; (b) 1638 MHz; (c) $\chi_{1360} - \chi_{1638}$. In panel (d) the linear polarization intensity is plotted in grayscale on the contours of the total intensity.

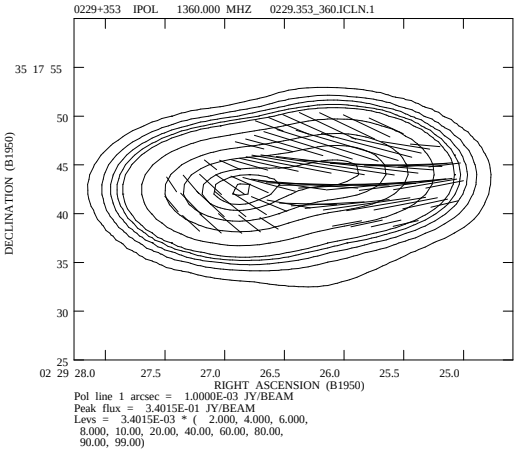
0229+353 IPOL 1360.000 MHZ 0229.353_360.ICLN.1
35 17 55
50
45
40
35
30
25
DECLINATION (B1950)
02 29 28.0 27.5 27.0 26.5 26.0 25.5 25.0
RIGHT ASCENSION (B1950)
Pol line 1 arcsec = 1.0000E-03 JY/BEAM
Peak flux = 3.4015E-01 JY/BEAM
Levs = 3.4015E-03 * (2.000, 4.000, 6.000,
8.000, 10.00, 20.00, 40.00, 60.00, 80.00,
90.00, 99.00)

(a)

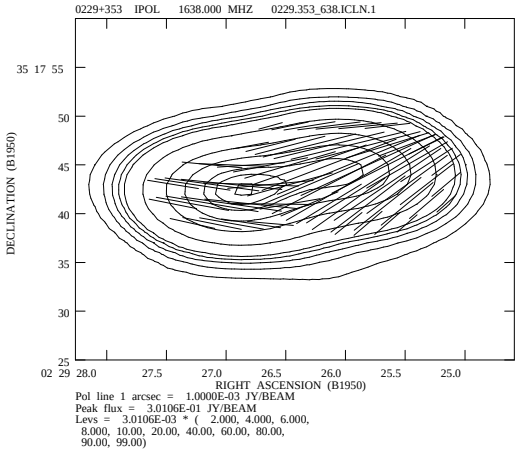
0229+353 IPOL 1638.000 MHZ 0229.353_638.ICLN.1
35 17 55
50
45
40
35
30
25
DECLINATION (B1950)
02 29 28.0 27.5 27.0 26.5 26.0 25.5 25.0
RIGHT ASCENSION (B1950)
Pol line 1 arcsec = 1.0000E-03 JY/BEAM
Peak flux = 3.0106E-01 JY/BEAM
Levs = 3.0106E-03 * (2.000, 4.000, 6.000,
8.000, 10.00, 20.00, 40.00, 60.00, 80.00,
90.00, 99.00)

(b)

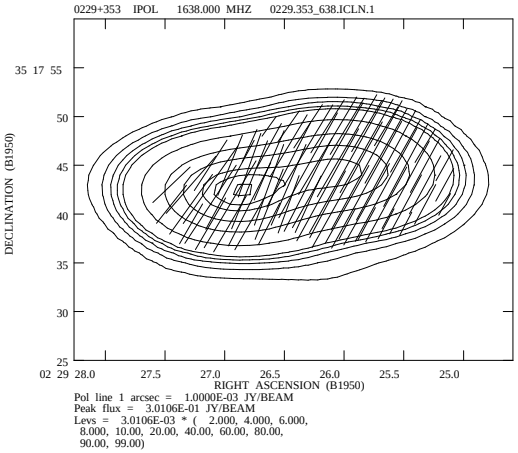
0229+353 IPOL 1638.000 MHZ 0229.353_638.ICLN.1
35 17 55
50
45
40
35
30
25
DECLINATION (B1950)
02 29 28.0 27.5 27.0 26.5 26.0 25.5 25.0
RIGHT ASCENSION (B1950)
Pol line 1 arcsec = 1.0000E-03 JY/BEAM
Peak flux = 3.0106E-01 JY/BEAM
Levs = 3.0106E-03 * (2.000, 4.000, 6.000,
8.000, 10.00, 20.00, 40.00, 60.00, 80.00,
90.00, 99.00)

(c)

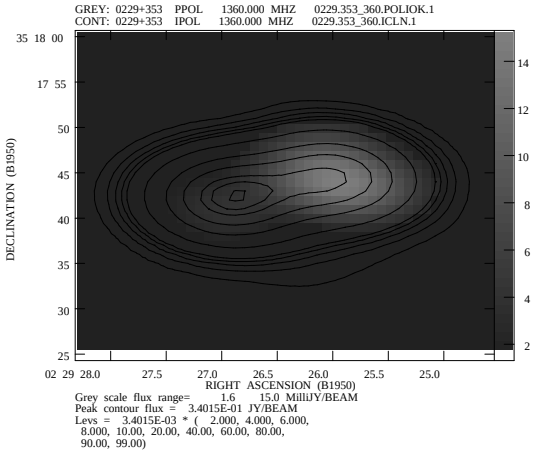
GREY: 0229+353 PPOL 1360.000 MHZ 0229.353_360.POLIOK.1
CONT: 0229+353 IPOL 1360.000 MHZ 0229.353_360.ICLN.1
35 18 00
17 55
50
45
40
35
30
25
DECLINATION (B1950)
14
12
10
8
6
4
2
02 29 28.0 27.5 27.0 26.5 26.0 25.5 25.0
RIGHT ASCENSION (B1950)
Grey scale flux range= 1.6 15.0 MilliJY/BEAM
Peak contour flux = 3.4015E-01 JY/BEAM
Levs = 3.4015E-03 * (2.000, 4.000, 6.000,
8.000, 10.00, 20.00, 40.00, 60.00, 80.00,
90.00, 99.00)

(d)

Figure 4-27. Maps of the source 0231+385. Panels (a) through (c) show the total intensity contours of the source along with the polarization position angles. The positive total intensity contours are 2, 4, 6, 8, 10, 20, 40, 60, 80, 90 and 99 percent of the peak intensity. The position angle of the vectors are that of the polarization position angles, and the lengths of the vectors are proportional to the polarized intensity. The position angles plotted are: (a) 1360 MHz ; (b) 1638 MHz; (c) $\chi_{1360} - \chi_{1638}$. In panel (d) the linear polarization intensity is plotted in grayscale on the contours of the total intensity.

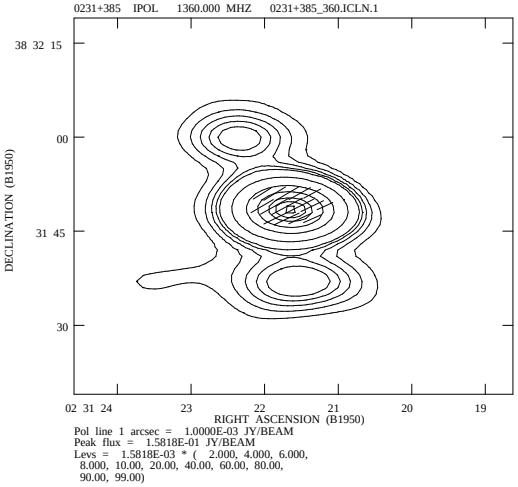
0231+385 IPOL 1360.000 MHZ 0231+385_360.ICLN.1
38 32 15
00
31 45
30
DECLINATION (B1950)
02 31 24
23
22
21
20
19
RIGHT ASCENSION (B1950)
Pol line 1 arcsec = 1.0000E-03 JY/BEAM
Peak flux = 1.5818E-01 JY/BEAM
Levs = 1.5818E-03 * (2.000, 4.000, 6.000,
8.000, 10.00, 20.00, 40.00, 60.00, 80.00,
90.00, 99.00)

(a)

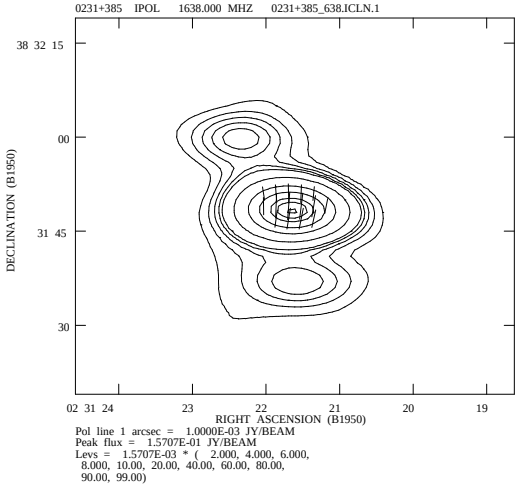
0231+385 IPOL 1638.000 MHZ 0231+385_638.ICLN.1
38 32 15
00
31 45
30
DECLINATION (B1950)
02 31 24
23
22
21
20
19
RIGHT ASCENSION (B1950)
Pol line 1 arcsec = 1.0000E-03 JY/BEAM
Peak flux = 1.5707E-01 JY/BEAM
Levs = 1.5707E-03 * (2.000, 4.000, 6.000,
8.000, 10.00, 20.00, 40.00, 60.00, 80.00,
90.00, 99.00)

(b)

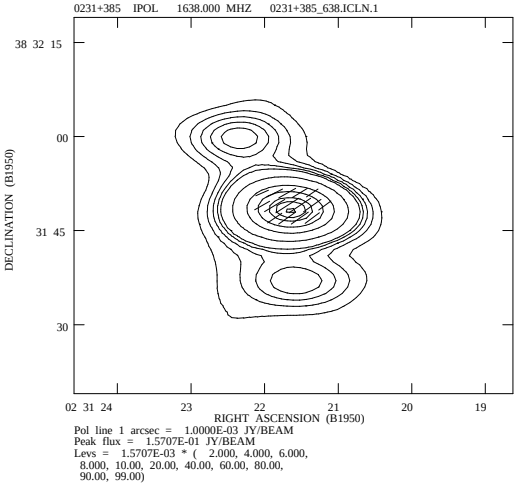
0231+385 IPOL 1638.000 MHZ 0231+385_638.ICLN.1
38 32 15
00
31 45
30
DECLINATION (B1950)
02 31 24
23
22
21
20
19
RIGHT ASCENSION (B1950)
Pol line 1 arcsec = 1.0000E-03 JY/BEAM
Peak flux = 1.5707E-01 JY/BEAM
Levs = 1.5707E-03 * (2.000, 4.000, 6.000,
8.000, 10.00, 20.00, 40.00, 60.00, 80.00,
90.00, 99.00)

(c)

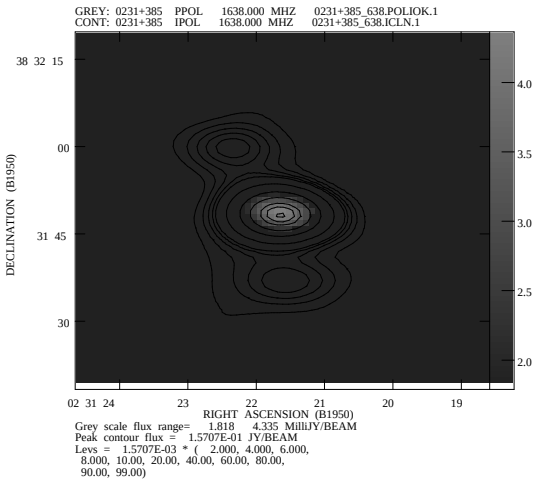
GREY: 0231+385 PPOL 1638.000 MHZ 0231+385_638.POLIOK.1
CONT: 0231+385 IPOL 1638.000 MHZ 0231+385_638.ICLN.1
38 32 15
00
31 45
30
DECLINATION (B1950)
4.0
3.5
3.0
2.5
2.0
02 31 24
23
22
21
20
19
RIGHT ASCENSION (B1950)
Grey scale flux range= 1.818 4.335 MilliJY/BEAM
Peak contour flux = 1.5707E-01 JY/BEAM
Levs = 1.5707E-03 * (2.000, 4.000, 6.000,
8.000, 10.00, 20.00, 40.00, 60.00, 80.00,
90.00, 99.00)

(d)

Figure 4-28. Maps of the source 0232+411. Panels (a) through (c) show the total intensity contours of the source along with the polarization position angles. The positive total intensity contours are 2, 4, 6, 8, 10, 20, 40, 60, 80, 90 and 99 percent of the peak intensity. The position angle of the vectors are that of the polarization position angles, and the lengths of the vectors are proportional to the polarized intensity. The position angles plotted are: (a) 1360 MHz ; (b) 1638 MHz; (c) $\chi_{1360} - \chi_{1638}$. In panel (d) the linear polarization intensity is plotted in grayscale on the contours of the total intensity.

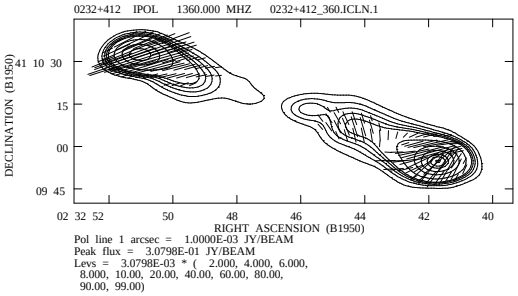
0232+412 IPOL 1360.000 MHZ 0232+412_360.ICLN.1
DECLINATION (B1950)
41 10 30
15
00
09 45
02 32 52
50
48
46
44
42
40
RIGHT ASCENSION (B1950)
Pol line 1 arcsec = 1.0000E-03 JY/BEAM
Peak flux = 3.0798E-01 JY/BEAM
Levs = 3.0798E-03 * (2.000, 4.000, 6.000,
8.000, 10.00, 20.00, 40.00, 60.00, 80.00,
90.00, 99.00)

(a)

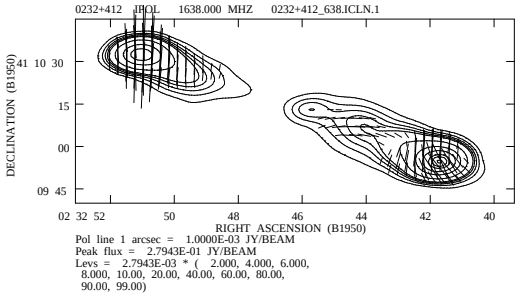
0232+412 IPOL 1638.000 MHZ 0232+412_638.ICLN.1
DECLINATION (B1950)
41 10 30
15
00
09 45
02 32 52
50
48
46
44
42
40
RIGHT ASCENSION (B1950)
Pol line 1 arcsec = 1.0000E-03 JY/BEAM
Peak flux = 2.7943E-01 JY/BEAM
Levs = 2.7943E-03 * (2.000, 4.000, 6.000,
8.000, 10.00, 20.00, 40.00, 60.00, 80.00,
90.00, 99.00)

(b)

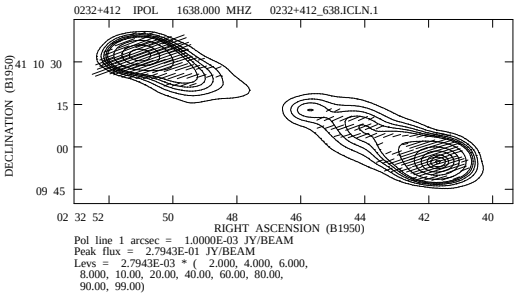
0232+412 IPOL 1638.000 MHZ 0232+412_638.ICLN.1
DECLINATION (B1950)
41 10 30
15
00
09 45
02 32 52
50
48
46
44
42
40
RIGHT ASCENSION (B1950)
Pol line 1 arcsec = 1.0000E-03 JY/BEAM
Peak flux = 2.7943E-01 JY/BEAM
Levs = 2.7943E-03 * (2.000, 4.000, 6.000,
8.000, 10.00, 20.00, 40.00, 60.00, 80.00,
90.00, 99.00)

(c)

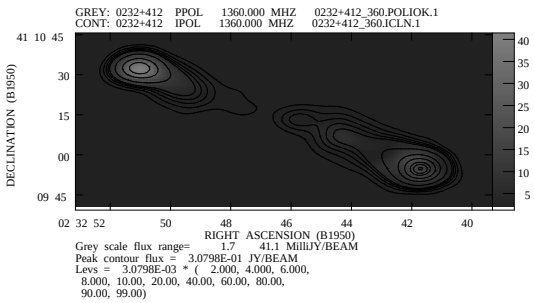
GREY: 0232+412 PPOL 1360.000 MHZ 0232+412_360.POLIOK.1
CONT: 0232+412 IPOL 1360.000 MHZ 0232+412_360.ICLN.1
DECLINATION (B1950)
41 10 45
30
15
00
09 45
02 32 52
50
48
46
44
42
40
RIGHT ASCENSION (B1950)
40
35
30
25
20
15
10
5
Grey scale flux range= 1.7 41.1 MilliJY/BEAM
Peak contour flux = 3.0798E-01 JY/BEAM
Levs = 3.0798E-03 * (2.000, 4.000, 6.000,
8.000, 10.00, 20.00, 40.00, 60.00, 80.00,
90.00, 99.00)

(d)

Figure 4-29. Maps of the source 0241+393. Panels (a) through (c) show the total intensity contours of the source along with the polarization position angles. The positive total intensity contours are 2, 4, 6, 8, 10, 20, 40, 60, 80, 90 and 99 percent of the peak intensity. The position angle of the vectors are that of the polarization position angles, and the lengths of the vectors are proportional to the polarized intensity. The position angles plotted are: (a) 1360 MHz ; (b) 1638 MHz; (c) $\chi_{1360} - \chi_{1638}$. In panel (d) the linear polarization intensity is plotted in grayscale on the contours of the total intensity.

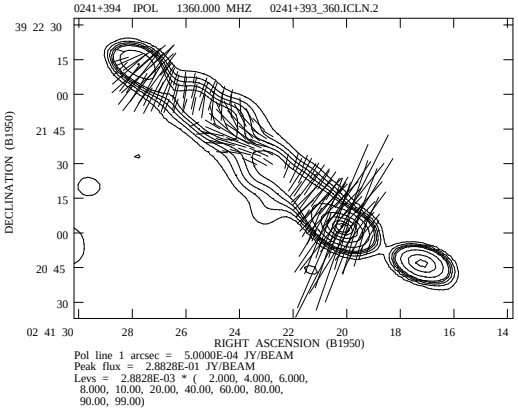
0241+394 IPOL 1360.000 MHZ 0241+393_360.ICLN.2
DECLINATION (B1950)
RIGHT ASCENSION (B1950)
Pol line 1 arcsec = 5.0000E-04 JY/BEAM
Peak flux = 2.8828E-01 JY/BEAM
Levs = 2.8828E-03 * (2.000, 4.000, 6.000,
8.000, 10.00, 20.00, 40.00, 60.00, 80.00,
90.00, 99.00)

(a)

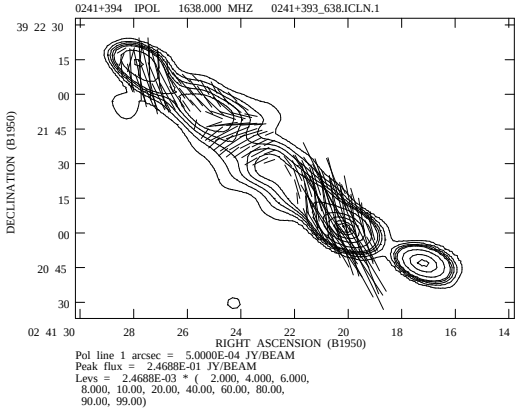
0241+394 IPOL 1638.000 MHZ 0241+393_638.ICLN.1
DECLINATION (B1950)
RIGHT ASCENSION (B1950)
Pol line 1 arcsec = 5.0000E-04 JY/BEAM
Peak flux = 2.4688E-01 JY/BEAM
Levs = 2.4688E-03 * (2.000, 4.000, 6.000,
8.000, 10.00, 20.00, 40.00, 60.00, 80.00,
90.00, 99.00)

(b)

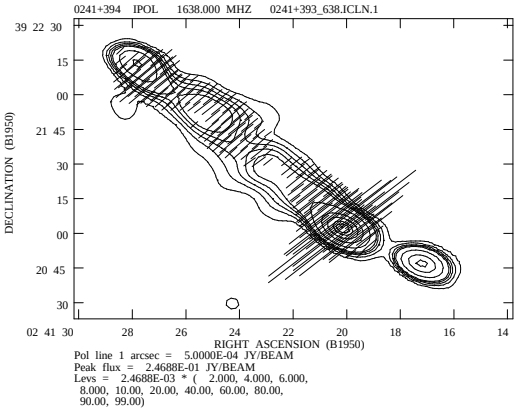
0241+394 IPOL 1638.000 MHZ 0241+393_638.ICLN.1
DECLINATION (B1950)
RIGHT ASCENSION (B1950)
Pol line 1 arcsec = 5.0000E-04 JY/BEAM
Peak flux = 2.4688E-01 JY/BEAM
Levs = 2.4688E-03 * (2.000, 4.000, 6.000,
8.000, 10.00, 20.00, 40.00, 60.00, 80.00,
90.00, 99.00)

(c)

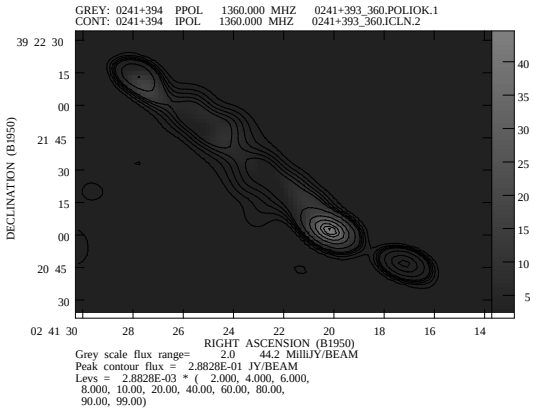
GREY: 0241+394 PPOL 1360.000 MHZ 0241+393_360.POLIOK.1
CONT: 0241+394 IPOL 1360.000 MHZ 0241+393_360.ICLN.2
DECLINATION (B1950)
RIGHT ASCENSION (B1950)
Grey scale flux range= 2.0 44.2 MilliJY/BEAM
Peak contour flux = 2.8828E-01 JY/BEAM
Levs = 2.8828E-03 * (2.000, 4.000, 6.000,
8.000, 10.00, 20.00, 40.00, 60.00, 80.00,
90.00, 99.00)

(d)

Figure 4-30. Maps of the source 0244+377. Panels (a) through (c) show the total intensity contours of the source along with the polarization position angles. The positive total intensity contours are 2, 4, 6, 8, 10, 20, 40, 60, 80, 90 and 99 percent of the peak intensity. The position angle of the vectors are that of the polarization position angles, and the lengths of the vectors are proportional to the polarized intensity. The position angles plotted are: (a) 1360 MHz ; (b) 1638 MHz; (c) $\chi_{1360} - \chi_{1638}$. In panel (d) the linear polarization intensity is plotted in grayscale on the contours of the total intensity.

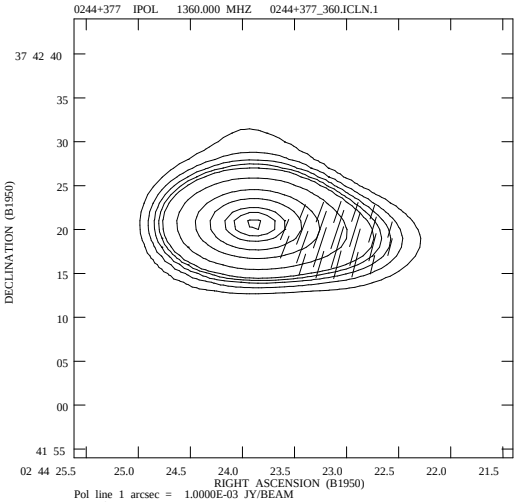
0244+377 IPOL 1360.000 MHZ 0244+377_360.ICLN.1
37 42 40
35
30
25
20
15
10
05
00
41 55
DECLINATION (B1950)
02 44 25.5
25.0
24.5
24.0
23.5
23.0
22.5
22.0
21.5
RIGHT ASCENSION (B1950)
Pol line 1 arcsec = 1.0000E-03 JY/BEAM
Peak flux = 5.8534E-01 JY/BEAM
Levs = 5.8534E-03 * (2.000, 4.000, 6.000,
8.000, 10.00, 20.00, 40.00, 60.00, 80.00,
90.00, 99.00)

(a)

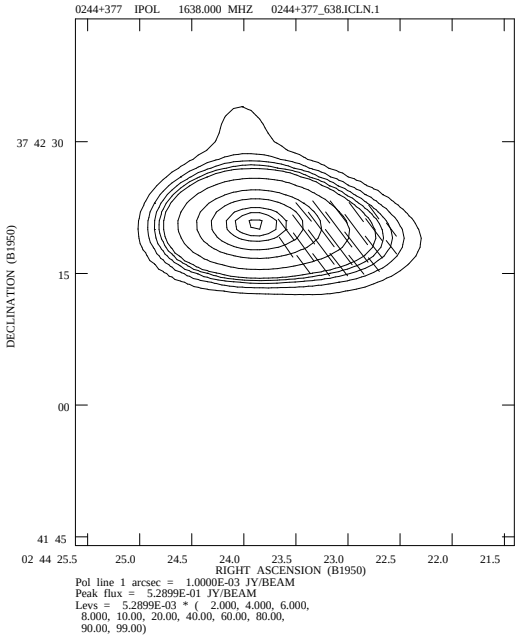
0244+377 IPOL 1638.000 MHZ 0244+377_638.ICLN.1
37 42 30
15
00
41 45
DECLINATION (B1950)
02 44 25.5
25.0
24.5
24.0
23.5
23.0
22.5
22.0
21.5
RIGHT ASCENSION (B1950)
Pol line 1 arcsec = 1.0000E-03 JY/BEAM
Peak flux = 5.2899E-01 JY/BEAM
Levs = 5.2899E-03 * (2.000, 4.000, 6.000,
8.000, 10.00, 20.00, 40.00, 60.00, 80.00,
90.00, 99.00)

(b)

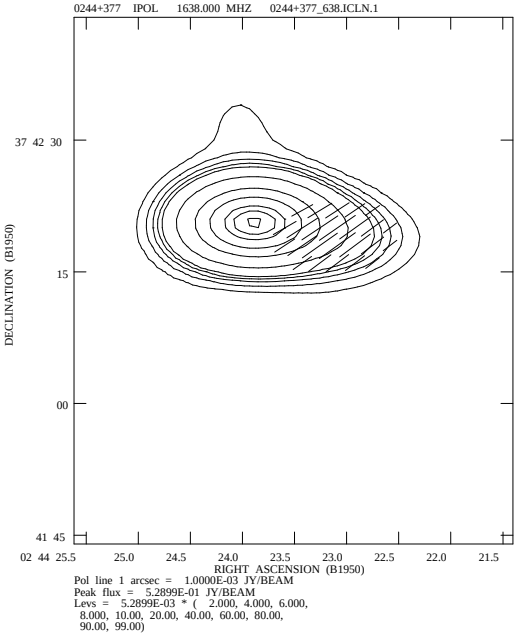
0244+377 IPOL 1638.000 MHZ 0244+377_638.ICLN.1
37 42 30
15
00
41 45
DECLINATION (B1950)
02 44 25.5
25.0
24.5
24.0
23.5
23.0
22.5
22.0
21.5
RIGHT ASCENSION (B1950)
Pol line 1 arcsec = 1.0000E-03 JY/BEAM
Peak flux = 5.2899E-01 JY/BEAM
Levs = 5.2899E-03 * (2.000, 4.000, 6.000,
8.000, 10.00, 20.00, 40.00, 60.00, 80.00,
90.00, 99.00)

(c)

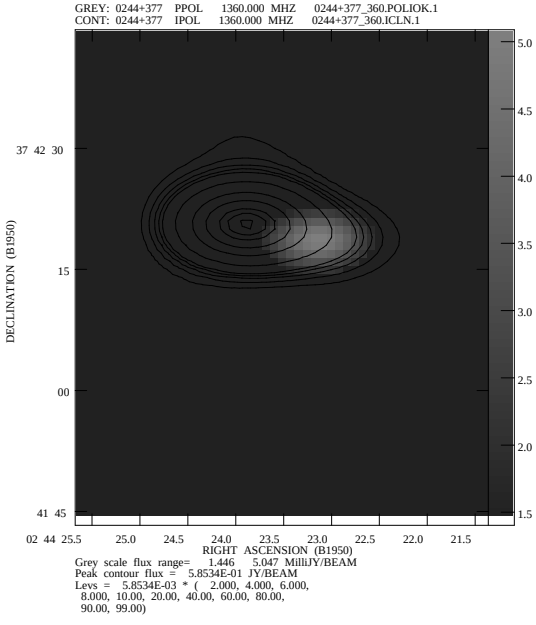
GREY: 0244+377 PPOL 1360.000 MHZ 0244+377_360.POLIOK.1
CONT: 0244+377 IPOL 1360.000 MHZ 0244+377_360.ICLN.1
37 42 30
15
00
41 45
DECLINATION (B1950)
02 44 25.5
25.0
24.5
24.0
23.5
23.0
22.5
22.0
21.5
RIGHT ASCENSION (B1950)
5.0
4.5
4.0
3.5
3.0
2.5
2.0
1.5
Grey scale flux range= 1.446 5.047 MilliJY/BEAM
Peak contour flux = 5.8534E-01 JY/BEAM
Levs = 5.8534E-03 * (2.000, 4.000, 6.000,
8.000, 10.00, 20.00, 40.00, 60.00, 80.00,
90.00, 99.00)

(d)

Figure 4-31. Maps of the source 0246+392. Panels (a) through (c) show the total intensity contours of the source along with the polarization position angles. The positive total intensity contours are 2, 4, 6, 8, 10, 20, 40, 60, 80, 90 and 99 percent of the peak intensity. The position angle of the vectors are that of the polarization position angles, and the lengths of the vectors are proportional to the polarized intensity. The position angles plotted are: (a) 1360 MHz ; (b) 1638 MHz; (c) $\chi_{1360} - \chi_{1638}$. In panel (d) the linear polarization intensity is plotted in grayscale on the contours of the total intensity.

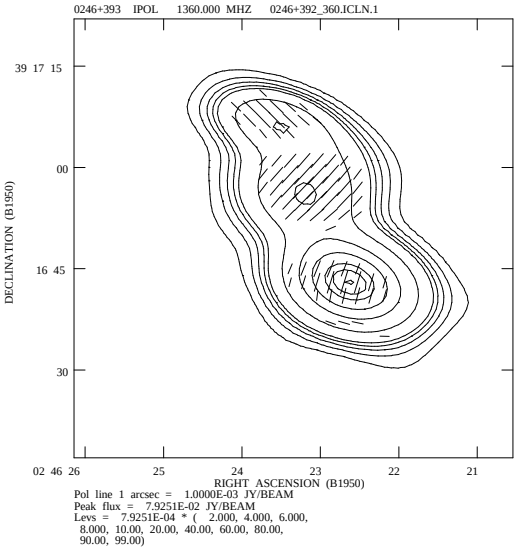
0246+393 IPOL 1360.000 MHZ 0246+392_360.ICLN.1
39 17 15
00
16 45
30
DECLINATION (B1950)
02 46 26
25
24
23
22
21
RIGHT ASCENSION (B1950)
Pol line 1 arcsec = 1.0000E-03 JY/BEAM
Peak flux = 7.9251E-02 JY/BEAM
Levs = 7.9251E-04 * (2.000, 4.000, 6.000,
8.000, 10.00, 20.00, 40.00, 60.00, 80.00,
90.00, 99.00)

(a)

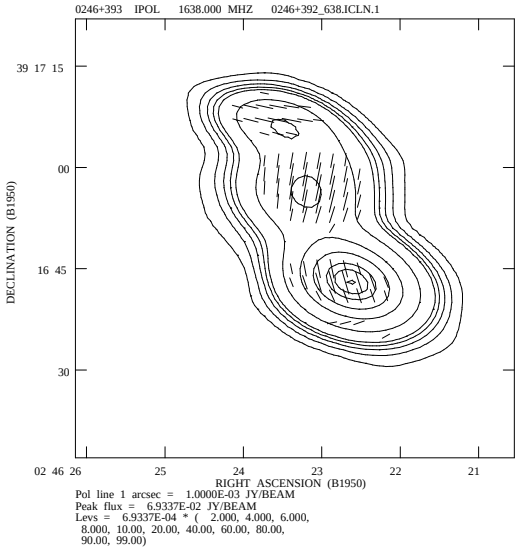
0246+393 IPOL 1638.000 MHZ 0246+392_638.ICLN.1
39 17 15
00
16 45
30
DECLINATION (B1950)
02 46 26
25
24
23
22
21
RIGHT ASCENSION (B1950)
Pol line 1 arcsec = 1.0000E-03 JY/BEAM
Peak flux = 6.9337E-02 JY/BEAM
Levs = 6.9337E-04 * (2.000, 4.000, 6.000,
8.000, 10.00, 20.00, 40.00, 60.00, 80.00,
90.00, 99.00)

(b)

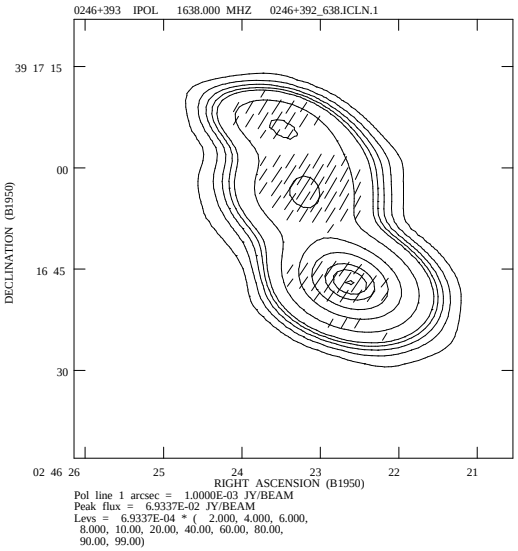
0246+393 IPOL 1638.000 MHZ 0246+392_638.ICLN.1
39 17 15
00
16 45
30
DECLINATION (B1950)
02 46 26
25
24
23
22
21
RIGHT ASCENSION (B1950)
Pol line 1 arcsec = 1.0000E-03 JY/BEAM
Peak flux = 6.9337E-02 JY/BEAM
Levs = 6.9337E-04 * (2.000, 4.000, 6.000,
8.000, 10.00, 20.00, 40.00, 60.00, 80.00,
90.00, 99.00)

(c)

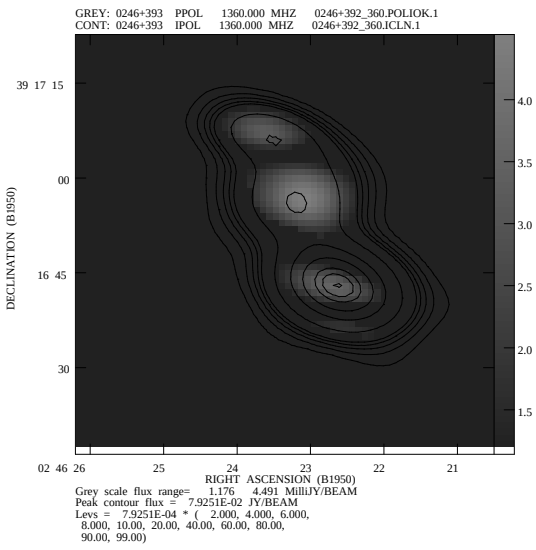
GREY: 0246+393 PPOL 1360.000 MHZ 0246+392_360.POLIOK.1
CONT: 0246+393 IPOL 1360.000 MHZ 0246+392_360.ICLN.1
39 17 15
00
16 45
30
DECLINATION (B1950)
4.0
3.5
3.0
2.5
2.0
1.5
02 46 26
25
24
23
22
21
RIGHT ASCENSION (B1950)
Grey scale flux range= 1.176 4.491 MilliJY/BEAM
Peak contour flux = 7.9251E-02 JY/BEAM
Levs = 7.9251E-04 * (2.000, 4.000, 6.000,
8.000, 10.00, 20.00, 40.00, 60.00, 80.00,
90.00, 99.00)

(d)

Figure 4-32. Maps of the source 0247+393. Panels (a) through (c) show the total intensity contours of the source along with the polarization position angles. The positive total intensity contours are 2, 4, 6, 8, 10, 20, 40, 60, 80, 90 and 99 percent of the peak intensity. The position angle of the vectors are that of the polarization position angles, and the lengths of the vectors are proportional to the polarized intensity. The position angles plotted are: (a) 1360 MHz ; (b) 1638 MHz; (c) $\chi_{1360} - \chi_{1638}$. In panel (d) the linear polarization intensity is plotted in grayscale on the contours of the total intensity.

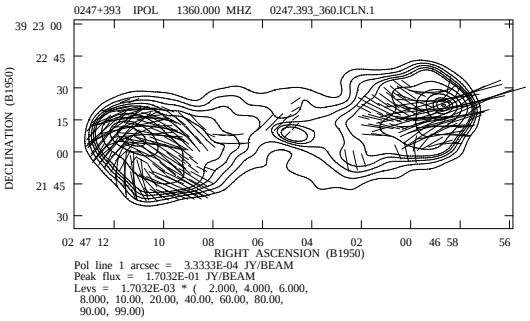
0247+393 IPOL 1360.000 MHZ 0247.393_360.ICLN.1
DECLINATION (B1950)
RIGHT ASCENSION (B1950)
Pol line 1 arcsec = 3.3333E-04 JY/BEAM
Peak flux = 1.7032E-01 JY/BEAM
Levs = 1.7032E-03 * (2.000, 4.000, 6.000,
8.000, 10.00, 20.00, 40.00, 60.00, 80.00,
90.00, 99.00)

(a)

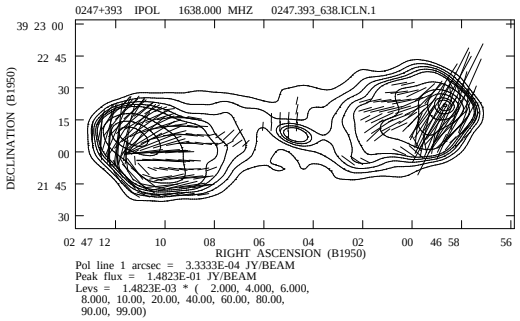
0247+393 IPOL 1638.000 MHZ 0247.393_638.ICLN.1
DECLINATION (B1950)
RIGHT ASCENSION (B1950)
Pol line 1 arcsec = 3.3333E-04 JY/BEAM
Peak flux = 1.4823E-01 JY/BEAM
Levs = 1.4823E-03 * (2.000, 4.000, 6.000,
8.000, 10.00, 20.00, 40.00, 60.00, 80.00,
90.00, 99.00)

(b)

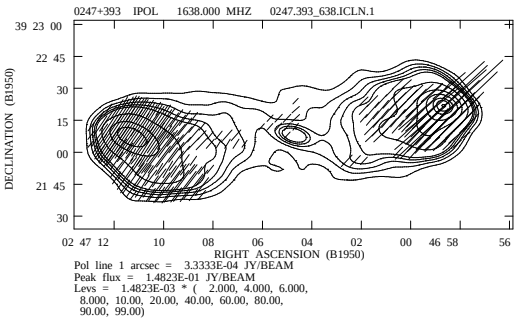
0247+393 IPOL 1638.000 MHZ 0247.393_638.ICLN.1
DECLINATION (B1950)
RIGHT ASCENSION (B1950)
Pol line 1 arcsec = 3.3333E-04 JY/BEAM
Peak flux = 1.4823E-01 JY/BEAM
Levs = 1.4823E-03 * (2.000, 4.000, 6.000,
8.000, 10.00, 20.00, 40.00, 60.00, 80.00,
90.00, 99.00)

(c)

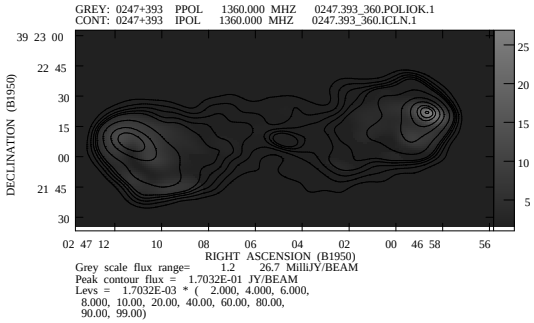
GREY: 0247+393 PPOL 1360.000 MHZ 0247.393_360.POLIOK.1
CONT: 0247+393 IPOL 1360.000 MHZ 0247.393_360.ICLN.1
DECLINATION (B1950)
RIGHT ASCENSION (B1950)
Grey scale flux range= 1.2 26.7 MilliJY/BEAM
Peak contour flux = 1.7032E-01 JY/BEAM
Levs = 1.7032E-03 * (2.000, 4.000, 6.000,
8.000, 10.00, 20.00, 40.00, 60.00, 80.00,
90.00, 99.00)

(d)

Figure 4-33. Maps of the source 0247+404. Panels (a) through (c) show the total intensity contours of the source along with the polarization position angles. The positive total intensity contours are 2, 4, 6, 8, 10, 20, 40, 60, 80, 90 and 99 percent of the peak intensity. The position angle of the vectors are that of the polarization position angles, and the lengths of the vectors are proportional to the polarized intensity. The position angles plotted are: (a) 1360 MHz ; (b) 1638 MHz; (c) $\chi_{1360} - \chi_{1638}$. In panel (d) the linear polarization intensity is plotted in grayscale on the contours of the total intensity.

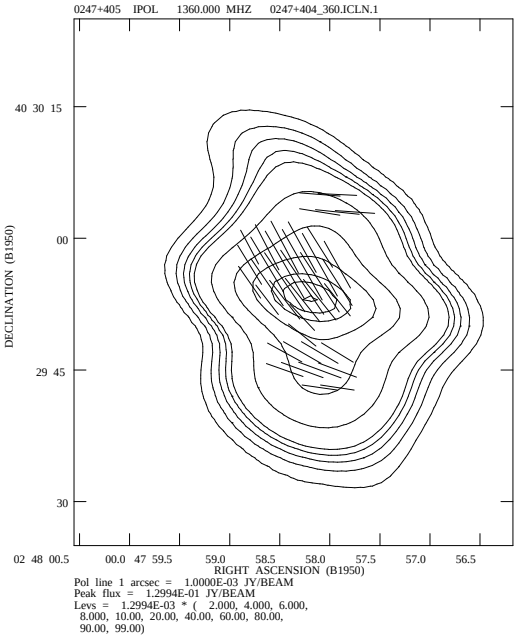
0247+405 IPOL 1360.000 MHZ 0247+404_360.ICLN.1
40 30 15
00
29 45
30
DECLINATION (B1950)
02 48 00.5
00.0 47 59.5 59.0 58.5 58.0 57.5 57.0 56.5
RIGHT ASCENSION (B1950)
Pol line 1 arcsec = 1.0000E-03 JY/BEAM
Peak flux = 1.2994E-01 JY/BEAM
Levs = 1.2994E-03 * (2.000, 4.000, 6.000,
8.000, 10.00, 20.00, 40.00, 60.00, 80.00,
90.00, 99.00)

(a)

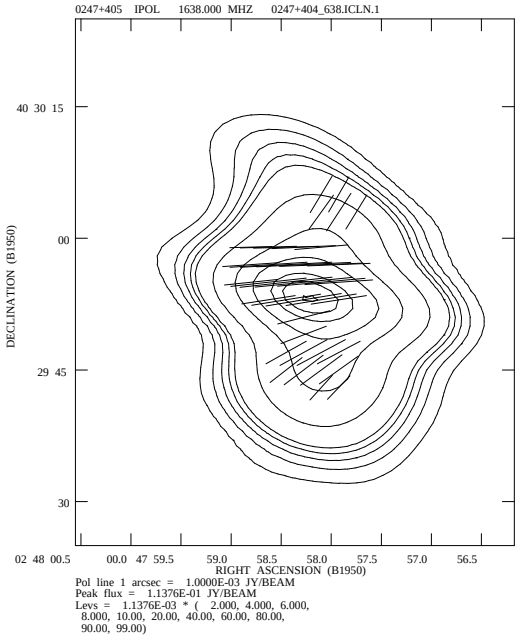
0247+405 IPOL 1638.000 MHZ 0247+404_638.ICLN.1
40 30 15
00
29 45
30
DECLINATION (B1950)
02 48 00.5
00.0 47 59.5 59.0 58.5 58.0 57.5 57.0 56.5
RIGHT ASCENSION (B1950)
Pol line 1 arcsec = 1.0000E-03 JY/BEAM
Peak flux = 1.1376E-01 JY/BEAM
Levs = 1.1376E-03 * (2.000, 4.000, 6.000,
8.000, 10.00, 20.00, 40.00, 60.00, 80.00,
90.00, 99.00)

(b)

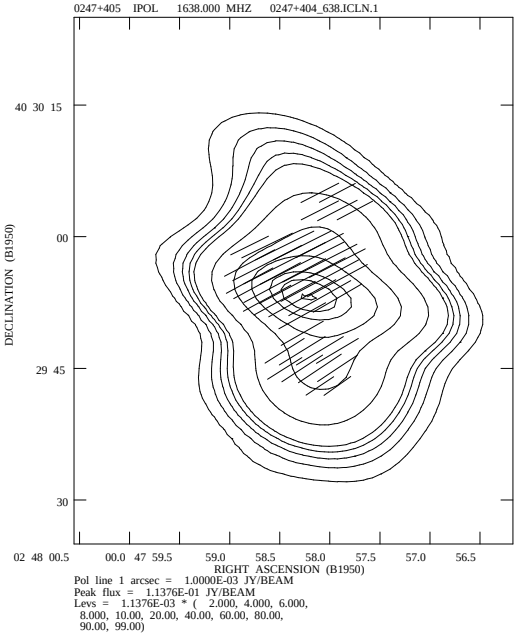
0247+405 IPOL 1638.000 MHZ 0247+404_638.ICLN.1
40 30 15
00
29 45
30
DECLINATION (B1950)
02 48 00.5
00.0 47 59.5 59.0 58.5 58.0 57.5 57.0 56.5
RIGHT ASCENSION (B1950)
Pol line 1 arcsec = 1.0000E-03 JY/BEAM
Peak flux = 1.1376E-01 JY/BEAM
Levs = 1.1376E-03 * (2.000, 4.000, 6.000,
8.000, 10.00, 20.00, 40.00, 60.00, 80.00,
90.00, 99.00)

(c)

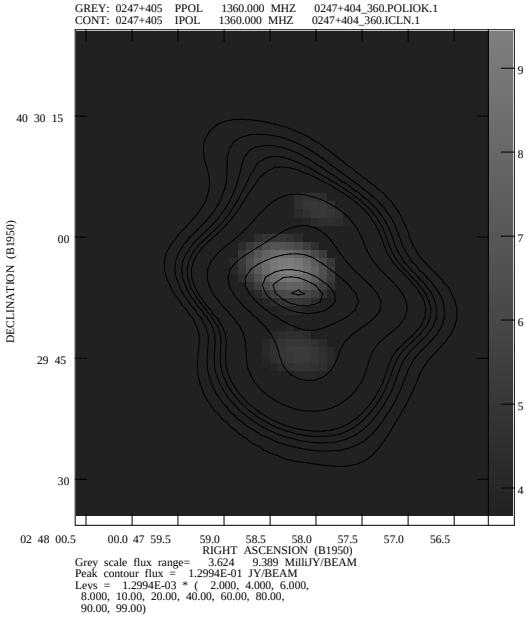
GREY: 0247+405 PPOL 1360.000 MHZ 0247+404_360.POLIOK.1
CONT: 0247+405 IPOL 1360.000 MHZ 0247+404_360.ICLN.1
40 30 15
00
29 45
30
DECLINATION (B1950)
02 48 00.5
00.0 47 59.5 59.0 58.5 58.0 57.5 57.0 56.5
RIGHT ASCENSION (B1950)
9
8
7
6
5
4
Grey scale flux range= 3.624 9.389 MilliJY/BEAM
Peak contour flux = 1.2994E-01 JY/BEAM
Levs = 1.2994E-03 * (2.000, 4.000, 6.000,
8.000, 10.00, 20.00, 40.00, 60.00, 80.00,
90.00, 99.00)

(d)

Figure 4-34. Maps of the source 0250+358. Panels (a) through (c) show the total intensity contours of the source along with the polarization position angles. The positive total intensity contours are 2, 4, 6, 8, 10, 20, 40, 60, 80, 90 and 99 percent of the peak intensity. The position angle of the vectors are that of the polarization position angles, and the lengths of the vectors are proportional to the polarized intensity. The position angles plotted are: (a) 1360 MHz ; (b) 1638 MHz; (c) $\chi_{1360} - \chi_{1638}$. In panel (d) the linear polarization intensity is plotted in grayscale on the contours of the total intensity.

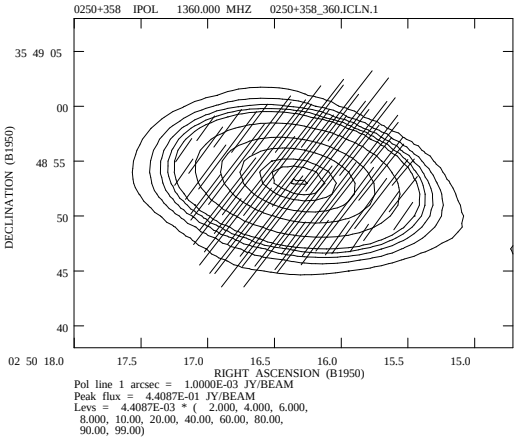
0250+358 IPOL 1360.000 MHZ 0250+358_360.ICLN.1
35 49 05
00
48 55
50
45
40
DECLINATION (B1950)
02 50 18.0
17.5
17.0
16.5
16.0
15.5
15.0
RIGHT ASCENSION (B1950)
Pol line 1 arcsec = 1.0000E-03 JY/BEAM
Peak flux = 4.4087E-01 JY/BEAM
Levs = 4.4087E-03 * (2.000, 4.000, 6.000,
8.000, 10.00, 20.00, 40.00, 60.00, 80.00,
90.00, 99.00)

(a)

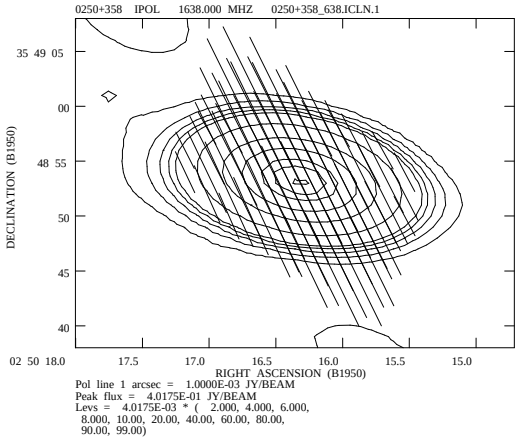
0250+358 IPOL 1638.000 MHZ 0250+358_638.ICLN.1
35 49 05
00
48 55
50
45
40
DECLINATION (B1950)
02 50 18.0
17.5
17.0
16.5
16.0
15.5
15.0
RIGHT ASCENSION (B1950)
Pol line 1 arcsec = 1.0000E-03 JY/BEAM
Peak flux = 4.0175E-01 JY/BEAM
Levs = 4.0175E-03 * (2.000, 4.000, 6.000,
8.000, 10.00, 20.00, 40.00, 60.00, 80.00,
90.00, 99.00)

(b)

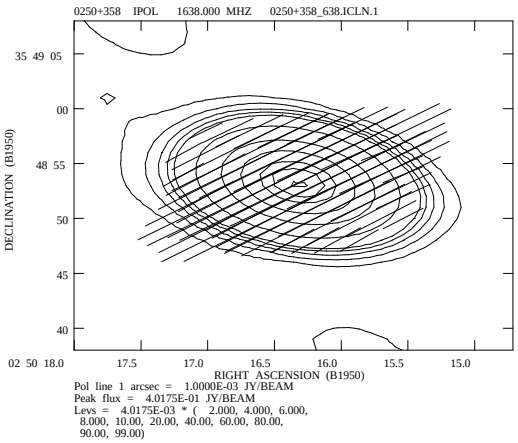
0250+358 IPOL 1638.000 MHZ 0250+358_638.ICLN.1
35 49 05
00
48 55
50
45
40
DECLINATION (B1950)
02 50 18.0
17.5
17.0
16.5
16.0
15.5
15.0
RIGHT ASCENSION (B1950)
Pol line 1 arcsec = 1.0000E-03 JY/BEAM
Peak flux = 4.0175E-01 JY/BEAM
Levs = 4.0175E-03 * (2.000, 4.000, 6.000,
8.000, 10.00, 20.00, 40.00, 60.00, 80.00,
90.00, 99.00)

(c)

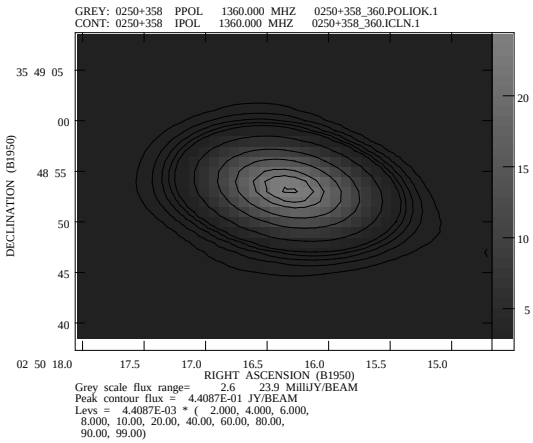
GREY: 0250+358 PPOL 1360.000 MHZ 0250+358_360.POLIOK.1
CONT: 0250+358 IPOL 1360.000 MHZ 0250+358_360.ICLN.1
35 49 05
00
48 55
50
45
40
DECLINATION (B1950)
02 50 18.0
17.5
17.0
16.5
16.0
15.5
15.0
RIGHT ASCENSION (B1950)
20
15
10
5
Grey scale flux range= 2.6 23.9 MilliJY/BEAM
Peak contour flux = 4.4087E-01 JY/BEAM
Levs = 4.4087E-03 * (2.000, 4.000, 6.000,
8.000, 10.00, 20.00, 40.00, 60.00, 80.00,
90.00, 99.00)

(d)

Figure 4-35. Maps of the source 0251+393. Panels (a) through (c) show the total intensity contours of the source along with the polarization position angles. The positive total intensity contours are 2, 4, 6, 8, 10, 20, 40, 60, 80, 90 and 99 percent of the peak intensity. The position angle of the vectors are that of the polarization position angles, and the lengths of the vectors are proportional to the polarized intensity. The position angles plotted are: (a) 1360 MHz ; (b) 1638 MHz; (c) $\chi_{1360} - \chi_{1638}$. In panel (d) the linear polarization intensity is plotted in grayscale on the contours of the total intensity.

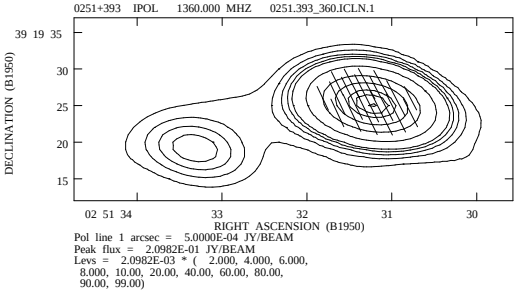
0251+393 IPOL 1360.000 MHZ 0251.393_360.ICLN.1
39 19 35
30
25
20
15
DECLINATION (B1950)
02 51 34
33
32
31
30
RIGHT ASCENSION (B1950)
Pol line 1 arcsec = 5.0000E-04 JY/BEAM
Peak flux = 2.0982E-01 JY/BEAM
Levs = 2.0982E-03 * (2.000, 4.000, 6.000,
8.000, 10.00, 20.00, 40.00, 60.00, 80.00,
90.00, 99.00)

(a)

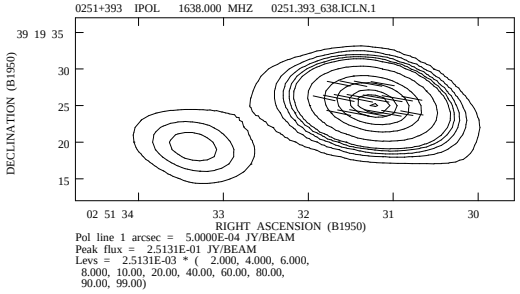
0251+393 IPOL 1638.000 MHZ 0251.393_638.ICLN.1
39 19 35
30
25
20
15
DECLINATION (B1950)
02 51 34
33
32
31
30
RIGHT ASCENSION (B1950)
Pol line 1 arcsec = 5.0000E-04 JY/BEAM
Peak flux = 2.5131E-01 JY/BEAM
Levs = 2.5131E-03 * (2.000, 4.000, 6.000,
8.000, 10.00, 20.00, 40.00, 60.00, 80.00,
90.00, 99.00)

(b)

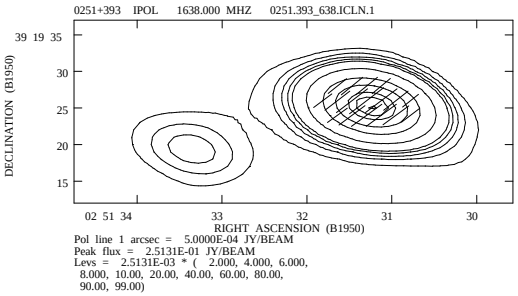
0251+393 IPOL 1638.000 MHZ 0251.393_638.ICLN.1
39 19 35
30
25
20
15
DECLINATION (B1950)
02 51 34
33
32
31
30
RIGHT ASCENSION (B1950)
Pol line 1 arcsec = 5.0000E-04 JY/BEAM
Peak flux = 2.5131E-01 JY/BEAM
Levs = 2.5131E-03 * (2.000, 4.000, 6.000,
8.000, 10.00, 20.00, 40.00, 60.00, 80.00,
90.00, 99.00)

(c)

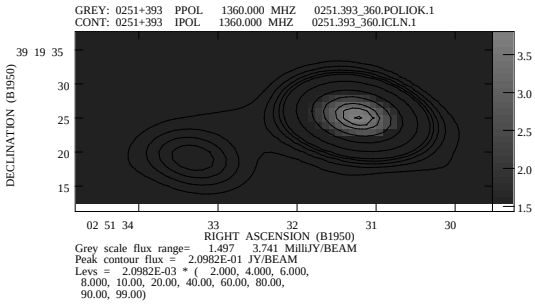
GREY: 0251+393 PPOL 1360.000 MHZ 0251.393_360.POLIOK.1
CONT: 0251+393 IPOL 1360.000 MHZ 0251.393_360.ICLN.1
39 19 35
30
25
20
15
DECLINATION (B1950)
3.5
3.0
2.5
2.0
1.5
02 51 34
33
32
31
30
RIGHT ASCENSION (B1950)
Grey scale flux range= 1.497 3.741 MilliJY/BEAM
Peak contour flux = 2.0982E-01 JY/BEAM
Levs = 2.0982E-03 * (2.000, 4.000, 6.000,
8.000, 10.00, 20.00, 40.00, 60.00, 80.00,
90.00, 99.00)

(d)

Figure 4-36. Maps of the source 0254+409. Panels (a) through (c) show the total intensity contours of the source along with the polarization position angles. The positive total intensity contours are 2, 4, 6, 8, 10, 20, 40, 60, 80, 90 and 99 percent of the peak intensity. The position angle of the vectors are that of the polarization position angles, and the lengths of the vectors are proportional to the polarized intensity. The position angles plotted are: (a) 1360 MHz ; (b) 1638 MHz; (c) $\chi_{1360} - \chi_{1638}$. In panel (d) the linear polarization intensity is plotted in grayscale on the contours of the total intensity.

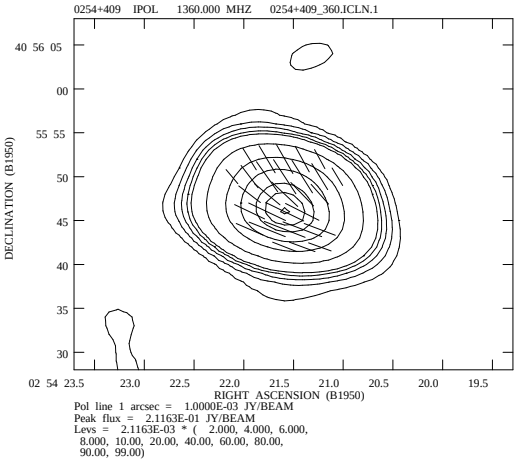
0254+409 IPOL 1360.000 MHZ 0254+409_360.ICLN.1
DECLINATION (B1950)
RIGHT ASCENSION (B1950)
Pol line 1 arcsec = 1.0000E-03 JY/BEAM
Peak flux = 2.1163E-01 JY/BEAM
Levs = 2.1163E-03 * (2.000, 4.000, 6.000,
8.000, 10.00, 20.00, 40.00, 60.00, 80.00,
90.00, 99.00)

(a)

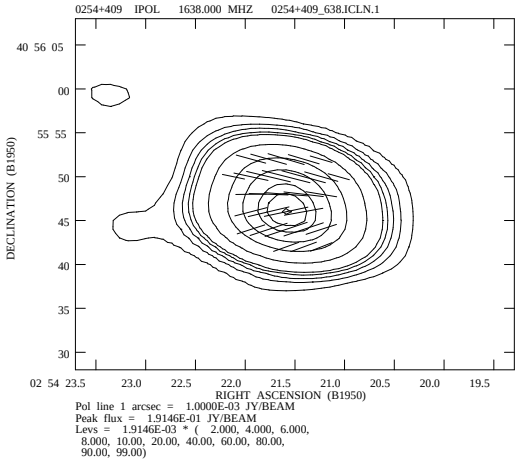
0254+409 IPOL 1638.000 MHZ 0254+409_638.ICLN.1
DECLINATION (B1950)
RIGHT ASCENSION (B1950)
Pol line 1 arcsec = 1.0000E-03 JY/BEAM
Peak flux = 1.9146E-01 JY/BEAM
Levs = 1.9146E-03 * (2.000, 4.000, 6.000,
8.000, 10.00, 20.00, 40.00, 60.00, 80.00,
90.00, 99.00)

(b)

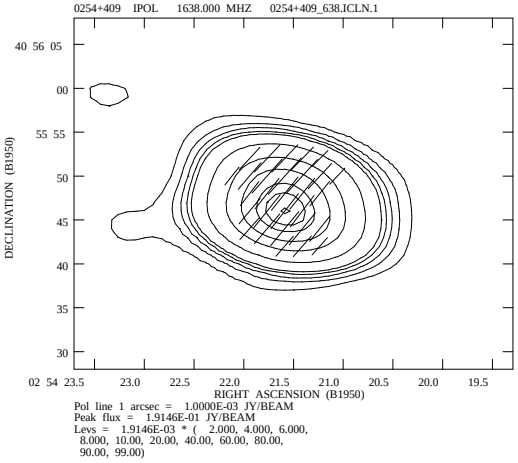
0254+409 IPOL 1638.000 MHZ 0254+409_638.ICLN.1
DECLINATION (B1950)
RIGHT ASCENSION (B1950)
Pol line 1 arcsec = 1.0000E-03 JY/BEAM
Peak flux = 1.9146E-01 JY/BEAM
Levs = 1.9146E-03 * (2.000, 4.000, 6.000,
8.000, 10.00, 20.00, 40.00, 60.00, 80.00,
90.00, 99.00)

(c)

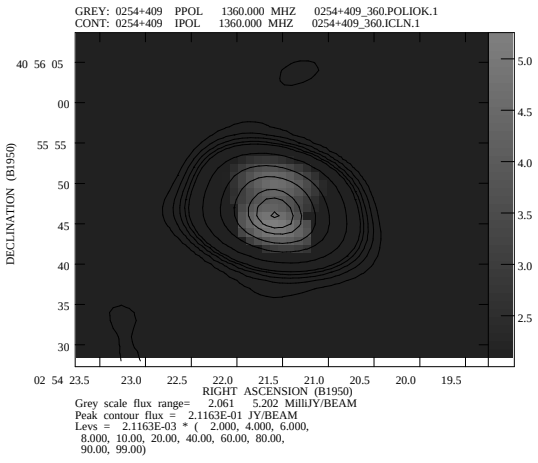
GREY: 0254+409 PPOL 1360.000 MHZ 0254+409_360.POLIOK.1
CONT: 0254+409 IPOL 1360.000 MHZ 0254+409_360.ICLN.1
DECLINATION (B1950)
RIGHT ASCENSION (B1950)
Grey scale flux range= 2.061 5.202 MilliJY/BEAM
Peak contour flux = 2.1163E-01 JY/BEAM
Levs = 2.1163E-03 * (2.000, 4.000, 6.000,
8.000, 10.00, 20.00, 40.00, 60.00, 80.00,
90.00, 99.00)

(d)

Figure 4-37. Maps of the source 0255+355. Panels (a) through (c) show the total intensity contours of the source along with the polarization position angles. The positive total intensity contours are 2, 4, 6, 8, 10, 20, 40, 60, 80, 90 and 99 percent of the peak intensity. The position angle of the vectors are that of the polarization position angles, and the lengths of the vectors are proportional to the polarized intensity. The position angles plotted are: (a) 1360 MHz ; (b) 1638 MHz; (c) $\chi_{1360} - \chi_{1638}$. In panel (d) the linear polarization intensity is plotted in grayscale on the contours of the total intensity.

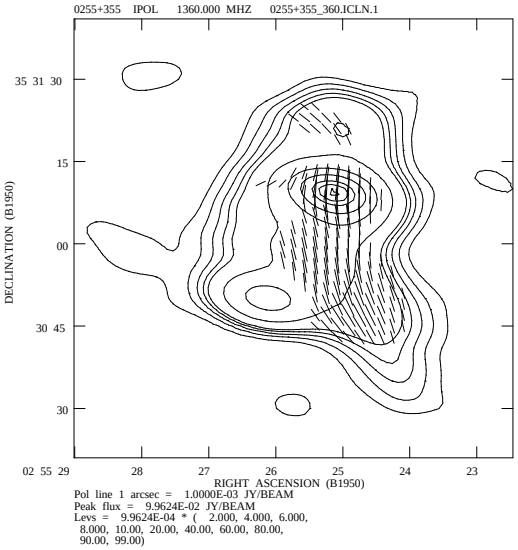
0255+355 IPOL 1360.000 MHZ 0255+355_360.ICLN.1
35 31 30
15
00
30 45
30
DECLINATION (B1950)
02 55 29
28
27
26
25
24
23
RIGHT ASCENSION (B1950)
Pol line 1 arcsec = 1.0000E-03 JY/BEAM
Peak flux = 9.9624E-02 JY/BEAM
Levs = 9.9624E-04 * (2.000, 4.000, 6.000,
8.000, 10.00, 20.00, 40.00, 60.00, 80.00,
90.00, 99.00)

(a)

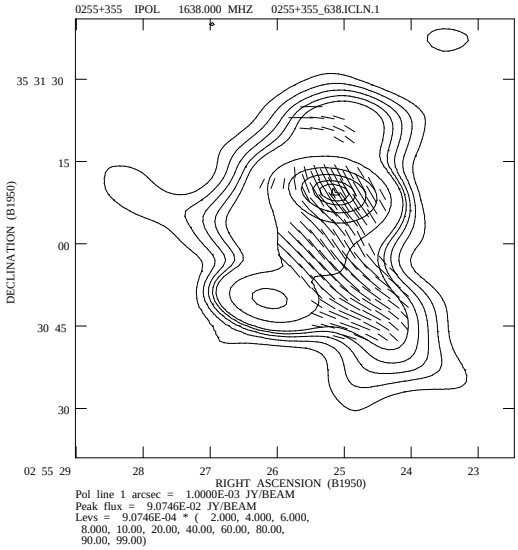
0255+355 IPOL 1638.000 MHZ 0255+355_638.ICLN.1
35 31 30
15
00
30 45
30
DECLINATION (B1950)
02 55 29
28
27
26
25
24
23
RIGHT ASCENSION (B1950)
Pol line 1 arcsec = 1.0000E-03 JY/BEAM
Peak flux = 9.0746E-02 JY/BEAM
Levs = 9.0746E-04 * (2.000, 4.000, 6.000,
8.000, 10.00, 20.00, 40.00, 60.00, 80.00,
90.00, 99.00)

(b)

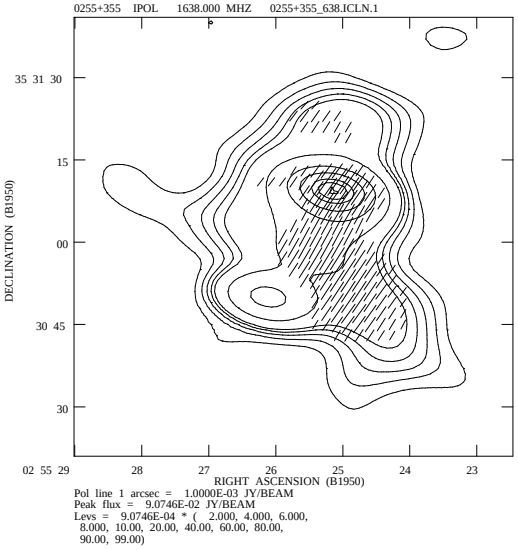
0255+355 IPOL 1638.000 MHZ 0255+355_638.ICLN.1
35 31 30
15
00
30 45
30
DECLINATION (B1950)
02 55 29
28
27
26
25
24
23
RIGHT ASCENSION (B1950)
Pol line 1 arcsec = 1.0000E-03 JY/BEAM
Peak flux = 9.0746E-02 JY/BEAM
Levs = 9.0746E-04 * (2.000, 4.000, 6.000,
8.000, 10.00, 20.00, 40.00, 60.00, 80.00,
90.00, 99.00)

(c)

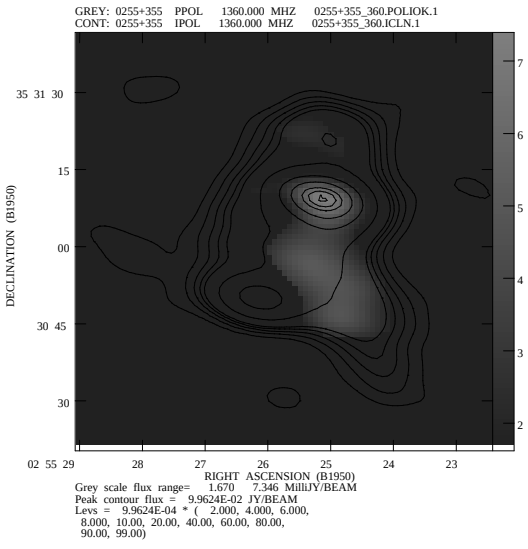
GREY: 0255+355 PPOL 1360.000 MHZ 0255+355_360.POLIOK.1
CONT: 0255+355 IPOL 1360.000 MHZ 0255+355_360.ICLN.1
35 31 30
15
00
30 45
30
DECLINATION (B1950)
02 55 29
28
27
26
25
24
23
RIGHT ASCENSION (B1950)
7
6
5
4
3
2
Grey scale flux range= 1.670 7.346 MilliJY/BEAM
Peak contour flux = 9.9624E-02 JY/BEAM
Levs = 9.9624E-04 * (2.000, 4.000, 6.000,
8.000, 10.00, 20.00, 40.00, 60.00, 80.00,
90.00, 99.00)

(d)

Figure 4-38. Maps of the source 0256+423. Panels (a) through (c) show the total intensity contours of the source along with the polarization position angles. The positive total intensity contours are 2, 4, 6, 8, 10, 20, 40, 60, 80, 90 and 99 percent of the peak intensity. The position angle of the vectors are that of the polarization position angles, and the lengths of the vectors are proportional to the polarized intensity. The position angles plotted are: (a) 1360 MHz ; (b) 1638 MHz; (c) $\chi_{1360} - \chi_{1638}$. In panel (d) the linear polarization intensity is plotted in grayscale on the contours of the total intensity.

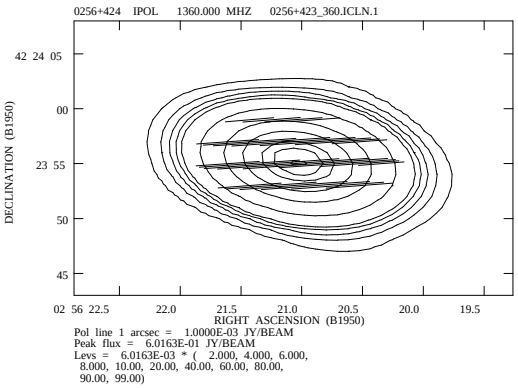
0256+424 IPOL 1360.000 MHZ 0256+423_360.ICLN.1
DECLINATION (B1950)
42 24 05
00
23 55
50
45
02 56 22.5
22.0
21.5
21.0
20.5
20.0
19.5
RIGHT ASCENSION (B1950)
Pol line 1 arcsec = 1.0000E-03 JY/BEAM
Peak flux = 6.0163E-01 JY/BEAM
Levs = 6.0163E-03 * (2.000, 4.000, 6.000,
8.000, 10.00, 20.00, 40.00, 60.00, 80.00,
90.00, 99.00)

(a)

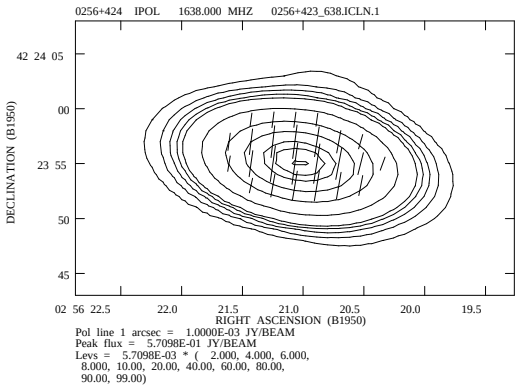
0256+424 IPOL 1638.000 MHZ 0256+423_638.ICLN.1
DECLINATION (B1950)
42 24 05
00
23 55
50
45
02 56 22.5
22.0
21.5
21.0
20.5
20.0
19.5
RIGHT ASCENSION (B1950)
Pol line 1 arcsec = 1.0000E-03 JY/BEAM
Peak flux = 5.7098E-01 JY/BEAM
Levs = 5.7098E-03 * (2.000, 4.000, 6.000,
8.000, 10.00, 20.00, 40.00, 60.00, 80.00,
90.00, 99.00)

(b)

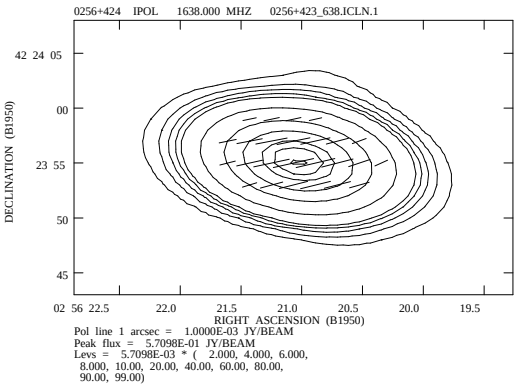
0256+424 IPOL 1638.000 MHZ 0256+423_638.ICLN.1
DECLINATION (B1950)
42 24 05
00
23 55
50
45
02 56 22.5
22.0
21.5
21.0
20.5
20.0
19.5
RIGHT ASCENSION (B1950)
Pol line 1 arcsec = 1.0000E-03 JY/BEAM
Peak flux = 5.7098E-01 JY/BEAM
Levs = 5.7098E-03 * (2.000, 4.000, 6.000,
8.000, 10.00, 20.00, 40.00, 60.00, 80.00,
90.00, 99.00)

(c)

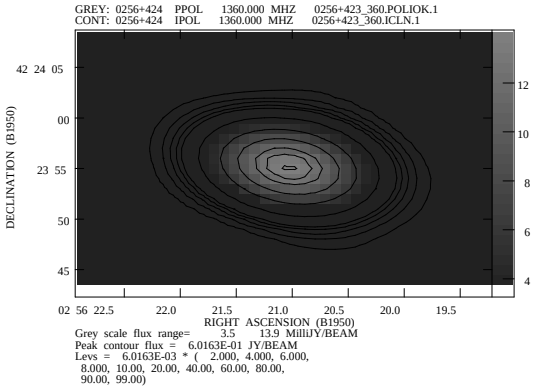
GREY: 0256+424 PPOL 1360.000 MHZ 0256+423_360.POLIOK.1
CONT: 0256+424 IPOL 1360.000 MHZ 0256+423_360.ICLN.1
DECLINATION (B1950)
42 24 05
00
23 55
50
45
02 56 22.5
22.0
21.5
21.0
20.5
20.0
19.5
RIGHT ASCENSION (B1950)
12
10
8
6
4
Grey scale flux range= 3.5 13.9 MilliJY/BEAM
Peak contour flux = 6.0163E-01 JY/BEAM
Levs = 6.0163E-03 * (2.000, 4.000, 6.000,
8.000, 10.00, 20.00, 40.00, 60.00, 80.00,
90.00, 99.00)

(d)

Figure 4-39. Maps of the source 0301+336. Panels (a) through (c) show the total intensity contours of the source along with the polarization position angles. The positive total intensity contours are 2, 4, 6, 8, 10, 20, 40, 60, 80, 90 and 99 percent of the peak intensity. The position angle of the vectors are that of the polarization position angles, and the lengths of the vectors are proportional to the polarized intensity. The position angles plotted are: (a) 1360 MHz ; (b) 1638 MHz; (c) $\chi_{1360} - \chi_{1638}$. In panel (d) the linear polarization intensity is plotted in grayscale on the contours of the total intensity.

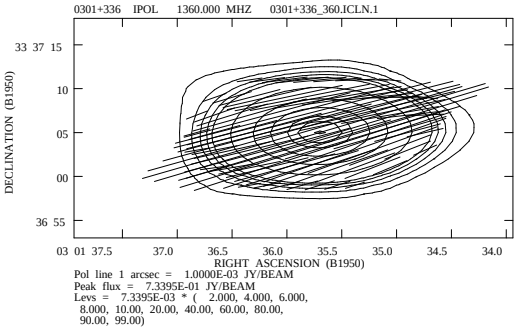
0301+336 IPOL 1360.000 MHZ 0301+336_360.ICLN.1
DECLINATION (B1950)
33 37 15
10
05
00
36 55
03 01 37.5
37.0
36.5
36.0
35.5
35.0
34.5
34.0
RIGHT ASCENSION (B1950)
Pol line 1 arcsec = 1.0000E-03 JY/BEAM
Peak flux = 7.3395E-01 JY/BEAM
Levs = 7.3395E-03 * (2.000, 4.000, 6.000,
8.000, 10.00, 20.00, 40.00, 60.00, 80.00,
90.00, 99.00)

(a)

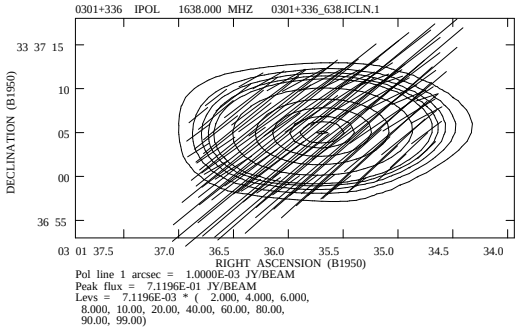
0301+336 IPOL 1638.000 MHZ 0301+336_638.ICLN.1
DECLINATION (B1950)
33 37 15
10
05
00
36 55
03 01 37.5
37.0
36.5
36.0
35.5
35.0
34.5
34.0
RIGHT ASCENSION (B1950)
Pol line 1 arcsec = 1.0000E-03 JY/BEAM
Peak flux = 7.1196E-01 JY/BEAM
Levs = 7.1196E-03 * (2.000, 4.000, 6.000,
8.000, 10.00, 20.00, 40.00, 60.00, 80.00,
90.00, 99.00)

(b)

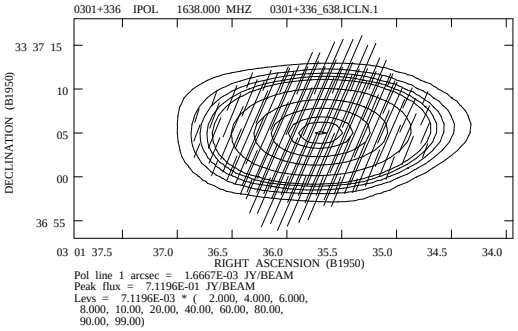
0301+336 IPOL 1638.000 MHZ 0301+336_638.ICLN.1
DECLINATION (B1950)
33 37 15
10
05
00
36 55
03 01 37.5
37.0
36.5
36.0
35.5
35.0
34.5
34.0
RIGHT ASCENSION (B1950)
Pol line 1 arcsec = 1.6667E-03 JY/BEAM
Peak flux = 7.1196E-01 JY/BEAM
Levs = 7.1196E-03 * (2.000, 4.000, 6.000,
8.000, 10.00, 20.00, 40.00, 60.00, 80.00,
90.00, 99.00)

(c)

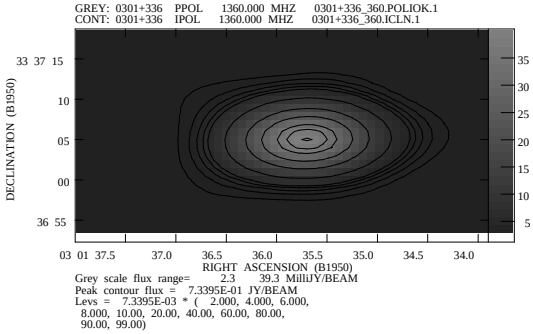
GREY: 0301+336 PPOL 1360.000 MHZ 0301+336_360.POLIOK.1
CONT: 0301+336 IPOL 1360.000 MHZ 0301+336_360.ICLN.1
DECLINATION (B1950)
33 37 15
10
05
00
36 55
35
30
25
20
15
10
5
03 01 37.5
37.0
36.5
36.0
35.5
35.0
34.5
34.0
RIGHT ASCENSION (B1950)
Grey scale flux range= 2.3 39.3 MilliJY/BEAM
Peak contour flux = 7.3395E-01 JY/BEAM
Levs = 7.3395E-03 * (2.000, 4.000, 6.000,
8.000, 10.00, 20.00, 40.00, 60.00, 80.00,
90.00, 99.00)

(d)

Figure 4-40. Maps of the source 0301+350. Panels (a) through (c) show the total intensity contours of the source along with the polarization position angles. The positive total intensity contours are 2, 4, 6, 8, 10, 20, 40, 60, 80, 90 and 99 percent of the peak intensity. The position angle of the vectors are that of the polarization position angles, and the lengths of the vectors are proportional to the polarized intensity. The position angles plotted are: (a) 1360 MHz ; (b) 1638 MHz; (c) $\chi_{1360} - \chi_{1638}$. In panel (d) the linear polarization intensity is plotted in grayscale on the contours of the total intensity.

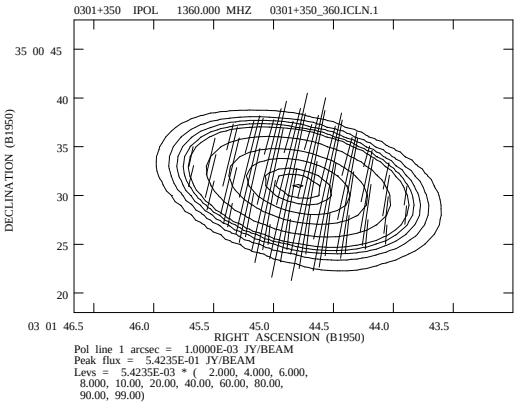
0301+350 IPOL 1360.000 MHZ 0301+350_360.ICLN.1
35 00 45
40
35
30
25
20
DECLINATION (B1950)
03 01 46.5 46.0 45.5 45.0 44.5 44.0 43.5
RIGHT ASCENSION (B1950)
Pol line 1 arcsec = 1.0000E-03 JY/BEAM
Peak flux = 5.4235E-01 JY/BEAM
Levs = 5.4235E-03 * (2.000, 4.000, 6.000,
8.000, 10.00, 20.00, 40.00, 60.00, 80.00,
90.00, 99.00)

(a)

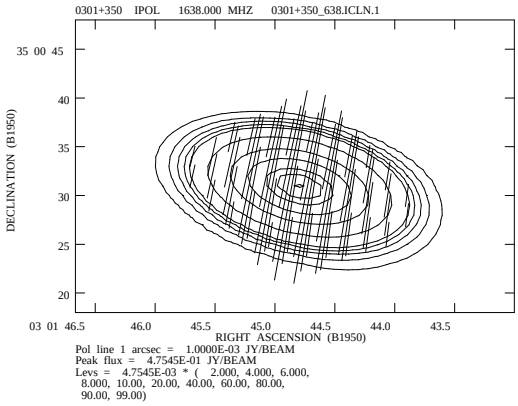
0301+350 IPOL 1638.000 MHZ 0301+350_638.ICLN.1
35 00 45
40
35
30
25
20
DECLINATION (B1950)
03 01 46.5 46.0 45.5 45.0 44.5 44.0 43.5
RIGHT ASCENSION (B1950)
Pol line 1 arcsec = 1.0000E-03 JY/BEAM
Peak flux = 4.7545E-01 JY/BEAM
Levs = 4.7545E-03 * (2.000, 4.000, 6.000,
8.000, 10.00, 20.00, 40.00, 60.00, 80.00,
90.00, 99.00)

(b)

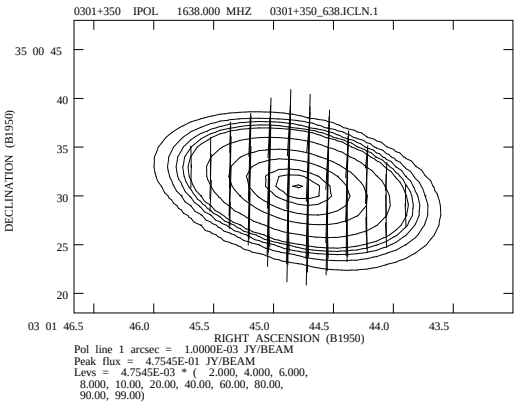
0301+350 IPOL 1638.000 MHZ 0301+350_638.ICLN.1
35 00 45
40
35
30
25
20
DECLINATION (B1950)
03 01 46.5 46.0 45.5 45.0 44.5 44.0 43.5
RIGHT ASCENSION (B1950)
Pol line 1 arcsec = 1.0000E-03 JY/BEAM
Peak flux = 4.7545E-01 JY/BEAM
Levs = 4.7545E-03 * (2.000, 4.000, 6.000,
8.000, 10.00, 20.00, 40.00, 60.00, 80.00,
90.00, 99.00)

(c)

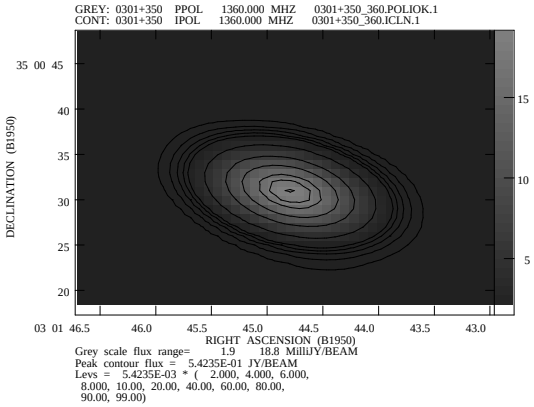
GREY: 0301+350 PPOL 1360.000 MHZ 0301+350_360.POLIOK.1
CONT: 0301+350 IPOL 1360.000 MHZ 0301+350_360.ICLN.1
35 00 45
40
35
30
25
20
DECLINATION (B1950)
15
10
5
03 01 46.5 46.0 45.5 45.0 44.5 44.0 43.5 43.0
RIGHT ASCENSION (B1950)
Grey scale flux range= 1.9 18.8 MilliJY/BEAM
Peak contour flux = 5.4235E-01 JY/BEAM
Levs = 5.4235E-03 * (2.000, 4.000, 6.000,
8.000, 10.00, 20.00, 40.00, 60.00, 80.00,
90.00, 99.00)

(d)

Figure 4-41. Maps of the source 0302+341. Panels (a) through (c) show the total intensity contours of the source along with the polarization position angles. The positive total intensity contours are 2, 4, 6, 8, 10, 20, 40, 60, 80, 90 and 99 percent of the peak intensity. The position angle of the vectors are that of the polarization position angles, and the lengths of the vectors are proportional to the polarized intensity. The position angles plotted are: (a) 1360 MHz ; (b) 1638 MHz; (c) $\chi_{1360} - \chi_{1638}$. In panel (d) the linear polarization intensity is plotted in grayscale on the contours of the total intensity.

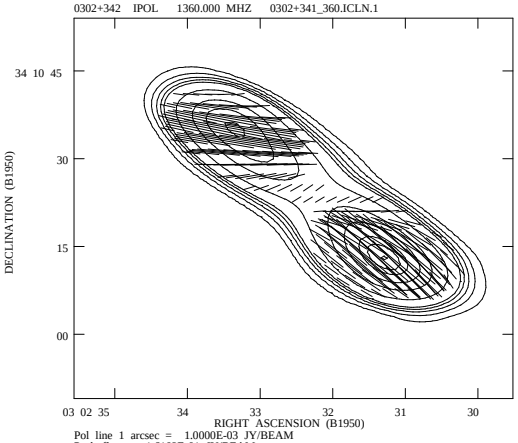
0302+342 IPOL 1360.000 MHZ 0302+341_360.ICLN.1
34 10 45
30
15
00
DECLINATION (B1950)
03 02 35
34
33
32
31
30
RIGHT ASCENSION (B1950)
Pol line 1 arcsec = 1.0000E-03 JY/BEAM
Peak flux = 1.6102E-01 JY/BEAM
Levs = 1.6102E-03 * (2.000, 4.000, 6.000,
8.000, 10.00, 20.00, 40.00, 60.00, 80.00,
90.00, 99.00)

(a)

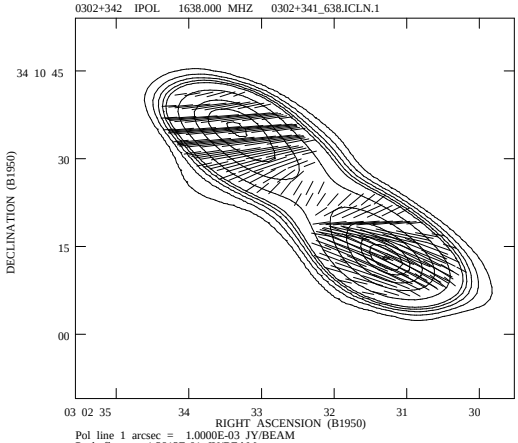
0302+342 IPOL 1638.000 MHZ 0302+341_638.ICLN.1
34 10 45
30
15
00
DECLINATION (B1950)
03 02 35
34
33
32
31
30
RIGHT ASCENSION (B1950)
Pol line 1 arcsec = 1.0000E-03 JY/BEAM
Peak flux = 1.3913E-01 JY/BEAM
Levs = 1.3913E-03 * (2.000, 4.000, 6.000,
8.000, 10.00, 20.00, 40.00, 60.00, 80.00,
90.00, 99.00)

(b)

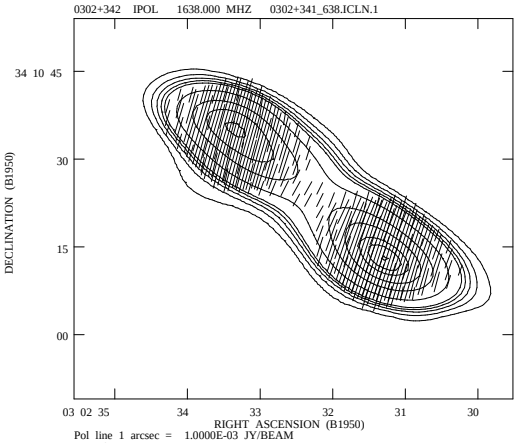
0302+342 IPOL 1638.000 MHZ 0302+341_638.ICLN.1
34 10 45
30
15
00
DECLINATION (B1950)
03 02 35
34
33
32
31
30
RIGHT ASCENSION (B1950)
Pol line 1 arcsec = 1.0000E-03 JY/BEAM
Peak flux = 1.3913E-01 JY/BEAM
Levs = 1.3913E-03 * (2.000, 4.000, 6.000,
8.000, 10.00, 20.00, 40.00, 60.00, 80.00,
90.00, 99.00)

(c)

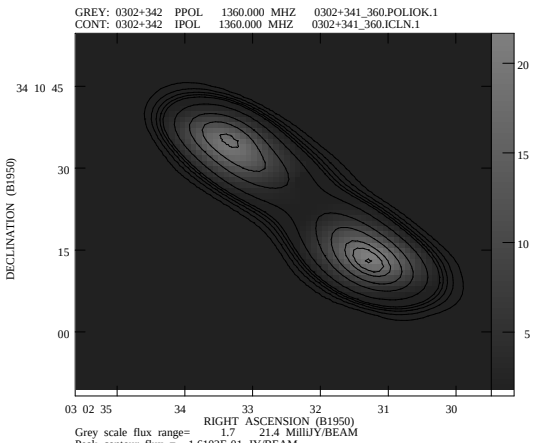
GREY: 0302+342 PPOL 1360.000 MHZ 0302+341_360.POLIOK.1
CONT: 0302+342 IPOL 1360.000 MHZ 0302+341_360.ICLN.1
34 10 45
30
15
00
DECLINATION (B1950)
20
15
10
5
03 02 35
34
33
32
31
30
RIGHT ASCENSION (B1950)
Grey scale flux range= 1.7 21.4 MilliJY/BEAM
Peak contour flux = 1.6102E-01 JY/BEAM
Levs = 1.6102E-03 * (2.000, 4.000, 6.000,
8.000, 10.00, 20.00, 40.00, 60.00, 80.00,
90.00, 99.00)

(d)

Figure 4-42. Maps of the source 0302+405. Panels (a) through (c) show the total intensity contours of the source along with the polarization position angles. The positive total intensity contours are 2, 4, 6, 8, 10, 20, 40, 60, 80, 90 and 99 percent of the peak intensity. The position angle of the vectors are that of the polarization position angles, and the lengths of the vectors are proportional to the polarized intensity. The position angles plotted are: (a) 1360 MHz ; (b) 1638 MHz; (c) $\chi_{1360} - \chi_{1638}$. In panel (d) the linear polarization intensity is plotted in grayscale on the contours of the total intensity.

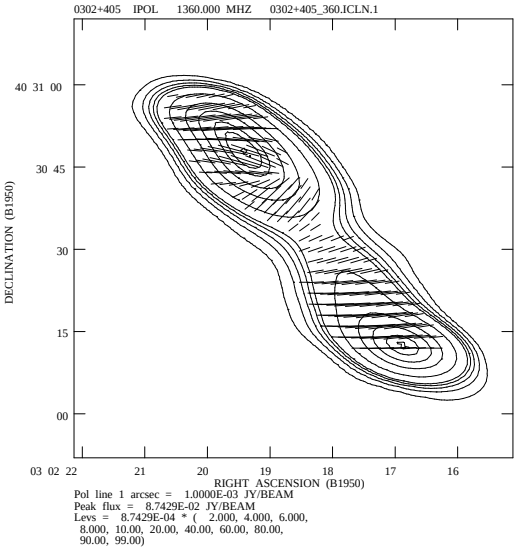
0302+405 IPOL 1360.000 MHZ 0302+405_360.ICLN.1
DECLINATION (B1950)
40 31 00
30 45
30
15
00
03 02 22
21
20
19
18
17
16
RIGHT ASCENSION (B1950)
Pol line 1 arcsec = 1.0000E-03 JY/BEAM
Peak flux = 8.7429E-02 JY/BEAM
Levs = 8.7429E-04 * (2.000, 4.000, 6.000,
8.000, 10.00, 20.00, 40.00, 60.00, 80.00,
90.00, 99.00)

(a)

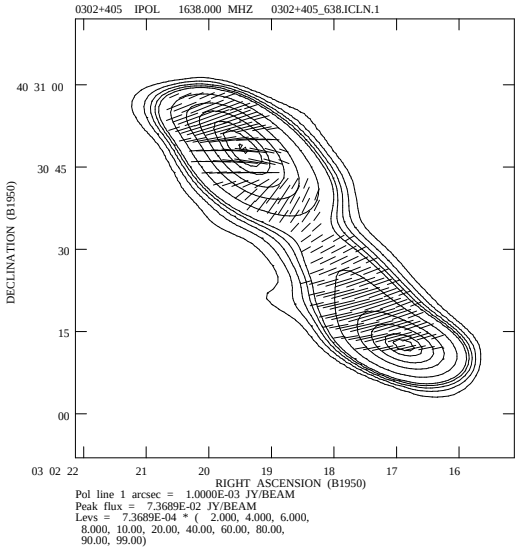
0302+405 IPOL 1638.000 MHZ 0302+405_638.ICLN.1
DECLINATION (B1950)
40 31 00
30 45
30
15
00
03 02 22
21
20
19
18
17
16
RIGHT ASCENSION (B1950)
Pol line 1 arcsec = 1.0000E-03 JY/BEAM
Peak flux = 7.3689E-02 JY/BEAM
Levs = 7.3689E-04 * (2.000, 4.000, 6.000,
8.000, 10.00, 20.00, 40.00, 60.00, 80.00,
90.00, 99.00)

(b)

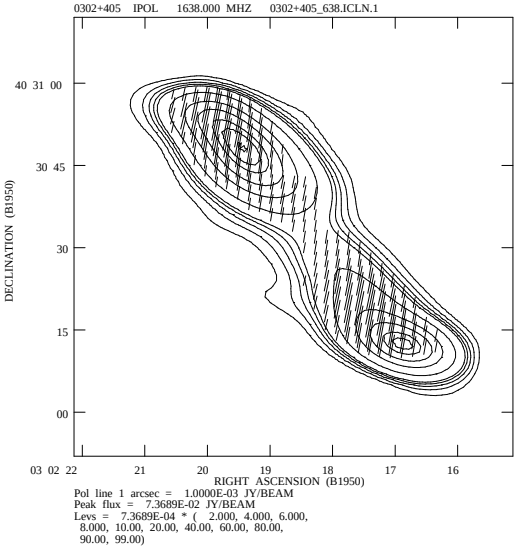
0302+405 IPOL 1638.000 MHZ 0302+405_638.ICLN.1
DECLINATION (B1950)
40 31 00
30 45
30
15
00
03 02 22
21
20
19
18
17
16
RIGHT ASCENSION (B1950)
Pol line 1 arcsec = 1.0000E-03 JY/BEAM
Peak flux = 7.3689E-02 JY/BEAM
Levs = 7.3689E-04 * (2.000, 4.000, 6.000,
8.000, 10.00, 20.00, 40.00, 60.00, 80.00,
90.00, 99.00)

(c)

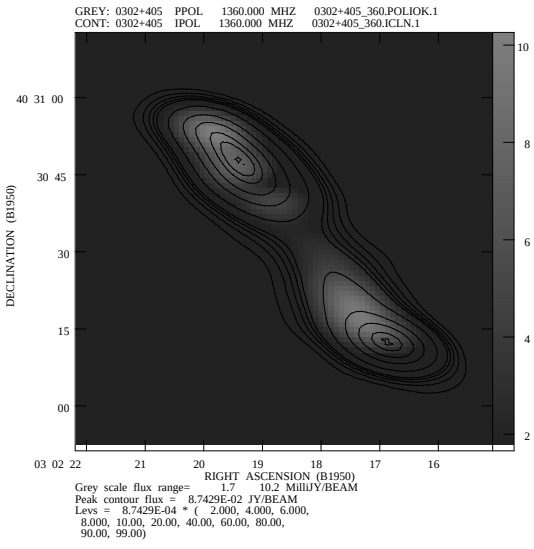
GREY: 0302+405 PPOL 1360.000 MHZ 0302+405_360.POLIOK.1
CONT: 0302+405 IPOL 1360.000 MHZ 0302+405_360.ICLN.1
DECLINATION (B1950)
40 31 00
30 45
30
15
00
03 02 22
21
20
19
18
17
16
RIGHT ASCENSION (B1950)
10
8
6
4
2
Grey scale flux range= 1.7 10.2 MilliJY/BEAM
Peak contour flux = 8.7429E-02 JY/BEAM
Levs = 8.7429E-04 * (2.000, 4.000, 6.000,
8.000, 10.00, 20.00, 40.00, 60.00, 80.00,
90.00, 99.00)

(d)

Figure 4-43. Maps of the source 0248+430. Panels (a) through (c) show the total intensity contours of the source along with the polarization position angles. The positive total intensity contours are 2, 4, 6, 8, 10, 20, 40, 60, 80, 90 and 99 percent of the peak intensity. The position angle of the vectors are that of the polarization position angles, and the lengths of the vectors are proportional to the polarized intensity. The position angles plotted are: (a) 1360 MHz ; (b) 1638 MHz; (c) $\chi_{1360} - \chi_{1638}$. In panel (d) the linear polarization intensity is plotted in grayscale on the contours of the total intensity.

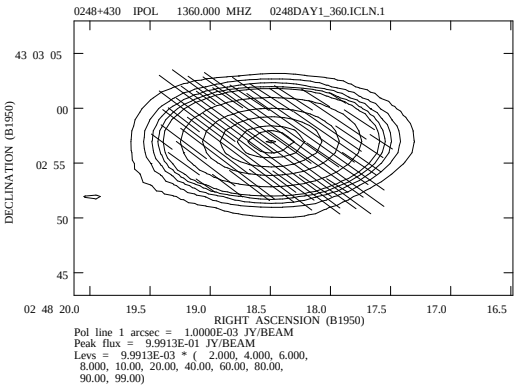
0248+430 IPOL 1360.000 MHZ 0248DAY1_360.ICLN.1
DECLINATION (B1950)
43 03 05
00
02 55
50
45
02 48 20.0
19.5
19.0
18.5
18.0
17.5
17.0
16.5
RIGHT ASCENSION (B1950)
Pol line 1 arcsec = 1.0000E-03 JY/BEAM
Peak flux = 9.9913E-01 JY/BEAM
Levs = 9.9913E-03 * (2.000, 4.000, 6.000,
8.000, 10.00, 20.00, 40.00, 60.00, 80.00,
90.00, 99.00)

(a)

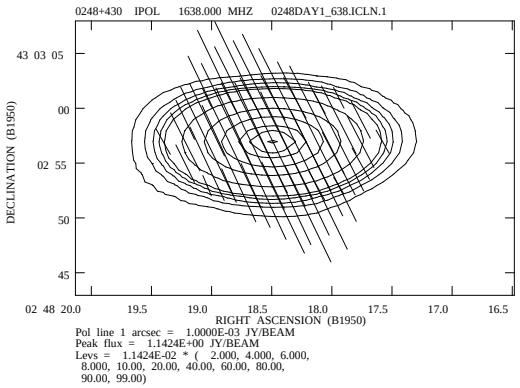
0248+430 IPOL 1638.000 MHZ 0248DAY1_638.ICLN.1
DECLINATION (B1950)
43 03 05
00
02 55
50
45
02 48 20.0
19.5
19.0
18.5
18.0
17.5
17.0
16.5
RIGHT ASCENSION (B1950)
Pol line 1 arcsec = 1.0000E-03 JY/BEAM
Peak flux = 1.1424E+00 JY/BEAM
Levs = 1.1424E-02 * (2.000, 4.000, 6.000,
8.000, 10.00, 20.00, 40.00, 60.00, 80.00,
90.00, 99.00)

(b)

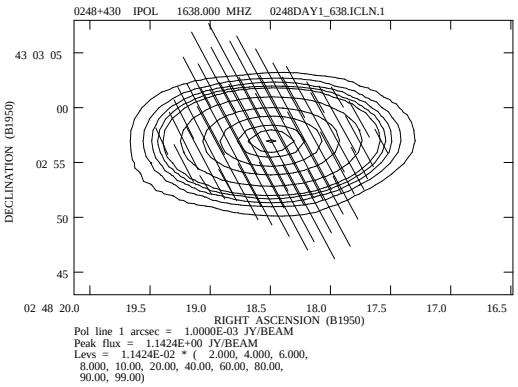
0248+430 IPOL 1638.000 MHZ 0248DAY1_638.ICLN.1
DECLINATION (B1950)
43 03 05
00
02 55
50
45
02 48 20.0
19.5
19.0
18.5
18.0
17.5
17.0
16.5
RIGHT ASCENSION (B1950)
Pol line 1 arcsec = 1.0000E-03 JY/BEAM
Peak flux = 1.1424E+00 JY/BEAM
Levs = 1.1424E-02 * (2.000, 4.000, 6.000,
8.000, 10.00, 20.00, 40.00, 60.00, 80.00,
90.00, 99.00)

(c)

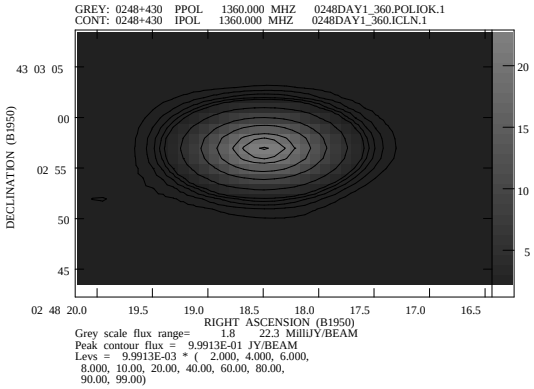
GREY: 0248+430 PPOL 1360.000 MHZ 0248DAY1_360.POLIOK.1
CONT: 0248+430 IPOL 1360.000 MHZ 0248DAY1_360.ICLN.1
DECLINATION (B1950)
43 03 05
00
02 55
50
45
02 48 20.0
19.5
19.0
18.5
18.0
17.5
17.0
16.5
RIGHT ASCENSION (B1950)
20
15
10
5
Grey scale flux range= 1.8 22.3 MilliJY/BEAM
Peak contour flux = 9.9913E-01 JY/BEAM
Levs = 9.9913E-03 * (2.000, 4.000, 6.000,
8.000, 10.00, 20.00, 40.00, 60.00, 80.00,
90.00, 99.00)

(d)

CHAPTER 5

THE LARGE SCALE VARIATIONS IN THE EMISSION MEASURE AND THE ROTATION MEASURE DUE TO GALACTIC STRUCTURE

5.1 Introduction

Before turning to the main theme of this paper, which is the characteristics of mesoscale fluctuations in δn and $\delta\vec{B}$ in the interstellar medium, we consider the smooth trends in emission measure and rotation measure which may be discerned in Figure 4-2. These trends contain information on the large scale pattern for the galactic magnetic field and plasma density which is of interest in its own right.

5.2 Models of the Galactic Electron Density

We have used several simple models for the interstellar electron density and magnetic field in order to determine the contribution of galactic structure to rotation measure differences between different extragalactic radio sources. These models used combinations of two electron density models and three magnetic field models. The first electron density model consists of the Reynolds layer with a classic Strömgren sphere to model the contribution of the H II region associated with ξ Per (this model hereafter is referred to as the Reynolds + Strömgren, or R + S, model). The Strömgren sphere is modeled as a sphere of uniform density ($n_\xi = 0.5$ cm^{-3}) surrounding ξ Per, the radius of which is given by the equation

$$R^3 = \frac{3Q(H^o)}{4\pi\alpha_B n_\xi^2} \tag{5.1}$$

(Osterbrock 1989) where Q(H^o) is the number of photoionizing photons emitted by ξ Per per second and α_B is the recombination coefficient of Hydrogen to all levels but the ground state. For an O7V star, such as ξ Per, Q(H^o) $\sim 10^{48.7}$ photons/sec and for a gas temperature of 10,000 K, $\alpha_B = 2.6 \cdot 10^{-13}$ cm^3 s^{-1}, giving R $\sim$ 85 pc (Osterbrock 1989). The electron density for this model is then given by

$$n_e = 0.0275 \exp\left(\frac{-z}{1 \text{ Kpc}}\right)(1 - \Theta(r)) + 0.5\Theta(r) \text{ cm}^{-3} \tag{5.2}$$

where r is the distance from ξ Per and $\Theta(r) = 1$ for r $\leq$ R and is zero otherwise. The second electron density model is that of Taylor and Cordes (hereafter referred to as the TC model)(Taylor and Cordes 1993). This model is based on pulsar dispersion measures (DM) and scattering measures (SM) and allows for a variation of n_e with galactic radius as well as height above the galactic plane, and also accounts for spiral arms in the galaxy. A modified version of the Taylor and Cordes model was also used in which the mid-plane density of the diffuse galactic electrons was changed from 0.019 cm^{-3} to 0.027 cm^{-3} providing a more realistic value for this region of the sky. The galactic radial cutoff distance A_a in the Taylor and Cordes model was also extended from 8.5 Kpc to 15 Kpc. Cordes and Lazio (1995) are in the process of determining the radial extent of ionized matter in the galaxy and suspect that the Cordes and Taylor model needs to extend the galactic radial cutoffs to larger galactocentric radii. If this does indeed turn out to be the case then the change in density used above may not be necessary due to the longer path lengths through the galaxy created by using a larger value of A_a.

To test the viability of each of these models, we calculated the correlation coefficient between the observed H_α map of Reynolds (1980) and the model emission measure map obtained from each of the aforementioned models for the interstellar electron density. For these calculations we assumed a filling factor of 0.25. The standard

deviation of the residual emission measures (observed - model) was also calculated. To improve the degree of fit, we permitted ourselves the option of slight adjustments to the nominal mid-plane density. These adjustments are described further below.

The results of this test of the various electron density models are given in Table 5-1. Column 1 gives the model under consideration and column 2 gives the correlation coefficient between the emission measure map calculated from that density model and the observed emission measure map. Column 3 gives the standard deviation of the residuals. For purposes of comparison, the mean observed emission measure over this field, outside of the strong H_α emission region associated with the H II region of ξ Per, is 5.2 $cm^{-6}pc$.

The prominent band of enhanced emission measure at the left hand side of the field is almost certainly distinct from the mean background medium modeled by the Reynolds' layer and the Taylor and Cordes model. This recognition was the basis of the "Reynolds + Strömgren" model. We therefore repeated the goodness of fit calculations for the Reynolds' layer model and the Taylor and Cordes model, using only the portion of the field exterior to the enhanced band. These results are presented in the lower portion of Table 5-1.

The Reynolds + Strömgren model provides the best overall fit to the data, as indicated by the highest correlation coefficient and lowest RMS residual. This result is perhaps not surprising, given that it is the only model which specifically accounts for the region of enhanced H_α emission. From the lower portion of Table 5-1 we see that the Taylor and Cordes model provides a much better representation of the portion of our field away from the putative H II region. The second of the two entries for this model represents an upward adjustment to the mid-plane density from 0.019 cm^{-3} to 0.027 cm^{-3}, to provide a better fit to the observations. The same degree of improvement

could have been achieved by retaining the nominal mid-plane density of the Taylor and Cordes model and lowering the filling factor of the diffuse medium.

5.3 Models of the Galactic Magnetic Field

Modeling the rotation measures also requires a model for the galactic magnetic field. The first magnetic field model, based on Rand and Lyne (1995), consists of an azimuthal galactic magnetic field which has a sinusoidal modulation of the amplitude of the magnetic field in galactocentric distance. The model presented by Rand and Lyne (1995) was developed from a set of measurements of pulsar rotation measure and dispersion measure. Rand and Lyne (1995) find an amplitude of the sinusoidal field (equal to the maximum value of the interstellar field) $B_o = 2.1 \pm 0.2$ μG, with a reversal every 2600 ± 300 pc in the radial direction. According to their model, the nearest neutral line is 400 ± 70 pc from the sun, in the direction of the galactic center. However, they find no compelling evidence that magnetic field reversals occur for galactocentric radii outside of the Solar Circle (i.e. for $R \geq R_{\odot}$). Rand and Lyne also find evidence that at least one of the field reversal boundaries does not lie along a line of constant galactocentric radius. Hence, we use an azimuthally directed magnetic field with a constant amplitude of $B_o = 2.1 \pm 0.2$ μG for this model. Hereafter we will refer to this model as the "RL" model.

Clegg et al. (1992), however, find evidence that at least one magnetic field reversal does occur outside of the Solar Circle. The second magnetic field model is then taken to be the model of Rand and Lyne (1995) with magnetic field reversals also occurring outside of the Solar Circle. In fitting this model to our rotation measure data, we found values for the radial wavelength and neutral line location of the magnetic field outside of the Solar Circle to be consistent with those listed above for the Rand and

Lyne model. However, our rotation measure data require a substantially higher value of $B_o \sim 3 - 4$ μG. The nature of this discrepancy is discussed further below.

The third magnetic field model consists of a bisymmetric magnetic field of pitch angle $\sim 12°$ with abrupt field reversals at the leading edge of spiral arms, similar to the model of Rand and Kulkarni (1989) (see their Figure 5). In this model, the magnetic field follows the spiral arms with boundaries between field reversals (neutral lines) occurring at the leading edges of the spiral arms, and a sinusoidal modulation of the amplitude of the magnetic field in a direction perpendicular to the spiral arms. For the region of our observations we only need to deal with two spiral arms: the Orion-Cygnus Arm and the Perseus Arm. The leading edges of these arms are given by the following equation (Rand and Kulkarni 1989):

$$r = a \exp(k\theta) \text{ Kpc} \tag{5.3}$$

where $k = 0.22$ rad^{-1} , and θ and r are galactocentric coordinates with the direction $\theta = 0°$ parallel to $l = 90°$. Equation (5.3) thus gives the location of the magnetic neutral lines. For the Orion-Cygnus Arm we use $a = 4./\exp(\frac{3}{2}\pi k)$ and for the Perseus Arm we use $a = 4./\exp(\pi k)$. The magnetic field direction at the sun is toward $l = 78°$ and the strength of the magnetic field is considered as an adjustable quantity, subject to the constraints of independent observations.

5.4 Models of the Galactic Rotation Measure

Various combinations of the electron density and magnetic field models were then used to generate models of the galactic rotation measure in the direction of our field. A comparison of these models with observed rotation measures is presented in Table 5-2. The two sources which have positive rotation measures were excluded from these comparisons since only negative rotation measures are predicted by the

models. For purposes of comparison the mean rotation measure across the field is -57.9 rad m^{-2}. The first and second columns list the electron density and magnetic field models used in the comparison. For the magnetic field models, "RL" indicates the Rand and Lyne model, "Az" indicates the azimuthal magnetic field model with field reversals outside of the Solar Circle and "Bi" indicates the bisymmetric spiral magnetic field model. The third column gives the maximum amplitude of the magnetic field used in the model. The amplitude of the magnetic field was chosen so that the mean rotation measure from the model equals the mean rotation measure from the data. The fourth column gives the correlation coefficient between the rotation measure model and the data. The fifth column gives the standard deviation of the residual between the rotation measure model values and the data. The sixth and seventh columns are the same as the fourth and fifth columns, respectively, computed such that the region affected by ξ Per's H II region is omitted from the analysis. None of the six combinations of electron density and galactic magnetic field models are clearly superior in terms of matching the observed rotation measure. However, the models which include magnetic field reversals outside of the Solar Circle have larger correlation coefficients and smaller standard deviations of the residuals. This can be taken as evidence weakly in favor of magnetic field reversals occurring outside of the Solar Circle.

It should be kept in mind in this analysis that the models for the electron density and the galactic magnetic field were determined by observations which sampled a very large volume of the interstellar medium. They are therefore indicators of the global structure of the interstellar plasma. The observations discussed in this paper, on the other hand, probe a much smaller volume of the interstellar medium. It is therefore natural to expect that plasma density and magnetic field perturbations on scales much smaller than galactic structure, but much larger than turbulence, could significantly distort the true "mean" quantities from those adopted here.

The residuals found by subtracting the rotation measures predicted by the various models in Table 5-2 are shown in Figures 5-1 through 5-6. A large discrepancy between the models and the data does exist in the area of the H II region associated with ξ Per in that all the models predict rotation measures that are too negative in this region. The differences between the models and the data are much less for the region west of the H II region. As noted above, the value for the strength of the magnetic field, B_o, which we need to account for our rotation measures is larger than that previously quoted by Rand and Kulkarni (1989) and Rand and Lyne (1995) for both the "Az" and "Bi" magnetic field models. We now discuss the possible resolutions of this discrepancy.

The edge of the H II region associated with ξ Per lies roughly at a Right Ascension of $2^h\ 50^m$ and the edge of radio Loop II also lies roughly at a Right Ascension of $2^h\ 50^m$ in this region of the sky. It is easy to notice that the magnitude of the rotation measures is largest inside of radio Loop II (RA $\leq 2^h\ 50^m$) (see Figure 4-2). The rotation measures inside of the H II region (RA $\geq 2^h\ 50^m$) tend to have magnitudes which are significantly less than those inside of radio Loop II. Thus, it seems likely that a magnetic anomaly associated with one of these features is causing the observed discrepancies. In fact, it is the contention of Vallée (1984) that a magnetic bubble is associated with radio Loop II with a shell magnetic field strength of 10 μG. Another possibility is that the length between magnetic field reversals in this region of the sky is different from those of the model or that the boundary between magnetic field reversals may lie along a curve which differs significantly from the boundaries assumed in the models.

Alternatively, it is possible that the magnetic anomaly is associated with the H II region, and that the part of Figures 4-2 and Figures 5-1 through 5-6 with RA $\leq 2^h\ 50^m$ are more representative of the general ISM. It is worth noting that the values of the interstellar magnetic field we report in Table 5-2 are relatively close to the values which Cox (1988) argues must be present on the basis of dynamical

considerations. It is certainly reasonable to speculate that expansion of the H II region associated with ξ Per has produced a local distortion of the galactic magnetic field, which manifests itself as a rotation measure anomaly. It is worth emphasizing that, to first order, the obvious plasma density enhancement associated with the H II region is not responsible for the large rotation measure residuals in this part of the sky, since it has been accommodated in the Reynolds + Strömgren density model. A perturbation in the interstellar magnetic field is therefore indicated. However, to higher order the density enhancement might be partially responsible to the extent that our estimate of the plasma density in the H II region is in error. In summary, the fact that we have found a larger value for the galactic magnetic field strength than previous investigations using pulsar data may be the result of a magnetic anomaly in this region of the sky or due to the incorrect modeling of the magnetic field in this region of the sky.

There is indeed evidence that the characteristics of the galactic magnetic field change significantly in the direction of the H II region. There are three extragalactic sources known to the authors that lie between the enhanced H_α emission region and ξ Per whose rotation measures have been determined. These sources and their rotation measures are as follows: 0313+3426 with RM $= +29 \pm 3$ rad m^{-2}, 0314+4141 with RM $= +18 \pm 1$ rad m^{-2} and 0333+3208 with RM $= +58 \pm 1$ rad m^{-2} (Broten et al. 1987). These rotation measures indicate that the rotation measure becomes more positive as we enter the H II region. There is also a pulsar (0320+39) which also lies between the enhanced H_α emission region and ξ Per. This pulsar has a dispersion measure of DM $= 25.8 \pm .5$ cm^{-3} pc, a rotation measure of RM $= 58 \pm 3$ rad m^{-2} and temporal broadening of pulses at the standard frequency of 1 GHz of $\tau_s = 0.107$ μsec (Taylor et al. 1993). These values then indicate that the line of sight component of the magnetic field is $B_\parallel = +2.8 \pm .2$ μG and, with the estimated distance to the pulsar being 1.47 Kpc, that $C_n^2 = 10^{-2.9}$ m$^{-20/3}$ for the line of sight to the pulsar. This value

for $B_{\parallel}$ is significantly different from the value $B_{\parallel} = -0.8$ μG found from the rotation measure models described above. It is also worth noting that all three magnetic field models discussed above predict that the line of sight component of the galactic magnetic field should be negative towards the pulsar. It thus appears quite plausible that there is a magnetic field anomaly associated with the H II region of ξ Per.

Reynolds et al. (1995) have made a detailed comparison of the H_α and H I emission in this region. They have identified several filaments, loops and H_α – H I clouds that lie in this region of the sky. We do not, however, see any signatures in the measured rotation measures which correspond to any of these structures except for their Region A. Region A is the enhanced H_α emission region that is associated with the H II region of ξ Per where we observe a dramatic change in the rotation measures as described above. It is also possible that the rotation measures are sampled too sparsely to identify some of the regions in Reynolds et al. (1995) on the rotation measure map in Figure 4-2.

Table 5-1. Comparison of model emission measure with data.

Model Compared With Data	Correlation Coefficient	Standard Deviation cm^{-6} pc
Reynolds Layer	0.60	5.45
Reynolds + Strömgren	0.69	4.72
Taylor and Cordes	0.60	7.17
Taylor and Cordes[1]	0.60	4.97
Excluding ξ Per's H II Region		
Reynolds Layer	0.65	1.84
Taylor and Cordes	0.65	3.35
Taylor and Cordes[1]	0.65	1.77

[1] The Taylor and Cordes model was modified so that the mid-plane density of the diffuse electrons with a scale height of 880 pc was 0.027 cm^{-3} rather than 0.019 cm^{-3}.

Table 5-2. Comparison of model rotation measure with data.

Model		B_o	All Sources		East of H II Region	
n_e	$\vec{B}$	μ G	correlation coefficient	σ rad m^{-2}	correlation coefficient	σ rad m^{-2}
R+S	RL	2.0	.28	22.07	.49	15.44
TC[1]	RL	2.1	.42	20.83	.50	16.51
R+S	Az	4.6	.50	15.33	.68	15.33
TC[1]	Az	3.7	.70	18.46	.67	14.47
R+S	Bi	2.7	.63	17.99	.66	13.43
TC[1]	Bi	3.6	.65	17.53	.65	13.56

[1] The Taylor and Cordes model was modified so that the mid-plane density of the diffuse electrons with a scale height of 880 pc was 0.027 cm^{-3} rather than 0.019 cm^{-3}.

Figure 5-1. Rotation measure residuals (model RM - observed RM) obtained by subtracting the (R+S, RL) galactic model for rotation measure from the observed data. The measured emission measure is shown in grayscale while the rotation measure is shown as a circle for negative rotation measure residuals and as a diamond for positive rotation measure residuals. The size of the symbol is proportional to the magnitude of the rotation measure residual with a scale for the symbol size being shown on the left hand side of the figure.

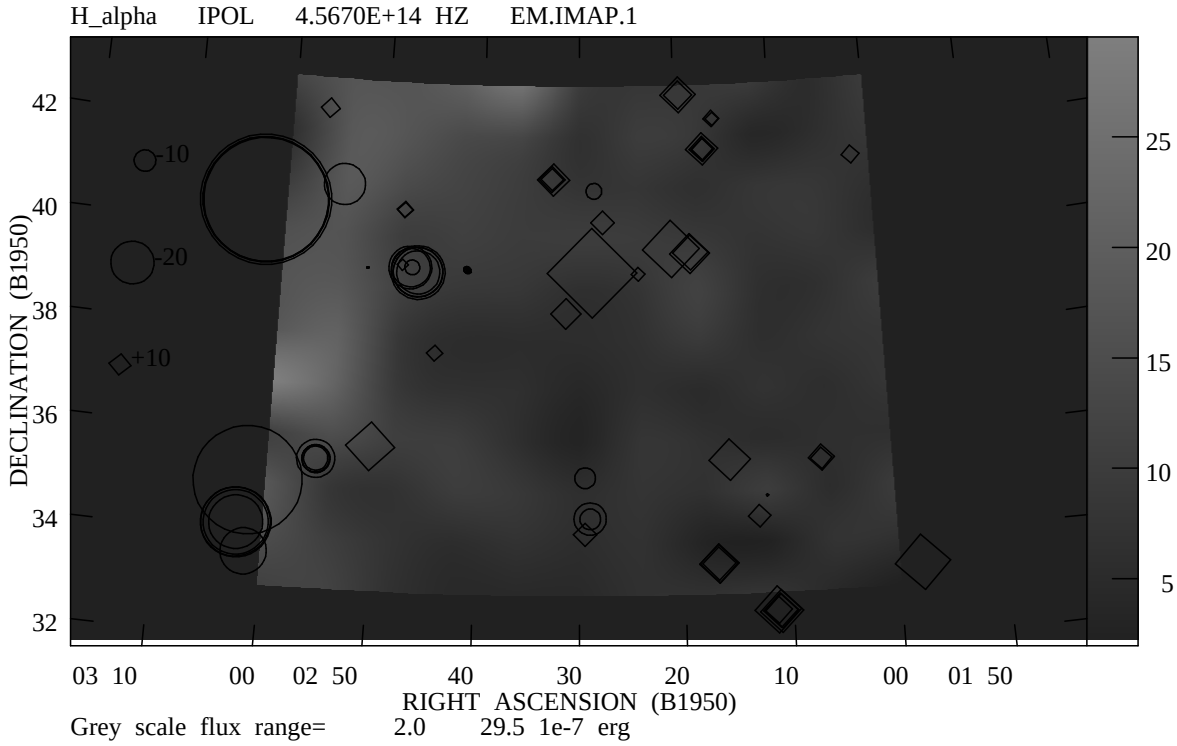
H_alpha IPOL 4.5670E+14 HZ EM.IMAP.1
42
40
38
36
34
32
DECLINATION (B1950)
-10
-20
+10
25
20
15
10
5
03 10
00
02 50
40
30
20
10
00
01 50
RIGHT ASCENSION (B1950)
Grey scale flux range= 2.0 29.5 1e-7 erg

Figure 5-2. Rotation measure residuals (model RM - observed RM) obtained by subtracting the (TC, RL) galactic model for rotation measure from the observed data. The measured emission measure is shown in grayscale while the rotation measure is shown as a circle for negative rotation measure residuals and as a diamond for positive rotation measure residuals. The size of the symbol is proportional to the magnitude of the rotation measure residual with a scale for the symbol size being shown on the left hand side of the figure.

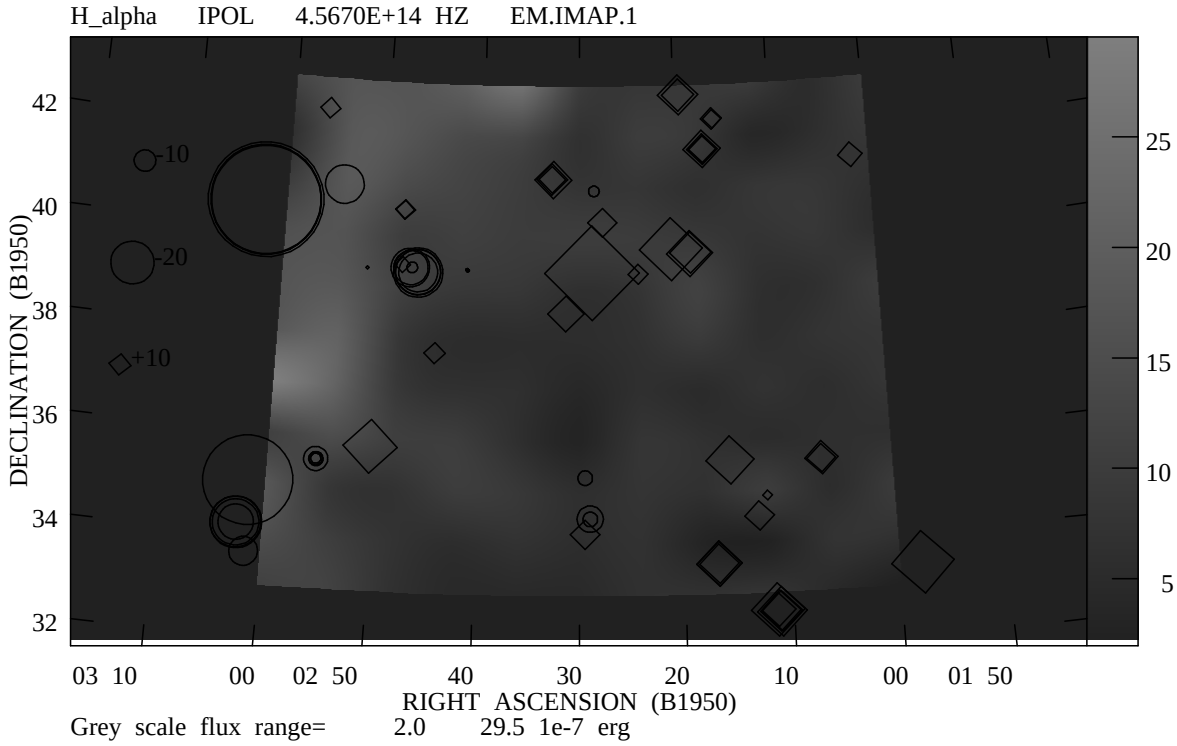
H_alpha IPOL 4.5670E+14 HZ EM.IMAP.1
42
40
38
36
34
32
DECLINATION (B1950)
-10
-20
+10
25
20
15
10
5
03 10
00
02 50
40
30
20
10
00
01 50
RIGHT ASCENSION (B1950)
Grey scale flux range= 2.0 29.5 1e-7 erg

Figure 5-3. Rotation measure residuals (model RM - observed RM) obtained by subtracting the (R+s, Az) galactic model for rotation measure from the observed data. The measured emission measure is shown in grayscale while the rotation measure is shown as a circle for negative rotation measure residuals and as a diamond for positive rotation measure residuals. The size of the symbol is proportional to the magnitude of the rotation measure residual with a scale for the symbol size being shown on the left hand side of the figure.

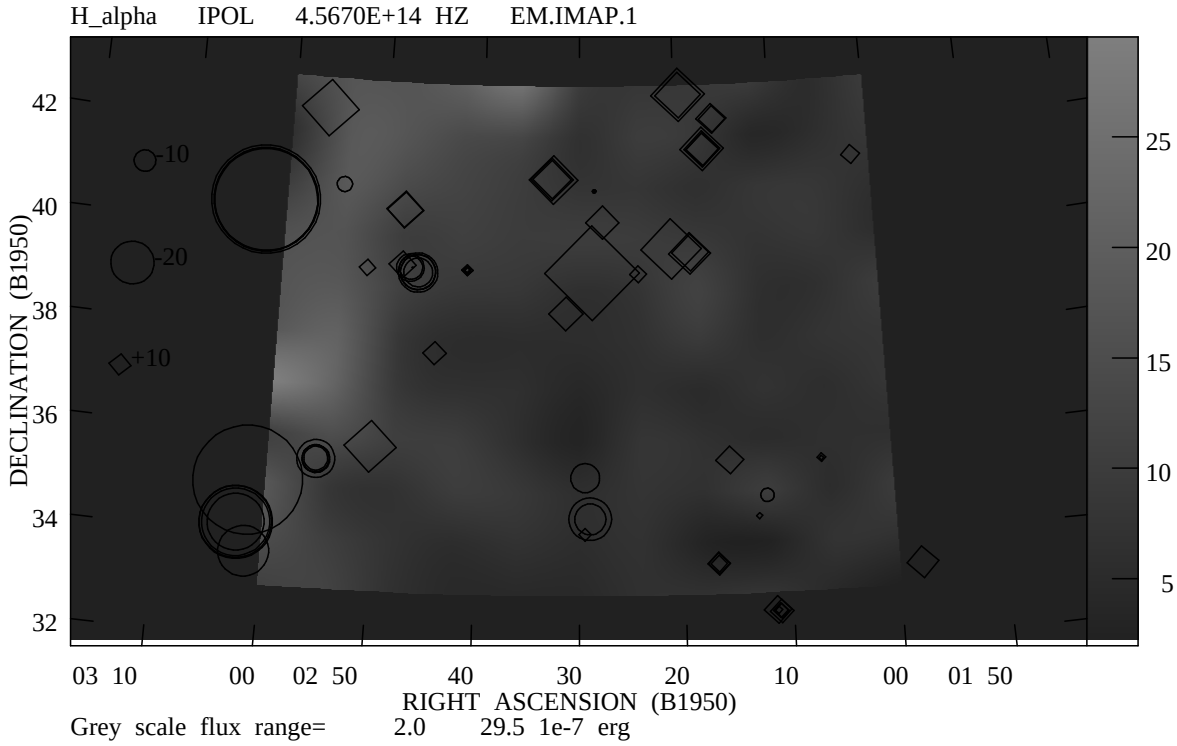
H_alpha IPOL 4.5670E+14 HZ EM.IMAP.1
42
40
38
36
34
32
DECLINATION (B1950)
-10
-20
+10
25
20
15
10
5
03 10
00
02 50
40
30
20
10
00
01 50
RIGHT ASCENSION (B1950)
Grey scale flux range= 2.0 29.5 1e-7 erg

Figure 5-4. Rotation measure residuals (model RM - observed RM) obtained by subtracting the (TC, Az) galactic model for rotation measure from the observed data. The measured emission measure is shown in grayscale while the rotation measure is shown as a circle for negative rotation measure residuals and as a diamond for positive rotation measure residuals. The size of the symbol is proportional to the magnitude of the rotation measure residual with a scale for the symbol size being shown on the left hand side of the figure.

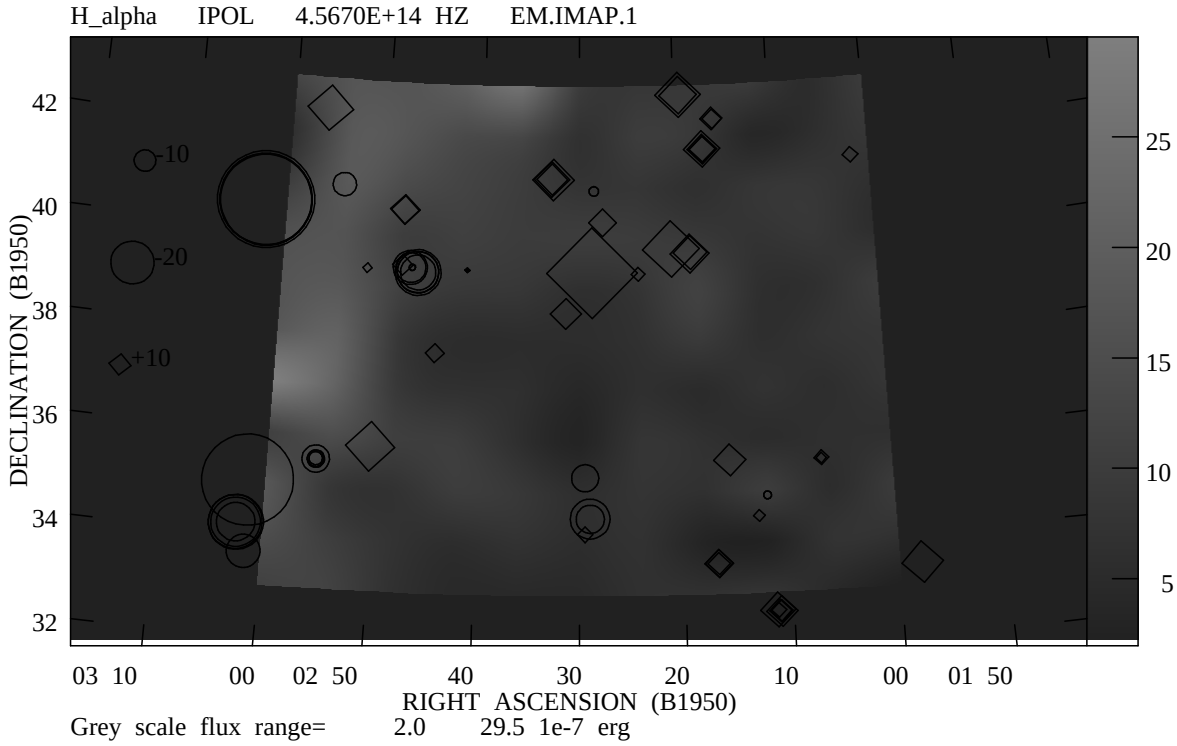
H_alpha IPOL 4.5670E+14 HZ EM.IMAP.1
42
40
38
36
34
32
DECLINATION (B1950)
-10
-20
+10
25
20
15
10
5
03 10
00
02 50
40
30
20
10
00
01 50
RIGHT ASCENSION (B1950)
Grey scale flux range= 2.0 29.5 1e-7 erg

Figure 5-5. Rotation measure residuals (model RM - observed RM) obtained by subtracting the (R+S, Bi) galactic model for rotation measure from the observed data. The measured emission measure is shown in grayscale while the rotation measure is shown as a circle for negative rotation measure residuals and as a diamond for positive rotation measure residuals. The size of the symbol is proportional to the magnitude of the rotation measure residual with a scale for the symbol size being shown on the left hand side of the figure.

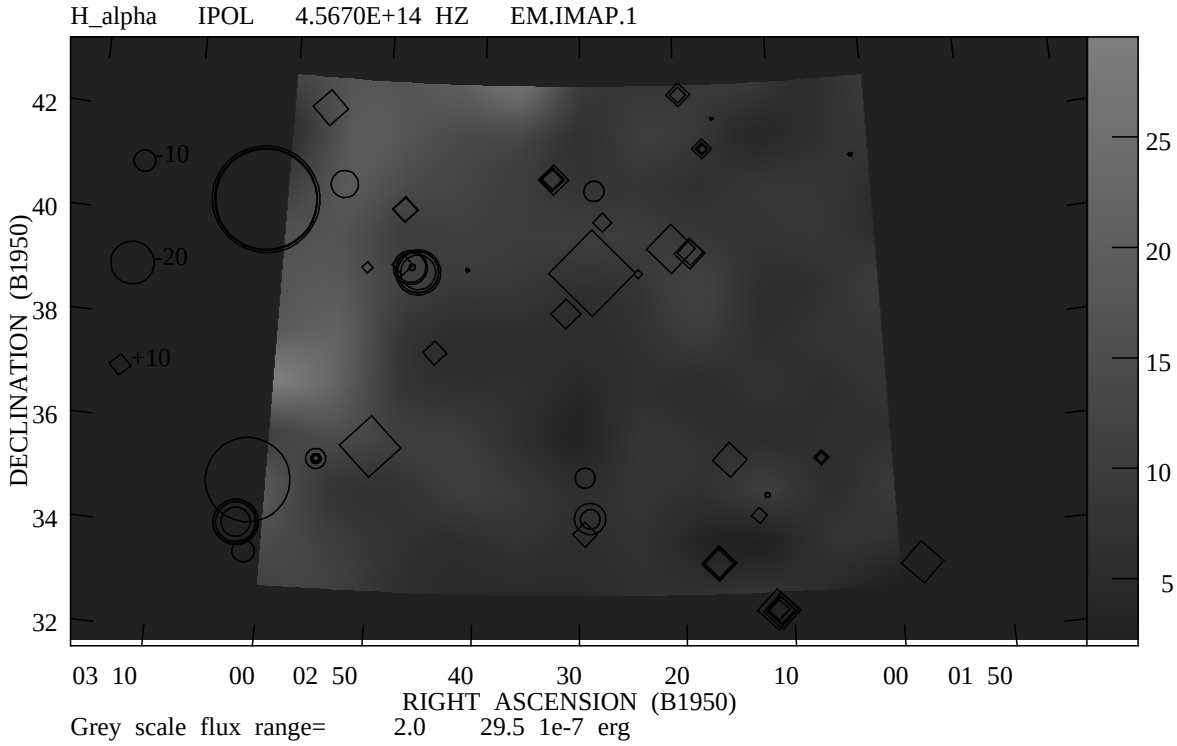
H_alpha IPOL 4.5670E+14 HZ EM.IMAP.1
42
40
38
36
34
32
DECLINATION (B1950)
-10
-20
+10
25
20
15
10
5
03 10
00
02 50
40
30
20
10
00
01 50
RIGHT ASCENSION (B1950)
Grey scale flux range= 2.0 29.5 1e-7 erg

Figure 5-6. Rotation measure residuals (model RM - observed RM) obtained by subtracting the (TC, Bi) galactic model for rotation measure from the observed data. The measured emission measure is shown in grayscale while the rotation measure is shown as a circle for negative rotation measure residuals and as a diamond for positive rotation measure residuals. The size of the symbol is proportional to the magnitude of the rotation measure residual with a scale for the symbol size being shown on the left hand side of the figure.

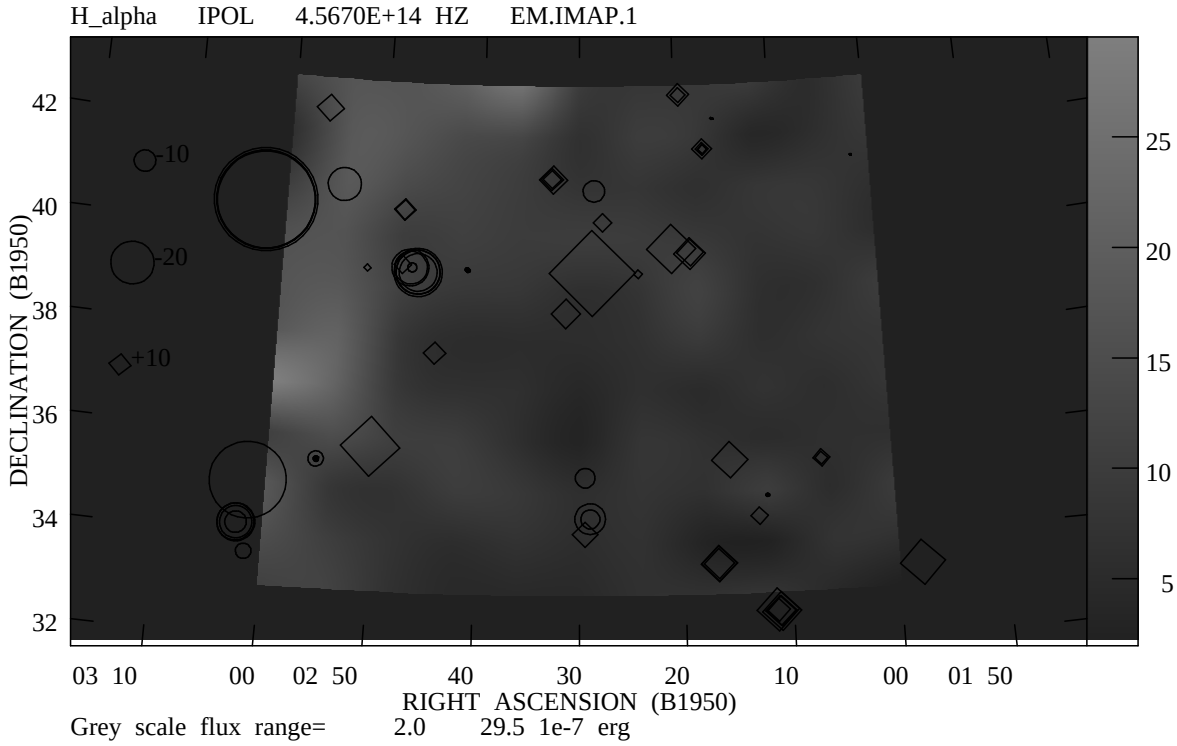
H_alpha IPOL 4.5670E+14 HZ EM.IMAP.1
42
40
38
36
34
32
DECLINATION (B1950)
-10
-20
+10
25
20
15
10
5
03 10
00
02 50
40
30
20
10
00
01 50
RIGHT ASCENSION (B1950)
Grey scale flux range= 2.0 29.5 1e-7 erg

CHAPTER 6
THE STRUCTURE FUNCTIONS OF THE EMISSION MEASURE AND THE ROTATION MEASURE

6.1 Introduction

The structure function $D_f(\delta x)$ of f(x) at δx is defined as the ensemble average of the square of the difference of f(x) and f(x + δx)

$$D_f(\delta x) = \langle [f(x) - f(x + \delta x)]^2 \rangle. \tag{6.1}$$

If f(x) has a correlation length of d, an RMS about the mean of f(x) of σ_f and a measurement error of Δ then the behavior of the structure function is as follows. As $\delta x \to 0$, $D_f(\delta x) \to \Delta^2$. For x < d $D_f(\delta x)$ increases from Δ^2 until x $\sim$ d. For x > d the structure function is constant at $D_f(\delta x) \sim 2\sigma_f^2$ since f(x) and f(x + δx) are uncorrelated for x > d. An example of this behavior for the structure function is shown in Figure 6-1 where we have chosen d $\sim$ 1 and $\Delta^2 = .2 \cdot \sigma_f^2$. The advantage of using structure functions to analyze data rather than using the correlation function is that the structure function can easily be formed for irregularly sampled data. The correlation function, however, is not easily obtained for irregularly sampled data.

6.2 The Measured Structure Functions

The rotation measure and emission measure structure functions were determined by averaging the squares of the differences of pairs of measured values, binned

in logarithmic intervals in $\delta\theta$.

$$\mathrm{D_{EM}}(\delta\theta_{\mathrm{k}}) = \frac{1}{\mathrm{N}} \sum_{\mathrm{i}=1}^{\mathrm{N}} \left[\mathrm{EM}(\theta) - \mathrm{EM}(\theta + \delta\theta_{\mathrm{k}})\right]^2 \tag{6.2}$$

and

$$\mathrm{D_{RM}}(\delta\theta_{\mathrm{k}}) = \frac{1}{\mathrm{N}} \sum_{\mathrm{i}=1}^{\mathrm{N}} \left[\mathrm{RM}(\theta) - \mathrm{RM}(\theta + \delta\theta_{\mathrm{k}})\right]^2 \tag{6.3}$$

where $\delta\theta_{\mathrm{k}}$ is a given bin in $\delta\theta$ and the summation is over the N pairs of components with $\delta\theta_{\mathrm{k}}$ in the desired interval. Here we take $\delta\theta$ to be the angular separation between two sources, or source components, on the sky. The error associated with the observed structure function in a given bin was taken to be the standard deviation of the mean of the sum (6.3). To weight properly the baselines $\delta\theta + \Delta$, neighboring $\delta\theta_{\mathrm{k}}$, which are not statistically independent from the measurement on $\delta\theta_{\mathrm{k}}$, we have weighted each component by one over the number of neighboring components. A component is considered to be a neighboring component if it is within an angle $\Delta = 0.01 \cdot \delta\theta_{\mathrm{k}}$ of a component defining the baseline $\delta\theta_{\mathrm{k}}$.

The experimental rotation measure and emission measure structure functions are shown in Figures 6-2 and 6-3, respectively. The functional forms of the observed rotation measure and emission measure structure functions for angular separations $\delta\theta > 1.0°$ were obtained by least squares fitting a power law of the form $\mathrm{D}\,(\delta\theta) = \mathrm{A}\ \delta\theta^{\mathrm{B}}$ to the data. The least squares fits (shown as dashed lines in Figures 6-2 and 6-3) give

$$\mathrm{D_{RM}}(\delta\theta > 1.0°) = (340 \pm 30)\ \delta\theta^{0.64\pm0.06}\ \mathrm{rad^2\ m^{-4}} \tag{6.4}$$

and

$$\mathrm{D_{EM}}(\delta\theta) = (10.0 \pm 0.5)\ \delta\theta^{0.73\pm0.04}\ \mathrm{cm^{-12}\ pc^2}. \tag{6.5}$$

In calculating the emission measure structure function, we have removed two apparently anomalous regions located at approximately RA $2^h\ 35^m$, DEC $+43°$ and RA $2^h\ 55^m$, DEC $+37°$. These two regions have emission measures which are approximately 10 cm^{-6} pc larger than the emission measures observed throughout the rest of the field and thus do not seem characteristic of the diffuse medium seen in the remainder of the field. These two bright emission measure regions thus have the affect of biasing the power of the observed structure function by a factor of two. Another argument for excluding these two regions is that no radio sources with usable rotation measures were observed in this part of the field. The rotation measure structure function thus contains no information on these regions or features. Excluding these two regions from the data set, the emission measure structure function shown in Figure 6-4 is obtained. A least squares fit to these data give

$$D_{EM}(\delta\theta) = (5.5 \pm 0.6)\ \delta\theta^{0.73\pm0.08}\ cm^{-12}\ pc^2. \tag{6.6}$$

The removal of any other two randomly chosen regions does not affect the observed emission measure structure function. Even if these two bright emission measure regions are typical features observed in the diffuse ISM, they are under-sampled in the available H_α data. Thus these two regions have been excluded from the emission measure structure function shown in all further analysis.

6.3 The Theoretical Structure Functions

In this section we consider theoretical models for the rotation measure structure function which can be compared with the observational results presented in Figures 6-2 and 6-4. These models incorporate various estimates for the intensity and spectral characteristics of the magnetic field and density fluctuations in the interstellar medium. Previous derivations of D_{RM} have been made by Simonetti et al. (1984),

but have assumed that the rotation measure fluctuations occur in $\vec{\beta} = n_e\vec{B}$ without segregating the contributions of density and magnetic field components. To the author's knowledge a derivation for D_{EM} has not been made in the literature. We will now derive D_{RM} and D_{EM} assuming that fluctuations occur separately in both the electron density and magnetic field. We will use the following geometry (see Figure 6-5): the observer is located at the origin of a rectangular coordinate system and observes the rotation measure and emission measure along two lines of sight separated by an angle $\delta\theta$. The random fluctuations in the electron density and magnetic field are described by the following:

$$n = n_o + \delta n \tag{6.7}$$

$$\vec{B} = \vec{B_o} + \delta\vec{B} \tag{6.8}$$

where n_o and $\vec{B_o}$ are the mean large scale components of the electron density and magnetic field described in Chapter 5. The quantities δn and $\delta\vec{B}$ are the spatially fluctuating components of the electron density and magnetic field respectively. The amplitudes of the fluctuations are assumed to be zero mean, isotropic Gaussian processes. It is also assumed that the fluctuations in the magnetic field and the electron density are related in such a fashion that

$$< \delta n|\delta\vec{B}| > \neq 0 \tag{6.9}$$

but

$$< \delta n \delta B_i >= 0 \tag{6.10}$$

where i=1,2,3 and δB_i is the component of $\delta\vec{B}$ along the i axis. Equation (6.10) most likely does not represent the actual case for the turbulence in the ISM. In reality the electron density fluctuations are most likely aligned along the magnetic field such as seen in the solar wind (Armstrong et al. 1990). Evidence for anisotropy of density

irregularities in the interstellar medium does indeed exist (Wilkinson et al. 1994 and Molnar et al. 1995), but the degree of anisotropy is not so pronounced as is the case for the solar wind (Armstrong et al. 1990). Although the difference in the observed anisotropy for the solar wind and interstellar medium may be due to greater randomization by line-of-sight integration for the latter medium, we feel it is premature at this point to take into account anisotropy of the turbulence. Finally, our observations are sensitive to ISM fluctuations on large scales, which are comparable in magnitude to the systematic field $\vec{B_o}$. For such large amplitude fluctuations there are no theoretical reasons for expecting anisotropic turbulence (Zank and Matthaues 1992). It is also assumed that the fluctuations in the electron density and magnetic field occur over the same size scales in the ISM. This assumption stems from the fact that events which put energy into the ISM, such as supernova explosions or stellar winds, will affect both the interstellar electron density and magnetic field on roughly the same size scales.

We now have the following relations and definitions to use in deriving the structure functions:

$$< \delta n > = 0 \tag{6.11}$$

$$< \delta B_i > = 0 \tag{6.12}$$

$$< \delta B_i \delta B_j >= 0 \quad \text{for } i \neq j \tag{6.13}$$

$$R_n(|\vec{r}|) \equiv < \delta n(\vec{r_o}) \delta n(\vec{r_o} + \vec{r}) > \tag{6.14}$$

$$R_B(|\vec{r}|) \equiv < \delta B_i(\vec{r_o}) \delta B_i(\vec{r_o} + \vec{r}) > = < \delta B_j(\vec{r_o}) \delta B_j(\vec{r_o} + \vec{r}) > \tag{6.15}$$

$$R_n^4(|\vec{r}|) \equiv < \delta n(\vec{r_o})^2 \delta n(\vec{r_o} + \vec{r})^2 > \tag{6.16}$$

$$R^4_{B_{ijkl}}(|\vec{r}|) \equiv < \delta B_i(\vec{r_o}) \delta B_j(\vec{r_o}) \delta B_k(\vec{r_o} + \vec{r}) \delta B_l(\vec{r_o} + \vec{r}) > \tag{6.17}$$

$$R_{nB}(|\vec{r}|) \equiv < \delta n(\vec{r_o}) \delta B_i(\vec{r_o}) \delta n(\vec{r_o} + \vec{r}) \delta B_i(\vec{r_o} + \vec{r}) > \tag{6.18}$$

where B_i is a component of the magnetic field along one of the axes (i.e. i,j,k, and l=1,2,3). The fact that R_n, R_B, R_n^4 and R_B^4 are only a function of the separation $|\vec{r}|$, independent of position, results from the assumptions of the homogeneity and isotropy of the turbulence.

Using the geometry shown in Figure 6-5, we will assume that the medium is a plane-parallel slab of thickness L in the z-direction. For a line of sight L′, at an angle $\delta\theta$ with the z-axis, we have $L' = L/\cos\delta\theta$. The equations for D_{RM} and D_{EM} are then

$$D_{EM}(\delta\theta) = < [\int_0^L n(z,0)^2 dz - \int_0^{L'} n(\zeta\cos\delta\theta, \zeta\sin\delta\theta)^2 d\zeta]^2 > \tag{6.19}$$

$$\begin{aligned} D_{RM}(\delta\theta) =< [&\int_0^L n(z,0)\vec{B}(z,0)\cdot d\vec{z} \\ &- \int_0^{L'} n(\zeta\cos\delta\theta, \zeta\sin\delta\theta)\vec{B}(\zeta\cos\delta\theta, \zeta\sin\delta\theta)\cdot d\vec{\zeta}]^2 > \end{aligned} \tag{6.20}$$

where $\hat{\zeta}$ is a unit vector along the line of sight L′. Applying the conditions in equations (6.11) through (6.18) and assuming that $Ll_o^{-1}\delta\theta < 1$ and $L \gg l_o$, so that we can let $\int_o^{L'} dz \int_0^L d\zeta \to \int_{-\infty}^{\infty} dy \int_0^L d\zeta$ where $y = \zeta - z$, we find (see Appendix A)

$$D_{EM}(\delta\theta) = 4C_n^2 \left[f(\alpha) n_o^2 + g(\alpha) q_o^{1-2\mu} C_n^2\right] L^{2\mu+1} \delta\theta^{2\mu} \tag{6.21}$$

$$D_{RM}(\delta\theta) = (0.81)^2 \left[f(\alpha)\left(n_0^2 C_B^2 + B_{oz}^2 C_n^2\right) + C_n^2 C_B^2 g(\alpha) q_o^{1-2\mu}\right] L^{2\mu+1} \delta\theta^{2\mu} \tag{6.22}$$

for $0.5 < \alpha < 4$ where $\mu = \alpha/2 - 1$,

$$f(\alpha) = \frac{4\pi^2 \Gamma(1-\mu)}{2^{2\mu}(2\mu+1)\mu\Gamma(1+\mu)} \tag{6.23}$$

$$g(\alpha) = \frac{2\pi^3 \Gamma(\mu-0.5)^2 \Gamma(1-\mu)}{\mu^2(2\mu+1)\Gamma(2\mu-1)\Gamma(\mu+1)} \tag{6.24}$$

and α is the spectral index of the power law describing the fluctuations with C_n^2 and C_B^2 being the renormalization constants. We have also made the assumption that the outer

scale for electron density fluctuations is the same as the outer scale for magnetic field fluctuations. Details of the derivation are given in the Appendix A. For Kolmogorov turbulence, $\alpha = 11/3$, equations (6.21) and (6.22) can be expressed as

$$D_{EM}(\delta\theta) = \left[15.316 \left(\frac{n_o}{0.1 \text{ cm}^{-3}} \right)^2 + 1.405 \left(\frac{l_o}{\text{pc}} \right)^{2/3} \left(\frac{C_n^2}{10^{-3.0} \text{ m}^{-20/3}} \right) \right] \times \left(\frac{C_n^2}{10^{-3.0} \text{ m}^{-20/3}} \right) \left(\frac{L}{\text{kpc}} \right)^{8/3} \left(\frac{\delta\theta}{\text{degrees}} \right)^{5/3} \tag{6.25}$$

$$D_{RM}(\delta\theta) = \left[251.226 \left\{ \left(\frac{n_o}{0.1 \text{ cm}^{-3}} \right)^2 \left(\frac{C_B^2}{10^{-13} \text{ m}^{-2/3} \ \mu\text{G}^2} \right) + \left(\frac{B_{oz}}{\mu\text{G}} \right)^2 \left(\frac{C_n^2}{10^{-3.0} \text{ m}^{-20/3}} \right) \right\} + 23.043 \left(\frac{C_n^2}{10^{-3.0} \text{ m}^{-20/3}} \right) \left(\frac{C_B^2}{10^{-13} \text{ m}^{-2/3} \ \mu\text{G}^2} \right) \left(\frac{l_o}{\text{pc}} \right)^{2/3} \right] \times \left(\frac{L}{\text{kpc}} \right)^{8/3} \left(\frac{\delta\theta}{\text{degrees}} \right)^{5/3}. \tag{6.26}$$

The expressions for the rotation measure and emission measure structure functions, equations (6.20) and (6.21), depend on several characteristics of the turbulence. These are α, the power law index of the spectra, C_n^2, C_B^2, the outer scale $l_o = \frac{2\pi}{q_o}$ and the mean characteristics of the interstellar plasma, n_o and $B_{oz} = B_{\parallel}$. Independent information from previous observations yields plausible initial estimates for all of these quantities. In addition, we used the observed structure functions to fine tune some of these quantities. A large body of interstellar scintillation data suggests $\alpha = 11/3$, the Kolmogorov value. The line of sight component of the magnetic field was chosen such that the mean rotation measure for this field is reproduced when combined with the electron density models. For a scale height of 1 kpc in the Reynolds layer, we find an average path length, L, of 2.9 kpc through the Reynolds layer for the region. Cordes et al. (1985) find a range of values for C_n^2 for the diffuse ISM with

$C_n^2 = 10^{-3.5}$ m$^{-20/3}$ being the average value. Armstrong et al. (1995), however, find a nominal value of $C_n^2 = 10^{-3.0}$ m$^{-20/3}$ for the diffuse ISM. The data of Armstrong et al. include measurements of the ISS turbulence on larger scale sizes than was available to Cordes et al. Since the Armstrong et al. data include information from larger scale sizes, and thus on scale sizes nearer to the size scale we are interested in, we adopt $C_n^2 = 10^{-3.0}$ m$^{-20/3}$ as the nominal value for the diffuse ISM. There is a pulsar (J0156+3949) that lies at the western edge of the region were the H_α measurements where made. This pulsar shows a dispersion measure of DM $= 59.0 \pm 6.0$, which indicates a value of $C_n^2 = 10^{-2.9} \rightarrow 10^{-3.6}$ m$^{-20/3}$ (see Figure 9 of Cordes et al. 1985). The pulsar 0320+39, which lies just to the east of the region of our observations has a measured value of $C_n^2 = 10^{-2.9 \pm .1}$ m$^{-20/3}$. With the lack of a direct measurement of C_n^2 within our region of observations we adopt a value of $C_n^2 = 10^{-3.0}$ m$^{-20/3}$. This choice is based on the nominal value of C_n^2 found by Armstrong et al. (1995) and is found to be consistent with data from the two pulsars on either side of the field. We have adopted a value of the outer scale of 3 pc. This choice was made from the observed structure functions and will be justified in Section 6.4. Assuming that the outer scale of the magnetic turbulence is also 3 pc, and further assuming that the RMS value of the magnetic field fluctuations on this scale is of the order (~ 1 μG), we have $C_B^2 = 3 \times 10^{-13}$ μG^2 m$^{-2/3}$.

With the above parameters for the characteristics of turbulence in the interstellar medium, we have for the model emission measure and rotation measure structure functions,

$$D_{EM}(\delta\theta) = 73.7\ \delta\theta^{5/3}\ \text{cm}^{-12}\ \text{pc}^2 \tag{6.27}$$

and

$$D_{RM}(\delta\theta) = 5906\ \delta\theta^{5/3}\ \text{rad}^2\ \text{m}^{-4} \tag{6.28}$$

If we consider that only fluctuations in the electron density cause rotation measure fluctuations (i.e. $\delta B = 0$), then we have

$$D_{RM}(\delta\theta) = 2611\ \delta\theta^{5/3}\ \text{rad}^2\ \text{m}^{-4} \tag{6.29}$$

for the rotation measure structure function. Equation (6.29) is equivalent to equation (6) of Simonetti (1988), with the value of $C_n^2 = 10^{-3.0}\ \text{m}^{-20/3}$ from above used, $L = 2.9$ kpc (a typical path length for this region), and $B_{\|} = -0.8\ \mu$G for the line of sight component of the magnetic field. The value of $B_{\|}$ was calculated from the galactic magnetic field models described in Chapter 5 and parameterized in Table 5-2.

In the derivation of the structure function, an expansion in terms of the powers of $Ll_0^{-1}\delta\theta$ was made assuming $Ll_o^{-1}\delta\theta < 1.0$. Using the values $L = 2900$ kpc and $l_o = 3$ pc we find that $Ll_o^{-1}\delta\theta = 1.0$ for $\delta\theta = 0.06°$. Thus for $\delta\theta > 0.06°$ this expansion breaks down. We would therefore expect the $\delta\theta^{5/3}$ behavior of the structure function to break down around $\delta\theta \sim 0.06°$. Physically, this critical lag corresponds to the angular size associated with the outer scale. Thus examination of empirical plots like Figures 6-2 and 6-4 allows one to measure the outer scale by noting the angular scale at which the power law functional form of the structure function changes.

6.4 Analysis of the Observed Structure Functions

6.4.1 Observed and Theoretical Structure Functions

In this section we consider the extent to which the observed structure functions shown in Figures 6-2 and 6-4 correspond to the theoretical estimates discussed in the preceding section. Both the magnitude and functional form of the structure function contain information on interstellar turbulence.

The first thing to note from Figures 6-2 and 6-4 is that the slopes for both structure functions are not in agreement with the expected $^5/_3$ value for angular

separations $\delta\theta \geq 1.0°$. What makes this particularly notable is that a power law with an exponent of 2/3 does indeed appear to be an appropriate representation of the data for both emission measure and rotation measure, rather than an unnatural fit to observations described by some quite different mathematical function. In addition, for angular lags $\delta\theta \geq 1.0°$, the predicted structure functions (equations 6.27 and 6.28) with a single Kolmogorov spectrum have larger variance than that which actually is observed. Recall that these predictions employ an extrapolation of Kolmogorov spectra to arbitrarily large scales.

6.4.2 Value of the Outer Scale

In our model for the interstellar turbulence described in Section 6.2, we chose an outer scale of 3 parsecs. Since the emission measure data are complete both spatially and in velocity for our region of observations, we can constrain the value of the outer scale by dividing the emission measure data into various velocity ranges. Figure 6-6 shows the emission measure structure function calculated for several velocity bins. Once again, the dashed line is a least squares fit to the data. The values for the least squares fits to these structure functions are listed in Table 6-1. The first column in Table 6-1 gives the velocity range for a given velocity bin while the second column gives the distance estimate for these velocities assuming that the velocities are due to galactic rotation (Reynolds 1980). The third and fourth columns list the parameters found for a least squares fit to the emission measure structure function for each velocity bin. For this region of the sky the more positive the velocity with respect to the local standard of rest, the nearer the gas is to the sun. What we observe is that at large distances the structure function is nearly constant for all angular separations. This is what is to be expected if we are looking at angular separations that are greater than the outer scale of the turbulence. As we look at the structure function for velocity bins

whose distances are closer to the sun, we observe that the structure function starts to approach a slope of ~ 1. However, even for the nearest gas, the structure function does not show a $^5/_3$ slope consistent with Kolmogorov turbulence. Since the gas at $V_{LSR} \geq -16$ km/s lies at a distance of ≤ 500 pc and shows that the outer scale for Kolmogorov turbulence is less than one degree, we can put an upper limit of 9 pc on the outer scale for turbulence in the interstellar medium. Galactic rotation models predict that all V_{LSR} in this region of the sky should be negative. Since we do observe gas at positive velocities and there is good evidence that this region is associated with the H II region of ξ Per, we can assume the distance to ξ Per of 400 pc for the distance to the gas at $V_{LSR} \geq 0$ km/s, thus giving an upper limit of ~ 7 pc for the outer scale of Kolmogorov turbulence in the interstellar medium.

We can also put a lower limit on the value for the outer scale of Kolmogorov turbulence in the ISM. This is achieved in the following manner. We know that the observed emission measure structure function does not exhibit the characteristic Kolmogorov slope of $^5/_3$. Thus, the prediction of equation (6.19) for a given C_n^2 and $q_o = \frac{2\pi}{l_o}$ (assuming the Kolmogorov value $\alpha = {}^{11}/_3$) cannot be a valid solution if it predicts a $\delta\theta^{5/3}$ emission measure structure function for angular lags on which the observations show $D_{EM} \propto \delta\theta^{.7}$. This can be stated as the condition

$$4C_n^2 \left[f(\alpha)n_o^2 + g(\alpha)q_o^{1-2\mu}C_n^2\right] L^{2\mu+1} \left(\frac{1^\circ}{57.3^\circ \text{ rad}^{-1}}\right)^{2\mu} \geq 5.5 \pm 0.6 \text{ cm}^{-12} \text{ pc}^2. \qquad (6.30)$$

We have relaxed the condition that equation (6.21) is only valid for $\delta\theta \leq \frac{2l_o}{L}$ and only require that the $\delta\theta^{5/3}$ power law (assuming Kolmogorov turbulence) of equation (6.21)

only be valid for $\delta\theta < 1.0°$. Using a value of $C_n^2 = 10^{-2.9}$ m$^{-20/3}$ in equation (6.30) with a path length of 2.9 kpc through the medium gives a lower limit of $l_o \geq 0.1$ pc.

6.4.3 The Influence of Galactic Structure

In spite of the uncertainty in modeling the large scale magnetic field in this region of the sky, we can still use these models to predict the contribution of galactic structure to the structure functions, which describe rotation measure variability attributable to interstellar turbulence. Values for the rotation measure (D_{RM}) and emission measure (D_{EM}) structure functions derived from the rotation measure and emission measure models are presented in Table 6-2. The structure functions were calculated directly from the model rotation measures. These calculations were carried out because the structure functions will be our basic tool for measuring interstellar turbulence, and as discussed by Simonetti et al. (1984), large scale, deterministic variations in the galactic rotation measure also contribute to the structure function. These contributions must be accurately estimated to allow determination of the turbulent component. We model both the emission measure and rotation measure structure functions by $D(\delta\theta) = A\delta\theta^B$, where $\delta\theta$ is in degrees. The first and second columns of Table 6-2 give the magnetic field and density models respectively. The third and fourth columns list the values of A and B found for the rotation measure structure function derived from the model rotation measures. The fifth and sixth columns list the values of A and B found for the emission measure function derived from the density models. The logarithmic slopes (corresponding to B in Table 6-2) for D_{RM} are near 2 as would be expected for the contribution of galactic structure to the structure functions (Simonetti et al. 1984). This is also the case for D_{EM} using the Taylor and Cordes electron density model. However, the Reynolds + Strömgren model has a logarithmic slope less than two, which is probably due to the fact that the H II region has been

added to this model. Thus we would not expect to find a slope of two like the simple model for the large scale structure contribution to the structure function, as discussed by Simonetti et al. (1984). Although the rotation measure models do not provide an entirely adequate description of the large scale rotation measures, they should provide an adequate estimate of the deterministic, galactic structure contribution to the measured structure functions. Using the fits in Table 6-2, we find that the galactic structure contribution is totally negligible at angular lags of order a degree, and approaches the order of several tens of percent of the observed value only for the largest angular lags of 10°. We conclude that large scale galactic variations will not affect the interpretation of the structure functions.

6.4.4 Modeling the Observed Turbulence

As has been discussed in section 6.4.1, the observed slopes for the emission measure and rotation measure structure functions are consistent with slopes of 2/3 rather than the Kolmogorov slope of 5/3. In section 6.4.2 we found that the outer scale of the Kolmogorov turbulence is in the range 0.1 pc $< l_o <$ 7 pc. For an average path length of L = 2900 pc through the ISM in the region of the sky, it would be expected that the $\delta\theta^{5/3}$ power law behavior of the structure function breaks down in the range $0.002° < \delta\theta < 0.14°$.

Since there are no data points for D_{EM} for $\delta\theta < 1°$ and there are only three data points for D_{RM} below $\delta\theta < 0.15°$, we are not able to directly measure the slope of the structure function indicative of Kolmogorov turbulence. However, the observed slopes for the emission measure and rotation measure structure functions with $\delta\theta > 1°$ suggest a slope of 2/3 which is consistent with two dimensional turbulence (Thompson et al. 1991). Thus we postulate a model in which the Kolmogorov turbulence in the ISM (at least for this region of the sky) is contained in thin sheets or

filaments. In this model, Kolmogorov turbulence ($D \propto \delta\theta^{5/3}$) is observed for angular separations corresponding to scale sizes smaller than the thickness of the thin sheets or filaments. For angular lags corresponding to scale sizes larger than the thickness of the thin sheets, the turbulence appears to be two dimensional and the structure functions at these angular lags are proportional to $\delta\theta^{2/3}$. Thus a slope of 2/3 for the two dimensional turbulence implies that $\alpha = 11/3$ for the three dimensional turbulence. Interstellar scintillation observations provide evidence for Kolmogorov density fluctuations on smaller scales (10^7 to 10^{14} cm) and we are assuming that a transition to two dimensional turbulence occurs on the scales we are measuring. We can thus use the information on the turbulence provided by the ISS measurements in our model for the structure functions.

The predictions in section 6.4.2 for the rotation measure and emission measure structure functions (equations 6.21 and 6.22) for Kolmogorov turbulence ($\alpha = 11/3$) are taken to be valid for $L l_o^{-1} \delta\theta \leq 1$. At $L l_o^{-1} \delta\theta = 1$ the structure functions are assumed to "turn over" to a power law with a logarithmic slope of 2/3. The structure functions predicted by this model have the following structural form

$$\begin{aligned} D_{EM}(\delta\theta) &= A\delta\theta^{2\mu} \text{ for } \delta\theta \leq \frac{l_o}{L} \\ &= A\frac{l_o}{L}\delta\theta^{2\mu-1} \text{ for } \delta\theta \geq \frac{l_o}{L} \end{aligned} \tag{6.31}$$

where

$$A = 4C_n^2 \left[f(\alpha) n_o^2 + g(\alpha) q_o^{1-2\mu} C_n^2 \right] L^{2\mu+1}$$

and

$$\begin{aligned} D_{RM}(\delta\theta) &= B\delta\theta^{2\mu} \text{ for } \delta\theta \leq \frac{l_o}{L} \\ &= B\frac{l_o}{L}\delta\theta^{2\mu-1} \text{ for } \delta\theta \geq \frac{l_o}{L} \end{aligned} \tag{6.32}$$

where

$$B = (0.81)^2 \left[f(\alpha) \left(n_0^2 C_B^2 + B_{oz}^2 C_n^2 \right) + C_n^2 C_B^2 g(\alpha) q_o^{1-2\mu} \right] L^{2\mu+1}.$$

Since we have prior knowledge that $C_n^2 = 10^{-3.0}$ m$^{-20/3}$, $n_o = 0.025$ cm^{-3}, $B_{oz} = -0.8$ μG and $L = 2900$ pc we first "fit" equation (6.31) to the measured emission measure structure function in order to determine the outer scale of the Kolmogorov turbulence. It should be noted that both the measured emission measure and rotation measure structure functions are consistent with a 2/3 slope. The outer scale is determined from the angular lag $\delta\theta_o$ at which the theoretical expression (6.21) intersects the least squares fit power law (equation 6.6). The outer scale is related to the corresponding angular scale by $l_o = \delta\theta_o L$. The result is an outer scale $l_o = 3 \pm 1$ pc. The resulting structure function (equation 6.31) is shown in Figure 6-7. The dashed line in Figure 6-7 is the least squares fitted power law (equation 6.6) and the solid line is the prediction of equation (6.31) with $C_n^2 = 10^{-3.0}$ m$^{-20/3}$ and $l_o = 3$ pc.

We now fit equation (6.32) to the measured rotation measure structure function to determine what values of C_B^2 are permissible. This is done in a similar manner as above, requiring that the theoretical expression (6.22) is equal to the least squares fit power law (equation 6.4) at $\delta\theta = \frac{l_o}{L}$, resulting in a value of $C_B^2 = (3 \pm 1) \times 10^{-13}$ m$^{-2/3}$ μG^2. The fit to the observed rotation measure structure function is shown in Figure 6-8. The dashed line shown in Figure 6-8 is the least squares fit of the power law to the data (equation 6.4) while the solid line is the prediction of equation (6.32) with $C_n^2 = 10^{-3.0}$ m$^{-20/3}$, $l_o = 3$ pc and $C_B^2 = 3 \times 10^{-13}$ m$^{-2/3}$ μG^2. For comparison we have plotted the prediction of equation (6.32) with $C_B^2 = 0$ as the dotted line in Figure 6-8. It is easily seen that all but two points are several sigma above the prediction of equation (6.32) with $C_B^2 = 0$ (i.e. electron density fluctuations only). This is the first separation of the magnetic field and density contributions to

rotation measure fluctuations in the interstellar medium. Our result may be taken as observational evidence of true magnetohydrodynamic turbulence in the ISM. It is worth noting that Hollweg et al. (1982) used an observational signature identical to ours, an excess in the rotation measure above what could be produced from density fluctuations alone, to infer the presence of magnetic field fluctuations and hydromagnetic waves in the solar corona. With $l_o = 3$ pc and $C_B^2 = 3 \times 10^{-13}$ m$^{-2/3}$ μG^2 we find that the amplitude of the magnetic field fluctuations is ~ 1.1 μG, which is about $30 - 50\%$ of the amplitude of the uniform magnetic field. This is the Kolmogorov spectrum portion of the fluctuating magnetic field. The total magnitude of the random field including a contribution from the two dimensional turbulence would be larger.

If we assume that a smaller value of C_n^2 is appropriate for this region, then the emission measure structure function requires a larger outer scale (see Figure 6-7 and equation 6.31). This leads to the result that the required value of C_B^2 needed to fit the observed rotation measure structure function decreases. If we let C_n^2 become larger then a smaller outer scale is needed and a larger value for C_B^2 is needed to model the observed rotation measure structure function. A lower limit of the value of C_B^2 can thus be obtained by assuming that $l_o = 7$ pc, the maximum value permitted (see section 6.4.2). The value of C_B^2 which results is $C_B^2 \geq 1.3 \times 10^{-13}$ m$^{-2/3}$ μG^2. The structure function which results from this set of parameters falls well below the measurements for the smallest angular lags. It is thus a less satisfactory model than the one shown in Figure 6-8.

We now address the question of determining the outer scale of the two dimensional turbulence (l_o^{2D}). The outer scale of the two dimensional turbulence can be estimated from the emission measure structure functions in the various velocity ranges (see Table 6-1 and Figure 6-6). From Table 6-1 it is easily seen that the measured slope of the emission measure structure function for the velocity range

$V_{LSR} = +8 \rightarrow +20$ km s^{-1} is consistent with a slope of 2/3 for angular lags from $\delta\theta = 1^\circ \rightarrow 10^\circ$. Since the H_α emission for this velocity range is at a distance of ~ 400 pc, we find $l_o^{2D} \geq 70$ pc. The emission measure structure function for the velocity range $V_{LSR} = -76 \rightarrow -64$ km s^{-1} is consistent with being a constant value. Since the H_α emission for this velocity range is at a distance of sim5500 pc, we find $l_o^{2D} \leq 96$ pc. Thus we have the limits 70 pc $\leq l_o^{2D} \leq 96$ pc for the outer scale of the two dimensional turbulence. Lazaryan and Shutenkov (1990) found an outer scale of 90 pc for the magnetic field fluctuations in the galactic background radiation towards the north galactic pole. It should be noted that the outer scale of the two dimensional turbulence is such that the corresponding angular sizes are $\sim 5^\circ$ (half the size of our region of observations) at a distance of 1 kpc. Thus the magnetic field anomaly discussed in Chapter 5 may well be due to magnetic field fluctuations with scale sizes near the outer scale of the two dimensional turbulence.

We have found that the observed emission measure and rotation measure structure functions are consistent with a model in which Kolmogorov turbulence is contained in thin sheets or filaments of about 3 pc thickness with $C_n^2 = 10^{-3.0}$ m$^{-20/3}$ and $C_B^2 = 3 \times 10^{-13}$ m$^{-2/3}$ μG^2. The level of Kolmogorov turbulence in this model is consistent with that inferred from ISS observations, and thus supports the idea of a power law spectrum spanning many decades of wave number (Armstrong et al. 1995). This model also indicates that magnetic field fluctuations are present in the ISM such that the turbulence in the ISM is truly magnetohydrodynamical turbulence.

6.5 Correlation of RM and EM

We have also computed the cross structure function for the observed emission measure and rotation measure values. The cross structure function is defined as

follows:

$$D_x(\delta\theta) = \frac{< [RM(\theta) - RM(\theta + \delta\theta)] [EM(\theta) - EM(\theta + \delta\theta)] >}{2\sigma_{RM}\sigma_{EM}} \quad (6.29)$$

where σ_{RM} and σ_{EM} are the standard deviation of the measured rotation measures and emission measures respectively. Note that the cross structure function can have negative values. For angular lags $\delta\theta = 1^\circ \rightarrow 4^\circ$, the cross structure function of emission measure and rotation measure is $D_x = 0.00 \pm 0.03$. This indicates that for angular lags $\delta\theta \leq 4^\circ$ there is no correlation between fluctuations in the emission measure and fluctuations in the rotation measure. For angular lags $\delta\theta \geq 4^\circ$, the cross structure function increases with increasing $\delta\theta$. This can easily be explained by noting that in the H II region of ξ Per the emission measure increases dramatically and the rotation measure becomes more positive. Thus for angular lags $\delta\theta \geq 4^\circ$, we interpret the increase in the cross structure function as being due to the H II region of ξ Per and the magnetic field anomaly that is most likely associated with the H II region.

As a cautionary note to the reader, it should be pointed out that the H_α measurements had a resolution of 0.8° while the rotation measure data had a resolution of $\sim 10''$. It is thus possible that the cross structure function is affected or biased by the highly dissimilar resolutions of the two data sets. However, even in the case of the solar wind, for which direct, in situ plasma measurements are available, the correlation between density and magnetic field fluctuations is lower than theoretically expected, for reasons which are not entirely understood (Bavassano and Bruno 1995).

6.6 The Nature of the Turbulence in the ISM

For angular separations $\delta\theta \geq 1.0^\circ$, the emission measure and rotation measure structure functions are consistent with a logarithmic slope of $^2/_3$. This slope is what is found for two dimensional turbulence (Thompson et al. 1991). One explanation of our results is that for angular separations $\delta\theta \leq 0.06^\circ$ we are seeing Kolmogorov

turbulence and for angular separations $\delta\theta \geq 0.06^\circ$ we are seeing effectively two dimensional turbulence. This situation could arise if the Kolmogorov turbulence is contained within thin sheets or filaments. For angular separations corresponding to distances less than the thickness of a thin sheet or filament, we would be probing the isotropic Kolmogorov turbulence inside the feature and would find a slope of $^5/_3$ for the structure functions. For angular separations greater than the thickness of the thin sheet or filament, the turbulence would appear two dimensional and we would then expect to find a slope of $^2/_3$. This effect is actually observed for the Earth's troposphere (Thompson et al. 1991). Another possible explanation would be that for gas near the sun we are sampling separations less than the outer scale where the structure functions should have a slope of $^5/_3$ while for the most distant gas we are sampling separations greater than the outer scale where the structure functions should be constant. Thus the observed structure function would appear to have a slope that is an "average" of these two cases and would be near to $^2/_3$. However, the analysis of the velocity data for the emission measures argues against this since Kolmogorov turbulence is not even observed for the gas nearest to the sun (see Table 6-1).

It is quite plausible that the turbulence in the interstellar medium lies in thin shells or filaments in this region of the sky. The strong emission measure features on the eastern side of the region shown in Figure 4-1 are possibly associated with the H II region of ξ Per, lying at the edge of a classical Strömgren sphere surrounding ξ Per. The velocities of these emission measure features also suggest that they are possibly the ionized edge of an H I cloud, which is itself part of an expanding shell of H I associated with Per OB2 (Reynolds 1988 and Sancisi 1984). If these features are in fact the ionized edges of H I clouds then the plasma at a small distance from the sun would lie in a thin sheet in this region. This would mean that we would be capable of resolving the Kolmogorov turbulence inside the thin sheet at small angular

separations, while at larger angular separations we would observe the turbulence as being two dimensional. Reynolds et al. (1995) have also identified several more filaments and loops in the H_α and H I emissions from this region of the sky. The H_α emission from other galaxies commonly show that filaments, shells and loops exist in the H_α structure (Walterbos and Braun 1994, Tenorio-Tagle and Bodenheimer 1988). In the Magellanic Clouds, it is found that the typical thickness of a shell filament is of the order of 5 pc (Kennicutt and Bresolin 1995). In our own galaxy, the H_α emission exhibits filamentary structure for angular scales $\geq 1^\circ$ (Rand 1994). The filaments of H_α could be the result of holes in the H II regions surrounding hot stars, whereby ionizing radiation could escape in small beams into the surrounding medium. Such filaments surrounding H II regions are seen in the Magellanic Clouds (Kennicutt and Bresolin 1995). The H_α filaments could also be the result of shocks seen edge on. Radio Loop II traverses the eastern side of our region with the edge of its shell following the western side of the bright emission measure features. It is not known if radio Loop II has any association with these emission measure features. Since Loop II is an old supernova remnant at a distance of $\sim$ 300 pc (Spoelstra 1984) it could also contribute to the "thin sheet morphology" of the turbulence. Loop II would have presumably swept up the magnetic field and gas of the interstellar medium as it expanded, leaving behind a shell structure in both the magnetic field and electron density. Wilkinson and Smith (1974) have estimated that the scale sizes of magnetic field irregularities in the galactic radio loops range from 0.1 pc to $\sim$ 5 pc. It is thus quite clear that there are several relatively nearby features which can produce shell like and filamentary features in the interstellar plasma. This would then be capable of giving rise to a composite structure function for rotation measure and emission measure in which Kolmogorov turbulence is seen for small angular separations while for larger angular separations the turbulence appears in two dimensional sheets and filaments causing the structure function to have

an entirely different slope. The size scales of the these features (~ 5 pc) are also in rough accord with the apparent outer scale of 3 pc found from our observations.

It is interesting to note that the observations of Simonetti et al. (1984) from $l = 70° \rightarrow 110°$ and $b = -45° \rightarrow +5°$ (his region 1), which is inside the boundaries of Loop II, show that the rotation measure structure function has a logarithmic slope of ~ 1 for angular separations $\delta\theta \geq 1°$. This result is similar to what we observe although our observations are concentrated in another part of Loop II. Further observations by Simonetti and Cordes (1986 and 1988) (see Figure 10 in Simonetti and Cordes 1986 and Figure 1 in Simonetti and Cordes 1988) show that for angular separations $\delta\theta \leq 0.1°$ in this region, the rotation measure structure function is consistent with the Kolmogorov slope of $^5/_3$ although they did not make this interpretation of their data. For Simonetti's region 3, concentrated from $l = 180° \rightarrow 220°$ and $b = 10° \rightarrow 50°$, an area near the galactic plane which is not inside a galactic loop, and also for his region about the North Galactic Pole ($b \geq 60°$) the rotation measure structure functions are both consistent with a logarithmic slope of zero for angular separations $\delta\theta \geq 1°$. This would indicate that the outer scale for all the turbulence (Kolmogorov and two dimensional) in the interstellar medium is $\leq 1°$ in these directions. It is inviting to speculate that since no galactic loops exist in these regions, we would not expect to see a slope of $^2/_3$ at large angular separations since there is no large, nearby shell in the interstellar magnetic field and electron density to produce a two dimensional turbulent spectra. We would thus see the rotation measure structure function increase with a $^5/_3$ slope until it reached the outer scale at which the structure function would become constant for larger angular separations. Most likely the two dimensional turbulence occurs in the nearby shell of a supernova remnant. The observations of Simonetti et al. (1984, 1986 and 1988), when combined with our data, seem to suggest that the angular

scale corresponding to the spatial outer scale for Kolmogorov turbulence in the ISM is $\leq 1.0°$ over most of the sky.

Table 6-1. Least squares fit to emission measure structure function for various velocity ranges.

V_{LSR}(km/s)	Distance(Kpc)[1]	A	B
$-76 \rightarrow -64$	5.4	0.11 ± 0.01	0.13 ± 0.07
$-64 \rightarrow -52$	4.5	0.18 ± 0.1	0.33 ± 0.05
$-52 \rightarrow -40$	3.6	0.19 ± 0.01	0.39 ± 0.03
$-40 \rightarrow -28$	2.6	0.16 ± 0.1	0.44 ± 0.04
$-28 \rightarrow -16$	1.6	0.23 ± 0.02	0.56 ± 0.05
$-16 \rightarrow -4$	0.5	0.71 ± 0.06	0.68 ± 0.06
$-4 \rightarrow +8$	≤ 0.5	1.31 ± 0.07	0.90 ± 0.04
$+8 \rightarrow +20$	≤ 0.5	0.54 ± 0.04	0.76 ± 0.06
All Velocities	. . .	10.0 ± 0.5	0.73 ± 0.04

[1]The distance values for each velocity bin were adapted from Reynolds (1980).

Note: The data are least squares fits of the structure functions to the formula:$D = A\delta\theta^B$.

Table 6-2. Predicted galactic contribution to rotation measure and emission measure structure functions from galactic models.

Model		RM		EM	
$\vec{B}$	n_e	A	B	A	B
RL	R+S	3.9 ± 0.5	2.16 ± 0.07	0.74 ± 0.06	1.07 ± 0.06
RL	TC[1]	4.2 ± 0.6	2.15 ± 0.07	0.06 ± 0.08	1.87 ± 0.08
Az	R+S	2.1 ± 0.3	2.11 ± 0.06	0.74 ± 0.06	1.07 ± 0.06
Az	TC[1]	2.0 ± 0.5	2.4 ± 0.1	0.06 ± 0.08	1.87 ± 0.08
Bi	R+S	5.0 ± 1.0	2.4 ± 0.1	0.74 ± 0.06	1.07 ± 0.06
Bi	TC[1]	6.0 ± 1.0	2.3 ± 0.1	0.06 ± 0.08	1.87 ± 0.08

[1] The Taylor and Cordes model was modified so that the mid-plane density of the diffuse electrons with a scale height of 880 pc was 0.027 cm^{-3} rather than 0.019 cm^{-3}.

Note: The data are least squares fits of the structure functions to the formula:$D = A\delta\theta^B$.

Figure 6-1. An example structure function for a function f(x) which is assumed to have a measurement error of $.2\sigma_f^2$ and a standard deviation about the mean of σ_f for all measured values. The correlation length of f(x) is ~ 1.

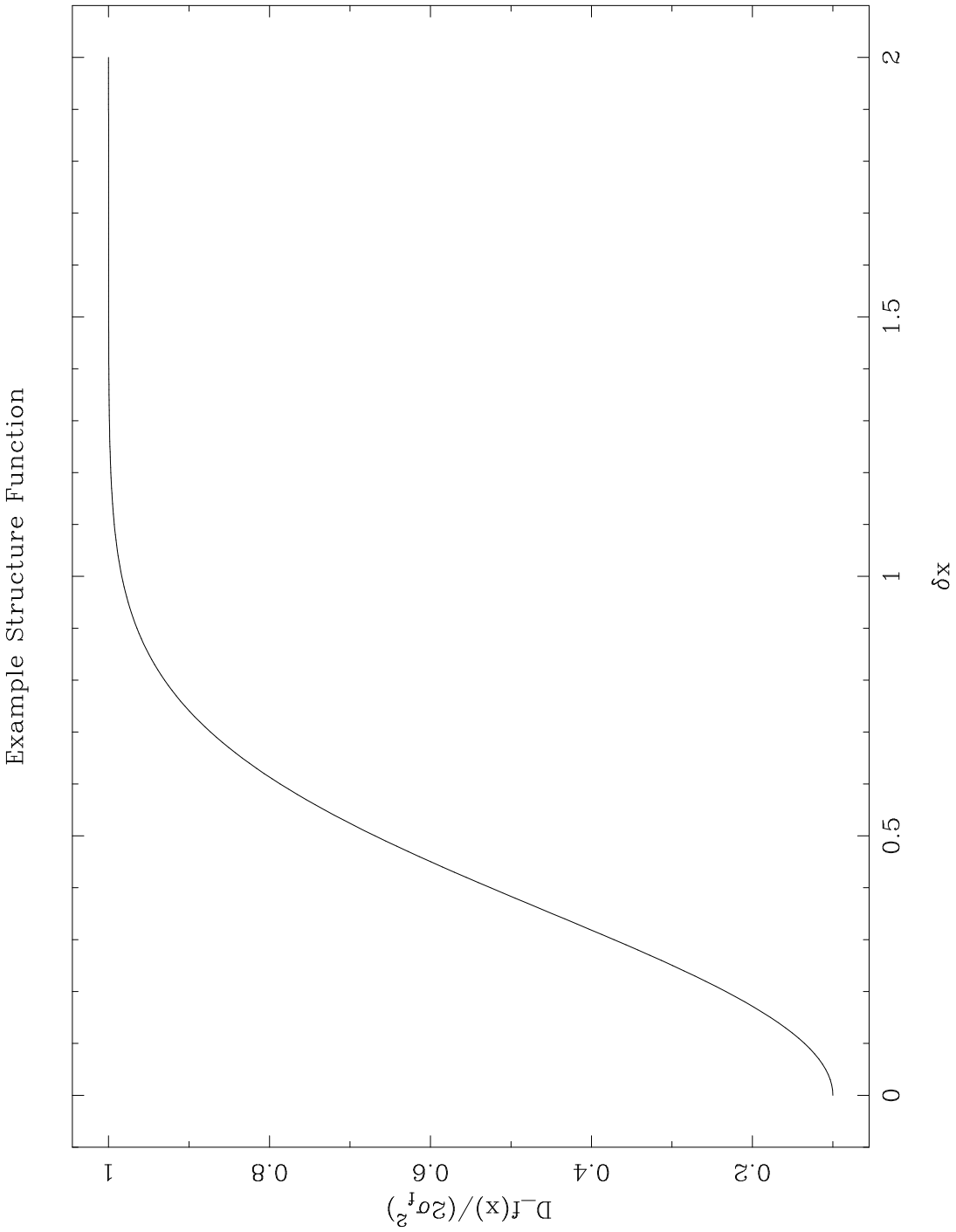
Example Structure Function
D_f(x)/(2σ_f^2)
δx
0
0.5
1
1.5
2
0.2
0.4
0.6
0.8
1

Figure 6-2. Plot showing the rotation measure structure function. The dashed line corresponds to the least squares fit to data point with $\delta\theta \geq 1.0°$, equation (6.4).

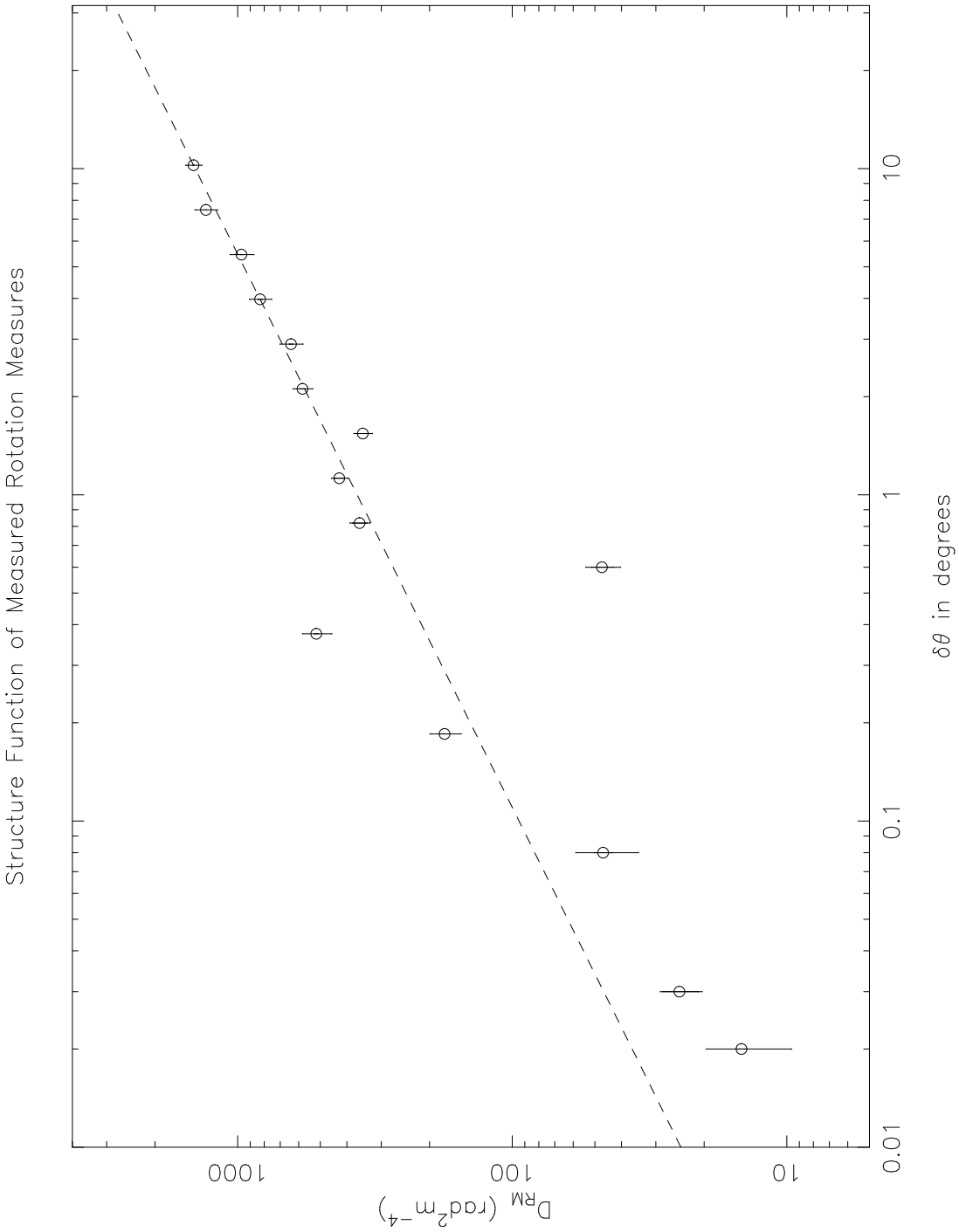
Structure Function of Measured Rotation Measures
D_{RM} (rad^{2}m^{-4})
1000
100
10
0.01
0.1
1
10
$\delta\theta$ in degrees

Figure 6-3. Plot showing the emission measure structure function. The dashed line represents the least squares fit to all data points, equation (6.5).

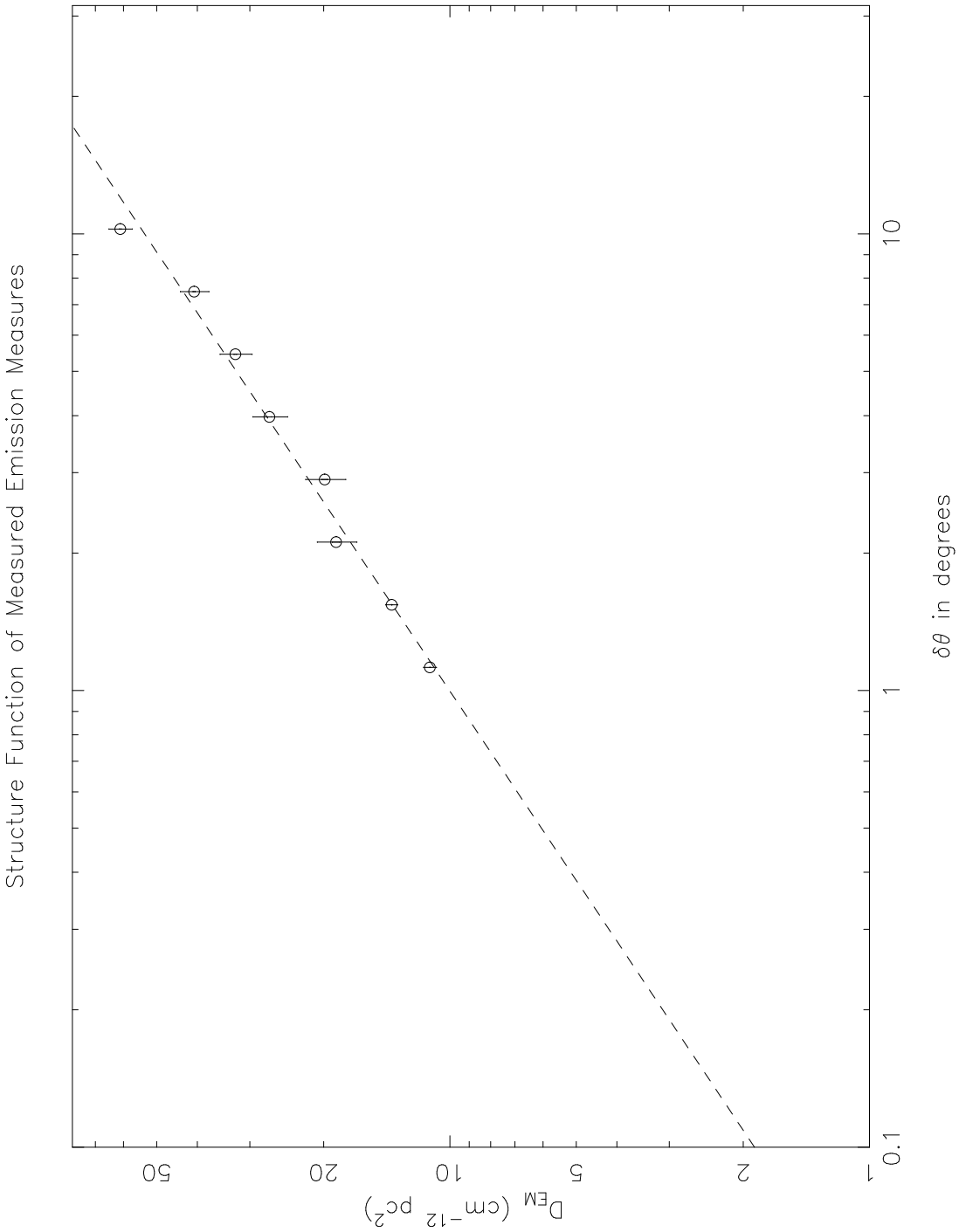
Structure Function of Measured Emission Measures
D_{EM} (cm^{-12} pc^2)
1
2
5
10
20
50
0.1
1
10
$\delta\theta$ in degrees

Figure 6-4. Plot showing the emission measure structure function. The two regions of anomalous H_α emission have been removed. The dashed line represents the least squares fit to all data points, equation (6.6).

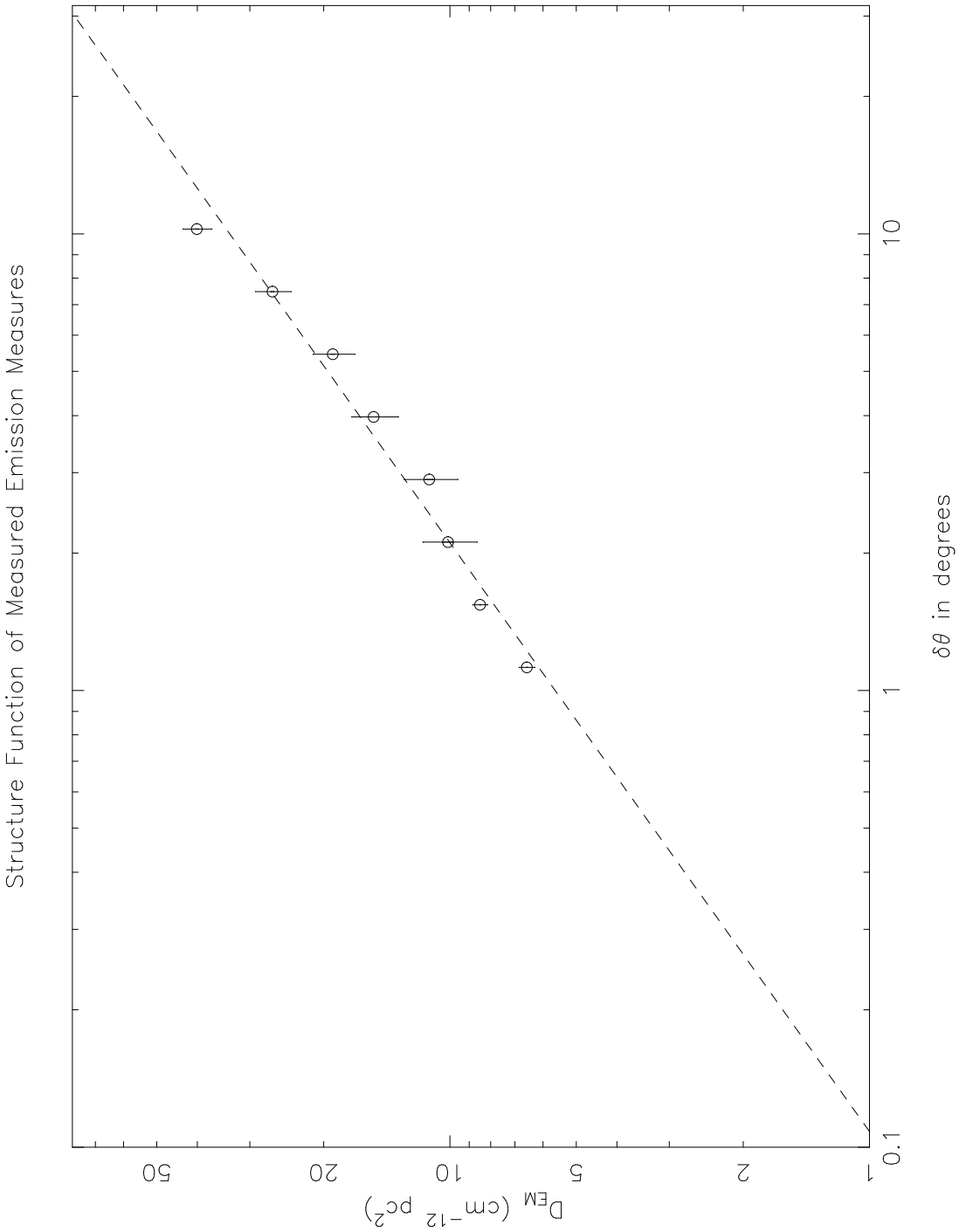
Structure Function of Measured Emission Measures
D_{EM} (cm^{-12} pc^2)
50
20
10
5
2
1
0.1
1
10
$\delta\theta$ in degrees

Figure 6-5. Geometry for the calculation of the structure functions of rotation measure and emission measure. Two lines of sight of length L and L$'$ are separated by an angle $\delta\theta$. The two lines of sight lie in a plane defined by the vectors $\hat{z}$ and $\hat{y}$.

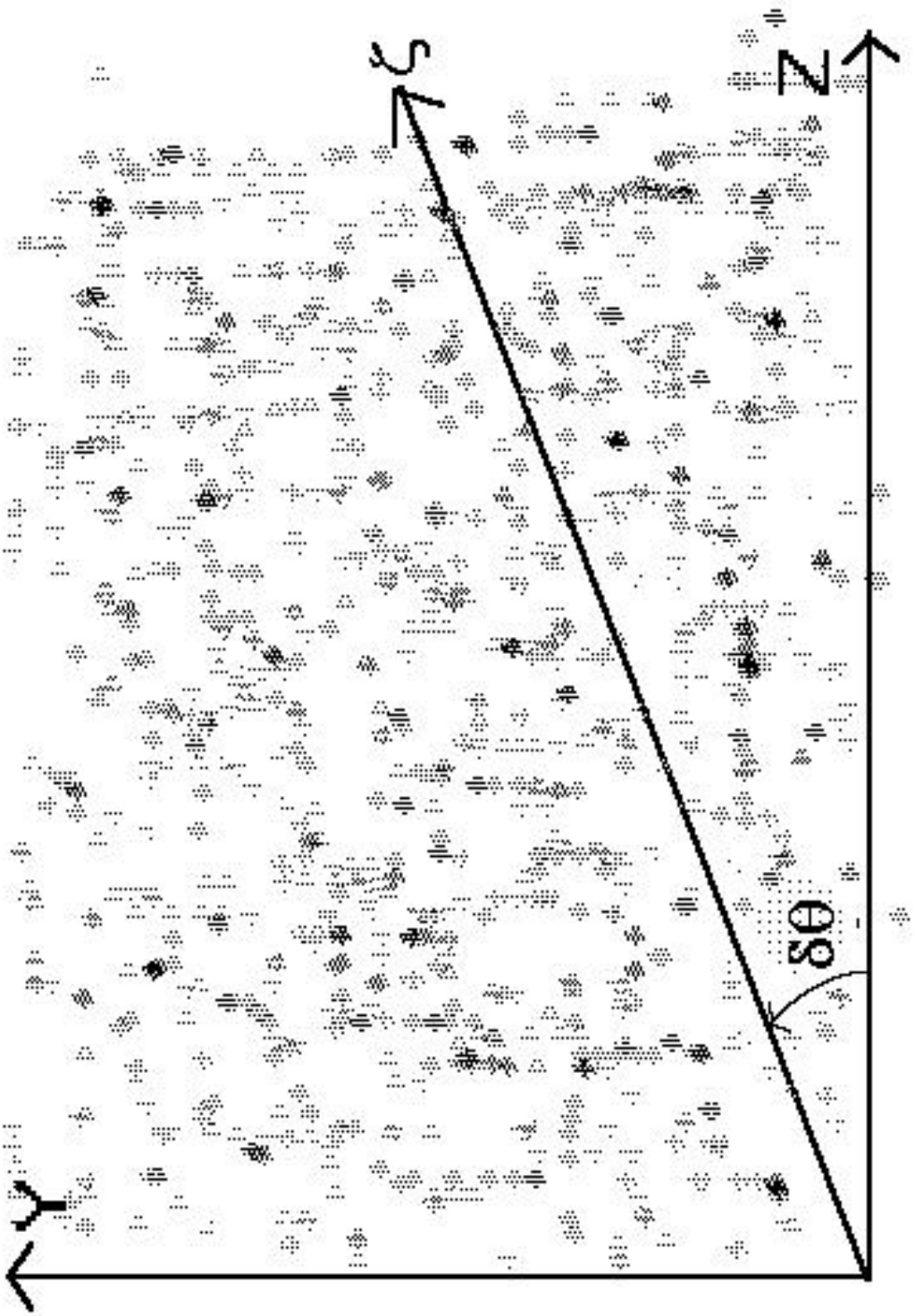
S
N
θ

Figure 6-6. Plot showing the emission measure structure function for several different velocity ranges. The dashed lines represent the least squares fit to all data points (see Table 6-1). The velocity ranges shown are: panel (a) -64 km/s $<$ v $<$ -52 km/s; panel (b) -40 km/s $<$ v $<$ -28 km/s; panel (c) -16 km/s $<$ v $<$ -4 km/s; (d) $+8$ km/s $<$ v $<$ $+20$ km/s.

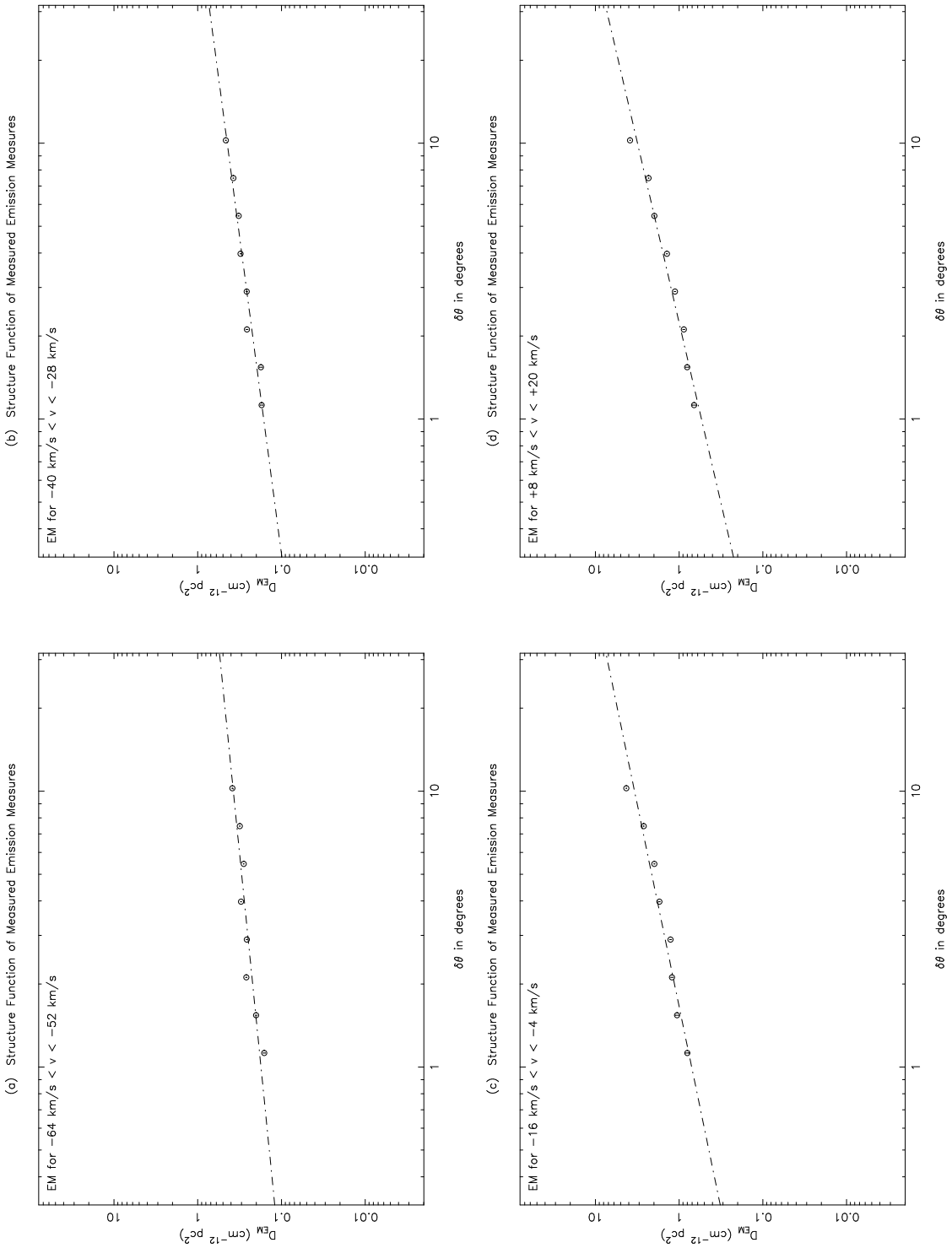
(a) Structure Function of Measured Emission Measures
EM for −64 km/s < v < −52 km/s
(b) Structure Function of Measured Emission Measures
EM for −40 km/s < v < −28 km/s
(c) Structure Function of Measured Emission Measures
EM for −16 km/s < v < −4 km/s
(d) Structure Function of Measured Emission Measures
EM for +8 km/s < v < +20 km/s
D_EM (cm^-12 pc^2)
δθ in degrees
0.01
0.1
1
10

Figure 6-7. Plot showing the emission measure structure function. The dashed line represents the least squares fit to all data points, equation (6.5). The solid line is the prediction of the model (equation 6.31).

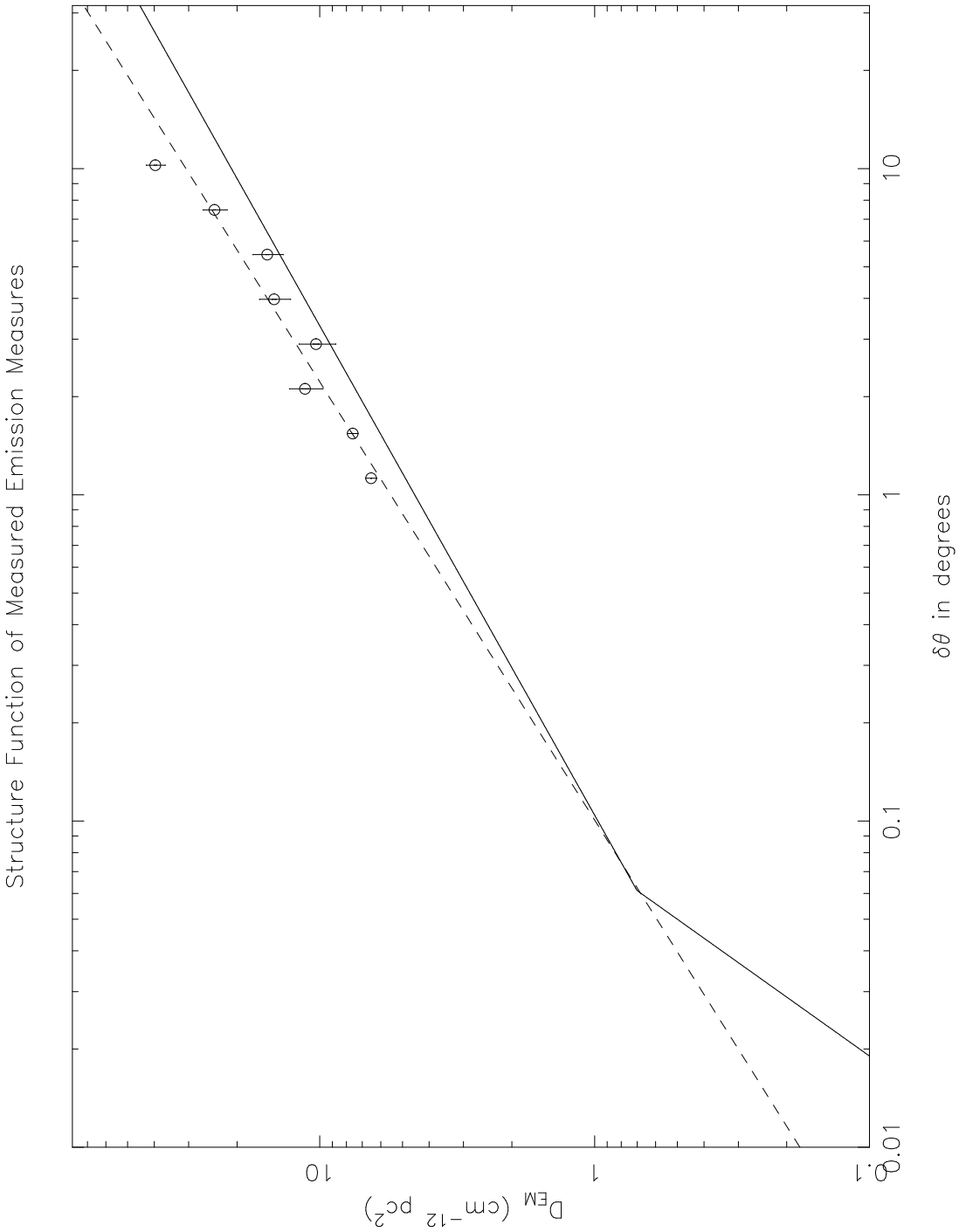
Structure Function of Measured Emission Measures
D_{EM} (cm^{-12} pc^2)
0.1
1
10
0.01
0.1
1
10
$\delta\theta$ in degrees

Figure 6-8. Plot showing the rotation measure structure function. The dashed line corresponds to the least squares fit to data point with $\delta\theta \geq 1.0°$, equation (6.4). The solid line is the prediction of the model (equation 6.32). The dotted line is the prediction of the model (equation 6.32) with no magnetic field fluctuations.

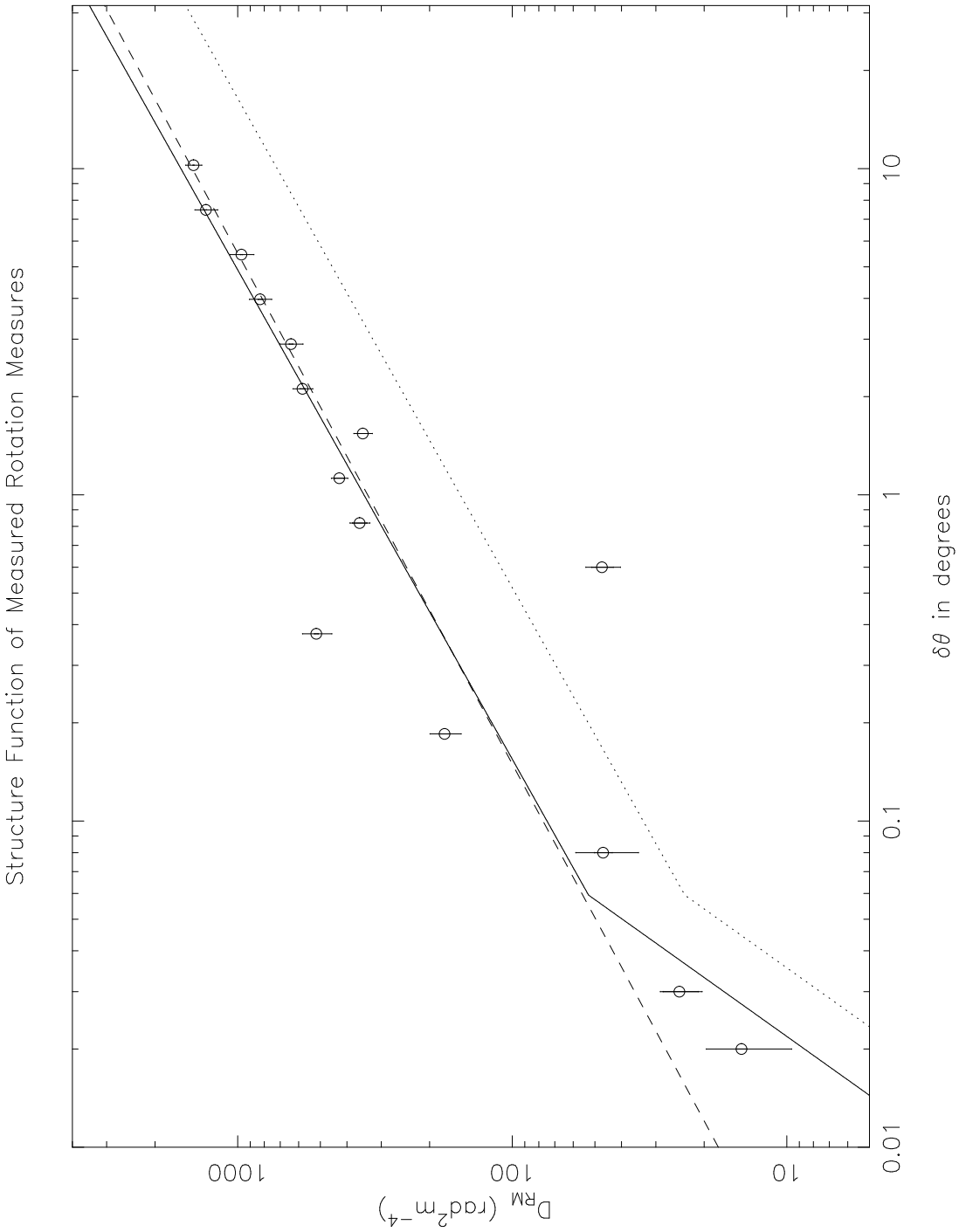
Structure Function of Measured Rotation Measures
D_{RM} (rad^{2}m^{-4})
1000
100
10
0.01
0.1
1
10
$\delta\theta$ in degrees

CHAPTER 7
HEATING OF THE DIFFUSE INTERSTELLAR MEDIUM VIA TURBULENT WAVE DISSIPATION

In this chapter we consider the heating of the interstellar medium (ISM) due to magnetohydrodynamic (MHD) waves which are postulated to comprise the observed turbulence in the ISM. In light of the measurements of the outer scale of the turbulence in the ISM and the measurement of the strength of the turbulent magnetic field presented in this thesis along with the recent measurements of the inner scale of the turbulence in the ISM by Molnar et al. (1995) and the determination of the plasma density in the scattering regions from H_α measurements (Reynolds 1991), we can now completely describe the turbulence in the ISM on observational grounds. The only qualification to this statement is that the magnetic field fluctuations are assumed to have the same power law behavior as the electron density fluctuations and the spectrum is assumed to have the same inner and outer scale as the electron density fluctuations. This is not an entirely unreasonable assumption to make for the ISM. These new measurements allow us to apply the theoretical expressions for the heating rates for various MHD wave damping mechanisms presented by Spangler (1991) to the diffuse interstellar medium.

Spangler (1991) assumed that the turbulence in the ISM is consists of an ensemble of compressible MHD waves which are distributed homogeneously throughout the ISM. The electron density fluctuations are produced by MHD waves, such as Alfvén and magnetosonic waves. Spangler (1991) determined the heating rate for H II region

envelopes and the warm ionized medium (WIM) assuming an outer scale in the range 10^{11} cm to 10^{18} cm and a turbulent magnetic field strength of 0.3 μG. The reader is referred to Spangler (1991) for a detailed discussion of how the turbulence is modeled as MHD waves. It should be emphasized that Spangler (1991) considered wave damping in the regions responsible for heavy interstellar scattering. In this chapter we consider the same microphysical arguments for the more diffuse phase of the ISM responsible for relatively light interstellar scattering. As a result of the data presented in this thesis, we have good estimates of the characteristics of the turbulence and background plasma in this part of the interstellar medium.

We will only consider the damping of the MHD waves due to linear Landau damping, ion-neutral collisional damping and the parametric decay instability. Other damping processes have been shown to contribute much less to the heating of the ISM (Spangler 1991). We also consider the heating of the diffuse gas comprising the Reynolds' layer in addition to the regions considered by Spangler (1991).

The cooling rates for the regions discussed by Spangler (1991) were derived from the cooling functions of Reynolds (1990) for H II regions. We will adopt the same cooling function as Spangler (1991) which is

$$\mathrm{L} = 5 \times 10^{-24} \mathrm{n_e^2} \text{ erg s}^{-1} \text{ cm}^{-3} \tag{7.1}$$

for a gas temperature of $\mathrm{T} \sim 10^4$ K, which is relevant for the regions of the ISM discussed here. Spangler (1991) found the heating rate due to linear Landau damping to be

$$\epsilon_{\mathrm{LLD}} = 1.2 \times 10^{-20} \theta^2 \mathrm{F}(\beta) \left(\frac{\mathrm{V_A}}{10^6 \text{ cm s}^{-1}} \right) \left(\frac{\mathrm{b_T}}{\mu\mathrm{G}} \right)^2 \left(\frac{\mathrm{l_i}}{10^8 \text{ cm}} \cdot \frac{\mathrm{l_o^2}}{10^{34} \text{ cm}^2} \right)^{-1/3} \tag{7.2}$$

in erg s^{-1} cm^{-3} where

$$\mathrm{F}(\beta) = \left(\frac{\mathrm{v_i}}{\mathrm{V_A}} \right)^2 \left(\frac{\mathrm{V_A}}{\mathrm{v_e}} \right) + 5 \left(\frac{\mathrm{v_i}}{\mathrm{V_A}} \right) \exp\left[-\frac{\mathrm{V_A^2}}{2\mathrm{v_i^2} \cos^2 \theta} \right] \tag{7.3}$$

for an obliquely propagating fast magnetosonic wave in a medium with Kolmogorov turbulence. In equations (7.2) and (7.3), the Alfvén speed is given by

$$V_A = 2.2 \times 10^{11} \frac{B(G)}{\sqrt{n(cm^{-3})}} \text{ cm s}^{-1}, \tag{7.4}$$

v_i and v_e are the thermal ion and electron velocities, respectively, b_T^2 is the variance of the turbulent magnetic field strength, β is the ratio of the gas pressure to the magnetic field pressure and θ is the angle between the direction of wave propagation and the static magnetic field. For a plasma with $\beta \sim 1$, $F(\beta) \simeq 1$. For the obliquely propagating fast magnetosonic wave, the density compressions are given by (Spangler 1991 and Sakurai 1994)

$$\left(\frac{\delta n}{n_o}\right) = \tau \left(\frac{\delta b}{B_o}\right) \sin\theta \tag{7.5}$$

where δn is the density fluctuation, n_o is the mean density, δb is the amplitude of the wave, B_o is the large scale magnetic field strength along which the wave propagates, τ is a coefficient of order unity and θ is as defined above. If the same spectrum, outer scale and inner scale characterize both the density and magnetic field fluctuations in the ISM then we have $C_n^2 \propto \langle(\delta n)^2\rangle$ and $C_B^2 \propto \langle(\delta b)^2\rangle$ with the same proportionality constant for each relationship. Thus equation (7.5) can be rewritten as

$$\sin^2\theta = \left(\frac{B_o}{n_o}\right)^2 \left(\frac{C_n^2}{C_b^2}\right) \tag{7.6}$$

and we can estimate θ for different regions of the ISM from the observed properties: $B_o \sim 3$ μG, $C_n^2 = 10^{-3.0}$ m$^{-20/3}$ and $C_b^2 = 3 \times 10^{-13}$ m$^{-2/3}$ μG^2.

In Table 7-1 we list the properties of the regions of the ISM being considered in this chapter. We give the name of the region in the first column, the density in column 2, the fractional ionization in column 3, the Alfvén speed in column 4, the collisional frequency in column 5 and θ in column 6 for the various regions of the ISM which

we are considering. For the diffuse ISM, Reynolds (1995) found that the hydrogen is at least 40% ionized. We have thus calculated the heating rates for the diffuse ISM assuming that it is either 50% or 100% ionized. Reynolds (1991) also found that the diffuse ionized hydrogen exists in clumps with an average density of 0.08 cm^{-3}. For the diffuse ISM, the above parameters in equation (7.6) yield $\sin\theta > 1$. For purposes of the present calculation we adopt a value of $\theta \sim 30^\circ$ thus obtaining a lower limit to the heating from linear Landau damping. If θ is much larger than 30° then the damping rate predicted by equation (7.2) is no longer valid. For the H II region envelopes we use the value of $\theta = 3^\circ$ derived from equation (7.6). It should be noted that the region of the sky considered in this thesis has no features that could be labeled as H II region envelopes. Before continuing, it is worth emphasizing that equation (7.6) is meaningful only if the density fluctuations responsible for interstellar scintillation arise from oblique propagation of MHD waves.

For ion-neutral collisional damping Spangler (1991) found the heating rate to be

$$\begin{aligned} \epsilon_{\rm IN}(\text{ergs s}^{-1}\ \text{cm}^{-3}) &= 7.7\times10^{-14}\nu_{\rm o}\left(\frac{\rm b_T}{\mu \rm G}\right)^2\left(\frac{\rm k_o}{\rm k_c}\right)^{2\mu-1} \qquad {\rm k_o} < {\rm k_c} \\ &= 7.7\times10^{-14}\nu_{\rm o}\left(\frac{\rm b_T}{\mu \rm G}\right)^2 \qquad {\rm k_o} > {\rm k_c} \end{aligned} \tag{7.7}$$

where ${\rm k_o} = \frac{2\pi}{\rm l_o}$, n is the number density of hydrogen and

$$\rm k_c = \frac{\left(1+\frac{\rho_i}{\rho_n}\right)\nu_o}{V_A}, \tag{7.8}$$

$\rho_{\rm i}$ and $\rho_{\rm n}$ being the mass density of ionized and neutral species and $\nu_{\rm o}$ being the collision frequency. The collision frequency is given by

$$\nu_{\rm o} = 1.3\times10^{-10}{\rm n_e}\ \ {\rm s}^{-1} \tag{7.9}$$

in a medium were the hydrogen is fully ionized and helium has the standard cosmic abundance (Spangler 1991), and by

$$\nu_o = 1.9 \times 10^{-9} n(H) \ \ s^{-1} \tag{7.10}$$

for partially ionized hydrogen with a neutral hydrogen density of n(H) (in cm^{-3}) at a temperature of $T \sim 10^4$ K (McIvor 1977). The collisional frequency is greater for the partially ionized hydrogen since $H - H^+$ collisions become more important at lower ionization fractions. Finally for the heating rate due to the parametric decay instability Spangler (1991) finds

$$\epsilon_{DI} = 5.6 \times 10^{-24} \left(\frac{V_A}{10^6 \text{ cm s}^{-1}} \right) \left(\frac{3 \ \mu G}{B_o} \right) \left(\frac{b_T}{\mu G} \right)^3 \left(\frac{10^{17} \text{ cm}}{l_o} \right) \ln \left(\frac{k_i}{10^8 k_o} \right) \tag{7.11}$$

where $k_i = \frac{2\pi}{l_i}$.

We can now determine the heating rate of the ISM due to the damping of the MHD waves which are assumed to comprise the turbulence observed in the ISM. We take the mean large scale magnetic field to be $B_o \sim 3 \ \mu G$, the outer scale to be in the range 0.1 pc $< l_o <$ 7.0 pc with the most likely value being 3 ± 1 pc. The inner scale is taken to be the value determined by Molnar et al. (1995) $l_i = 300 \pm 150$ km. In Figures 7-1 through 7-4 we compare the cooling rates of the three regions to the heating rates of the damping mechanisms considered above. In Figures 7-1 through 7-4, the dashed line represents the linear Landau damping heating rate, the dot-dash line represents the ion-neutral collisional damping heating rate, the dotted line is the parametric decay instability heating rate and the solid line with hash marks represents the cooling rate. The most likely range for the value of the outer scale (3 ± 1 pc) is shown as the shaded region. In the following discussion we shall only consider the heating rates within the shaded region.

For the H II region envelopes we find that all the heating rates for damping mechanisms are smaller than the cooling rate (see Figure 7-1). If the properties for the magnetic field fluctuations and electron density fluctuations that we have observed for the diffuse ISM are applicable to H II region envelopes, then the turbulent heating rate is $\sim 1\%$ of the cooling rate. However, many lines of sight which show enhanced interstellar scintillation close to H II regions, and thus plausibly pass through extended H II region envelopes (Spangler 1991). It is thus likely that the value $C_n^2 = 10^{-3.0}$ m$^{-20/3}$ used in determining the curves in Figure 7-1 is not correct and that a more realistic value is in the range $C_n^2 = 10^{-3.0} \rightarrow 1$ m$^{-20/3}$ (Cordes et al. 1985). This would cause θ, as determined from equation (7.6), to increase, resulting in an increase in the heating rate due to linear Landau damping. For $C_n^2 = 1$ m$^{-20/3}$ it is found that the heating rate of H II region envelopes due to linear Landau damping is equal to the cooling rate if the outer scale is ~ 3 pc. It is also possible that the amplitude of the magnetic field fluctuations in the H II region envelopes is larger, which would further increase the heating rate due to linear Landau damping.

For the WIM, we see from Figure 7-2 that the heating rates for linear Landau damping and the parametric decay instability are greater than the cooling rate. The heating rate due to ion-neutral collisions is $\sim 2/3$ the cooling rate of the WIM. Finally, we consider the diffuse ISM, which is characteristic of the part of the interstellar medium probed by the observations in this thesis. We find that all three damping mechanisms produce heating rates greater than the cooling rate of the diffuse ISM if it is 50% ionized (see Figure 7-3). If the diffuse ISM is 100% ionized (see Figure 7-4), then then the heating rates for linear Landau damping and the parametric decay instability are greater than the cooling rate of the diffuse ISM. The ion-neutral damping heating rate is $\sim 20\%$ of the cooling rate of the diffuse ISM if it is 100% ionized. If the

observed turbulence in the ISM is composed of MHD waves we find that the damping of these waves would contribute too much heating to the WIM and the diffuse ISM.

It is not clear whether the turbulence measured in Chapter 7 exists in the diffuse ISM or in higher density regions (i.e. the H II envelope of ξ Per or the supernova remnant observed as radio Loop II). Since we seem to observe the turbulence occurring in thin sheets or filaments it is possible that this consists of turbulence inside of the higher density shell like regions. If this is indeed the case, then it is possible for the turbulence to be entirely comprised of MHD waves. However, the largest observed density seen in this region is $n_e \sim 0.5$ cm^3 (Reynolds 1988) which is more indicative of the WIM than of H II region envelopes.

If a significant portion of the observed turbulence is in the diffuse ISM, as does seem to be the case for this region of the sky, then we must conclude that the interstellar turbulence does not consist of MHD waves. This arises because the MHD waves would heat the diffuse ISM faster than it could cool and thus cause it to reach higher temperatures than are observed. It is therefore possible that the turbulence theory of Higdon (1984, 1986) may be more relevant for the diffuse ISM. Higdon showed that the heating rate of the turbulence is greatly reduced if the turbulence is comprised of highly elongated, field-oriented irregularities or non-propagating entropy structures rather than an ensemble of MHD waves. Higdon's (1984) "cloud shell H II region" has similar properties to those of the diffuse ISM discussed above. Higdon estimated that this region has an outer scale of $l_o \sim 0.7$ pc and that its heating rate is $\sim 20\%$ of the cooling rate for his model of the turbulence in the ISM. Molnar et al. (1995) have found evidence for anisotropy in the turbulence on small spatial scales which may be interpreted as support for the model of Higdon. It thus seems likely that the turbulence model for the ISM of Higdon (1984, 1986) may provide abetter description of the observed turbulence than does the model of Spangler (1991).

Ferriere, Zweibel and Shull (1988), Bykov and Toptygin (1987), McIvor (1977) and Kulsrud and Pearce (1969) have all previously examined this subject and have also concluded that wave heating would overpower the radiative cooling capabilities of the diffuse ISM. However, these previous authors were forced to make estimates of various quantities, such as the outer scale of the turbulence and the variance of the magnetic field, for which data now exist. We have been able to put more stringent constraints on the wave heating rates of the ISM due to the recent measurements of these quantities which were not previously available. This allows us to rule out the possibility that turbulence in the diffuse ISM is composed entirely of MHD waves.

Table 7-1. Properties of regions were the turbulent ISM may reside.

Region	$n_e(cm^{-3})$	% ionized	$V_A(10^6$ cm $s^{-1})$	ν_o (s^{-1})	θ
H II envelopes	4.0	100	0.33	5.2×10^{-10}	3°
WIM	0.25	68	1.32	2.24×10^{-10}	44°
Diffuse ISM	0.08	50	2.33	2.28×10^{-10}	. . .
Diffuse ISM	0.08	100	2.33	1.04×10^{-11}	. . .

Figure 7-1. Comparison of the heating rate due to MHD wave damping and the cooling rate of H II region envelopes. The solid line with hash marks indicates the cooling rate, the dashed line represents the heating due to linear Landau damping, the dash-dot line represents the ion-neutral collision damping heating rate and the dotted lined gives the heating rate due to the parametric decay instability. The most likely range for the value of the outer scale is shown as the shaded region.

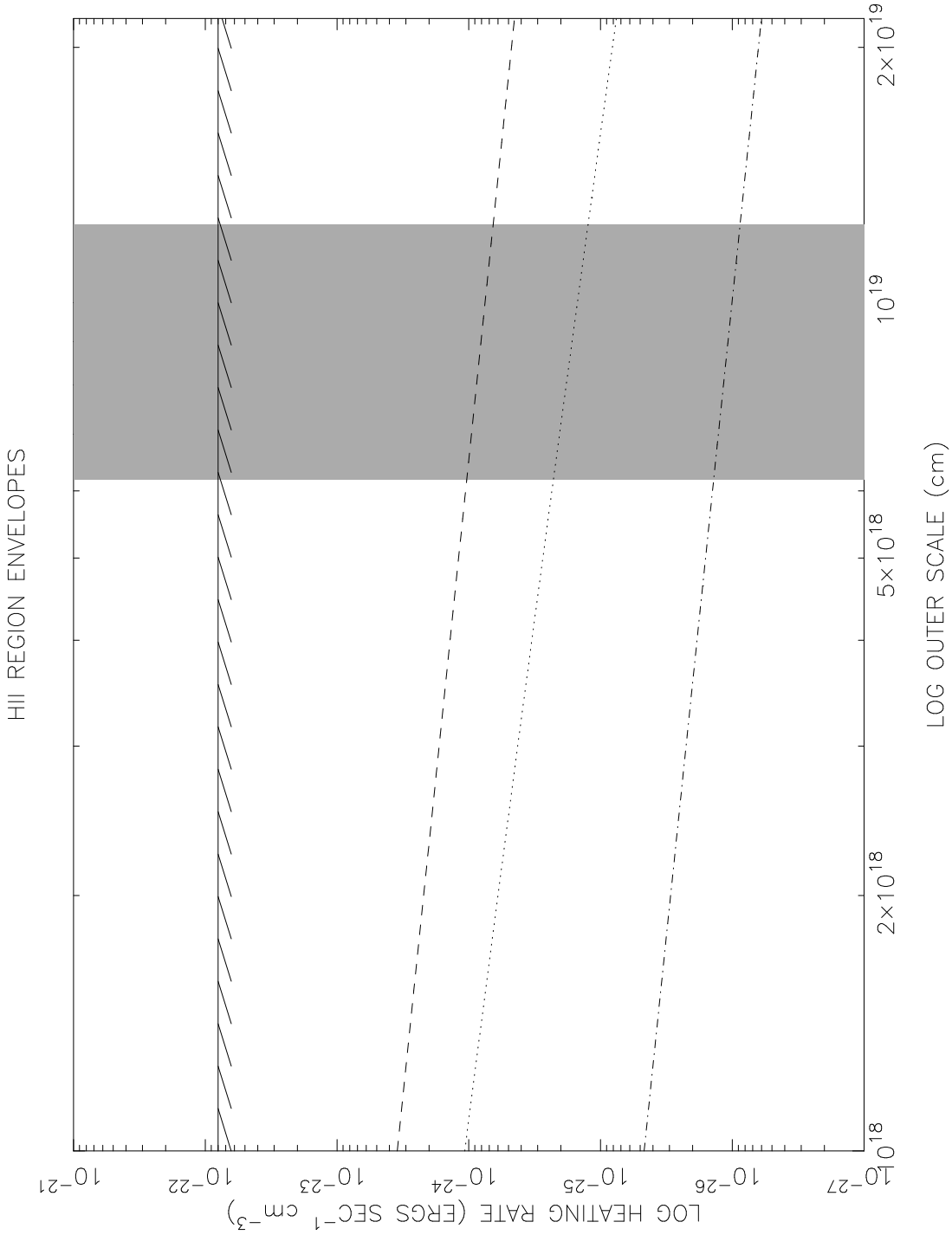
HII REGION ENVELOPES
LOG HEATING RATE (ERGS SEC^{-1} cm^{-3})
10^{-21}
10^{-22}
10^{-23}
10^{-24}
10^{-25}
10^{-26}
10^{-27}
LOG OUTER SCALE (cm)
10^{18}
2×10^{18}
5×10^{18}
10^{19}
2×10^{19}

Figure 7-2. Comparison of the heating rate due to MHD wave damping and the cooling rate in the warm ionized medium. The solid line with hash marks indicates the cooling rate, the dashed line represents the heating due to linear Landau damping, the dash-dot line represents the ion-neutral collision damping heating rate and the dotted lined gives the heating rate due to the parametric decay instability. The most likely range for the value of the outer scale is shown as the shaded region.

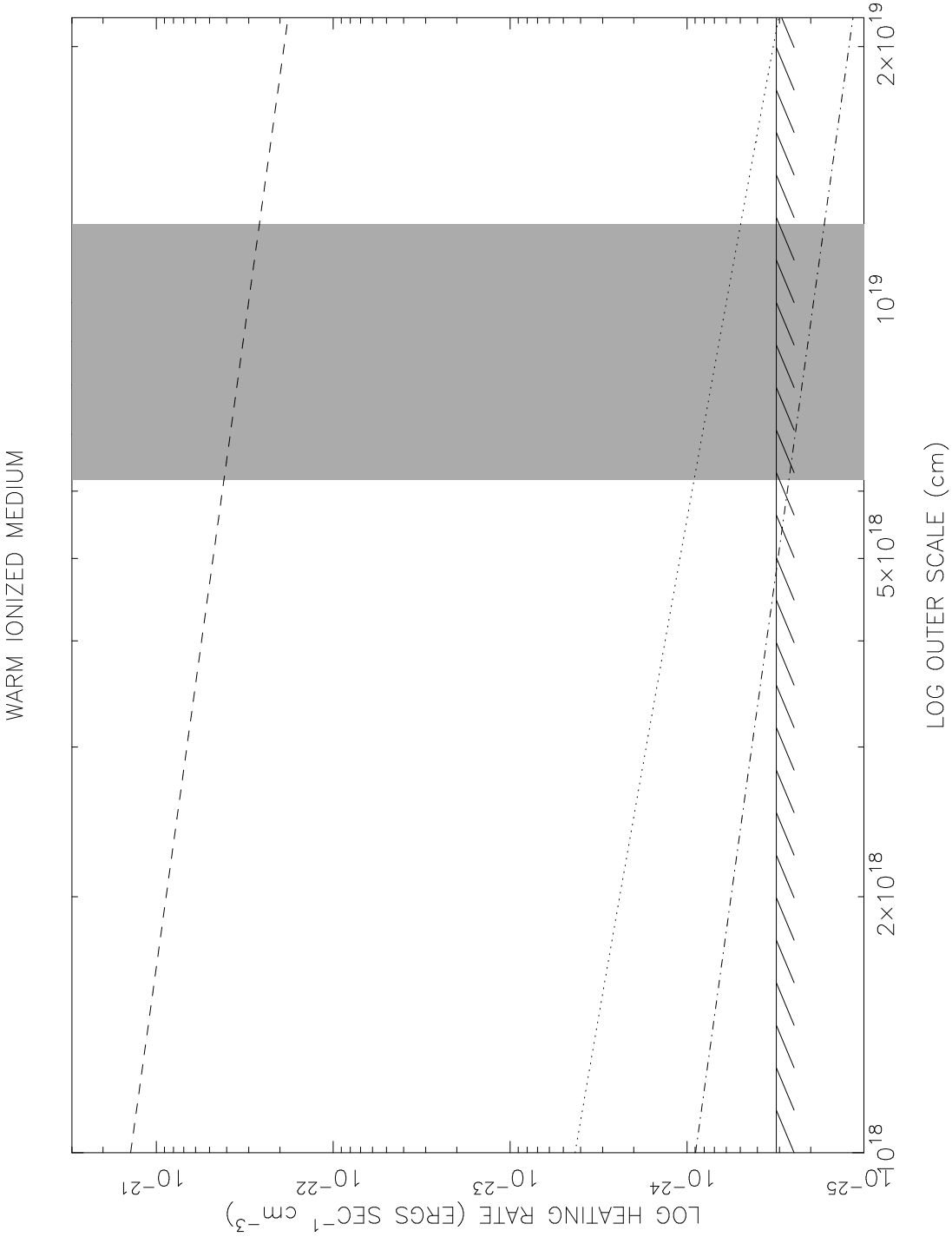
WARM IONIZED MEDIUM
LOG HEATING RATE (ERGS SEC^{-1} cm^{-3})
10^{-21}
10^{-22}
10^{-23}
10^{-24}
10^{-25}
LOG OUTER SCALE (cm)
10^{18}
2×10^{18}
5×10^{18}
10^{19}
2×10^{19}

Figure 7-3. Comparison of the heating rate due to MHD wave damping and the cooling rate of the diffuse ISM if it is 50% ionized. The solid line with hash marks indicates the cooling rate, the dashed line represents the heating due to linear Landau damping, the dash-dot line represents the ion-neutral collision damping heating rate and the dotted lined gives the heating rate due to the parametric decay instability. The most likely range for the value of the outer scale is shown as the shaded region.

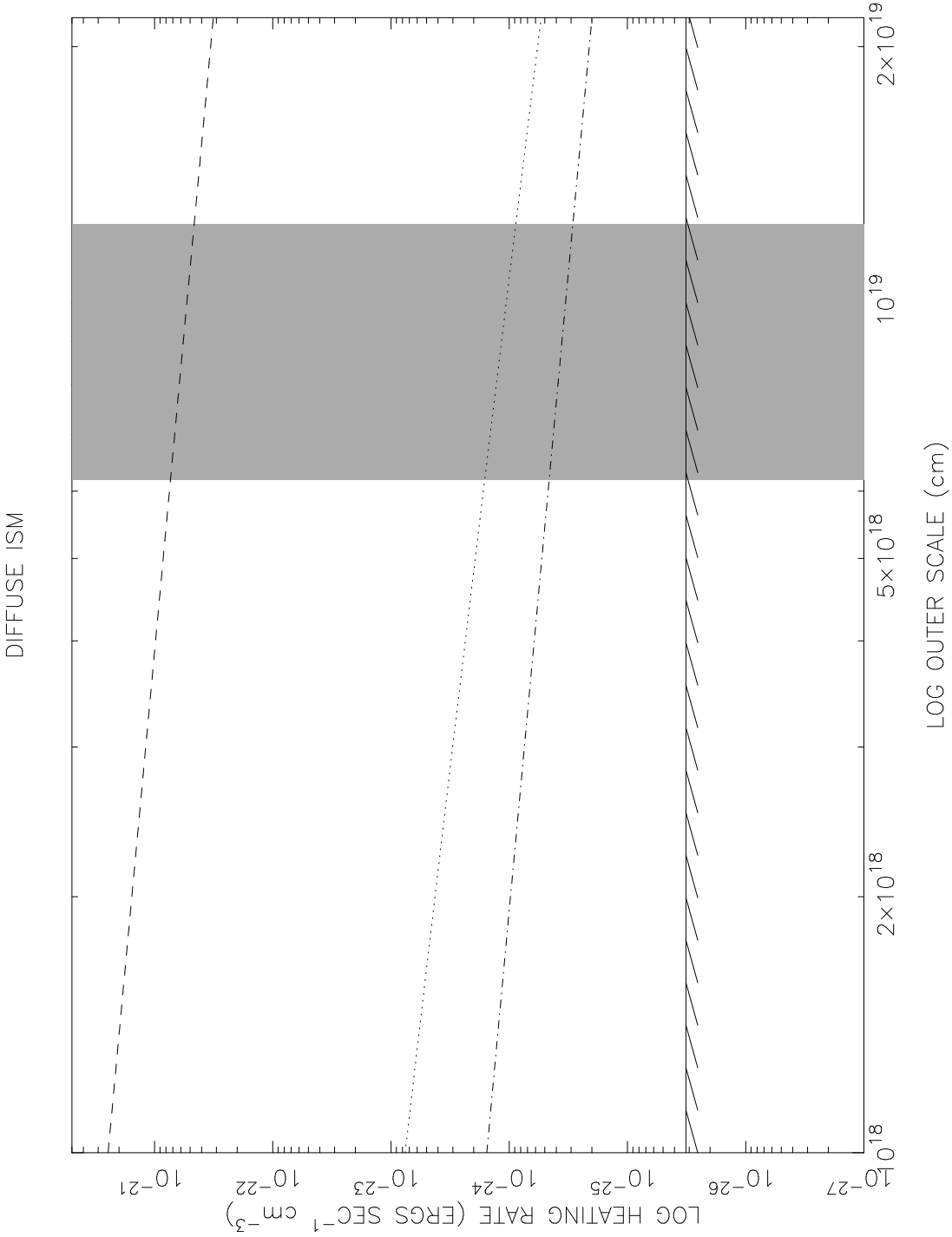
DIFFUSE ISM
LOG HEATING RATE (ERGS SEC^{-1} cm^{-3})
10^{-21}
10^{-22}
10^{-23}
10^{-24}
10^{-25}
10^{-26}
10^{-27}
10^{18}
2×10^{18}
5×10^{18}
10^{19}
2×10^{19}
LOG OUTER SCALE (cm)

Figure 7-4. Comparison of the heating rate due to MHD wave damping and the cooling rate of the diffuse ISM if it is 100% ionized. The solid line with hash marks indicates the cooling rate, the dashed line represents the heating due to linear Landau damping, the dash-dot line represents the ion-neutral collision damping heating rate and the dotted lined gives the heating rate due to the parametric decay instability. The most likely range for the value of the outer scale is shown as the shaded region.

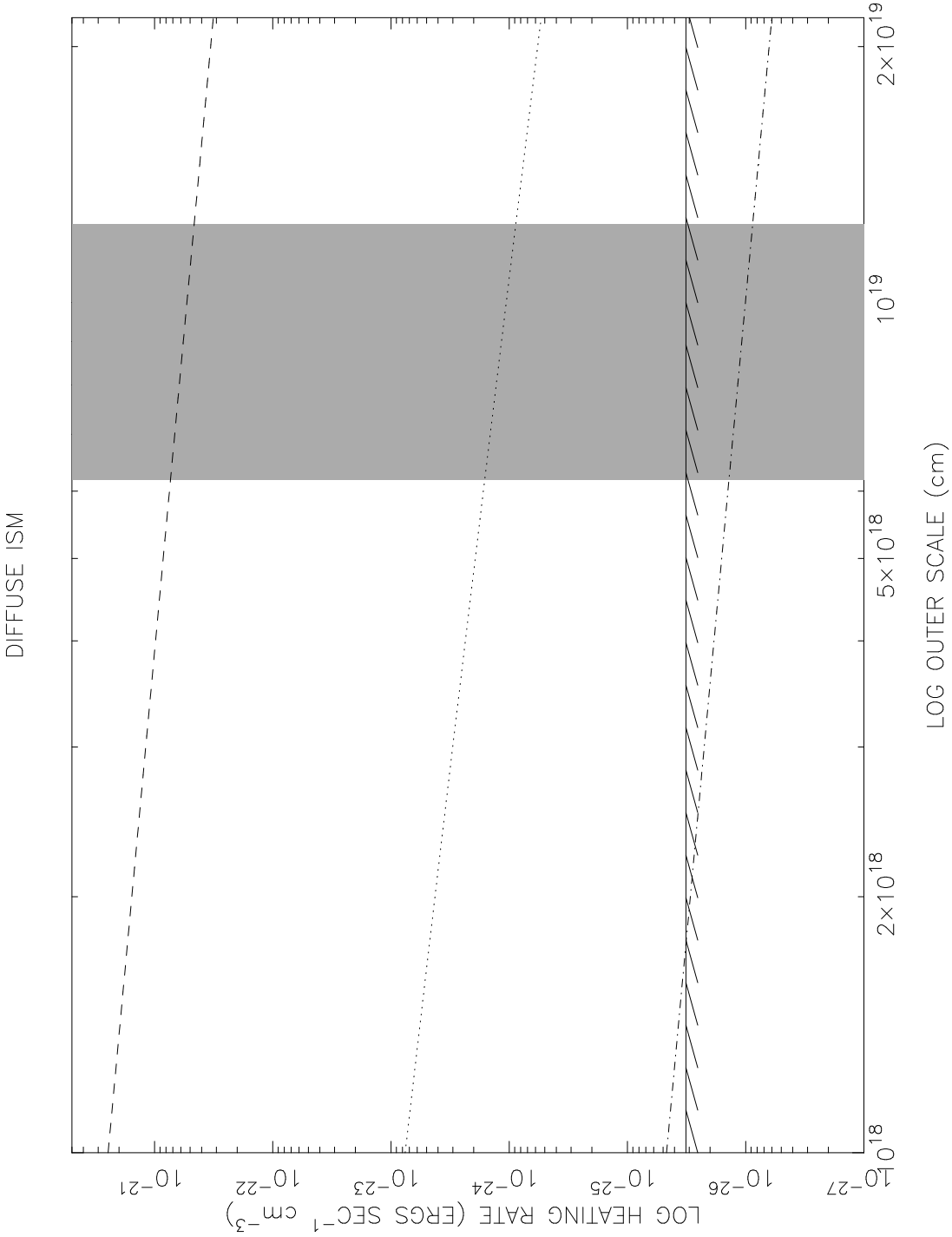
DIFFUSE ISM
LOG HEATING RATE (ERGS SEC^{-1} cm^{-3})
10^{-21}
10^{-22}
10^{-23}
10^{-24}
10^{-25}
10^{-26}
10^{-27}
LOG OUTER SCALE (cm)
10^{18}
2×10^{18}
5×10^{18}
10^{19}
2×10^{19}

CHAPTER 8

SUMMARY AND CONCLUSIONS

We have measured the rotation measures of 38 extragalactic radio sources in a region of the sky where the H_α intensity has been mapped out spatially and in velocity. The emission measure across this region can be modeled with the Reynolds layer or the galactic electron density model of Taylor and Cordes. However, we have to include a model of the H II region of ξ Per in order to completely account for the observed H_α emission. Use of three standard models for the galactic magnetic field with these density models fails to account for the mean characteristics of the rotation measure observed in this part of the sky. For the model rotation measures to agree with the observed ones, we conclude that the strength of the fields in spiral arms must be of order $3 - 4$ μG, larger than indicated by previous investigations. In addition, to account for the rotation measure gradient across our field, we must posit a magnetic field anomaly, associated with either the ξ Per H II region, or radio Loop II. It is also a possibility that this magnetic field anomaly is the result of a magnetic field fluctuation with a size scale near the outer scale of the observed two dimensional turbulence.

We have developed an improved ionospheric Faraday rotation model for the use in the calibration of polarization observations of radioastronomical sources. The RMS scatter in the polarization position angles about the mean of $5^\circ - 7^\circ$ found using the AIPS model in ionospheric Faraday rotation calibration for these sources have generally been treated as marginally acceptable values during periods of high solar activity. However, using the improved ionospheric Faraday rotation model of

ionospheric Faraday rotation calibration we have shown that the RMS scatter about the mean in polarization position angle can be reduced by better than a factor of two. This is achieved because the improved ionospheric Faraday rotation model provides a more realistic and up to date model of the ionosphere than does the AIPS model. It was found that the AIPS model uses an out of date model for the geomagnetic field and that the slab model of the ionosphere can create problems for sources near the horizon, especially near sunset or sunrise and when the geomagnetic field undergoes large changes along the line of sight. The use of the model developed in this thesis allows for higher precision calibration of polarization data obtained with the VLA. This results in the calibrated data having a larger signal to noise in Q and U when the model developed in this thesis is used, compared to when the FARAD model is used.

We have found that for angular separations $\delta\theta \geq 1.0°$, neither the rotation measure nor emission measure structure functions adhere to a functional form appropriate if the turbulence had a Kolmogorov spectrum on all scales. This statement even holds for the emission measure structure function of the gas nearest to the sun, as determined from the emission measure data in various velocity ranges. However, for these angular separations both the emission measure and rotation measure structure functions have logarithmic slopes of $^2/_3$, indicative of two dimensional turbulence. We also have made the first detection of the contribution of magnetic field fluctuations to rotation measure fluctuations on large scales in the ISM. This indicates that the turbulence in the ISM is actually magnetohydrodynamical turbulence. We find that a model in which the three dimensional, Kolmogorov turbulence responsible for interstellar scintillations is contained within thin sheets or filaments of ~ 3 pc thickness is consistent with the observed data. For scale sizes larger than the thickness of the thin sheets or filaments the turbulence appears to be two dimensional with and outer scale

of 70 pc $< l_o^{2D} <$ 96 pc. From an analysis of the structure functions we conclude that the outer scale for the Kolmogorov turbulence is 3 ± 1 pc.

The heating rate of the ISM due to the damping of MHD waves which possibly comprise the observed turbulence in the ISM was also investigated. It was found that MHD wave damping would heat the ISM faster than it could cool for the WIM and diffuse ISM. This indicates that the electron density fluctuations in the diffuse ISM do not arise from the oblique propagation of MHD waves. An alternative explanation of the nature of the turbulence in the ISM is that it is composed of highly elongated, field oriented structures and non-propagating entropy structures. If this is the case then the heating rate of the ISM due to the turbulence is expected to be much less than the heating rate due to the damping of MHD waves.

APPENDIX A
EXPRESSIONS FOR THE EMISSION MEASURE AND ROTATION MEASURE STRUCTURE FUNCTIONS

Using the geometry shown in Figure 6-5, we will assume that the medium is a plane-parallel slab of thickness L' in the z-direction. For a line of sight L, at an angle $\delta\theta$ with the z-axis, we have $L = L'/\cos\delta\theta$. The equations for D_{RM} and D_{EM} are then

$$D_{EM}(\delta\theta) = < [\int_0^{L'} n(z,0)^2 dz - \int_0^{L} n(\zeta\cos\delta\theta, \zeta\sin\delta\theta)^2 d\zeta]^2 > \tag{A.1a}$$

$$D_{RM}(\delta\theta) = < [\int_0^{L'} n(z,0)\vec{B}(z,0)\cdot d\vec{z} - \int_0^{L} n(\zeta\cos\delta\theta, \zeta\sin\delta\theta)\vec{B}(\zeta\cos\delta\theta, \zeta\sin\delta\theta)\cdot d\vec{\zeta}]^2 > \tag{A.1b}$$

where $\hat{\zeta}$ is a unit vector along the line of sight L.

The random fluctuations in the electron density and magnetic field are described by the following:

$$n = n_o + \delta n \tag{A.2}$$

$$\vec{B} = \vec{B_o} + \delta\vec{B} \tag{A.3}$$

where n_o and $\vec{B_o}$ are the mean large scale components of the electron density and magnetic field described in Chapter 5. The quantities δn and $\delta\vec{B}$ are the spatially fluctuating components of the electron density and magnetic field respectively. The amplitudes of the fluctuations are assumed to be zero mean, isotropic Gaussian processes. It is also

assumed that the fluctuations in the magnetic field and the electron density are related in such a fashion that

$$< \delta n |\delta \vec{B}| > \neq 0 \tag{A.4}$$

but

$$< \delta n \delta B_i > = 0 \tag{A.5}$$

where i=1,2,3 and δB_i is the component of $\delta \vec{B}$ along the i axis. Equation (A.5) most likely does not represent the actual case for the turbulence in the ISM. In reality the electron density fluctuations are most likely aligned along the magnetic field such as seen in the solar wind (Armstrong et al. 1990). Evidence for anisotropy of density irregularities in the interstellar medium does indeed exist (Wilkinson et al. 1994 and Molnar et al. 1995), but the degree of anisotropy is not so pronounced as is the case for the solar wind (Armstrong et al. 1990). Although the difference in the observed anisotropy for the solar wind and interstellar medium may be due to greater randomization by line-of-sight integration for the latter medium, we feel it is premature at this point to take into account anisotropy of the turbulence. Finally, our observations are sensitive to ISM fluctuations on large scales, which are comparable in magnitude to the systematic field $\vec{B_o}$. For such large amplitude fluctuations there are no theoretical reasons for expecting anisotropic turbulence (Zank and Matthaues 1992). It is also assumed that the fluctuations in the electron density and magnetic field occur over the same size scales in the ISM. This assumption stems from the fact that events which put energy into the ISM, such as supernova explosions or stellar winds, will affect both the interstellar electron density and magnetic field on roughly the same size scales.

We now have the following relations and definitions to use in deriving the structure functions:

$$< \delta n > = 0 \tag{A.6}$$

$$< \delta B_i > = 0 \tag{A.7}$$

$$< \delta B_i \delta B_j >= 0 \quad \text{for } i \neq j \tag{A.8}$$

$$R_n(|\vec{r}|) \equiv < \delta n(\vec{r_o}) \delta n(\vec{r_o} + \vec{r}) > \tag{A.9}$$

$$R_B(|\vec{r}|) \equiv < \delta B_i(\vec{r_o}) \delta B_i(\vec{r_o} + \vec{r}) > = < \delta B_j(\vec{r_o}) \delta B_j(\vec{r_o} + \vec{r}) > \tag{A.10}$$

$$R_n^4(|\vec{r}|) \equiv < \delta n(\vec{r_o})^2 \delta n(\vec{r_o} + \vec{r})^2 > \tag{A.11}$$

$$R^4_{B_{ijkl}}(|\vec{r}|) \equiv < \delta B_i(\vec{r_o}) \delta B_j(\vec{r_o}) \delta B_k(\vec{r_o} + \vec{r}) \delta B_l(\vec{r_o} + \vec{r}) > \tag{A.12}$$

$$R_{nB}(|\vec{r}|) \equiv < \delta n(\vec{r_o}) \delta B_i(\vec{r_o}) \delta n(\vec{r_o} + \vec{r}) \delta B_i(\vec{r_o} + \vec{r}) > \tag{A.13}$$

where B_i is a component of the magnetic field along one of the axes (i.e. i,j,k, and l=1,2,3). The fact that R_n, R_B, R_n^4 and R_B^4 are only a function of the separation $|\vec{r}|$, independent of position, results from the assumptions of the homogeneity and isotropy of the turbulence.

Applying the conditions in equations (A.2)-(A.13) we find

$$\begin{aligned} D_{EM}(\delta\theta) =& \Psi_{EM}(\delta\theta) + 8n_0^2 \left[\int_0^{L'} dz \int_0^L d\zeta (< \delta n(z,0) \delta n(\zeta,0) > - < \delta n(z,0) \delta n(\zeta, \zeta\delta\theta) >) \right] \\ & + 2[\int_0^{L'} dz \int_0^L d\zeta (< \delta n(z,0)^2 \delta n(\zeta,0)^2 > - < \delta n(z,0)^2 \delta n(\zeta, \zeta\delta\theta)^2 >) \\ =& \Psi_{EM}(\delta\theta) + \int_0^{L'} dz \int_0^L d\zeta [8n_0^2 R_n(z-\zeta,0) + 2R_n^4(z-\zeta,0) \\ & - 8n_o^2 R_n(z-\zeta, \zeta\delta\theta) - 2R_n^4(z-\zeta, \zeta\delta\theta)] \end{aligned} \tag{A.14}$$

$$\begin{aligned} D_{RM}(\delta\theta) =& \Psi_{RM}(\delta\theta) + (0.81)^2 \left\{ 2n_0^2 \int_0^{L'} dz \int_0^L d\zeta \, [< \delta B_z(z,0) \delta B_z(\zeta,0) > \right. \\ & - < \delta B_z(z,0) \delta B_z(\zeta, \zeta\delta\theta) >] \\ & + 2B_{oz}^2 \int_0^{L'} dz \int_0^L d\zeta \, [< \delta n(z,0) \delta n(\zeta,0) > - \cos(\delta\theta) < \delta n(z,0) \delta n(\zeta, \zeta\delta\theta) >] \end{aligned}$$

$$
\begin{aligned}
&+2\int_0^{L'} dz \int_0^{L} d\zeta \,[< \delta n(z,0)\delta B_z(z,0)\delta n(\zeta,0)\delta B_z(\zeta,0) > \\
&-\cos(\delta\theta) < \delta n(z,0)\delta B_z(z,0)\delta n(\zeta,\zeta\delta\theta)\delta B_z(\zeta,\zeta\delta\theta) >] \\
&+2B_{oz}B_{oy}\sin(\delta\theta)\int_0^{L'} dz \int_0^{L} d\zeta \,[\cos(\delta\theta) < \delta n(z,0)\delta n(\zeta,0) > \\
&- < \delta n(z,0)\delta n(\zeta,\zeta\delta\theta) >] \\
&+ \left(B_{oy}^2 - B_{oz}^2\right)\sin^2(\delta\theta)\int_0^{L'} dz \int_0^{L} d\zeta < \delta n(z,0)\delta n(\zeta,0) > \Bigg\} \\
=&\Psi_{RM}(\delta\theta) + (0.81)^2 \Bigg\{ 2n_0^2 \int_0^{L'} dz \int_0^{L} d\zeta \,[R_B(z-\zeta,0) \\
&-R_B(z-\zeta,\zeta\delta\theta)] \\
&+2B_{oz}^2 \int_0^{L'} dz \int_0^{L} d\zeta \,[R_n(z-\zeta,0) - \cos(\delta\theta)R_n(z-\zeta,\zeta\delta\theta)] \\
&+2\int_0^{L'} dz \int_0^{L} d\zeta \,[R_{nB}(z-\zeta,0) - \cos(\delta\theta)R_{nB}(z-\zeta,\zeta\delta\theta)] \\
&+2B_{oz}B_{oy}\sin(\delta\theta)\int_0^{L'} dz \int_0^{L} d\zeta \,[\cos(\delta\theta)R_n(z-\zeta,0) - R_n(z-\zeta,\zeta\delta\theta)] \\
&+ \left(B_{oy}^2 - B_{oz}^2\right)\sin^2(\delta\theta)\int_0^{L'} dz \int_0^{L} d\zeta R_n(z-\zeta,0) \Bigg\}
\end{aligned}
\tag{A.15}
$$

where $\Psi_{EM}(\delta\theta)$ and $\Psi_{RM}(\delta\theta)$ are geometric components due to the structure of the medium.

$$
\begin{aligned}
\Psi_{EM}(\delta\theta) =& n_o^4 L^2 \delta\theta^2 \\
\Psi_{RM}(\delta\theta) =& \left[n_o B_{oz}\left(L' - L\cos(\delta\theta)\right) - n_o B_{oy} L\sin(\delta\theta)\right]^2
\end{aligned}
\tag{A.16}
$$

We have ignored all three point correlations in deriving the above equations since we are assuming that the turbulent fluctuations are Gaussian processes.

Armstrong et al. (1995) have shown evidence that the electron density fluctuations can be described with a single power law from the spatial scales of 10^6 m up to $\sim 10^{18}$ m where our rotation measure survey is sensitive. This power law is a

Kolmogorov power law and has a logarithmic slope $\sim 11/3$. Thus we will assume for further analysis that the electron density and magnetic field fluctuations are described by power laws with the same outer scale ($q_o = \frac{2\pi}{l_o}$) so that we have

$$< \delta n(\vec{r_o}) \delta n(\vec{r_o} + \vec{r}) >= \int d^3q \, \frac{C_n^2 e^{-i\vec{q}\cdot\vec{r}}}{(q_0^2 + q^2)^{\alpha/2}} \tag{A.17}$$

$$< \delta B_i(\vec{r_o}) \delta B_i(\vec{r_o} + \vec{r}) >= \int d^3q \, \frac{C_B^2 e^{-i\vec{q}\cdot\vec{r}}}{(q_0^2 + q^2)^{\alpha/2}} \tag{A.18}$$

The four point correlations in (A.1) and (A.14) are analyzed using the following identity

$$\begin{aligned} < x_1(t_1)x_2(t_2)x_3(t_3)x_4(t_4) >= & k_4(t_1,t_2,t_3,t_4) + < x_1(t_1)x_2(t_2) >< x_3(t_3)x_4(t_4) > \\ & + < x_1(t_1)x_3(t_3) >< x_2(t_2)x_4(t_4) > \\ & + < x_1(t_1)x_4(t_4) >< x_2(t_2)x_3(t_3) > \end{aligned} \tag{A.19}$$

where k_4 is the fourth order cumulant which is zero for Gaussian processes (Nicholson 1982). Applying equation (A.19) to the four point correlation terms $R_n^4(x - x', y - y')$ and $R_{nB}^4(x - x', y - y')$ we find

$$R_n^4(x - x', y - y') = R_n(x, y)R_n(x', y') + 2\left[R_n(x - x', y - y')\right]^2 \tag{A.20}$$

$$R_{nB}^4(x - x', y - y') = R_n(x - x', y - y')R_B(x - x', y - y'). \tag{A.21}$$

Using equations (A.20) and (A.21) we can now rewrite the structure functions as

$$\begin{aligned} D_{EM}(\delta\theta) = & \Psi_{EM}(\delta\theta) + 8n_o^2\left[I_1(z - \zeta, 0, n) - I_1(z - \zeta, \zeta\delta\theta, n)\right] \\ & + 4\left[I_2(z - \zeta, 0, n, n) - I_2(z - \zeta, \zeta\delta\theta, n, n)\right] \end{aligned} \tag{A.22a}$$

and

$$\begin{aligned} D_{RM}(\delta\theta) =& \Psi_{RM}(\delta\theta) + (0.81)^2 \left\{ 2n_0^2 \left[I_1(z-\zeta, 0, B) - I_1(z-\zeta, \zeta\delta\theta, B) \right] \right. \\ &+ 2B_{oz}^2 \left[I_1(z-\zeta, 0, n) - \cos(\delta\theta) I_1(z-\zeta, \zeta\delta\theta, n) \right] \\ &+ 2 \left[I_2(z-\zeta, 0, n, B) - I_2(z-\zeta, \zeta\delta\theta, n, B) \right] \\ &+ 2B_{oz}B_{oy} \sin(\delta\theta) \left[\cos(\delta\theta) I_1(z-\zeta, 0, n) - I_1(z-\zeta, \zeta\delta\theta, n) \right] \\ &\left. + \left(B_{oy}^2 - B_{oz}^2 \right) \sin(\delta\theta) I_1(z-\zeta, 0, n) \right\} \end{aligned} \tag{A.22b}$$

where

$$I_1(x-x', y-y', k) = \int_0^{L'} dz \int_0^{L} d\zeta R_k((x-x', y-y') \tag{A.22}$$

$$I_2(x-x', y-y', j, k) = \int_0^{L'} dz \int_0^{L} d\zeta R_j((x-x', y-y') R_k((x-x', y-y') \tag{A.23}$$

with j and k being either n or B and we have utilized the fact that the power spectra for the electron density (A.17) and the magnetic field (A.18) are are of the same functional form. In obtaining equation (A.22a) we have utilized the fact that

$$\int_0^{L} dz \int_0^{L} d\zeta R_n(z, 0) = \int_0^{L'} dz \int_0^{L} d\zeta R_n(\zeta, \zeta\delta\theta) \tag{A.24}$$

which arises due to the fact that the turbulence is isotropic and homogeneous. The integrals in (A.24) involve averages of the fluctuations in the electron density at two points which are always along the same line of sight. Thus through a simple rotation of the axes we see that the integrals are indeed equal for homogeneous, isotropic turbulence.

The structure functions can now be easily integrated. We will first look at the term $I_1(z-\zeta, 0)$. Inserting the power law functional form used in equations (A.17) and (A.18) we obtain

$$I_1(z-\zeta, 0, k) = \int_0^{L'} dz \int_0^{L} d\zeta \int_0^{\infty} q_r dq_r \int_{-\pi}^{\pi} dq_\phi \int_{-\infty}^{\infty} dq_z \frac{C_k^2 e^{-iq_z(z-\zeta)}}{[q_o^2 + q_z^2 + q_r^2]^{\alpha/2}} \tag{A.25}$$

where we have adopted a cylindrical coordinate system whose axis is the z axis with $q_\theta = 0°$ being parallel to the y axis. We now make the approximations that $(L,\ L') \gg l_o$ and $\delta\theta \leq 1$ rad. Since the correlation of $< \delta n(\vec{r_o})\delta n(\vec{r_o} + \vec{r}) >$ goes to zero when $|\vec{r}| \gg l_0$, we can allow the limits on the integral over the z axis to go to infinity so that we have

$$I_1(z - \zeta, 0, k) = \int_{-\infty}^{\infty} dy \int_0^L d\zeta \int_0^{\infty} q_r dq_r \int_{-\pi}^{\pi} dq_\phi \int_{-\infty}^{\infty} dq_z \frac{C_k^2 e^{iq_z y}}{[q_o^2 + q_z^2 + q_r^2]^{\alpha/2}} \tag{A.26}$$

where we have also used the substitution $y = \zeta - z$ and recall that the limits on ζ are zero and infinity. Using the definition for the Dirac delta function

$$2\pi\delta(x) = \int_{-\infty}^{\infty} dy\ e^{ixy} \tag{(A.27)}$$

we find

$$\begin{aligned} I_1(z - \zeta, 0, k) &= 4\pi^2 L \int_0^{\infty} q_r dq_r \int_{-\infty}^{\infty} dq_z \frac{C_k^2 e^{-iq_z(z-\zeta)}\delta(q_z)}{[q_o^2 + q_z^2 + q_r^2]^{\alpha/2}} \\ &= 4\pi^2 L C_k^2 \int_0^{\infty} q_r dq_r \frac{1}{[q_o^2 + q_r^2]^{\alpha/2}}. \end{aligned} \tag{A.29}$$

For the case $\alpha < 2$ we use the substitution $q_r = q_o \tan\theta$ to obtain

$$I_1(z - \zeta, 0, k) = 4\pi^2 L C_k^2 q_o^{-2\mu} \int_0^{\pi/2} d\theta \sin\theta\, (\cos\theta)^{-1-2\mu} = \frac{-4\pi^2 L C_k^2}{2\mu} \frac{1}{q_o^{2\mu}} \tag{A.30}$$

where

$$\mu = \alpha/2 - 1. \tag{A.31}$$

For $\alpha > 2$ we find

$$I_1(z - \zeta, 0, k) = \frac{1}{2\mu} \frac{4\pi^2 L C_k^2}{q_o^{2\mu}} \tag{A.32}$$

through the direct integration of equation (A.29) so that

$$I_1(z - \zeta, 0, k) = \frac{4\pi^2 L C_k^2}{2|\mu|} \frac{1}{q_o^{2\mu}} \tag{A.33}$$

for $\alpha \neq 2$.

We can now evaluate the

$$\begin{aligned} I_2(z-\zeta,0,j,k) =& \int_0^L dz \int_0^L d\zeta \int_0^\infty q_r dq_r \int_{-\pi}^{\pi} dq_\phi \int_{-\infty}^{\infty} dq_z \frac{C_j^2 e^{-iq_z(z-\zeta)}}{[q_o^2+q_z^2+q_r^2]^{\alpha/2}} \\ & \times \int_0^\infty p_r dp_r \int_{-\pi}^{\pi} dp_\phi \int_{-\infty}^{\infty} dp_z \frac{C_k^2 e^{-ip_z(z-\zeta)}}{[p_o^2+p_z^2+p_r^2]^{\alpha/2}} \end{aligned} \tag{A.34}$$

term in a very similar manner. Recall that we have assumed that the outer scale for the electron density and magnetic field turbulence are the same so that $q_o = p_o$. Using equation (A.27), the approximations for L and $\delta\theta$ and $y = \zeta - z$ we find that

$$\begin{aligned} I_2(z-\zeta,0,j,k) =& 8\pi^3 L C_j^2 C_k^2 \int_0^\infty q_r dq_r \int_{-\infty}^{\infty} dq_z \frac{1}{[q_o^2+q_z^2+q_r^2]^{\alpha/2}} \\ & \times \int_0^\infty p_r dp_r \int_{-\infty}^{\infty} dp_z \frac{1}{[q_o^2+p_z^2+p_r^2]^{\alpha/2}}. \end{aligned} \tag{A.35}$$

Now using the result (equation A.33) of the integration of equation (A.29) we find that

$$I_2(z-\zeta,0,j,k) = \frac{8\pi^3 C_j^2 C_k^2 L q_o^{1-4\mu}}{4\mu^2} \left[\int_{-\infty}^{\infty} \frac{dy}{[1+y^2]^{2\mu}}\right]^2 \tag{A.36}$$

were we have used the substitution $y = \frac{q_z}{q_o}$. Using the substitution $\tan\theta = y$ and integrating we find

$$I_2(z-\zeta,0,j,k) = \frac{8\pi^3 C_j^2 C_k^2 L q_o^{1-4\mu}}{4\mu^2} \frac{2^{4\mu-2}\Gamma(2\mu-0.5)^2}{\Gamma(4\mu-1)} \tag{A.37}$$

for $\alpha \neq 3/2$.

We now turn our attention to the integration of the $I_1(z-\zeta,\zeta\delta\theta,k)$ term. Using equations (A.17) and (A.18) we have

$$\begin{aligned} & I_1(z-\zeta,\zeta\delta\theta,k) = \\ & \int_0^L dz \int_0^L d\zeta \int_0^\infty q_r dq_r \int_{-\pi}^{\pi} dq_\phi \int_{-\infty}^{\infty} dq_z \frac{C_k^2 e^{-iq_z(z-\zeta)-iq_r\zeta\delta\theta\cos q_\phi}}{[q_o^2+q_z^2+q_r^2]^{\alpha/2}}. \end{aligned} \tag{A.38}$$

We now use equation (A.27) and the relation

$$\int_{-\pi}^{\pi} dq_\phi e^{-iq_r \zeta \delta\theta \cos q_\phi} = 2\pi J_o(q_r \zeta \delta\theta) \tag{A.39}$$

along with the approximations $L \gg l_o$ and $\delta\theta \ll 1$ to find

$$I_1(z-\zeta, \zeta\delta\theta, k) = 4\pi^2 C_k^2 \int_0^L d\zeta \int_0^\infty dq_r \frac{q_r J_o(q_r \zeta \delta\theta)}{[q_o^2 + q_r^2]^{\mu+1}} \tag{A.40}$$

where J_o is the zeroth order Bessel function. Integrating over dq_r we find

$$I_1(z-\zeta, \zeta\delta\theta, k) = 4\pi^2 C_k^2 \int_0^L d\zeta \left(\frac{\zeta\delta\theta}{q_o}\right)^\mu \frac{K_\mu(q_o \zeta \delta\theta)}{2^\mu \Gamma(\mu+1)} \tag{A.41}$$

for $\alpha > 0.5$ and K_μ is the modified Bessel function of order μ. Expanding $K_\mu(x)$ into a series,

$$K_\mu(x) = \frac{\Gamma(\mu+1)\Gamma(1-\mu)}{2\mu} \left[\sum_{m=0}^{\infty} \frac{\left(\frac{x}{2}\right)^{2m-\mu}}{m!\Gamma(m-\mu+1)} - \sum_{m=0}^{\infty} \frac{\left(\frac{x}{2}\right)^{2m+\mu}}{m!\Gamma(m+\mu+1)} \right] \tag{A.42}$$

we find

$$\begin{aligned} I_1(z-\zeta, \zeta\delta\theta, k) = & \frac{2\pi^2 C_k^2 L \Gamma(1-\mu)}{\mu 2^\mu q_o^{2\mu}} \left[\sum_{m=0}^{\infty} \frac{2^{\mu-2m} (q_o L \delta\theta)^{2m}}{m!\Gamma(m-\mu+1)\,(2m+1)} \right. \\ & \left. - \sum_{m=0}^{\infty} \frac{2^{-\mu-2m} (q_o L \delta\theta)^{2m+2\mu}}{m!\Gamma(m+\mu+1)\,(2\mu+2m+1)} \right]. \end{aligned} \tag{A.43}$$

.

Finally we have the integration of the

$$\begin{aligned} & I_2(z-\zeta, \zeta\delta\theta, j, k) = \\ & \int_0^L dz \int_0^L d\zeta \int_0^\infty q_r dq_r \int_{-\pi}^{\pi} dq_\phi \int_{-\infty}^{\infty} dq_z \frac{C_j^2 e^{-iq_z(z-\zeta) - iq_r \zeta\delta\theta \cos q_\phi}}{[q_o^2 + q_z^2 + q_r^2]^{\alpha/2}} \\ & \times \int_0^\infty p_r dp_r \int_{-\pi}^{\pi} dp_\phi \int_{-\infty}^{\infty} dp_z \frac{C_k^2 e^{-ip_z(z-\zeta) - ip_r \zeta\delta\theta \cos p_\phi}}{[q_o^2 + p_z^2 + p_r^2]^{\alpha/2}} \end{aligned} \tag{A.44}$$

term where we have already assumed that the outer scale for the two power laws are the same. Again we now use equations (A.27) and (A.39) along with the approximations $L \gg l_o$ and $\delta\theta \ll 1$ to find

$$I_2(z-\zeta,\zeta\delta\theta,k,j) = 8\pi^3 C_k^2 C_j^2 \int_0^L d\zeta \int_{-\infty}^{\infty} dq_z \int_0^{\infty} dq_r \frac{q_r J_o(q_r\zeta\delta\theta)}{[q_o^2+q_r^2+q_z^2]^{\mu+1}} \int_0^{\infty} dp_r \frac{p_r J_o(p_r\zeta\delta\theta)}{[q_o^2+p_r^2+q_z^2]^{\mu+1}} \tag{A.45}$$

where the Dirac delta function from the integration over dz has set $p_z = q_z$. From the integration of equation (A.40) we see that

$$I_2(z-\zeta,\zeta\delta\theta) = \frac{8\pi^3 C_j^2 C_k^2}{2^{2\mu}\Gamma(\mu+1)^2} \int_0^L d\zeta \int_{-\infty}^{\infty} dq_z \left(\zeta\delta\theta\right)^{2\mu} \left(q_o^2+q_z^2\right)^{-\mu} \left[K_\mu(\zeta\delta\theta\sqrt{q_o^2+q_z^2})\right]^2. \tag{A.46}$$

Using equation (A.42) to expand equation (A.46) and then integrating we get the result

$$\begin{aligned} I_2(z-\zeta,\zeta\delta\theta,j,k) = {} & \frac{2\pi^3 C_j^2 C_k^2 q_o^{-4\mu}\Gamma(1-\mu)^2}{2^{2\mu}(\delta\theta)\mu^2} \\ \times \sum_{m=0}^{\infty}\sum_{n=0}^{\infty} \Bigg[& \frac{2^{-2-4(m+n)+6\mu}\left(Lq_o\delta\theta\right)^{2(m+n)+1}\Gamma(2\mu-m-n-.5)^2}{m!n!\Gamma(m-\mu+1)\Gamma(n-\mu+1)(2m+2n+1)\Gamma(4\mu-2m-2n-1)} \\ & + \frac{2^{-2-4(m+n)-2\mu}\left(Lq_o\delta\theta\right)^{2(m+n)+4\mu+1}\Gamma(-m-n-.5)^2}{m!n!\Gamma(m+\mu+1)\Gamma(n+\mu+1)(4\mu+2m+2n+1)\Gamma(-2m-2n-1)} \\ & - \frac{2^{-1-4(m+n)+2\mu}\left(Lq_o\delta\theta\right)^{2(m+n)+2\mu+1}\Gamma(\mu-m-n-.5)^2}{m!n!\Gamma(m+\mu+1)\Gamma(n-\mu+1)(2m+2n+2\mu+1)\Gamma(2\mu-2m-2n-1)} \Bigg]. \end{aligned} \tag{A.47}$$

Upon performing the integrations and keeping the lowest order terms in $\delta\theta$ since $L \gg l_o$ and $\delta\theta \ll 1$ rad we find

$$D_{EM}(\delta\theta) = 4C_n^2\left[f(\alpha)n_o^2 + g(\alpha)q_o^{1-2\mu}C_n^2\right] L^{2\mu+1}\delta\theta^{2\mu} \tag{A.48}$$

$$\begin{aligned} D_{RM}(\delta\theta) = {} & (0.81)^2\left[f(\alpha)\left(n_0^2C_B^2 + B_{oz}^2C_n^2\right) + C_n^2C_B^2 g(\alpha)q_o^{1-2\mu}\right] \\ & \times L^{2\mu+1}\delta\theta^{2\mu} \end{aligned} \tag{A.49}$$

for $0.5 < \alpha < 4$ and $\alpha \neq 1.5, 2$ where

$$\mathrm{f}(\alpha) = \frac{4\pi^2\Gamma(1-\mu)}{2^{2\mu}(2\mu+1)\mu\Gamma(1+\mu)} \tag{A.50}$$

and

$$\mathrm{g}(\alpha) = \frac{2\pi^3\Gamma(\mu-0.5)^2\Gamma(1-\mu)}{\mu^2(2\mu+1)\Gamma(2\mu-1)\Gamma(1+\mu)}. \tag{A.51}$$

REFERENCES

Armstrong, J. W., Coles, W. A., Kojima, M. and Rickett, B. J. 1990 Ap.J., 358, 686

Armstrong, J. W., Rickett, B. J. and Spangler, S. R. 1995 Ap.J., 443, 209

Bavassano, B. and Bruno, R. 1995, JGR, 100, 9475

Bent, R.B., Llewellyn, S.K. and Schmid, P.E. 1972 Space Res. XII, 1185

Bignell, C. 1982, Polarimetry, in Synthesis Mapping: Proceedings of the NRAO-VLA Workshop, edited by A. R. Thompson and L. R. D'Addario, Lect. Ser. 6

Bilitza, D. 1986 Radio Sci., 21, 343

Bilitza, D. 1985 Adv. Space Res. 5, 15

Broten, N. W., Macleod, J. M.and Vallée, J. P. 1987, Ap.Sp.Sci., 141, 303

Bykov, A.M. and Toptygin, I.N. 1987, Ap&SS, 138, 341

Cesarsky, C. J. 1980 ARA&A, 18, 289

Chapman and Bartels, 1940, Geophysics, Oxford

Chevalier, R. and Fransson, C. 1984 Ap.J. (Letters), 279, L43

Ching, B.K. and Chui, Y.T. 1973 J. Atm. Terr. Phys. 35, 1615

Chiu, Y. T. 1975, J. Atm. Terr. Phys., 37, 1563

Cioffi, D. F. and Jones, T. W. 1980 A.J., 85, 368

Clark, B. G. 1980 Astr.Ap., 89, 377

Clegg, A. W., Cordes, J. M., Simonetti, J. H. and Kulkarni, S. R. 1992 Ap.J., 386, 143

Condon, J. J. and Broderick, J. J. 1986 A.J., 92, 94

Cordes, J. M. and Lazio, T. J. W. 1995, BAAS, 27, 885

Cordes, J. M., Weisberg, J. M. and Boriakoff, V. 1985 Ap.J., 288, 221

Cox, D. P. 1988, in Supernova Remnants in the Interstellar Medium, IAU Colloquium 101, R. S. Roger and T. L. Landecker, ed., Oxford Univ. Press, p 73

Davies, K. 1965 Ionospheric Radio Propagation, National Bureau of Standards Monograph 80

Davies, K., Fritz, R.B., Grubb, R.N. and Jones, J.E. 1975 Radio Sci., 10, 785

Ferriere, K.M., Zweibel, E.G. and Shull, J.M. 1988, Ap.J., 332, 984

Garrington, S.T., Leahy, J.P., Conway, R.G. and Laing, R.A. 1988 Nature, 331, 147

Gauss, C.F. 1839, Allgemeine Theorie Des Erdmagnetismus, in "Resultate aus den Beobachtungen des Magnetischen Vereins im Jahre 1838", Ed. C.F. Gauss and W. Weber, Weidmann, Leipzig

Ge, J. P. and Owen, F. N. 1993 A.J.,105, 778

Higdon, J.C. 1984 Ap.J., 285, 109

Higdon, J.C. 1986 Ap.J., 309, 342

Hollweg, J. V., Bird, M. K., Volland, H., Edenhofer, P., Stelzried, C. T. and Seidel, B. L. 1982, J. Geophys. Research, 87, 1

Kennicutt Jr., R. C. and Bresolin, F. 1995, A.J., 109, 594

Kraus, J. D 1986, in Radio Astronomy 2nd edition, Cygnus-Quasar Books, Ohio

Kulsrud, R.M. and Pearce, W.P. 1969 Ap.J., 156, 445

Laing, R.A. 1988 Nature, 331, 149

Lazaryan, A.L. and Shutenkov, V.P. 1990, Sov. Astron. Letters, 16, 297

Lazio, T. J., Spangler, S. R. and Cordes, J. M. Ap.J., 363, 515

Marsch, E. 1991 "MHD Turbulence in the Solar Wind", in Physics of the Inner Heliosphere 2, R. Schwenn and E. Marsch, editors, (Springer Verlag: Berlin)

McIvor, I. 1977 M.N.R.A.S., 178, 85

Minter, A. H. and Spangler, S. R. 1992 "Precision Correction of Radioastronomical Polarization Measurements for Ionospheric Faraday Rotation", Bull. Am. Astron. Soc., 24, 743

Molnar, L. A., Mutel, R. L., Reid, M. J. and Johnston, K. J. 1995 Ap.J., 438, 708

Nicholson, D. R. 1982, Statistical Theories of Fluid Turbulence, University of Iowa Research Report 82-20, p. 110

Osterbrock, D. E. 1989 Astrophysics of Gaseous Nebulae and Active Galactic Nuclei, University Science Books, Mill Valley, Ca.

Peddie, N. W. 1982 J. Geomagn. Geoelectr., 34, 309

Perley, R.A., Schwab, F.R. and Bridel, A.H. 1989, "Synthesis Imaging in Radio Astronomy", Astronomical Society of the Pacific Conference Series, Volume 6

Press, W.H, Flannery, B.P, Teukolsy, S.A. and Vetterling, W.T 1989 in "Numerical Recipes", p 472, Cambridge University Press

Ramanamurty, Y.V. and Rawer, K. 1990, Adv. Space Res. 10(8), 15, 35

Rand, R. J. and Kulkarni, S. R. 1989 Ap.J., 343, 760

Rand, R. J. and Lyne, A. G. 1995 M.N.R.A.S., 268 , 497

Rand, R. J. 1994, To Appear In Gas Disks in Galaxies, Proceedings of IAU Joint Discussion 1

Ratcliffe, J.A. and Weekes, K. 1960 "Physics of the Upper Atmosphere", Academic Press, New York

Rawer, K. and Bilitza, D. 1989 J. Atm. Terr. Phys., 51, 781

Reynolds, R. J. 1980 Ap.J., 236, 153

Reynolds, R. J. 1988 A.J., 96, 670

Reynolds, R. J. 1990 Ap.J., 349, L17

Reynolds, R. J. 1991 Ap.J. (Letters), 372, L17

Reynolds, R. J., Tufte, S. L., Kung, D. T., Mc Cullough, P. R. and Heiles, C. 1995 Ap.J., in press.

Rickett, B. J. 1990 Ann. Rev. Astr. Ap. 28, 561

Rikitake, T. and Honkura, Y. 1985 Solid Earth Geomagnetism, Terra Scientific Publishing Company, Tokyo

Rotterging, H.J.A, Lacy, M., Miley, G.K., Chambers, K.C. and Saunders, R. 1994 Astr.Ap.Suppl.,108,79

Sakurai, T. and Spangler, S. R. 1994 Radio Science, 29, 635

Sancisi, R. 1984 In Galactic Radio Astronomy, IAU Symposium No. 60, edited by F. J. Kerr and S. C. Simonson III, p. 115

Simard-Normandin, M. and Kronberg, P. P. 1980 Ap.J., 242, 74

Simard-Normandin, M., Kronberg, P. P. and Button, S. 1981 Ap.J.Suppl., 45, 97

Simonetti, J. H., Cordes, J. M. and Spangler S. R. 1984 Ap.J., 284, 126

Simonetti, J. H. and Cordes, J. M. 1986 Ap.J., 310, 160

Simonetti, J. H. and Cordes, J. M. 1988 in Radio Wave Scattering In The Interstellar Medium, AIP Conference Proceedings 174, p. 135, ed: Cordes, J. M., Rickett, B. J. and Backer, D. C.

Spangler, S. R., Fanti, R.,Gregorini, L. and Padrielli, L. 1989 Astr.Ap., 209, 315

Spangler, S. R. 1991 Ap.J., 376, 540

Spoelstra, T. A. 1977 Usp. Fiz. Nauk, 121, 679

Spoelstra, T. A. 1984 Astr.Ap., 135, 238

Taylor, J. H. and Cordes, J. M. 1993 Ap.J., 411, 674

Taylor, J. H., Manchester, R. N. and Lyne, A. G. 1993 Ap.J.Suppl.,88,529

Tenorio-Tagle, G. and Bodenheimer, P. 1988, Ann.Rev.Astr.Ap., 26, 145

Thompson, A. R., Moran, J. M. and Swenson Jr., G. W. 1991, in Interferometry and Synthesis in Radio Astronomy

Vallée, J.P. 1984 Astr.Ap., 136, 373

Valley, S.L. 1965 "Handbook of Geophysics and Space Environments", Air Force Cambridge Research Laboratories

Walterbos, R. A. M. and Braun, R. 1994 Ap.J., 431,156

Wilkinson, A. and Smith, F.G. 1974, M.N.R.A.S., 167, 593

Wilkinson, P. N., Narayan, R. and Spencer, R. E. 1994 M.N.R.A.S., 269, 67

Zank, G. P. and Matthaeus, W. H. 1992 J. Plasma Phys., 48, 85